DET NATURVIDENSKABELIGE FAKULTET
KØBENHAVNS UNIVERSITET

Generation and application of entanglement of room temperature ensembles of atoms

PhD thesis

Hanna Krauter

Danish National Research Foundation
Center for Quantum Optics (QUANTOP)
Niels Bohr Institute
Graduate School of Science

Academic supervisor: Prof. Eugene S. Polzik
Evaluation committee:
NBI local head: Prof. Per Hedegård
External referees: Prof. Tilman Pfau
Prof. Anna Sanpera

Thesis submitted: 11.1.2011
Defense date: 21.2.2011

Summary

In this thesis different experiments on entanglement involving room temperature ensembles of Cesium atoms are described. The key ingredient is a controlled dispersive interaction of a light field with the ensemble of atoms. To this end the previously existing description of the light atom interface was refined. With this new understanding an experiment on steady state entanglement between the spin states of two atomic ensembles was proposed and experimentally realized.

With a completely different approach, spin squeezing of the collective spin state of an atomic ensemble was generated. The spin noise reduction relies on the creation of superposition states within the single atoms of the ensemble via a Raman transition. The atomic state is reconstructed and squeezing of approximately 3dB is reported.

One application of entanglement is quantum teleportation. In the presented setup a light state was teleported successfully to a single atomic ensemble. Light atom entanglement generated by dispersive interaction was used as a resource together with quantum measurement and feedback to realize the state transfer with a fidelity exceeding the classical benchmark.

Resumé

Denne afhandling beskriver forskellige eksperimenter med ensembler af cæsiumatomer ved stuetemperatur. Det vigtigste indhold er en undersøgelse af, hvordan lys og atomer vekselvirker på en kontrolleret måde, når lyset har en frekvens relativt langt fra atomernes egenfrekvens. I dette arbejde udvikles en mere præcis beskrivelse af visse detaljer ved denne vekselvirkning end hvad tidligere er blevet præsenteret. Denne nye beskrivelse bruges til at foreslå og udføre et eksperiment, der viser at to atomare ensembler er i en ligevægtstilstand, hvori de er sammenfiltrede ("entangled").

I en anden sammenhæng beskrives et andet eksperiment, der viser, at det er muligt at "squeeze" det atomare ensembles samlede "spin"-tilstand. Reduktionen i støjen af spintilstanden skyldes at de enkelte atomer er i en superpositionstilstand tilvejebragt via Ramanovergange. Den atomare tilstand blev rekonstrueret og her rapporteres det, at den observerede squeezing var 3dB.

En mulig anvendelse af sammenfiltring er i forbindelse med kvanteteleportation. Her præsenteres et eksperiment, hvor det lykkedes at teleportere en kvantetilstand fra lysfeltet til det atomare ensemble. Processen havde en højere "fidelity", end hvad der er muligt ved klassiske vekselvirningsprocesser.

Abstract

In this thesis different experiments on entanglement involving a room temperature ensemble of Cesium atoms are described. The key ingredient is a controlled dispersive interaction of a light field with the ensemble of atoms which can be combined with quantum measurement and feedback. Based on this light atom interface several experiments on entanglement generation and application are realized. Steady state entanglement between two macroscopic ensembles of atoms is reported on and spin squeezing of a single ensemble due to internal single atom entanglement is reported on. Finally, light atom entanglement is utilized to realize quantum teleportation of a light state to an atomic ensemble.

Preface

This thesis represents an attempt to present most of the work that I have been a part of in the research group of professor Eugene Polzik in QUANTOP (the Danish National Research Foundation Center for Quantum Optics) at the Niels Bohr Institute, University of Copenhagen.

The experimental setup in which all described experiments were realized was - though always under continuous development - to a large extend present when I joined the group and a lot of the details can be found in PhD theses of previous students [JSC+04, SJP07]. I repeat some aspects here where I find it instructive for understanding. Part of the experimental achievements discussed in the course of the thesis are also published in [1, 2, 3, 4, 7, 10].

All of the experimental efforts reported on have been achieved as a group effort under the conduct of Eugene Polzik. Due to the close collaboration with the PhD students Jacob Sherson and Kasper Jensen, there is a certain overlap with their PhD theses. The names of everyone who I have been cooperating with for specific achievements are represented in the author listings of the relevant publications, but I want to name some of my coworkers here, to all of whom I am very grateful.

The teleportation experiment was performed together with Jacob Sherson, of whom I received my introduction to the experiment and who has invested a huge amount of time in helping me to get acquainted with the setup and theory of the experiment. Shortly after, Thomas Fernholz joined the group as a post doc and working together with him on the single atom squeezing experiment has been very inspirational and instructive. Partly due to my family extension, my PhD period has a big overlap with Kasper Jensen, and our long successful teamwork included work on the spin squeezing experiment and the steady state entanglement. Wojtek Wasilewski joined the group in my absence and worked out new ideas for both the theoretical understanding and the experimental realization of the experiment. The discussions with him supplied me with new insight to the experiment. The realization of steady state atomic entanglement was accompanied by a close collaboration with the theorist Christine Muschik and her supervisor Ignacio Cirac. Lately Jonas Meyer Petersen has joined the group and has contributed to the atomic entanglement

experiment. Jonas Neergaard Nielsen and Bo Meholt cooperated with us when the squeezed light source was used on the experiment and waited patiently for our lengthy calibration measurements.

I thank my advisor Eugene Polzik for all of his support and valuable mentoring in the course of my PhD. I also want to thank Jörg Helge Müller for his patient instruction on daily experimental and all other issues amongst others the writing of my thesis. Also, I want to thank Anders Sørensen who advised me on theoretical problems.

It has been a great pleasure working together with all the Quantoppies. The good atmosphere in the group has made this experience a pleasure.

I want to conclude with expressing my thankfulness to my family, old and new, without whose understanding it would not have been possible to accomplish any of this.

Contents

Chapter 1

Introduction

The chore topic of this thesis, atomic entanglement, is a research field with great activity today. Already since its conceptual origin - the widely known paper of Einstein, Podolsky and Rosen [EPR35] - entanglement has been one of the most controversial and discussed elements of quantum mechanics. This, as Einstein put it "spukhafte Fernwirkung" ("spooky action in the distance" [Ein71]), was attempted to be explained by hidden variables, which would elucidate the strange connection of two systems separated in space. However, John Bell [B+64] introduced inequalities, which showed a discrepancy between predictions made by quantum mechanics and any local hidden variable theory. This way he formed an indicator, which could be used to test quantum theory. If one were able to produce an entangled pair, correlation measurements on the two constituents in different bases should yield a number that would contradict any classical, local theory. In [CS78] several experiments were introduced that granted the possibility of such an investigation.
The first entanglement - and violation of Bell's inequality was shown with polarization entangled photons, emitted in a radiative atomic cascade [ADR82]. Later continuous variable entanglement similar to entanglement originally proposed in [EPR35] was realized for the quadratures of two light beams [OPKP92]. This kind of entanglement experiment does not display any violation of Bell's inequality due to the Gaussian nature of the light states and the homodyne measurement scheme, but the inseparability of the states of the two components can be shown elsewise [DGCZ00].

Atomic entanglement proved to be harder to achieve. The main difficulty - to engineer an entangling interaction between two atomic systems - was first solved by the exchange of a single photon of two Rydberg atoms in a cavity [HMN+97]. Shortly after, deterministic two atom entanglement was shown in ion traps [TWK+98]. Many experimental realizations of quantum information ideas followed in ion traps. Despite enormous experimental complexity, those

setups pocess tremendous advantages compared to other systems due to unmatched long lifetimes and a high degree of control [RLR+04, LOJ+05].

The first atomic entanglement of continuous variables was established by a collective quantum non demolition measurement (QND) on two macroscopic atomic ensembles in the setup that is the basis of all experiments discussed in this thesis [JKP01]. The QND approach has since become one of the standard spin squeezing techniques used in several experiments [KMB00, AWO+09, TVLK08, TFNT09, SSLV10].

One of the reasons for the apparent high interest nowadays in achieving and improving entanglement between different systems is rooted in more than the desire to make a point in supporting quantum mechanics. The fields of quantum communication and quantum information rely heavily on entanglement as a resource. For instance, to overcome the limitations of quantum communications, due to imperfect communication channels, the idea of a repeater [BDCZ98] was brought forward. Moreover, the concept of quantum networks [Kim08] depends on coupling between stationary systems (memories) and information carriers. The interface between atomic ensembles and light is one possible realization. An example is the scheme for quantum communication between two atomic ensembles proposed by Duan, Lukin, Cirac and Zoller (DLCZ) [DLCZ01], which has quantum memories, and single pairs of entangled photons as building blocks. That this approach is not too far from reality becomes clear considering that in [CDRF+05] the generation of entanglement between two atomic memories, following this idea was reported. The two atomic systems are two distant atomic ensembles, consisting of 10^5 Cesium atoms in a MOT.

A whole range of other fields of research are directed towards establishing the required resources for quantum information processing [ZBB+05], amongst others are cavity QED and several solid state systems such as quantum dots, superconducting qubits and impurity spins in solids. A lot of experimental and theoretical efforts lie in the discrete regime with qubits as the basic components. However, also for continuous variables there is a lot of development in the field of quantum communication and information [BvL05, CCLP07].

Another - more straight forward - application of entanglement and squeezing is the improvement of metrology experiments, such as atomic clocks, and atomic spectroscopy [PMM05, KBM98, LBS+04, RCK+06].

In this thesis I will report on different experiments on entanglement of the collective spins of a macroscopic atomic system at room temperature. The basis of the experiments is an atom light quantum interface, where light is coupled off resonantly to a well prepared atomic ensemble. An illustration of the experimental scenario is shown in figure 1.1. Part of the presented work is devoted

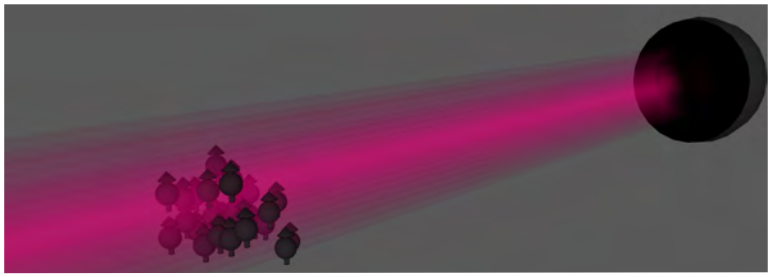

Figure 1.1: An ensemble of oriented atoms interacting with light. After the interaction the light is measured. Those components are the key ingredients for teleportation, light-atom and atom-atom entanglement.

to establish a more accurate understanding of the underlying dispersive interaction of light with oriented atomic ensembles.

The interaction leaves the atoms and the light in an entangled state. This entanglement can be utilized to realize teleportation of a light state on to the atoms [1]. The correlations between light and atoms can also be used to two-mode squeeze the spins of two atomic ensembles by a measurement on light. In an earlier realization in the same setup [JKP01] the entanglement lifetime was limited due to different decoherence mechanisms. In recent years a new concept of generating quantum states has been brought forward where carefully designing the environment of the system of interest leads to a situation where the system is dissipatevly driven into the desired state ([PCZ96, KBD+08, VWC09, VMC10] and many others). Combining this thought with the original idea of measurement induced squeezing and a better understanding of the light atom interface enabled us to produce an atomic steady state in which two atomic ensembles are entangled. Such an experiment can be run over hours and the atomic ensembles remain entangled. This means that one just has to turn the interaction "off" to have readily available entanglement [7].

With a totally different scheme, internal entanglement of the spin of single atoms can be prepared. Again a dispersive light interaction is used to control the atomic system. Via a Raman process it is possible to reach a situation, where the single atoms are in a superposition state of the internal level structure - leading to the possibility of reduced spin noise. This way squeezed spin states of the collective ensemble can be produced [2].

The mentioned experiments which are the main topic of this thesis cover a wide range of the field of quantum optics. Therefore, their concepts are put into perspective of the respective fields in the introduction of the relevant chapters.

This work is divided in three parts: the theoretical background containing chapters 2 and 3, the experimental methods with chapters 4 and 5 and finally the description of the experiments on generation and application of entangle-

ment in chapters 6, 7 and 8.
To specify, the theory behind the underlying light atom interface is presented in chapters 2 and 3. While chapter 2 gives a summary of a previously established theoretical approach [HSP10, She06], whose understanding is essential for the discussed experiments, chapter 3 gives a detailed description of the extension of the theory for higher coupling ranges.

In chapter 4 the details of the experimental system are disclosed, including characteristic measures of atoms and light. Chapter 5 is concerned with the quantum noise properties of the atomic and light system. In this context different kinds of entanglement are introduced together with an entanglement criterion based on the noise properties of the entangled systems.

Chapter 6 details the experiment on teleportation of a light state onto an atomic ensemble and the theory behind the experiment. In chapter 7 an experiment on spin squeezing of an atomic ensemble by squeezing the spin of the single atoms is presented. And finally in chapter 8 the generation of atomic steady state entanglement is detailed.

The thesis in concluded with a short summary of other experiments, that have been conducted in the same experimental setup, during the time between the start and end of my PhD. I close with a conclusion and outlook.

Part I

Theoretical background

Chapter 2

Light atom interface

In this chapter I will discuss the light-atom interface that provides the basis for the experiments discussed in the thesis (in accordance with [SJP07, HSP10],[3]). The applied dispersive interaction of a macroscopic light beam with an ensemble of atoms at room temperature will turn out to be a versatile tool to implement a great number of different interesting experiments at the quantum level.

The two macroscopic systems that are used, namely light and atoms, are characterized by continuous variables (CV). For the different quantum experiments discussed later, it is often useful to consider canonical operators which will be introduced in the first section. Then, the interaction will be described in detail and the following, simple equations will be used throughout the entire thesis.

2.1 Light and atoms

When talking about an interface of two different systems, it is convenient to have a common language to handle both systems. When experiments are discussed that involve a state transfer (as in chapter 6 and section 9.2) this is even a necessity. As mentioned above, we chose to describe our systems in the language of canonical operators $\hat{x}$ and $\hat{p}$ with $[\hat{x}, \hat{p}] = i$ and the variances[1]:

$$\mathrm{Var}(\hat{x}) \cdot \mathrm{Var}(\hat{p}) \geq \frac{1}{4} \tag{2.1}$$

which will be introduced in the following. The discussion of the dynamics of the system will be carried through in the Heisenberg picture.

[1] $\mathrm{Var}(\hat{O}) = \langle (\hat{O} - \langle \hat{O} \rangle)^2 \rangle$, $\hbar = 1$

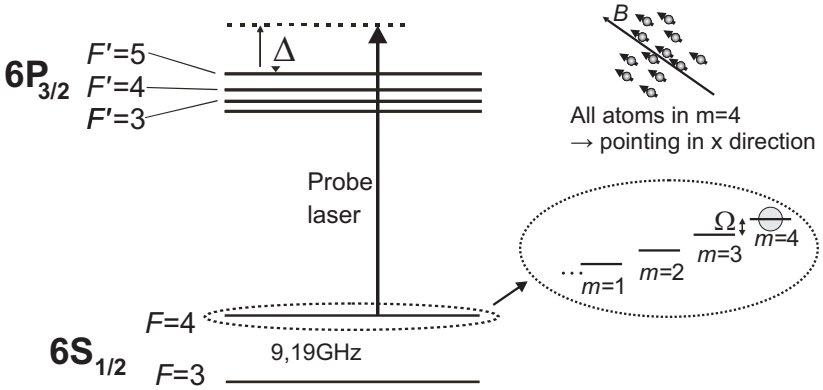

Figure 2.1: Level scheme of Cesium. The figure on the left shows the level scheme of the D_2 line of Cesium. All the atoms are pumped into the $F = 4, m = 4$ state such that they are oriented along x. The magnetic field leads to a splitting of the magnetic sublevels by the Larmor frequency Ω.

2.1.1 Atomic variables

The atomic system consists of an ensemble of about $10^{11} - 10^{12}$ Cesium atoms at room temperature situated in a glass cell. The corresponding experimental details will be discussed in depth in section 4.1.1.

The considered atomic variables are the projections of the collective internal angular momentum of all atoms in the different directions, given by the sum of the total angular momenta of the individual atoms $\hat{f}_i^k$:

$$\hat{J}_i = \sum_k^{N_a} \hat{f}_i^k \tag{2.2}$$

with $i = x, y, z$. Since the ensemble contains such a vast amount of atoms those spin variables are quasi continuous. The collective spin follows, as do the individual spins, the commutation relation of angular momentum[2],

$$[\hat{J}_y, \hat{J}_z] = i\hat{J}_x, \tag{2.3}$$

so the Heisenberg uncertainty principle for the variances reads

$$\mathrm{Var}(\hat{J}_y) \cdot \mathrm{Var}(\hat{J}_z) \geq \frac{\langle J_x \rangle^2}{4}. \tag{2.4}$$

In our setting, the atomic spins are all oriented along the x-direction. This is achieved by pumping the atoms optically into $F = 4, m = 4$ of the $6S_{1/2}$ ground state (see figure 2.1), the method of which will be discussed in section 4.1.2. The maximal value of the spin component in x-direction is $J = 4 \cdot N_a$,

[2] $\hbar = 1$

where N_a is the number of atoms. The spins $\hat{J}_y, \hat{J}_z$ of the fully oriented state in the perpendicular directions follow Gaussian probability distributions with a mean value of 0 and a minimum uncertainty meaning that the variances $\mathrm{Var}(\hat{J}_y) = \mathrm{Var}(\hat{J}_z) = \frac{J}{2}$. This is easily understood. We consider all atoms in $F = 4, m = 4$. Since there are many independent atoms, we can assume $\langle J_x^2 \rangle = \sum \langle (j_x^i)^2 \rangle \approx F^2 \cdot N_a$ and therefore,

$$\begin{aligned} \mathrm{Var}(\hat{J}_y) &= \langle \hat{J}_y^2 \rangle = \langle \hat{J}_z^2 \rangle = \sum_k \langle \hat{j}_y^k \rangle^2 = \frac{F \cdot (F+1) N_a - \langle J_x^2 \rangle}{2} \\ &= \frac{F}{2} \cdot N_a = \frac{J}{2}. \end{aligned} \tag{2.5}$$

This minimum uncertainty state is called a coherent spin state (CSS) and is the starting point of all our experiments.

For highly oriented many atom systems we can use the Holstein-Primakoff approximation [HP40, Kit63]. We identify the fully oriented state as the ground state of a harmonic oscillator and introduce collective atomic creation and annihilation operators $b^\dagger$ and b. Then $\hat{J}_x = J - b^\dagger b$ is decreased along with every atomic excitation. On the right of figure 2.1 the atomic level structure of the hyperfine ground state we use (F=4) is drawn. All the atoms start in the $m = 4$ ground state and an excitation in the described formalism leads to one atom in the $m = 3$ state distributed over the whole ensemble. We introduce the canonical atomic operators

$$\hat{x} = \frac{\hat{J}_y}{\sqrt{J}} \approx \frac{1}{\sqrt{2}}(\hat{b} + \hat{b}^\dagger), \quad \hat{p} = \frac{\hat{J}_z}{\sqrt{J}} \approx \frac{-i}{\sqrt{2}}(\hat{b} - \hat{b}^\dagger), \tag{2.6}$$

which follow the commutation relation $[\hat{x}, \hat{p}] \approx i$.
When evaluating experiments, we normalize the transversal spin components by the mean of the macroscopic spin over the interaction time $\langle J_x \rangle$ instead of J. In this way, the commutator is kept constant also when the mean spin is slightly reduced, e.g. due to decay or losses. This is exceedingly important, when we evaluate the noise properties of the atomic states as the commutator sets the minimum uncertainty noise.

In figure 2.2 a phase space diagram for a displaced atomic coherent state is shown. Note that the displacement is connected to the collective excitation

$$d = \sqrt{\hat{x}^2 + \hat{p}^2} = \sqrt{\hat{n}_a + \tfrac{1}{2}} \tag{2.7}$$

with $\hat{n}_a = b^\dagger b$.

I want to add here that the Holstein-Primakoff approximation is very convenient and will supply us with a very intuitive picture of the experiment. How-

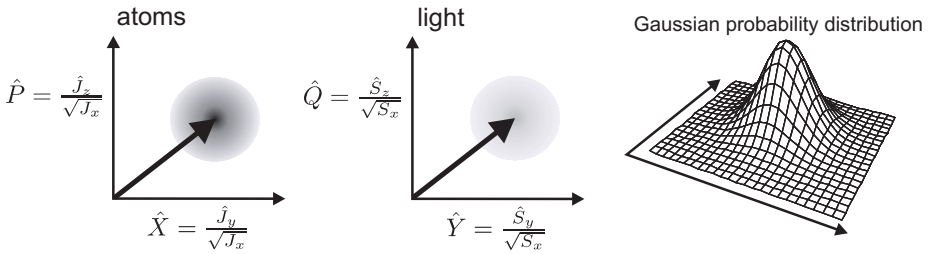

Figure 2.2: Phase space diagrams for the quadratures of light and atoms. The variables follow Gaussian probability distributions. The displacements are given by the number of excitations of the atomic state and the number of photons in the quantum polarization. Note that those numbers are very small compared to the total number of photons and atoms.

ever, in some situations which need to be carefully evaluated the theory will still hold, even if we venture further away from the CSS, assuming we normalize with the true length of the macroscopic spin $\langle J_x \rangle$ and not its maximal value J. In this way the commutator of $\hat{x}$ and $\hat{p}$ is still held approximately constant, the noise properties might change dramatically, though.

In the experiment a magnetic field is added in the x-direction. This is described by the Hamiltonian $\hat{H}_B = \hbar\Omega\hat{J}_x$ which leads to a precession of $\hat{J}_y$ and $\hat{J}_z$ around the x-axis with the Larmor frequency Ω. Ω is given by the magnetic field $\Omega = g_F\mu_B/\hbar B$. In our case, with a magnetic field B of around 0.9 Gauss, this frequency lies at 2π320 kHz. In the following, the operators in the rotating frame are often the variables of interest:

$$\hat{x}' = \hat{x}\cos(\Omega t) \pm \hat{p}\sin(\Omega t) \tag{2.8}$$

$$\hat{p}' = \hat{p}\cos(\Omega t) \mp \hat{x}\sin(\Omega t). \tag{2.9}$$

The lower signs indicate the setting, where the macroscopic spin is oriented opposite to the magnetic field. Note that the definition of $\hat{x} = \pm\hat{J}_y/\sqrt{\langle J_x \rangle}$ changes sign for the two different orientations.
The creation operator in the rotating frame reads:

$$\hat{b}' = \frac{1}{\sqrt{2}}(\hat{x}' + i\hat{p}') = \hat{b}e^{\mp i\Omega t} \tag{2.10}$$

Later I will drop the prime for the operators in the rotating frame as those are the operators of interest.

2.1.2 Light Variables

To represent the light propagating in z-direction we look at the Stokes operators which characterize the polarization state of light. They are given by the differences of the number operators $\hat{n}_{\text{pol}}$ of the photons polarized in different orthogonal bases.

$$\begin{aligned} \hat{S}_x &= \tfrac{1}{2}(\hat{n}_x - \hat{n}_y), \\ \hat{S}_y &= \tfrac{1}{2}(\hat{n}_{+45^\circ} - \hat{n}_{-45^\circ}), \\ \hat{S}_z &= \tfrac{1}{2}(\hat{n}_{\text{rh}} - \hat{n}_{\text{lh}}), \end{aligned} \tag{2.11}$$

where the indices x, y of $\hat{n}_{\text{pol}}$ label photons polarized in x- or y-direction and $\pm 45^\circ$ the photons polarized in $\pm 45^\circ$-direction, while $\hat{S}_z$ is given by the difference of the number of right hand and left hand polarized photons. The Stokes operators are quantities for which measurement is fairly straightforward (see section 4.1.3), whereas the discussed atomic operators are much harder to access. The Stokes operators follow the commutation relations of angular momentum

$$[\hat{S}_y, \hat{S}_z] = i\hat{S}_x. \tag{2.12}$$

In the experiment we have a strong coherent light pulse, which is polarized in the x- or y-direction. In that way, S_x becomes a large classical value proportional to the flux of photons. Similar to the case of the atoms the considered variables are then canonical operators y and q, given by:

$$\hat{y} = \frac{\hat{S}_y}{\sqrt{|S_x|}}, \quad \hat{q} = \pm\frac{\hat{S}_z}{\sqrt{|S_x|}} \rightarrow [\hat{y}, \hat{q}] \approx i. \tag{2.13}$$

where the two signs stand for x- or y-polarized light. When we consider a y-polarized local oscillator, which is the setting in all experiments discussed in this thesis, those variables are the quadrature operators of light in x-polarization:

$$\hat{y} = \frac{1}{\sqrt{2}}(\hat{a}_x + \hat{a}_x^\dagger), \quad \hat{q} = \frac{1}{\sqrt{2}i}(\hat{a}_x - \hat{a}_x^\dagger) \tag{2.14}$$

with the creation and annihilation operators $\hat{a}_x, \hat{a}_x^\dagger$. This means that there is a strong classical field polarized in y-direction (local oscillator) and the weak quantum field, which we are interested in, polarized in x-direction.
Normally, the creation and annihilation operators are defined in the k-space such that $[\hat{a}(k), \hat{a}^\dagger(k')] = \delta(k - k')$. We are interested in position space operators for which $[\hat{a}(z,t), \hat{a}^\dagger(z',t)] = c\delta(z - z')$ holds. After this normalization $\hat{a}^\dagger(z)\hat{a}(z)$ describes the flux of photons in the "quantum" polarization at position z[3].

[3]The Stokes operators are also normalized accordingly: $\hat{S}_i(z,t) \rightarrow c\hat{S}_i$

Since the atoms are placed in a magnetic field and the atomic spins are rotating with frequency Ω, it is useful to look at the cosine and sine modes of the light operators at this frequency:

$$\begin{aligned}
\hat{q}_c(z) &= \pm\sqrt{\frac{2}{|S_x|T}}\int_0^T \hat{S}_z(z,t)\cos(\Omega t)dt = \sqrt{\tfrac{2}{T}}\int_0^T \hat{q}(z,t)\cos(\Omega t)dt, \\
\hat{y}_c(z) &= \sqrt{\frac{2}{|S_x|T}}\int_0^T \hat{S}_y(z,t)\cos(\Omega t)dt, \\
\hat{q}_s(z) &= \pm\sqrt{\frac{2}{|S_x|T}}\int_0^T \hat{S}_z(z,t)\sin(\Omega t)dt, \\
\hat{y}_s(z) &= \sqrt{\frac{2}{|S_x|T}}\int_0^T \hat{S}_y(z,t)\sin(\Omega t)dt,
\end{aligned} \tag{2.15}$$

where T is the interaction duration.
The measurement of the light modes at higher frequencies is very helpful, since the technical noise at low frequencies (DC) makes measurements at the quantum level difficult.
For several reasons it will become necessary later on to introduce light modes with a different temporal shape. In our setting this means that we introduce a mode function $f(t)$, other than a simple top-flat profile used above, and use it as the envelope for the cosine and sine modes, i.e.

$$\hat{q}_{c,f}(z,t) = \tfrac{1}{N_f}\int_0^T \hat{q}(z,t)\cos(\Omega t)\cdot f(t)dt. \tag{2.16}$$

N_f is a normalizing factor such that the commutator $[\hat{y}_k, \hat{q}_k] = i$ for the canonical variables remains valid. Those kind of light modes will be introduced due to different effects of the interaction such as back action of light onto its self mediated via the atoms due to the magnetic field (section 2.2.3) and exponential decay or growth of the observables due to higher order effects from the Hamiltonian (see section 3.1).

In figure 2.2 the representation of the two systems is shown in phase space diagrams. The sets of variables follow Gaussian probability distributions, fully characterized by the mean values and variances. At the beginning of most experiment, the atoms and the light systems are set as coherent states, i.e. states with minimum uncertainty of $\frac{1}{2}$ in both quadratures.

2.2 Interaction

The scenario we are considering is a dispersive interaction of light with the atomic transition from the $6S_{1/2,F=4}$ ground state to the $6P_{3/2}$ excited state. Coming from the known dipole interaction with the electric field $\mathbf{E}$ and the dipole moment $\mathbf{d}$, $\hat{H}_i$ is the interaction Hamiltonian for every single atom:

$$\hat{H}_i = \mathbf{d}_i \cdot \mathbf{E}. \tag{2.17}$$

Starting from 2.17 an effective Hamiltonian can be derived, concerned only with the ground state of the atomic spins. The full derivation has been carried through in various different places [Jul03, HWPC05, HSP10] and will therefore not be repeated here. To arrive at the desired effective Hamiltonian which only concerns the ground state coherences and populations of $F = 4$ standard techniques are applied. Slowly varying operators are introduced and, since the detunings we are interested in are big compared to the line width of the atomic transition, the population of the excited levels is small and we can apply adiabatic elimination.

The effective interaction Hamiltonian reads [SJP07, Jul03, She06][4]:

$$\begin{aligned} \hat{V} &= -\frac{\hbar\gamma\lambda^2}{8A\Delta 2\pi}\int_0^L (a_0\hat{\phi}(z,t)n_A + a_1\hat{S}_z(z,t)\hat{j}_z(z,t) \\ &+ a_2[\hat{\phi}(z,t)\hat{j}_z^2 - \hat{S}_-(z,t)\hat{j}_+^2 - \hat{S}_+(z,t)\hat{j}_-^2])dz \\ = \ldots &+ a_2[\hat{\phi}\hat{j}_z^2 - 2(\hat{j}_x^2 - \hat{j}_y^2)\hat{S}_x - 2(\hat{j}_x\cdot\hat{j}_y + \hat{j}_y\cdot\hat{j}_x)\hat{S}_y]dz, \end{aligned} \tag{2.18}$$

where λ is the wavelength of light L is the interaction length given by the length of our atomic ensemble, A is the cross section of the sample and $\hat{\phi}$ the photon flux. All spin operators are depending on position and time. The atomic operators at different positions of the sample are defined as $\hat{j}_k(z,t) = \sum_i^{N_a}\delta(z-z_i)\hat{j}_k^i(t)$, where $\hat{j}_k^i$ is the spin of atom i at position z_i such that the collective spin can be calculated as $\hat{J}_k(t) = \int_0^L \hat{j}_k(z,t)dz$.

The prefactors a_0, a_1 and a_2 can be calculated for the specific setting, with the ground state $F = 4$ and a detuning Δ from $F = 5$ of the $6P_{3/2}$ excited state and are stated in [Jul03]. In graph 2.3a the prefactors are shown. For typical detunings the fraction a_2/a_1 lies around 0.01 as can be seen in figure 2.3b. In the following (section 2.2.1) the a_2 terms will therefore be neglected. However, later on in chapter 3, the effect of those terms will be discussed thoroughly and the dominant term for our experimental realization will be included. It will become evident that moving to a stronger coupling regime by increas-

[4]Note that this is with slightly different definition of the spin operators as stated below, which leads to a missing factor of ρA. Because of this there was also introduced an $n_A = \sum_i^{N_a}\delta(z-z_i)$ such that $\int_0^L n_A(z) = N_a$

ing the interaction duration, the number of atoms or the light power, the additional term in the Hamiltonian will lead to dynamics which open up for new experimental possibilities. Also, we need to discuss the effects of these higher order terms on the protocols where a weaker coupling was used and thus the simplified Hamiltonian is employed to describe the experiment.

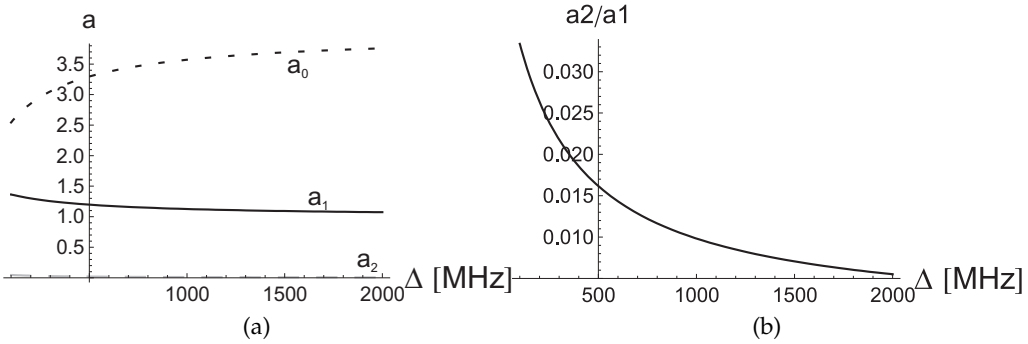

Figure 2.3: The prefactors of the terms of the Hamiltonian are shown for the D_2 line with $F = 4$ as ground state in (a). In (b) the ratio of the vector and the scalar parts are shown.

A more intuitive picture of the interaction can be established by looking at a spin $\frac{1}{2}$ atom, sketched in figure 2.4. Considering two ground states and two excited states one arrives at an effective Hamiltonian ([DCZP00],[1]), which only includes two terms similar to the first terms of 2.18: $\hat{V} \propto a_0\hat{\Phi}N_a + a_1\hat{S}_z\hat{J}_z$. Looking closer at this it becomes evident that the first expression just gives rise to the same shift to all levels of the ground state. This is not interesting for the dynamics. The second term causes a displacement of $\hat{S}_y$ due to the spin in z-direction. This corresponds to a rotation of the linear polarization proportional to $\hat{J}_z$ and is known as Faraday rotation. This rotation originates in the different phases the left-hand circular and right-hand circular polarized photons acquire due to the circular birefringence arising from the spin in z-direction. At the same time the atomic angular momentum in y-direction is displaced corresponding to S_z. The underlying effect is rooted in the different AC Stark shifts, which the two different ground levels experience, due to different numbers of photons with right- and left-hand circular polarization in the probe light.

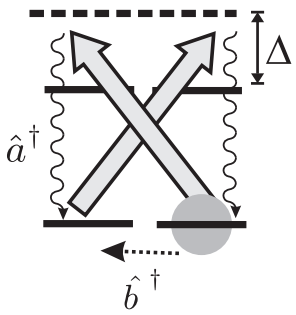

Figure 2.4: Level-scheme of spin $\frac{1}{2}$ in x-direction with off-resonant y-polarized light depicted by the thick arrows, while the photons created in y direction are depicted by the wavy arrows.

2.2.1 Input output relations for the QND Hamiltonian

The dynamics of the light and atom variables can be deduced with the help of Heisenberg's equation of motion using the full Hamiltonian:

$$\hat{H} = \hat{H}_{\text{light}} + \hat{H}_a + \hat{V} \tag{2.19}$$

First we will consider the simplified interaction Hamiltonian

$$\begin{aligned} \hat{V} &= -\frac{\hbar\gamma\lambda^2}{8A\Delta 2\pi}\int_0^L (a_1 \hat{S}_z(z,t)\hat{j}_z(z,t))dz \\ &= \hbar\cdot a\int_0^L (\hat{p}^*(z,t)\cdot\hat{q}(z,t))dz \\ &= \hbar\cdot a\int_0^L (\hat{a}^\dagger b^{*\dagger} - \hat{a}^\dagger b^* + H.c.)dz, \end{aligned} \tag{2.20}$$

with $a = \frac{\gamma\lambda^2 a_1}{8A\Delta 2\pi}\sqrt{S_x J}$ and where $\hat{p}^*(z,t) = \hat{j}_z(z,t)/\sqrt{FN_a}$ is an atomic variable depending on position. We arrive at our atomic canonical operators by integrating over the sample: $\hat{p}(t) = \int_0^L \hat{p}^*(z,t)dz$. Note that $\hat{p}^*$ and $\hat{x}^*$ do not follow a canonical commutation relation, but $[\hat{x}^*(z,t), \hat{p}^*(z',t)] = [\hat{j}_y(z,t), \hat{j}_z(z',t)]/(FN_a)$ $= i\langle\hat{j}_x\rangle_z/(FN_a)\delta(z-z')$ where we assume that $\langle j_x\rangle_z$ is the same over all z. Similarly $\hat{b}^*$ is the corresponding position depending unnormalized annihilation operator.
The light Hamiltonian for a single transverse mode is given by
$\hat{H}_{\text{Light}} = \sum_k |k|c\hbar(\hat{a}_k^\dagger\hat{a}_k + \frac{1}{2})$. We are looking at the operators $a(z)$[5], for which the Heisenberg equation of motion leads to

$$\frac{\partial a}{\partial t} + c\frac{\partial}{\partial z}a = -\frac{i}{\hbar}[a, \hat{V}]. \tag{2.21}$$

By defining new operators with a retarded time variable $\hat{a}'(z,t') = \hat{a}(z, t = t' + z/c)$ [HSP10] we arrive at the simpler equation $c\frac{\partial}{\partial z}a' = -i[a', \hat{H}]$. For our setting, clearly $t' \approx t$. Note that this is equivalent to assuming that L/c is small compared to all characteristic timescales. In the following those will be the variables and operators of interest, so we drop the prime and for the light operators we have the equations.

$$\frac{\partial}{\partial z}\hat{y} = -i[\hat{y}, \hat{V}], \quad \frac{\partial}{\partial z}\hat{q} = -i[\hat{q}, \hat{V}]. \tag{2.22}$$

[5] $a(z) = \frac{1}{\sqrt{2\pi}}\int_{-\infty}^{\infty} e^{ikz}a_k dk$

Without a magnetic field the equations for the atomic operators read

$$\begin{aligned} \frac{\partial}{\partial t}\hat{x}^* &= -i[\hat{x}^*, \hat{V}] \quad , \quad \frac{\partial}{\partial t}\hat{p}^* = -i[\hat{p}^*, \hat{V}], \\ \frac{\partial}{\partial t}\hat{x} &= -i\int_0^L [\hat{x}^*, \hat{V}]dz \quad , \quad \frac{\partial}{\partial t}\hat{p} = -i\int_0^L [\hat{p}^*, \hat{V}]dz. \end{aligned} \tag{2.23}$$

This leaves us with

$$\begin{aligned} \hat{q}' &= 0, \ \hat{y}' = a\hat{p}^*, \\ \dot{\hat{p}} &= 0, \ \dot{\hat{x}} = a\hat{q}, \end{aligned} \tag{2.24}$$

where the prime denotes the spatial derivative. The $\hat{q}$-quadrature of light and the $\hat{p}$-quadrature of the atoms are conserved. Thus we can easily obtain the operators after the interaction. For the light we integrate the equation over the length of the sample and obtain:

$$\begin{aligned} \hat{q}(z = L, t) &= \hat{q}(z = 0, t), \\ \hat{y}(z = L, t) &= \hat{y}(z = 0, t) + a\hat{p}(t). \end{aligned} \tag{2.25}$$

The variables we are interested in - our measured quantities - are the light variables, integrated over duration of the interaction. We define the input and output light operators before and after the cell as $\hat{q}^{\text{out}} = \frac{1}{\sqrt{T}}\int_0^T \hat{q}(z = L, t)dt, \hat{q}^{\text{in}} = \frac{1}{\sqrt{T}}\int_0^T \hat{q}(z = 0, t)dt, \ldots$. The atomic input and output operators are just defined at time 0 and T. We get set of input-output relations for the variables of light and atoms with $\kappa_{\text{QND}} = a\sqrt{T}$:

$$\hat{q}^{\text{out}} = \hat{q}^{\text{in}}, \ \hat{y}^{\text{out}} = \hat{y}^{\text{in}} + \kappa_{\text{QND}}\,\hat{p}^{\text{in}}, \tag{2.26}$$

$$\hat{p}^{\text{out}} = \hat{p}^{\text{in}}, \ \hat{x}^{\text{out}} = \hat{x}^{\text{in}} + \kappa_{\text{QND}}\,\hat{q}^{\text{in}}. \tag{2.27}$$

These simple equations are highly interesting. After the interaction $\hat{y}^{\text{out}}$ carries information about $\hat{p}^{\text{in}}$, while $\hat{p}$ is not changed via the interaction. $\hat{y}^{\text{out}}$ can be measured, providing information about the unchanged atomic $\hat{p}$. This is known as a quantum non demolition (QND) measurement and is an important quantum mechanical concept for generating squeezing and entanglement.

Adding a magnetic field in x-direction, which is the situation in the experiment we desire to describe, will complicate those simple equations, but in section 2.2.4 we will apply a trick to regain the same simple structure of the input-output equations discussed here. There, light is sent through two cells with oppositely orientated macroscopic spins and again a QND measurement can be conducted, but this time on collective variables of the two cells.

2.2.2 Input output relations in a magnetic field

As mentioned above, in our experimental realization, a magnetic field is applied in the direction of the macroscopic spin. The atomic Hamiltonian $\hat{H}_{\text{atoms}} = \hbar\Omega\hat{J}_x$ leads to a Larmor precession of the atomic spin around the x-axis and we introduce the spin operators in the rotating frame as stated in 2.8. To achieve better understanding the interaction Hamiltonian expressed in equation 2.20 can be rephrased in terms of the rotating frame creation and annihilation operator 2.10.

$$\hat{V}_\uparrow = \hbar \cdot \tilde{a} \int_0^L (\hat{a}^\dagger e^{-i\omega t} \hat{b^*}^\dagger e^{-i\Omega t} - \hat{a} e^{i\omega t} \hat{b^*}^\dagger e^{-i\Omega t} + H.c) dz \tag{2.28}$$

$$= \hbar \cdot \tilde{a} \int_0^L (\hat{a}_+^\dagger \hat{b'^*}^\dagger - \hat{a}_-^\dagger \hat{b'^*} + H.c) dz. \tag{2.29}$$

$\hat{a}^\dagger_{+(-)}$ is the creation operator for a photon in the upper (lower) Ω-sideband. It is very important to note here that this is only true for the setting where the magnetic field is pointing in the same direction as the macroscopic spin. When J is oriented opposite to the magnetic field the Hamiltonian reads:

$$\hat{V}_\downarrow = \hbar\tilde{a} \int_0^L (\hat{a}_-^\dagger \hat{b'}^{*\dagger} - \hat{a}_+^\dagger \hat{b'}^* + H.c.). \tag{2.30}$$

$\hat{b'}^{*\dagger}$ is the atomic creation operator in the rotating frame shuffling one atom away from the fully oriented state, as is depicted in figure 2.5 for both settings with the spin parallel and antiparallel to the B-field. One excitation is accompanied by the production of photons of different frequencies in the two cases. In 2.5a where the macroscopic orientation is in the same direction as the field, the photon lies in the upper sideband while for the antiparallel setting it is the lower sideband.

2.2.3 Single atomic ensemble

Now I want to derive the evolution of the canonical operators for light and the atomic spins in the rotating frame with the simple Hamiltonian from equation 2.20 for a situation as shown in figure 2.6 where a light beam interacts with one, oriented atomic ensemble. In the following the equations will always be stated for the case of the macroscopic spin aligned with the magnetic field and for the case where they are antiparallel ($\langle J_x \rangle \approx \pm J$). In those cases the canonical operators of the atoms are defined slightly differently. The definition of one quadrature, $\hat{x} = \pm\frac{\hat{J}'_y}{\sqrt{J}}$ changes sign. $\hat{p} = \frac{\hat{J}'_z}{\sqrt{J}}$ is the same for both settings. The atomic spins are defined in the rotating frame. It is easily understood that this way the commutator remains $[\hat{x}, \hat{p}] = \pm i\frac{\langle J_x \rangle}{J} \approx i$.

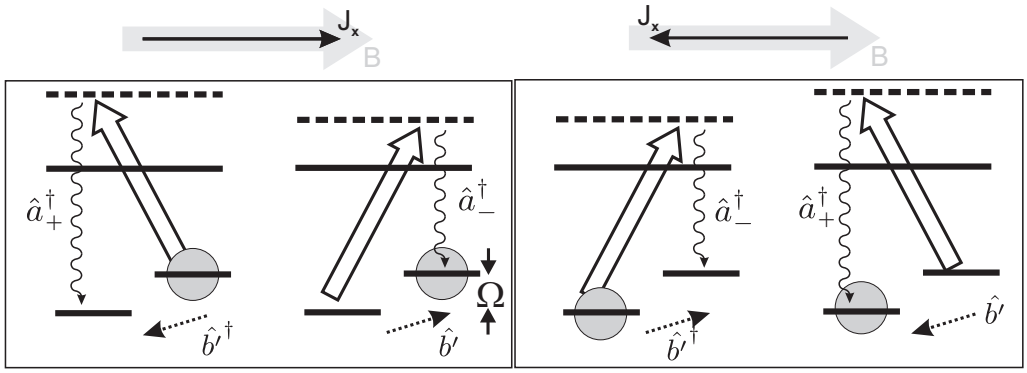

(a) $(\hat{a}_+^\dagger \hat{b'}^\dagger - \hat{a}_- \hat{b'}^\dagger) + h.c$ (b) $(\hat{a}_-^\dagger \hat{b'}^\dagger - \hat{a}_+ \hat{b'}^\dagger) + h.c$

Figure 2.5: The process of the Hamiltonian is depicted. In our case, all the atoms start in the m=4 level. The strong light field is seen as a superposition of σ_+ and σ_- polarized photons and is depicted with the thick arrow. In (a), where the B-field and J_x have the same sign, the production of one collective atomic excitation is accompanied by one photon in the upper sideband. In (b), B-field and J_x have the opposite sign one atomic excitation is produced together with a photon in the lower sideband.

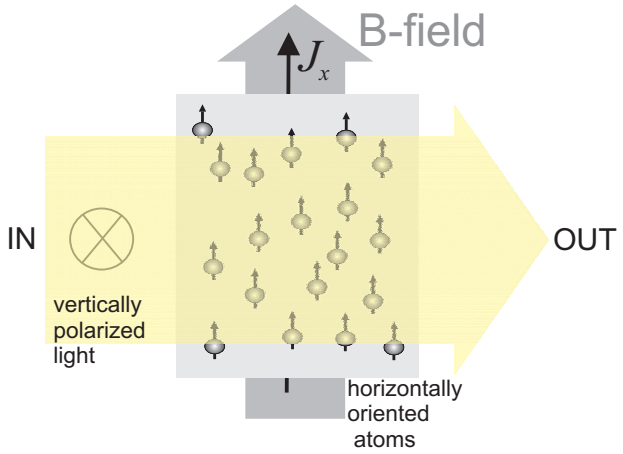

Figure 2.6: A top view of the interaction setup is depicted. A strong, vertically polarized light beam is sent through the atoms which are all oriented in the same direction as the bias magnetic field.

When we extend the equations 2.26 for the magnetic field, one of the light variables still remains unchanged, while the other is changed by the rotating spin. Thus we get,

$$\begin{aligned} \hat{q}(z=L,t) &= \hat{q}(z=0,t), \\ \hat{y}(z=L,t) &= \hat{y}(z=0,t) + a(\hat{p}(t)\cos(\Omega t) + \hat{x}(t)\sin(\Omega t)), \end{aligned} \tag{2.31}$$

where the different components of the rotating spin effect the light at different times. Before those equations can be integrated, we need to find the time dependence of the atomic operators in the rotating frame. Including the magnetic field, their equations of motion read

$$\dot{\hat{x}} = a\hat{q}\cos(\Omega t), \quad \dot{\hat{p}} = \mp a\hat{q}\sin(\Omega t). \tag{2.32}$$

Since $\hat{q}(z,t)$remains unchanged in the interaction, this leads to

$$\hat{x}(t) = \hat{x}(0) + a\int_0^t \hat{q}(z=0,t')\cos(\Omega t')dt', \tag{2.33}$$

$$\hat{p}(t) = \hat{p}(0) \mp a\int_0^t \hat{q}(z=0,t')\sin(\Omega t')dt'. \tag{2.34}$$

Finally, we get the input-output relations for the atomic operators:

$$\boxed{\begin{aligned} \hat{x}^{\text{out}} &= \hat{x}^{\text{in}} + \frac{\kappa_{\text{QND}}}{\sqrt{2}}\hat{q}_c^{\text{in}}, \\ \hat{p}^{\text{out}} &= \hat{p}^{\text{in}} \mp \frac{\kappa_{\text{QND}}}{\sqrt{2}}\hat{q}_s^{\text{in}}. \end{aligned}} \tag{2.35}$$

The cosine and sine light modes are defined in 2.15 and $\kappa_{\text{QND}} = a\sqrt{T}$.

Reconsidering equation 2.31 we take a closer look at the atomic contribution on the light quadrature $\hat{y}$ after the interaction which oscillates with frequency Ω. The two signals at this frequency, which are out of phase by $\pi/2$, are proportional to the two atomic quadratures. Therefore, it might be interesting to look for example at the cosine mode of $\hat{y}$. This means we multiply the equation with $\sqrt{\frac{2}{T}}\cos(\Omega t)$ and integrate over the interaction duration T. When we consider $T \gg 1/\Omega$ and the evolution of the equations much slower than $\frac{1}{\Omega}$, terms proportional to $\cos(\Omega t)\sin(\Omega t)$ can be set equal to zero as their effect averages out, when the integration is done. The integral over the square of the

cosine will only give a factor $\frac{T}{2}$. Using the result 2.35, the light equation reads

$$\begin{aligned}\hat{y}_c^{\text{out}} &= \hat{y}_c^{\text{in}} + \frac{\kappa_{\text{QND}}}{\sqrt{2}}\hat{p}^{\text{in}} \mp \kappa_{\text{QND}}^2\sqrt{\frac{2}{T^3}}\int_0^T dt\cos^2(\Omega t)\int_0^t dt'\hat{q}\sin(\Omega t') \\ &= \hat{y}_c^{\text{in}} + \frac{\kappa_{\text{QND}}}{\sqrt{2}}\hat{p}^{\text{in}} \mp \kappa_{\text{QND}}^2\sqrt{\frac{2}{T^3}}\int_0^T (\frac{T-t}{2})\hat{q}\sin(\Omega t)dt. \end{aligned} \tag{2.36}$$

Now, we would like to express the last term of the equation above as a sum of our well known sine light mode and an orthogonal contribution. This makes it easier to analyze commutators and variance of the output variable. We define

$$\hat{q}_{s,1} = \sqrt{\frac{24}{T^3}}\int_0^T (\frac{T}{2} - t)\sin(\Omega t)\hat{q}(t)dt \tag{2.37}$$

and $\hat{q}_{c,1}$ and $\hat{y}_{c(s),1}$ similarly which commute amongst each other:

$$[\hat{q}_{c(s),1}, \hat{y}_{c(s)}] = [\hat{q}_{c(s),1}, \hat{q}_{c(s)}] = 0. \tag{2.38}$$

The input-output relations for the light y quadrature then read:

$$\boxed{\begin{aligned}\hat{y}_c^{\text{out}} &= \hat{y}_c^{\text{in}} + \frac{\kappa_{\text{QND}}}{\sqrt{2}}\hat{p}^{\text{in}} \mp (\frac{\kappa_{\text{QND}}}{2})^2\cdot(\hat{q}_s^{\text{in}} + \frac{1}{\sqrt{3}}\hat{q}_{s,1}^{\text{in}}), \\ \hat{y}_s^{\text{out}} &= \hat{y}_s^{\text{in}} \pm \frac{\kappa_{\text{QND}}}{\sqrt{2}}\hat{x}^{\text{in}} \pm (\frac{\kappa_{\text{QND}}}{2})^2\cdot(\hat{q}_c^{\text{in}} + \frac{1}{\sqrt{3}}\hat{q}_{c,1}^{\text{in}}), \\ \hat{q}_{s(c)}^{\text{out}} &= \hat{q}_{s(c)}^{\text{in}}. \end{aligned}} \tag{2.39}$$

.

Even though the outputs of those two observables contain a number of non-commuting operators, they should of course still commute after the interaction. In fact, we routinely measure the cosine and sine modes of our operators over the interaction time:

$$\begin{aligned}[\hat{y}_c^{\text{out}}, \hat{y}_s^{\text{out}}] &= [\hat{y}_c^{\text{in}}, \pm\frac{\kappa_{\text{QND}}^2}{4}\hat{q}_c^{\text{in}}] \pm \frac{\kappa_{\text{QND}}^2}{2}[\hat{p}^{\text{in}}, \hat{x}^{\text{in}}] \mp \frac{\kappa_{\text{QND}}^2}{4}[\hat{q}_s^{\text{in}}, \hat{y}_s^{\text{in}}] = \\ &= \frac{\kappa_{\text{QND}}^2}{4}(\pm 1 \mp 2 \pm 1) = 0\end{aligned}$$

To summarize, the interaction of light with a single cell in a magnetic field equation is given by equations 2.35 and 2.39. Equations 2.35 show that the two atomic quadratures read out two orthogonal modes of the input light quadrature $\hat{q}$. At the same time $\hat{q}$ is still conserved. The $\hat{y}$-quadrature of light behaves in a more complicated way and shows quadratic effects in κ_{QND}. The reason for this is a back action of light on itself which can be understood as follows: while the light is sent through the atoms, the atomic spin in z-direction is causing

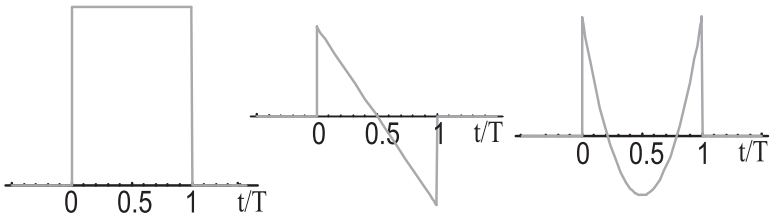

Figure 2.7: The zeroth, first and second order temporal modes are depicted - all of which are mutually orthogonal. The standard temporal mode is a top-hat mode. Via the underlying interaction in the magnetic field, the mode evolving linear in time in the middle is introduced. On the right the second order mode is depicted. The n-th mode includes a term of t^n.

a shift in $\hat{y}$ corresponding to the size of the collective spin in this direction - one can say that it is mapped on $\hat{y}$. At the same time the orthogonal transversal spin component is displaced corresponding to the other light quadrature $\hat{q}$. The two components of the spin, one of which is read out by the light while the other one maps one quadrature of the light, rotate in and out of each other. As a result a mapping of light onto itself occurs. This is a quadratic effect in κ_{QND}. It also leads to an inclusion of a higher order temporal mode into the input-output relations. This mode is linear in time and orthogonal to the original modes. The higher order temporal modes, the first of which are plotted in figure 2.7, follow their own input output relations, where all the $\hat{q}_{c/s,m}$ are conserved and the $\hat{y}_{c/s,m}$ couple to $\hat{q}_{c/s,m}$ and $\hat{q}_{c/s,m+1}$. In [HPC06] the higher order modes and their input/output relations are discussed in detail.

From the quantum mechanics point of view, the higher order effects are crucial as they make sure that it is not allowed to measure non commuting variables. Equations 2.39 show the output of two light operators which we can easily measure simultaneously (if we talk about time scales sufficiently larger than $1/\Omega$). Clearly, without the quadratic terms, increasing κ_{QND} would lead to the possibility of measuring $\hat{x}$ and $\hat{p}$. But if we now measure at a high κ_{QND}, the measurement will be dominated by noise contributions from the input light. The connection of light and atoms after the interaction is highly interesting. In section 5.3.2 it will be shown that the spin operators are entangled with the upper sideband quadratures of light for certain couplings or, if the macroscopic spin is aligned antiparallel to the magnetic field, with the lower sideband operators. Considering figures 2.5a and 2.5b, this can be intuitively understood, as one atomic excitation is accompanied by the production of a photon at the upper/lower sideband frequency.

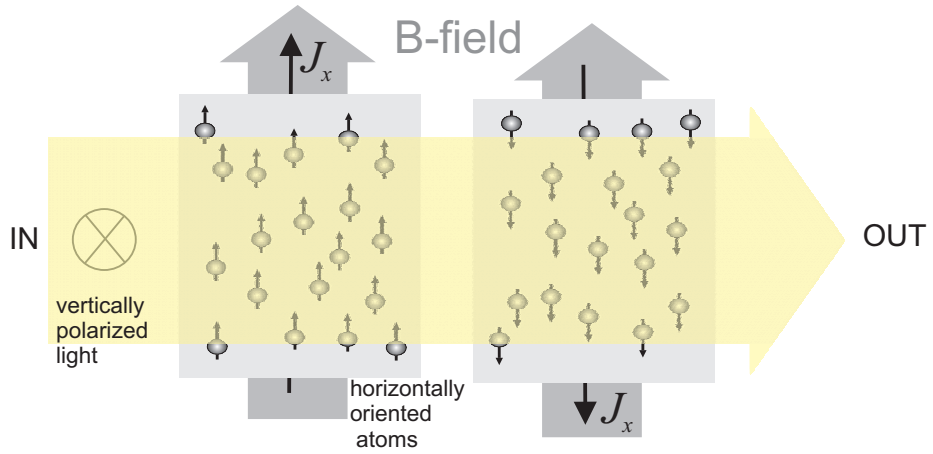

Figure 2.8: The interaction setup is depicted. A strong, vertically polarized light beam is sent through the two atomic ensembles that have macroscopic spins oriented in opposite direction.

2.2.4 Two oppositely oriented atomic ensembles

As mentioned earlier, we will now turn to a scenario where two atomic ensembles are involved. This looks at first glance more complicated, but when we calculate the input-output equations, they will be of a simpler form than in the case of the single atomic ensemble in a magnetic field. As a matter of fact, they will look similar to the QND case discussed in 2.2.1.
The setting is depicted in figure 2.8. A light beam is sent through two cells with oppositely oriented macroscopic spins. To begin, we define two sets of collective operators of the two cells in the following way:

$$\begin{aligned}
\hat{X}_c &= \frac{\hat{J}_{y,1} - \hat{J}_{y,2}}{\sqrt{2J}} = \frac{1}{\sqrt{2}}(\hat{x}_1 + \hat{x}_2), \\
\hat{P}_c &= \frac{\hat{J}_{z,1} + \hat{J}_{z,2}}{\sqrt{2J}} = \frac{1}{\sqrt{2}}(\hat{p}_1 + \hat{p}_2), \\
\hat{X}_s &= -\frac{\hat{J}_{z,1} - \hat{J}_{z,2}}{\sqrt{2J}} = -\frac{1}{\sqrt{2}}(\hat{p}_1 - \hat{p}_2), \\
\hat{P}_s &= \frac{\hat{J}_{y,1} + \hat{J}_{y,2}}{\sqrt{2J}} = \frac{1}{\sqrt{2}}(\hat{x}_1 - \hat{x}_2),
\end{aligned} \tag{2.40}$$

such that $[\hat{X}_k, \hat{P}_l] = i\delta_{kl}$ and $[\hat{X}_k, \hat{X}_l] = [\hat{P}_k, \hat{P}_l] = 0$.
It is easy to extract the output equations for the atoms from equation 2.35:

$$\boxed{\begin{aligned}
\hat{X}^{\text{out}}_{c,s} &= \hat{X}^{\text{in}}_{c,s} + \kappa_{\text{QND}}\,\hat{q}^{\text{in}}_{c,s}, \\
\hat{P}^{\text{out}}_{c,s} &= \hat{P}^{\text{in}}_{c,s}.
\end{aligned}}$$

(2.41)

Using 2.39 for the interaction with the second cell and inserting $\hat{y}_{c,s}^{\text{out}}$ from the interaction with the first cell as input, we also get a much simpler set of equations for the light variables:

$$\begin{aligned}\hat{y}_c^{\text{out}} &= \hat{y}_c^{\text{out, cell 1}} + \frac{\kappa_{\text{QND}}}{\sqrt{2}}\hat{p}_2^{\text{in}} + (\frac{\kappa_{\text{QND}}}{2})^2(\hat{q}_s^{\text{in}} + \frac{1}{\sqrt{3}}\hat{q}_{s,1}^{\text{in}}),\\ \hat{y}_s^{\text{out}} &= \hat{y}_s^{\text{out, cell 1}} - \frac{\kappa_{\text{QND}}}{\sqrt{2}}\hat{x}_2^{\text{in}} - (\frac{\kappa_{\text{QND}}}{2})^2(\hat{q}_c^{\text{in}} + \frac{1}{\sqrt{3}}\hat{q}_{c,1}^{\text{in}}).\end{aligned}$$

Inserting the output equations from the first cell:

$$\begin{aligned}\hat{y}_c^{\text{out, cell 1}} &= \hat{y}_c^{\text{in}} + \frac{\kappa_{\text{QND}}}{\sqrt{2}}\hat{p}_2^{\text{in}} - (\frac{\kappa_{\text{QND}}}{2})^2(\hat{q}_s^{\text{in}} + \frac{1}{\sqrt{3}}\hat{q}_{s,1}^{\text{in}}),\\ \hat{y}_s^{\text{out, cell 1}} &= \hat{y}_s^{\text{in}} + \frac{\kappa_{\text{QND}}}{\sqrt{2}}\hat{x}_2^{\text{in}} + (\frac{\kappa_{\text{QND}}}{2})^2(\hat{q}_c^{\text{in}} + \frac{1}{\sqrt{3}}\hat{q}_{c,1}^{\text{in}})\end{aligned}$$

we get the input-output relations for the light operators:

$$\boxed{\begin{aligned}\hat{y}_{c,s}^{\text{out}} &= \hat{y}_{c,s}^{\text{in}} + \kappa_{\text{QND}}\hat{P}_{c,s}^{\text{in}}\\ \hat{q}_{c,s}^{\text{out}} &= \hat{q}_{c,s}^{\text{in}}.\end{aligned}}$$

(2.42)

There are two sets of similar equations for two atomic modes characterized by the indices c and s. This is due to the fact that there are two cells. Essentially, we end up with a QND measurement of the two operators $\hat{P}_c$ and $\hat{P}_s$ similar to the simple case discussed in section 2.2.1 where the interaction of light with a single atomic ensemble without a magnetic field was investigated. Only now this is a simultaneous measurement of the sums of the transversal components of the spins of the two ensembles $\hat{J}_{y,1} + \hat{J}_{y,2}$ and $\hat{J}_{z,1} + \hat{J}_{z,2}$. This might appear strange at first glance, but the possibility was engineered by the two opposite macroscopic spins. This way, the commutator of the sums of the transversal spins of the two ensembles becomes zero:

$$[\hat{J}_{y,1} + \hat{J}_{y,2}, \hat{J}_{z,1} + \hat{J}_{z,2}] \approx i(\langle\hat{J}_{x,1}\rangle + \langle\hat{J}_{x,2}\rangle) = 0.$$

Now, it is possible to measure the two quantities at the same time.
These equations provide a basis for several interesting experiments. The most obvious one is utilizing the QND measurement of the collective spins to gain knowledge about the atomic state, with which several proposals and experiments are concerned amongst others [UTK06, ERIR+07, KNDM10]. How to utilize the measurements of the light state to reconstruct the atomic state is discussed in section 5.2.

The light measurement can also be used to achieve spin squeezing [AWO+09, TVLK08, TFNT09, SSLV10] translating in our case to entanglement between the two cells. Starting from the minimum uncertainty state (CSS) for both cells, one gains more information about the sum of the spins through a measurement on light. This experiment has already been conducted successfully [JKP01] and will be discussed in section 5.3.3 for a slightly different setting. The measurement concept is also used to achieve steady state entanglement as described in chapter 8.
Also a mapping protocol of a light state on atoms can be implemented. In the first step light is sent through atoms and one quadrature of light is mapped onto the atoms via this interaction (see equation 2.41). In a second step the results of a measurement on the $\hat{y}$-quadrature of light are fed back onto the atomic $\hat{P}$-quadrature. This experiment has been conducted for coherent light states [JSC+04] and, more recently, also displaced squeezed states have been mapped onto atoms [9], which is discussed briefly in section 9.2.

Chapter 3

Refined theoretical model for oriented atomic states

In this chapter a more complicated and - for highly oriented ensembles - more accurate approximation of the Hamiltonian is discussed and the input-output equations will be adjusted accordingly (in accordance with [5]). These adjustments will give rise to the description of new dynamics, enabling a range of novel experiments at higher couplings [5, 7]. It will also lead to the introduction of specific temporal modes for the light operators that couple optimally to the atomic variables.

Also corrections arising for experiments with lower coupling that were evaluated with the QND model derived in the previous chapter will be considered.

3.1 Higher order Hamiltonian

Now, I am going to have a closer look at the remaining parts of the Hamiltonian that we have neglected in the previous chapter. The full Hamiltonian has previously been considered in [KMS+05, MKP05]. The scenario we are limiting us to is the one of high orientation of all atomic spins in x-direction, so that $\hat{J}_x \approx 4N_a$. This means that it is a good approximation to only consider the upper two m levels $m = 4$ and $m = 3$. Then the transversal spins of the ensemble at position z for quantization in x-direction can be viewed as [5]:

$$\begin{aligned} \hat{j}_y(z) &\approx 2\sqrt{2}\sum_i^{n_z}(|4\rangle\langle 3|_i + |3\rangle\langle 4|_i) \text{ and} \\ \hat{j}_z(z) &\approx 2\sqrt{2}i\sum_i^{n_z}(|4\rangle\langle 3|_i - |3\rangle\langle 4|_i). \end{aligned} \tag{3.1}$$

Where in the spatial slice $z + dz$, there are n_z atoms. We also assume $\hat{j}_x(z) \approx \sum_i^{n_z}(4\,|4\rangle\,\langle 4|_i + 3\,|3\rangle\,\langle 3|_i) \approx 4 \cdot n_z$. When we consider a macroscopic spin which is oppositely oriented the levels of interest are $m = -4$ and $m = -3$.[1] The quadratic terms in the spin operators appearing in the Hamiltonian can then be expressed by linear combinations of the three spins and $\mathbb{1} = |4\rangle\,\langle 4| + |3\rangle\,\langle 3|$ (see Appendix A) such that the effective interaction Hamiltonian, stated in equation 2.18 is reduced to

$$\begin{aligned}\hat{V} &= -\frac{\hbar\gamma\lambda^2}{8A\Delta 2\pi}\int_0^L (a_1\hat{S}_z(z,t)\hat{j}_z(z,t) \mp a_2 \cdot 14\hat{j}_y(z,t)\hat{S}_y(z,t)) \\ &+ a_2(\mp 21\hat{j}_x + 56)\hat{S}_x + (a_0 + a_2(\mp\frac{7}{2}\hat{j}_x - 16))\hat{\phi}(z,t))dz. \end{aligned} \tag{3.2}$$

The justification of this approximation needs to be evaluated carefully in every considered situation, by checking the orientation of the spins of the ensembles which we wish to describe.

Let us turn to the terms proportional to a_2 that were neglected in chapter 2. Fortunately, a closer investigating of the impact of the discarded terms shows that only the first term proportional to $\hat{S}_y\hat{j}_y$ is important. The other terms give rise to much smaller corrections. That is to say that the part proportional to $\hat{S}_x$ leads to a rotation in the $\hat{S}_y$ and $\hat{S}_z$ plane. The rotational angle is small, on the order of a couple of degrees for our normal settings. Also the atoms experience rotation in the $\hat{j}_y$- $\hat{j}_z$ plane due to the terms proportional to $\hat{S}_x\hat{j}_x$ and $\hat{j}_x\hat{\phi}$. This is the linear Stark shift and can be seen as a shift in the Larmor frequency, while light is shone on the atoms. We will have to consider this for the experimental realization where the light is turned on and off, but the dynamics of the highly oriented atoms are not effected, except of a rotation at a different frequency that can be taken into account by adjusting the frequency of the rotating frame to the true rotation frequency.

Finally, since $\hat{\phi}$ is a constant of motion, the part of the Hamiltonian containing only $\hat{\phi}$ (and no atomic operator) is not contributing to the dynamics of our variables.

Thus we are left with

$$\begin{aligned}\hat{V} &= -\frac{\hbar\gamma\lambda^2}{8A\Delta 2\pi}\int_0^L (a_1\hat{S}_z(z,t)\hat{j}_z(z,t) \mp a_2 \cdot 14\hat{j}_y(z,t)\hat{S}_y(z,t)))dz \\ &= -\hbar \cdot a\int_0^L (\hat{p}^*(z,t)\hat{q}(z,t) + \xi^2\hat{x}^*(z,t)\hat{y}(z,t))dz. \end{aligned} \tag{3.3}$$

with the size of the correction of the QND Hamiltonian given by $\xi^2 = 14\frac{a_2}{a_1}$ and $a = \frac{\gamma\lambda^2 a_1}{8A\Delta 2\pi}\sqrt{S_x J}$, as before. The second line is only true for a y-polarized light beam which is our usual setting.

[1] $\hat{j}_y \approx 2\sqrt{2}\sum_i^{n_i}(|-4\rangle\,\langle -3|_i + |-3\rangle\,\langle -4|_i)$ and $\hat{j}_z \approx 2\sqrt{2}i\sum_i^{n_i}(|-4\rangle\,\langle -3|_i - |-3\rangle\,\langle -4|_i)$.

This Hamiltonian is valid for both orientations of J_x. As a reminder, the atomic operators with the star are as before unnormalized and we are only interested in the spatial integrals over them.

In Appendix A, the Heisenberg equations of motion are calculated for the full Hamiltonian, including the quadratic spin components. Then those equations are approximated in the same fashion as described above. The same result as in section 3.2 is obtained where the Heisenberg equations are derived directly from the approximated Hamiltonian 3.3.

A Hamiltonian $H \propto \hat{p}\hat{q}$ or $H \propto \hat{x}\hat{y}$, as discussed in section 2.2.1, is often referred to as a Quantum Non demolition (QND) Hamiltonian, because of the possibility of a QND measurement which it grants. $H \propto (\hat{p}\hat{q} + \hat{x}\hat{y})$ can be called a "swap" Hamiltonian. This refers to the possibility to use an interaction of this type by adjusting the interaction strength, in such a way that the two systems swap their quantum states. The Hamiltonian describing the underlying light atom interface in equation 3.3 is similar to the swap case, but with suppressed $\hat{x}$ and $\hat{y}$. This will give rise to input-output relations presented in section 3.2.1 that display a swap- but also a squeezing behavior, due to the asymmetry.

Again, let us consider the level scheme and the harmonic oscillator picture, as depicted in figure 2.5. We see that the effect takes its origin in a different strength of the two processes going away from (entanglement), and going towards (beam splitter) the ground state. In the presence of the magnetic field, for a macroscopic spin aligned with the magnetic field, this means:

$$V = \hbar \int_0^L (\chi_e \hat{a}_+^\dagger \hat{b^*}^\dagger - \chi_{BS} \hat{a}_- \hat{b^*}^\dagger + H.c) dz. \tag{3.4}$$

Again, for the antiparallel aligned macroscopic spin, the sidebands will exchange roles.

3.2 Input output relations

Starting with the interaction Hamiltonian 3.3, and keeping in mind that the atoms are situated in a magnetic field, the light operators after the cells read:

$$\begin{aligned} \hat{y}(L,t) &= \hat{y}(0,t) + a\hat{p} = \hat{y}(0,t) + a(\hat{p'} \cdot \cos(\Omega t) \pm \hat{x'} \cdot \sin(\Omega t)), \\ \hat{q}(L,t) &= \hat{q}(0,t) - a\xi^2 \hat{x} = \hat{q}(0,t) - a\xi^2(\mp \hat{p'} \cdot \sin(\Omega t) + \hat{x'} \cdot \cos(\Omega t)), \end{aligned} \tag{3.5}$$

where the prime stands for the variables in the rotating frame. The integration over the sample, is still straight forward here, because we are only interested in the atomic operators of the whole ensemble. For the atomic operators we also need to integrate the equations of motion for $\hat{x}^*$ and $\hat{p}^*$ over space. As

opposed to the simpler case before, those equations will contain $\hat{y}$ and $\hat{q}$ that are depending on the position. We have to make a simple assumption to be able to solve those equations. This assumption is based on the fact that the atoms at room temperature are moving very fast on our interaction time scale - they hit the walls around 10 times. We therefore conjecture that the atomic operators have no spatial dependance and we can take an average of the light variables over the sample:

$$\begin{aligned}\langle\hat{y}\rangle_L &= \tfrac{1}{L}\int_0^L \hat{y}(z,t)dz = \hat{y}(0,t) + \frac{a}{2}(\hat{p}'\cdot\cos(\Omega t) \pm \hat{x}'\cdot\sin(\Omega t)).\\ \langle\hat{q}\rangle_L &= \tfrac{1}{L}\int_0^L \hat{q}(z,t)dz = \hat{q}(0,t) - \frac{a\xi^2}{2}(\mp\hat{p}'\cdot\sin(\Omega t) + \hat{x}'\cdot\cos(\Omega t)).\end{aligned}$$

We assume that the atomic operators are effected by the average of the light operators which allows us to integrate the atomic equations of motion over the entire cell:

$$\begin{aligned}\dot{\hat{x}} &= a\langle\hat{q}\rangle_L \mp \Omega\hat{p} = a\hat{q}(0,t) - \frac{a^2\xi^2}{2}\hat{x} \mp \Omega\hat{p},\\ \dot{\hat{p}} &= -a\xi^2\langle\hat{y}\rangle_L \pm \Omega\hat{x} = -a\xi^2\hat{y}(0,t) - \frac{a^2\xi^2}{2}\hat{p} \pm \Omega\hat{x}.\end{aligned} \tag{3.6}$$

These equations can be solved for the rotating frame spins,[2] where we end up with

$$\begin{aligned}\hat{x}(t) &= \hat{x}^{\text{in}}e^{-\gamma_s t} + a\int_0^t e^{-\gamma_s(t-t')}\hat{q}(0,t')\cos(\Omega t')dt' \mp a\xi^2\int_0^t e^{-\gamma_s(t-t')}\hat{y}(0,t')\sin(\Omega t')dt'\\ \hat{p}(t) &= \hat{p}^{\text{in}}e^{-\gamma_s t} \mp a\int_0^t e^{-\gamma_s(t-t')}\hat{q}(0,t')\sin(\Omega t')dt' - a\xi^2\int_0^t e^{-\gamma_s(t-t')}\hat{y}(0,t')\cos(\Omega t')dt'\end{aligned} \tag{3.7}$$

The introduced decay or "swap" rate γ_s is defined as

$$\gamma_s = \tfrac{a^2\xi^2}{2}. \tag{3.8}$$

3.2.1 Two cell setting

Again the equations will become considerably simpler, when we move to the setting with two oppositely oriented ensembles depicted in figure 2.8. Because there is a principal difference to the earlier case where the light quadrature mapped on the atoms remained unchanged, we need to take a little more careful look at what happens to the equations 3.7 for the second cell. In the new

[2] Start with solving the equations for $\hat{\tilde{x}} = e^{\gamma_s t}\hat{x}'$ and $\hat{\tilde{p}} = e^{\gamma_s t}\hat{x}'$ with the time derivatives $\dot{\hat{\tilde{x}}} = e^{\gamma_s t}(a\hat{q}(0,t)\cos(\Omega t) - a\xi\hat{y}(0,t)\sin(\Omega t))$ and $\dot{\hat{\tilde{p}}} = e^{\gamma_s t}(-a\hat{q}(0,t)\sin(\Omega t) - a\xi\hat{y}(0,t)\cos(\Omega t))$

setting the input variables of light have already been changed by the first cell:

$$\begin{aligned}\hat{x}_2(t) &= \hat{x}_2^{\text{in}} e^{-\gamma_s t} + a\int_0^t e^{-\gamma_s(t-t')}\hat{q}(L,t')\cos(\Omega t')dt' + a\xi^2\int_0^t e^{-\gamma_s(t-t')}\hat{y}(L,t')\sin(\Omega t')dt',\\ \hat{p}_2(t) &= \hat{p}_2^{\text{in}} e^{-\gamma_s t} + a\int_0^t e^{-\gamma_s(t-t')}\hat{q}(L,t')\sin(\Omega t')dt' - a\xi^2\int_0^t e^{-\gamma_s(t-t')}\hat{y}(L,t')\cos(\Omega t')dt'.\end{aligned}$$

To express the solution in terms of the incoming light variables, we plug in equation 3.5 and 3.7 for the first cell and arrive at

$$\begin{aligned}\hat{x}_2(t) &= \hat{x}_2^{\text{in}} e^{-\gamma_s t} + a\int_0^t e^{-\gamma_s(t-t')}\hat{q}(0,t')\cos(\Omega t')dt' + a\xi^2\int_0^t e^{-\gamma_s(t-t')}\hat{y}(0,t')\sin(\Omega t')dt' + ...\\ &\quad +2\gamma_s\int_0^t (e^{-\gamma_s(t-t')}(\sin(2\Omega t')\cdot p_1(t') - \cos(2\Omega t')\cdot x_1(t'))dt'\\ \hat{p}_2(t) &= \hat{p}_2^{\text{in}} e^{-\gamma_s t} + a\int_0^t e^{-\gamma_s(t-t')}\hat{q}(0,t')\sin(\Omega t')dt' - a\xi^2\int_0^t e^{-\gamma_s(t-t')}\hat{y}(0,t')\cos(\Omega t')dt' ...\\ &\quad +2\gamma_s\int_0^t (e^{-\gamma_s(t-t')}(-\sin(2\Omega t')\cdot x_1(t') - \cos(2\Omega t')\cdot p_1(t'))dt'.\end{aligned} \tag{3.9}$$

The parts which are printed in gray contain integrals over terms which are formed of a product of components oscillating at 2Ω and the comparatively slowly varying atomic operators. These terms are then averaging out on a short time scale, so we omit them. Then the equations look as if there was no first cell. This effect can be better understood, when one sees that the roles of the sidebands are exchanged in the two cells, so that the strong effect of the light on cell 1 is not seen by cell 2. For two parallel oriented samples this would look very different. However, when we look at the collective variables of the cells, we will see that the operators from the two cells are far from independent (see following equation 3.10), because they interacted with the same light.

Now, it is easy to get to the atomic input-output relations for the combined atomic variables:

$$\boxed{\begin{aligned}\hat{X}_{c,s}^{\text{out}} &= \hat{X}_{c,s}^{\text{in}}\sqrt{1-\kappa^2\xi^2} + \kappa\hat{q}_{c,s+}^{\text{in}}\\ \hat{P}_{c,s}^{\text{out}} &= \hat{P}_{c,s}^{\text{in}}\sqrt{1-\kappa^2\xi^2} - \kappa\xi^2\hat{y}_{c,s+}^{\text{in}}.\end{aligned}} \tag{3.10}$$

The ingoing light operators are defined with an exponentially rising mode function as for examples $\hat{y}_{c+}^{\text{in}} = \frac{1}{N_+}\int_0^T e^{-\gamma_s(T-t)}\cos(\Omega t)\hat{y}(t)dt$ where N_+ is the normalization factor. The coupling constant is defined as $\kappa = \sqrt{1-e^{-2\gamma_s T}}/\xi$. Obviously this has the limit of the coupling constant κ_{QND} that was defined in the previous chapter. When κ is expanded around $\xi = 0$, we get $\kappa \approx a\sqrt{T} - \frac{1}{4}a^3\sqrt{T^3}\xi^2 + o(\xi^4)$.

The atomic equations can be plugged into equation 3.5 adapted for two oppositely oriented cells. Then we use the same trick as in section 2.2.3 by looking directly at the cosine and sine modes. Now we consider slightly different light modes that follow an exponential decay with γ_s and oscillate at Ω, for example the cosine mode of the $\hat{y}$-quadrature of light $\hat{y}^{\text{out}}_{c-} = \frac{1}{N_-}\int_0^T e^{-\gamma_s t}\cos(\Omega t)\hat{y}(t))dt$ where N_- is the normalization factor:

$$\begin{aligned}
\hat{y}^{\text{out}}_{c-} &= \sqrt{\frac{2\gamma_s}{1-e^{-\gamma_s T}}}\int_0^T \hat{y}(2L,t)e^{-\gamma_s t}\cos(\Omega t)dt \\
&= \hat{y}^{\text{in}}_{c-} + \frac{a}{N_-}\hat{P}^{\text{in}}_c\int_0^T \cos^2(\Omega t)e^{-2\gamma_s t}dt... \\
&- \frac{a\xi^2}{N_-}\int_0^T e^{-\gamma_s t}\cos^2(\Omega t)(\int_0^t e^{-\gamma_s(t-t')}\cos(\Omega t')\hat{y}(0,t')dt')dt \\
&= \hat{y}^{\text{in}}_{c-} + \kappa\hat{P}^{\text{in}}_c - \frac{1}{N_-}\int_0^T (e^{-\gamma_s t} - e^{-\gamma_s T}\cdot e^{-\gamma_s(T-t)})\hat{y}\cos(\Omega t)dt. \qquad (3.11)
\end{aligned}$$

We see that the operator with the exponentially falling input mode cancels. Thus the output variable that has an exponentially falling mode couples to the exponentially rising input mode, just as the atomic output operators in equation 3.10. For all light output operators with the exponential falling mode we have:

$$\boxed{\begin{aligned}
\hat{y}^{\text{out}}_{c,s-} &= \hat{y}^{\text{in}}_{c,s+}\sqrt{1-\kappa^2\xi^2} + \kappa\hat{P}^{\text{in}}_{c,s} \\
\hat{q}^{\text{out}}_{c,s-} &= \hat{q}^{\text{in}}_{c,s+}\sqrt{1-\kappa^2\xi^2} - \kappa\xi^2\hat{X}^{\text{in}}_{c,s},
\end{aligned}} \qquad (3.12)$$

which looks very similar to the atomic equations 3.10 where the different light modes behave like the collective atomic rotating spins.

Long interaction times

As mentioned earlier, we have now a situation where the output variables of the two systems display a swap behavior: the systems "exchange" quantum states. In the extreme case of very high coupling or long interaction times

$$\begin{aligned}
\hat{y}^{\text{out}}_{c,s-} &\to \frac{1}{\xi}\hat{P}^{\text{in}}_{c,s}, \qquad & \hat{q}^{\text{out}}_{c,s-} &\to \xi\hat{X}^{\text{in}}_{c,s} \\
\hat{X}^{\text{out}}_{c,s} &\to \frac{1}{\xi}\hat{q}^{\text{in}}_{c,s+}, \qquad & \hat{P}^{\text{out}}_{c,s} &\to \xi\hat{y}^{\text{in}}_{c,s+}. \qquad (3.13)
\end{aligned}$$

It is not a true swap because, while the original input is suppressed in both quadratures, the mapping of the new variables is not symmetric, so that the

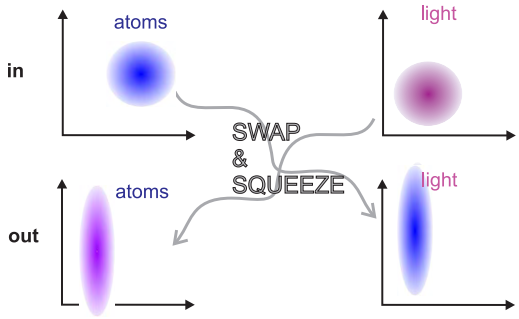

Figure 3.1: The states of light and atoms are swapped and squeezed.

final states are left in a swapped and squeezed version of the input states. The process is sketched in figure 3.1. In our case, where the collective operators of two systems are the variables of interest, this means entanglement of the two systems: for the atoms in the rotating spin of the two ensembles, and for the light in the quadratures of the upper and lower sidebands at Ω.

However, for now, we are not interested in this extreme case. As a matter of fact, in our experimental realization, we can not reach into this strong interaction regime, because dephasing and decoherence inhibit the observation of the long time effect.

Comparison to the QND model

Also for the weak and intermediate coupling, there are multiple discrepancies to the QND model. The first difference is the mode shape. The experimental realizations often feature coupling strengths κ around one in which case the exponential with $\gamma_s T = \ln(1-\kappa^2\xi^2)/2$ leads to a decay in the interaction time from 1 to 0.92. Thus the modes look very similar to the simple flat-top modes with an overlap of 0.9997. For a low coupling the flat-top modes are thus a good approximation. In addition, the pre-factors in the equations 3.10 and 3.12 have changed and can be compared to the QND equations 2.41 and 2.42. The coupling strength κ is now defined differently, the effect can be seen in graph 3.2a for values typically used. Also, there is a factor $1-\kappa^2\xi^2$ in front of the input operators of the original variable. This input suppression, which is the same in all four equations, can be seen as the solid line in figure 3.2b whereas in the QND equations the strength of the input remained unchanged. Finally $\hat{p}$ and $\hat{q}$ which were originally unperturbed are now also subject to change. The strength of their coupling to $\hat{x}$ and $\hat{y}$ is $\kappa\xi^2$ and is also shown in graph 3.2b as the dashed line.

When the results of earlier experiments are discussed, it will fortunately turn out that the QND approximations lead to comparatively small errors. This is

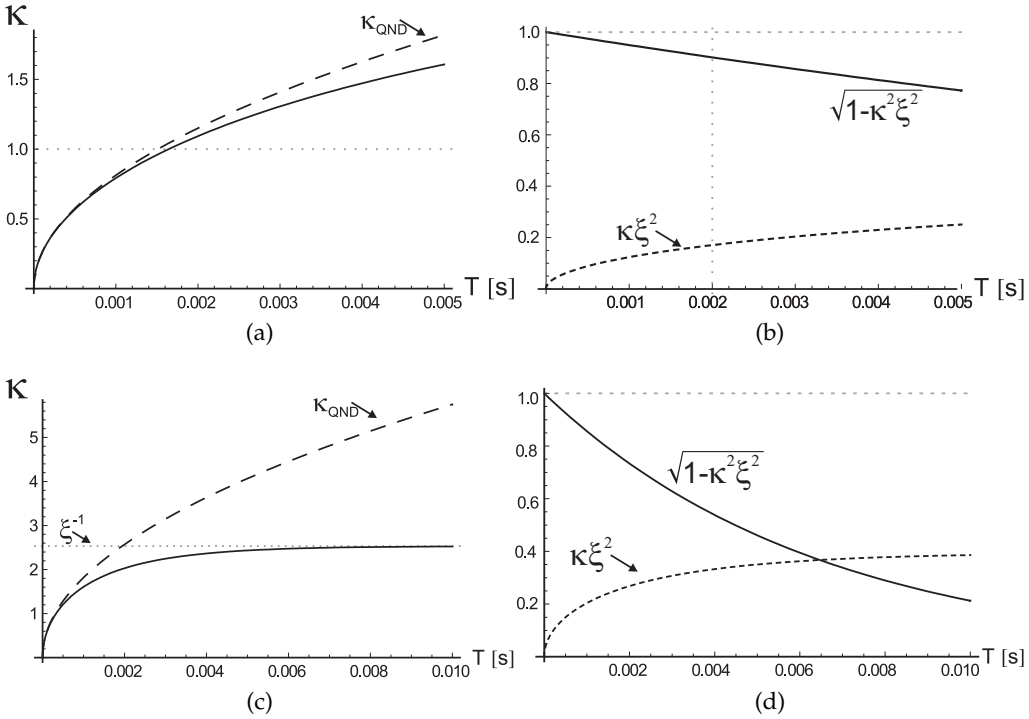

Figure 3.2: On the top left the coupling constant κ introduced in this chapter can be compared to the κ_{QND} introduced in chapter 2. κ_{QND} is shown with a dashed line. The parameters were chosen in such away that κ is close to one for $T = 2$ ms which is close to the setting where we run part of our experiments. On the right the suppression of the original input is shown with the solid line. In the QND-case there is no such suppression - the prefactor of the input operators remains to be one. Also the prefactor of the extra term in input-output relations which did not feature in the QND case is shown as the dashed line.
In the second row the light power was tripled, and a longer timescale is considered. Here the deviations from the simple model become crucial, but decoherence mechanisms will have to be included.

partly due to the fact that some flaws in the noise evaluations cancel each other to some extent. The noise from the atoms was underestimated, because the suppression of the light noise was not taken into account, but κ^2 was also set to be smaller, because it was measured via the CSS noise. In 6.4, the corrections arising for the teleportation experiment are discussed explicitly.

New proposals and limitations

The new equations can not only be used as a necessary correction to our former description. We can extract promising possibilities also in the experimental accessible regime. Analyzing the noise properties of the outputs it becomes clear that the quadratures are not symmetric anymore. Actually both systems become squeezed, as can be seen in figure 3.3 and it will turn out that this is

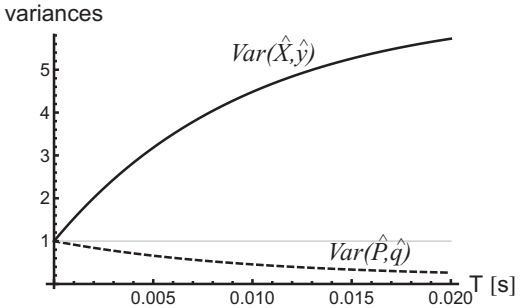

Figure 3.3: Variances of light and atomic sets of variables after the interaction with a certain duration T. As starting point we take minimum uncertainty case for both, light and atoms. $\hat{q}_{c,s-}$ and $\hat{P}$ become squeezed, while $\hat{y}_{c,s-}$ and $\hat{X}$ are anti squeezed.

still the case, when we include the effect of decoherence. In [5] two mode light squeezing is reported and in chapter 8 I am going to describe squeezing of the collective atomic operators, due to this effect.

In the second row of figure 3.2 the factors governing the interaction are shown for a light power around three times higher than our usual setting and for longer times. Here the differences compared to the QND are much more dramatic. κ saturates at $\frac{1}{\xi}$ and the input becomes considerably suppressed. As these graphs contain no contributions of decoherence, they are not sufficient to predict experimental outcomes, but still show the interesting possibilities of such an interaction. The atomic decay leads to the loss of atoms to $F = 3$. These atoms do, due to the large detuning, not participate in the interaction, but lead to a time dependent γ_s. Also there is a population transfer to the other magnetic sublevels in $F = 4$ bringing about additional noise, and, if the orientation is reduced a lot, the breakdown of the theory that is based on a two level model. It will turn out that the various decoherence mechanisms will lead to an additional decay of the transversal spin with a decay constant on the same order of magnitude as γ_s. Opposed to the effect described in this section, the additional decay will just add noise to the measurements. Part of this will be discussed in section 3.3.

3.2.2 Single cell

The atomic input-output equations for the setting depicted in figure 2.6 where a single oriented atomic ensemble is situated in a magnetic field, have already been expressed in 3.7. However, the equations for the light modes of interest have not explicitly been stated due to their complexity. The full input-output relations will be derived in this section.

Throughout the thesis the derived formulas will be used to see the effect of the higher order corrections on experiments that were evaluated with the simpler

model. But also proposals of new experiments, like atomic teleportation that is discussed in chapter 10, should be based on the more accurate model.
A lot of technical details are included in this section. This is partly due to the fact that there are different light modes which are worth considering. More specifically, it is possible to define rather complicated light modes, to achieve simple equations. The downside of this is that those light modes are not easily accessible for measurement. Therefore, I will also consider the modes that we usually measure to discuss the error made when the equations 2.39 are applied. If one does not want to follow the full derivation, this section can be skipped and the corrections will be discussed explicitly for every experiment where they are of relevance.

We saw previously that the single cell setting was more complicated, since in the two cell case the back action of light on itself is canceled out. There are two possible settings, one were the macroscopic spin is aligned with the magnetic fields and one where its antiparallel. The two sidebands in the Hamiltonian 3.4 that participate in the two processes with different weights exchange place.

The final atomic equations are easily obtained from equation 3.7:

$$\begin{aligned}\hat{x}^{\text{out}} &= \sqrt{1-\kappa^2\xi^2}\,\hat{x}^{\text{in}} + \frac{\kappa}{\sqrt{2}}\hat{q}^{\text{in}}_{c+} \mp \frac{\kappa\xi^2}{\sqrt{2}}\hat{y}^{\text{in}}_{s+},\\ \hat{p}^{\text{out}} &= \sqrt{1-\kappa^2\xi^2}\,\hat{p}^{\text{in}} \mp \frac{\kappa}{\sqrt{2}}\hat{q}^{\text{in}}_{s-} - \frac{\kappa\xi^2}{\sqrt{2}}\hat{y}^{\text{in}}_{c+}.\end{aligned} \tag{3.14}$$

The light equations for the falling modes can be calculated by integration:

$$\begin{aligned}\hat{y}^{\text{out}}_{c-} &= \frac{1}{2}(\hat{y}^{\text{in}}_{c-} + \sqrt{1-\kappa^2\xi^2}\hat{y}^{\text{in}}_{c+}) \mp \frac{1}{2\xi^2}(\hat{q}^{\text{in}}_{s-} - \sqrt{1-\kappa^2\xi^2}\hat{q}^{\text{in}}_{s+}) + \frac{\kappa}{\sqrt{2}}\hat{p}^{\text{in}},\\ \hat{y}^{\text{out}}_{s-} &= \frac{1}{2}(\hat{y}^{\text{in}}_{s-} + \sqrt{1-\kappa^2\xi^2}\hat{y}^{\text{in}}_{s+}) \pm \frac{1}{2\xi^2}(\hat{q}^{\text{in}}_{c-} - \sqrt{1-\kappa^2\xi^2}\hat{q}^{\text{in}}_{c+}) \pm \frac{\kappa}{\sqrt{2}}\hat{x}^{\text{in}},\\ \hat{q}^{\text{out}}_{c-} &= \frac{1}{2}(\hat{q}^{\text{in}}_{c-} + \sqrt{1-\kappa^2\xi^2}\hat{q}^{\text{in}}_{c+}) \pm \frac{\xi^2}{2}(\hat{y}^{\text{in}}_{s-} - \sqrt{1-\kappa^2\xi^2}\hat{y}^{\text{in}}_{s+}) - \frac{\kappa\xi^2}{\sqrt{2}}\hat{x}^{\text{in}},\\ \hat{q}^{\text{out}}_{s-} &= \frac{1}{2}(\hat{q}^{\text{in}}_{s-} + \sqrt{1-\kappa^2\xi^2}\hat{q}^{\text{in}}_{s+}) \mp \frac{\xi^2}{2}(\hat{y}^{\text{in}}_{c-} - \sqrt{1-\kappa^2\xi^2}\hat{y}^{\text{in}}_{c+}) \pm \frac{\kappa\xi^2}{\sqrt{2}}\hat{p}^{\text{in}}.\end{aligned} \tag{3.15}$$

The falling output modes couple thus to a linear combination of the rising and falling input modes. Therefore one needs to pay attention, when evaluating noise and mean value transfer in those equations, as the exponentially decaying and rising modes are not orthogonal. Later suitable orthogonal modes that are given by linear combinations of the two will be introduced.

To achieve simpler equations, new light modes can be defined like

$$\hat{\tilde{Y}}^{\text{out(in)}} = \frac{1}{\sqrt{2}\xi}(\hat{q}_{c-(+)} \mp \xi^2 \hat{y}_{s-(+)}), \quad \hat{\tilde{Q}}^{\text{out(in)}} = \frac{1}{\sqrt{2}\xi}(\mp\hat{q}_{s-(+)} - \xi^2 \hat{y}_{c-(+)}). \tag{3.16}$$

Note that the input operators have rising and the output operators falling exponential modes. Then the input-output equations are reduced to

$$\begin{aligned} \hat{x}^{\text{out}} &= \sqrt{1-\kappa^2\xi^2}\hat{x}^{\text{in}} + \kappa\hat{\tilde{Y}}^{\text{in}}, \quad \hat{p}^{\text{out}} = \sqrt{1-\kappa^2\xi^2}\hat{p}^{\text{in}} + \kappa\hat{\tilde{Q}}^{\text{in}}, \\ \hat{\tilde{Y}}^{\text{out}} &= \sqrt{1-\kappa^2\xi^2}\hat{\tilde{Y}}^{\text{in}} + \kappa\xi^2\hat{x}^{\text{in}}, \quad \hat{\tilde{Q}}^{\text{out}} = \sqrt{1-\kappa^2\xi^2}\hat{\tilde{Q}}^{\text{in}} + \kappa\xi^2\hat{p}^{\text{in}}. \end{aligned} \tag{3.17}$$

Those equations look reasonably simple, but they are experimentally not very convenient, since those light modes are not easily measurable.

To make a useful discussion of experimental results where the simple equations of section 2.2.3 were used, we need equations that look like the original equations 2.39 with a correction. So as the very last thing in this section, I will evaluate the single cell input-output relations, considering the scenario of the teleportation experiment discussed in chapter 6.
Let us first reexpress equation 3.15 for $\hat{y}_c^{\text{out}}$, such that it features only orthogonal modes. We introduce $f_{+\perp}(t) = af_+(t) + f_-(t)$, such that $\int_0^T f_{+\perp}(t)f_+(t)dt = 0$, implying that the exponentially rising mode $f_+(t) = \frac{1}{N_+}e^{-\gamma(T-t)}$ and $f_{+\perp}$ are orthogonal over the interaction time. Now, we can substitute the operators of the exponential falling modes by a linear combination of operators with orthogonal modes. The negative mode functions can be replaced by

$$f_-(t) = \frac{\gamma T}{\sinh(\gamma T)}f_+(t) - \sqrt{1 - \frac{\gamma^2 T^2}{\sinh(\gamma T)^2}} \cdot f_{+\perp}(t). \tag{3.18}$$

For now, I only want to evaluate the resulting equation for settings close to $\kappa = 1$, which is the working point of several experiments. For a detuning of $\Delta = 850MHz$, the overlap of $f_+(t)$ with the previously used flat-top mode and the overlap of $f_{+\perp}(t)$ with the first order temporal mode defined in equation 2.37 is 0.999584.

For the mentioned detuning $\kappa = 1$ translates into $\gamma_s T \approx 0.08$, and we can Taylor expand the output equations for $\gamma_s T$. Then we get for a reasonable expansion:

$$\begin{aligned} \hat{y}_c^{\text{out}} = \quad & \hat{y}_c^{\text{in}}(1 - \frac{\xi^2\kappa_{\text{QND}}^2}{4}) + (\frac{\kappa_{\text{QND}}}{\sqrt{2}} - \frac{\kappa_{\text{QND}}^3\xi^2}{4\sqrt{2}})\hat{p}^{\text{in}} \ldots \\ \mp \quad & \frac{\kappa_{\text{QND}}^2}{4}(\hat{q}_s(1 - \frac{\xi^2}{3}) - \frac{1}{\sqrt{3}}\hat{q}_{s,1} + \frac{\xi^2}{\sqrt{3}}\hat{y}_{c,1}) \end{aligned} \tag{3.19}$$

The $\kappa_{\text{QND}} = a\sqrt{J_x S_x T}$, also refers to the coupling constant introduced in chapter 2. The variance of this light output is plotted in figure 3.4 as the dashed line.

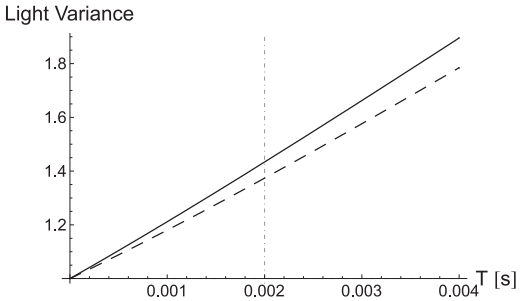

Figure 3.4: Variances of light quadrature $\hat{y}_{c,s}$ after the interaction with a certain duration T. The solid line is the noise expected without the correction and the dashed line is the noise with the correction. Clearly the QND theory overestimates the expected noise.

The noise coming from the atoms is slightly suppressed. The back action noise of light is overestimated, if one considers the equations in chapter 2, since there is also a suppression of the input light noise taking place. Anyhow, as mentioned before, a number of other things, like the method of the measurement of the coupling strength need to be considered, to evaluate the reconstruction mistake.

3.2.3 Comments to the input-output equations

In the last section we introduced exponentially decaying and rising modes. The decaying output light modes and the rising input light modes couple to the atoms. The equations were derived for very specific settings. Actually, the sign of γ_s can be flipped in different ways, such that the output modes would be exponentially rising. The sign can be changed, by changing the polarization of light, which leads to a sign change in the light quadrature operators, or by using a red detuned probe that changes the sign of a_2. This leads to a completely different scenario where $\hat{V} \propto \hat{p}\hat{q} - \xi^2\hat{x}\hat{y}$. The input operators are amplified, since $\sqrt{1-\xi^2\kappa^2} > 1$ and γs flips sign. Also κ^2 grows faster than linear with time, instead of saturating. For certain experiments, this setting might be beneficial. However, in the experiments conducted so far, we have experienced additional technical noise in our measurements. It is not clear today, if there is a fundamental problem with those measurements, or if the general sensitivity of our measurements combined with less invested time in those specific settings just lead to the observed behavior.

3.3 Effects of additional decay

In the experiment, the atoms are exposed to a whole range of effects that cause the transversal spin to decay. The atoms collide with the walls and other atoms, there is spontaneous emission and, since the observables of interest are magnetic coherences, magnetic field instabilities also lead to decoherence. Thus, experimentally, we will always see a decay of the mean values that is faster than a decay with γ_s introduced in the previous section. While the mean value is decaying, for us it is very important what happens to the noise of the observables. Here we will consider the known approach of Langevin noise operators [SZ97]. We extend the equations of motion of the atomic operators by adding an extra decay with γ_{extra} and to keep the quantum mechanical properties of the system valid, we add noise operators $\hat{f}_{x,p}$ with $Var(\hat{f}_{x,p}) = \frac{1}{2}$, simulating a decay towards the CSS. This seems like a rather contingent assumption. Anyhow, we know that the major decay contributions coming from spontaneous emission go towards the CSS[3], other decay contributions might lead to an admixture of the thermal state.

If we assume a decay towards a state with lower noise than the CSS impossible, the description will provide us with a best case scenario, when we attempt to make predictions about the outcome of an experiment. On the other hand, if we use the formulas derived in the following for atomic state reconstruction from the light noise measurement, they will provide us with a worst case scenario. This means that we will overestimate the atomic noise (see section 5.2).
We can test the atomic orientation and for short timescales the approximation will prove to be quite accurate, A thorough discussion of measurements on the decay will follow in section 4.3.

The extended atomic equations read

$$\begin{aligned} \dot{\hat{x}} &= a\hat{q}(0,t) - \frac{a^2\xi^2}{2}\hat{x} - \Omega\hat{p} - \gamma_{\text{extra}}\hat{x} + \sqrt{2\gamma_{\text{extra}}}\hat{f}_x, \\ \dot{\hat{p}} &= a\xi\hat{y}(0,t) - \frac{a^2\xi^2}{2}\hat{p} + \Omega\hat{x} - \gamma_{\text{extra}}\hat{p} + \sqrt{2\gamma_{\text{extra}}}\hat{f}_p. \end{aligned} \tag{3.20}$$

We will now define the new decay constant $\gamma = \gamma_s + \gamma_{\text{extra}}$. It is straight forward to solve those equations for the atoms in the single and two cell case. For more details, see appendix B. For the single cell, we get

[3] Atoms decaying to $F = 3$, effectively leave the system, which is similar to an admixture of vacuum; atoms decaying over an excitation of $F' = 5, m = 5$ can only decay into the CSS.

$$\begin{aligned}\hat{x}^{\text{out}} &= \sqrt{1-\kappa^2\xi^2}\hat{x}^{\text{in}} + \sqrt{1-\epsilon^2}\frac{\kappa}{\sqrt{2}}\hat{q}^{\text{in}}_{c+} \mp \sqrt{1-\epsilon^2}\frac{\kappa\xi^2}{\sqrt{2}}\hat{y}^{\text{in}}_{s+} + \epsilon\kappa\xi\hat{F}_{x+},\\ \hat{p}^{\text{out}} &= \sqrt{1-\kappa^2\xi^2}\hat{p}^{\text{in}} \mp \sqrt{1-\epsilon^2}\frac{\kappa}{\sqrt{2}}\hat{q}^{\text{in}}_{s+} - \sqrt{1-\epsilon^2}\frac{\kappa\xi^2}{\sqrt{2}}\hat{y}^{\text{in}}_{c+} + \epsilon\kappa\xi\hat{F}_{p+}.\\ &. \end{aligned} \tag{3.21}$$

with $\epsilon^2 = \frac{\gamma_{\text{extra}}}{\gamma}$ and for two cells:

$$\begin{aligned}\hat{X}^{\text{out}}_{c,s} &= \sqrt{1-\kappa^2\xi^2}\hat{X}^{\text{in}}_{c,s} + \sqrt{1-\epsilon^2}\kappa\hat{q}^{\text{in}}_{c,s+} + \epsilon\kappa\xi\hat{F}_{Xc,s+},\\ \hat{P}^{\text{out}}_{c,s} &= \sqrt{1-\kappa^2\xi^2}\hat{P}^{\text{in}}_{c,s} - \sqrt{1-\epsilon^2}\kappa\xi^2\hat{y}^{\text{in}}_{c,s+} + \epsilon\kappa\xi\hat{F}_{Pc,s+}.\end{aligned} \tag{3.22}$$

For light, the two cell case can in principle also be easily calculated for the exponentially decaying mode. The light modes read:

$$\begin{aligned}\hat{y}^{\text{out}}_{c,s-} = \epsilon^2\hat{y}^{\text{in}}_{c,s-} &+ \hat{y}^{\text{in}}_{c,s+}\sqrt{1-\kappa^2\xi^2}(1-\epsilon^2) + \kappa\sqrt{1-\epsilon^2}\hat{P}^{\text{in}}_{c,s}\\ &+ \epsilon\sqrt{1-\epsilon^2}\frac{1}{\xi}(\hat{F}_{p-} - \sqrt{1-\kappa^2\xi^2}\hat{F}_{p+}),\\ \hat{q}^{\text{out}}_{c,s-} = \epsilon^2\hat{q}^{\text{in}}_{c,s-} &+ \hat{q}^{\text{in}}_{c,s+}\sqrt{1-\kappa^2\xi^2}(1-\epsilon^2) - \kappa\xi^2\sqrt{1-\epsilon^2}\hat{X}^{\text{in}}_{c,s}\\ &+ \epsilon\sqrt{1-\epsilon^2}\frac{1}{\xi}(\hat{F}_{x-} - \sqrt{1-\kappa^2\xi^2}\hat{F}_{x+}).\end{aligned} \tag{3.23}$$

Again, it is important to note that the decaying and rising modes are not orthogonal. This means that operators, as for example $\hat{y}_{c,s-}$ and $\hat{y}_{c,s+}$, are not independent. So whenever noise measurements are taken, we have to formulate those equations in a way including only orthogonal modes. The full equations can be found in appendix B.

3.4 Limitations of the derived equations

While this extension of the simple QND model is supposed to yield a better description of the experiment in the higher coupling limit, there are a couple of crucial limitations that need to be considered.

The first is that linearizing of the quadratic spin terms only works for a very highly oriented ensemble, since it is only considering the upper two magnetic sub-levels. For some of our experiments this is not sufficient. In chapter 7 states are considered where a considerable amount of population is in the $m = 2$ level. To evaluate the atomic state via a dispersive readout with a low coupling a per-

turbational approach without the linearizing step was taken in appendix C.
In chapter 8 strong coupling is used to achieve atomic entanglement via the interaction leading to considerable spontaneous emission in all magnetic sublevels. The orientation will be tested to make sure that the model remains valid throughout the whole process. In some of those experiments, a weak pumping laser will be applied during the interaction, leading to a high degree of polarization throughout the whole model.

For timescales long compared to the decay of the longitudinal spin, γ_s will also be time dependent, as $\gamma_s \propto J_x$, so for long timescales this need to be considered.

Part II

Experimental methods

Chapter 4

Characterization of the experimental system

This chapter is devoted to the description of the experimental setup and measurements which characterize this system. There are many quantities that are of importance in our experiment. Here, we are mainly going to deal with what I would like to call classical measurements, implying that we are going to be concerned with mean values. However, those mean value measurements are not going to be enough to characterize the full system. Chapter 5 will therefore be concerned with quantum noise measurements which will supply us with another set of calibrations - like the shot noise of light, a different method of measuring κ and the detection efficiency.

First, the experimental systems - the atomic sample and the light sources - will be described. This is followed by an experimental analysis of the atomic states where the achieved orientation and the macroscopic spin will be measured. Also the coupling constant (section 4.14) can be determined just by mean value measurements. A rather long part of this chapter is devoted to measurements of the decay, since decoherence is one of the main limiting factor of our experiments.

4.1 Experimental system

In this section I will introduce the atomic system and the light sources. The experiment requires three light beams. Two are used for the preparation of the oriented state by optical pumping [Hap72]. Furthermore, the probe laser is needed for the desired interaction discussed in chapters 2 and 3 and finally the measurement on the Stokes operators is discussed

4.1.1 Atomic system

The atomic system consists of an ensemble of Cesium atoms at room temperature. Cesium is an alkali metal with only one stable isotope ^{133}Cs which has the nuclear spin of $I = 7/2$. Together with the outer electron this gives a ground state with the two hyperfine states $F = 4$ and $F = 3$. In figure 4.2 the ground state is shown together with the first excited states. There are two D-lines, the D_1 line corresponding to the $6^2S_{1/2} \rightarrow 6^2P_{1/2}$ transition and the D_2 line ($6^2S_{1/2} \rightarrow 6^2P_{3/2}$). Details can be found in [Ste03].

The atoms are situated in a glass cell with a paraffin coating[1]. Those coatings are known to protect the atomic spins from decoherence due to wall collisions [BB66, ABP+96, ABB+02]. At room temperature the Cesium atoms have a mean velocity of 235 m/s. This leads to around 10 wall collisions in one millisecond for cubic cells with a side length of 2.2cm. With help of the coatings we can achieve spin coherence times around 30-40 ms and lifetimes of the macroscopic spin up to 200ms, which stresses the quality of the used coatings. Recently, new alkane based coatings have been developed [6] which grant lifetimes of the macroscopic spin up to a second. The next generation of cells will be coated with this newly developed material.
On one side of the glass cube a glass finger is attached with solid Cesium in the end of the finger. The diameter of the hole between cell and finger is smaller than 1mm to avoid the exchange of atoms from cell body and the finger at a fast rate. On the left of figure 4.1a, the cubic glass cell is shown along with another cell design that was used previously. Glass plates with antireflection coatings are attached to the outer windows of the cells with help of an index matching fluid. This way the light losses for one passage can be reduced to around 8-10%. Currently efforts are made to use cells with antireflection coating on the inside to reduce reflection losses even further. However, this causes some problems in the production, since the windows have to be glued together after the coating was applied. Then the paraffin coating has to be layered on top and since the preparation for this procedure includes a heating cycle up to temperatures around 350°C the coatings need to be able to withstand higher temperatures. In the first attempt we have experienced some problems with the behavior of the cells after the gluing. It seems that the paraffin coating does not cover the cell surfaces properly. This could be due to some interaction with the glue. Since the atoms move rather fast, already a small uncoated surface suffices to degrade the performance considerably. Also when the prepared glass cell was filled with Cesium there appeared to be a reaction of the Cesium with some of the remaining components after the evacuation and the seiling of the cell, the reason of which remains unknown.

[1] The coatings we use are produced by M. Balabas.

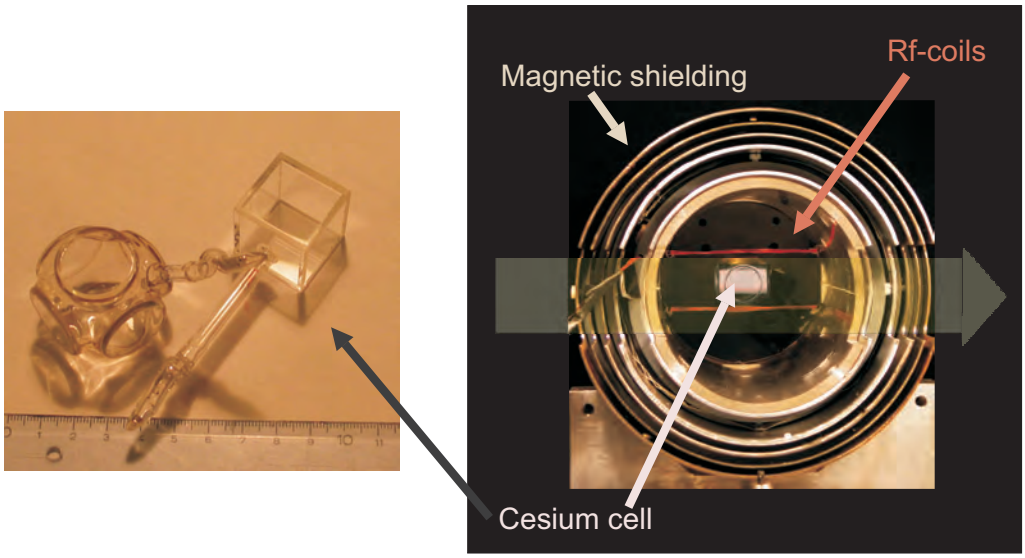

(a)

(b)

Figure 4.1: Experimental setup. On the left of (a) two glass cell, filled with Cesium are shown. The square glass cell is the latest design. It is situated in a magnetic shield shown on the right. The bias magnetic field of 0.9 G is pointing out of the picture plane here and is created by four coil pairs. The RF coils are oriented such that the RF field lies orthogonal to the bias field and macroscopic spin. Two apertures along the transversal direction allow the light beam to pass the cell. The pump beams are aligned in direction of the main axis and also a small and weak probe light beam to measure the macroscopic spin is directed that way. (b) shows the part of the setup where the interaction and measurement take place.

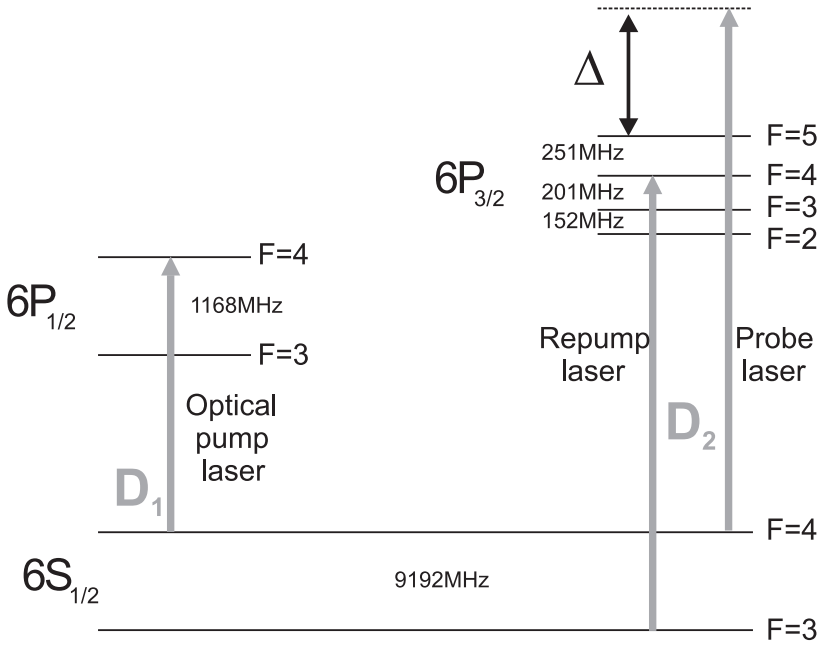

Figure 4.2: Level scheme of Cesium, including the ground levels and the first excited levels. The frequencies of the three lasers that are used, are depicted.

The cells contain around $2.5 \cdot 10^{11}$ atoms at room temperature (RT). By changing the temperature and thus the density of atoms with help of a heated or cooled air flow the number of atoms inside the cell can be reduced to around half the number of atoms and increased to around three times the number of atoms at RT. Due to the paraffin coating, the cells can not be heated up further. It will turn out that this is also not advisable, since a too high temperature induces additional technical noise which we observe in our atomic noise measurements, so that we find an optimum for most experiments at room temperature or at the temperature yielding around twice as many atoms in the cell.
For further protection, the glass cell is situated inside a magnetic shielding. It consists of layers of μ metal and iron and can be seen on the right of figure 4.1a. Since our measurement quantities are coherences of magnetic substates this protection against magnetic disturbances is crucial.

4.1.2 Pump lasers and state preparation

The pump lasers are grating stabilized diode lasers which are set up in Littrow configuration with diodes with different suitable gain profile. The lasers are homemade and used in a whole range of QUANTOP experiments [She06, Hil08, Win08].

Frequency stabilization of the pump lasers

The repump laser at 852nm is used to shuffle atoms from $F = 3$ to the $F = 4$ ground state. Its frequency is stabilized to the D_2 line $F = 3$ to $F' = 4$ transition by saturation absorption spectroscopy. Saturation absorption spectroscopy is a tool used to lock to a sharp atomic transition, even though the absorption profile is broadened due to atomic motion. At room temperature, every line is Doppler broadened to almost 200 MHz. On the D_2 line we will therefore only see two absorption dips 9.2 GHz apart, coming form the splitting of the ground states. The transitions to the different excited states can not be resolved, as they lie too close, compared to the Doppler broadening. To make them visible, a small portion of the beam coming from the diode laser is sent through a Cesium cell, attenuated and then sent back through the sample (see the right of figure 4.4 for the setup). The laser frequency is seen with different Doppler shifts for atoms moving with different velocities. Therefore the atoms see different frequencies for the two beams, coming from either side of the sample, as their velocity flips sign compared to the beam propagation. When the laser hits the exact frequency of a transition the atoms with zero velocity will absorb the light. If the beam is strong enough, it will saturate the transition, causing a decreased absorption in the reflected beam that is also resonant with the atoms at zero velocity. This can be seen as peaks inside the absorption profile. In figure 4.3 such a saturated absorption signal is shown for the D_2 line. Additionally to the spikes at the transition frequencies, also crossover peaks appear. These come from one velocity class of atoms in resonance with one transition of the atoms for the saturation beam and the neighboring transition for the reflected beam. Those peaks lie therefore exactly in between the true transitions. The lower curve in figure 4.3 shows the signal that we actually use as the error signal for locking. This differential signal is produced, by adding a modulation to the diode current at a certain frequency. With help of the resulting sidebands, the error signal is produced by mixing the photo detector signal with a signal with the original modulation frequency [BLLO83].

The pump laser at 894nm is locked to the D_1 line $F = 4$ to $F' = 4$ transition. On the D_1 line 4 distinct absorption dips can be seen, but to have a sharp stable frequency again saturated absorption spectroscopy is applied.

Pulsed optical pumping

Besides the right frequency the lasers also need to have a distinct polarization for the atomic state preparation. The pump beams are aligned in direction of the magnetic field and are either σ_+ or σ_- polarized. This way $m = 4$ or $m = -4$ is a dark state for the pump laser, as there are no exited $m' = \pm 5$ states

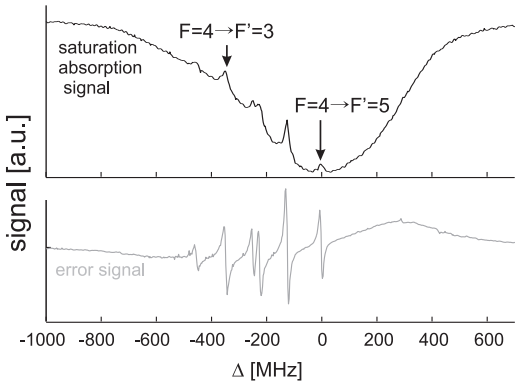

Figure 4.3: Saturation absorption spectroscopy signal. The black line shows the saturation absorption spectroscopy signal for the D_2-line, considering only the ground state $F = 4$. The gray line shows the error signal

available. The corresponding level scheme is depicted in the middle of figure 4.6. The atoms in all other magnetic sublevels of the ground state absorb the pump light and decay towards $F = 4$ or 3 and, depending on if the pump light was σ_+ or σ_- polarized move on average one m level up or down. When the pumping is conducted long enough with enough power all the atoms in $F = 4$ will end in $m = 4$. The repump laser pumps in the meantime those atoms which decay to $F = 3$ back to $F = 4$, so they are not lost to the pumping cycle. The powers used are around 3 to 5 mW for the repump laser and 0.5-2 mW for the pump laser.

Since the pump lasers are not to be shone on the atoms while the actual experiment takes place, they are turned on and off via acousto optical modulators (AOM). The AOMs are used with a 125MHz modulation and the first order of diffraction is directed to the atomic ensemble. The light can then easily be turned off by switching off the modulation. The frequency of the pump light is shifted by the modulation frequency. Fortunately the Doppler profile is broad enough, so that this does not matter, as long as we pump for long enough times. The pump pulses have usually a duration of 4-20 ms and the extinction of the input light, when turned off, lies around 0.1%.

4.1.3 Probe laser and Stokes measurement

Probe laser setup

The probe laser is detuned from the D_2 $F = 4$ to F′=5 line by Δ as depicted in the level scheme in figure 2.1. The detuning should be chosen in such a way that the frequency lies well outside the Doppler profile. Our typical detuning is 850 MHz. We use two different laser systems as the probe laser. One is a

distributed feedback laser (DFB) from Toptica[2]. The frequency selective device is a grating structure directly incorporated in the semiconductor chip. The frequency can be scanned by modulating temperature or the laser current, and can easily be varied over the D_2 lines without any mode hops. The output has extremely low amplitude noise at the RF-frequency of interest at 322kHz.
The laser is sent through an optical isolator and part of the light is taken out for the frequency stabilization. This fraction of light is sent through a fiber coupled electro optical modulator, used for intensity modulation. The modulations at around 1 GHz is done so strongly that almost nothing is left in the carrier, while the two sidebands become very strong. Then, depending on whether we wish to achieve red or blue detuning, we lock the blue or red sideband frequency to an atomic transition. We usually choose the first cross over peak of the red sideband as a locking point, so that our detuning is given by the modulation frequency minus half the splitting of $F' = 4$ and $F' = 5$, $\frac{\Delta_{45}}{2} = 125.5$MHz.

The other probe laser that can be used for the experiments is a Ti:Sa ring cavity laser[3] which is pumped with a Verdi[4] laser at 532nm with 8-10W pump power. This laser has higher output power (several hundred mW), which is useful for some of our applications. Especially experiments in which squeezed light is used profit from the narrow linewidth of the Ti:Sa laser and the high output power which allow for efficient production of broadband squeezed light [WKHW86] with standard optical-parametric-oscillator (OPO) techniques. The setup for this is discussed in detail in [SSP02, NNNH$^+$06] and I will just briefly describe it here for completeness. The output of the laser is frequency doubled by second harmonic generation in a nonlinear crystal. This is used as input for an optic parametric oscillator (OPO). Here parametric down conversion leads to an infrared light output that is quadrature squeezed. Combined with a local oscillator, the output can be used for our experiments. In this thesis, experiments with squeezed light are only discussed in passing. Most of the time when the Ti:Sa laser is employed, we use the local oscillator and a vacuum field in the quantum mode. However, the path which is used to produce squeezing, can be exploited to create displaced coherent states with help of two EOMs. This is discussed briefly in section 4.14.

The Ti:Sa laser is frequency locked with help of a beat lock to another laser with known, stable frequency. The beat lock requires much less laser power than we typically use for the sideband-modulation lock. A portion of light is mixed on a beamsplitter with a frequency stabilized laser, for example the DFB laser. The signal is detected with a fast photo diode[5] and the amplified sig-

[2] with the diode: LD-0852-0150-DFB-1
[3] We use microlase (now COHERENT) system as well as a homemade laser.
[4] Diode pumped solid state laser from Coherent
[5] Hamamatsu GaAs Metal-Semiconductor-Metal photo detector (G4176-03) on a Mini-circuits ZX85-12G-S+ Bias-T

nal is mixed with a oscillating signal at a frequency $f_{\mathbf{ref}}$, which will determine the detuning of the two lasers that are overlapped. This mixed signal is sent to a frequency discriminator[6] that compares the down mixed beating signal to a reference frequency which in our case lies at 65MHz. It produces an error signal which gives a negative output for input frequencies below 65MHz and a positive output for higher frequencies. Locking to this signal allows to lock to detunings of $\delta = \pm(f_{\mathbf{ref}} \pm 65\text{MHz})$. In figure 4.4 the schematics of the locks of the two probe lasers are shown.
Besides fixing the frequency to a certain detuning, the probe laser also needs to be shaped in time. In the previous section it was mentioned that the pump lasers are switched with AOMs. This approach is not taken with the probe light as we experience high excess amplitude noise on the edges of the pulses. Therefore we use an electro optical modulator (EOM) positioned between two polarization beam-splitters instead. The electro optical crystal changes the refractive index by applying an external voltage differently for two orthogonal polarizations. The reached suppression is of the order of 100-200.
Also, the beam has to be shaped in space. The atomic cells have a 2.2x2.2cm^2 cross section and the beam should fill as much as possible of this area and have a smooth intensity profile. The first option to achieve this is to use a very big collimated Gaussian beam and cut out the center with an iris to achieve a smooth beam profile. This introduced of course a lot of losses in the probe beam, as most of the beam is dumped. A better result is achieved, when a beam shaper[7] is used that converts a gaussian beam to a flat-top profile type beam. The achieved smoothness is satisfactory for both settings, as the remaining deviations in laser power are averaged out due to the atomic motion. The experiments described in chapters 8 and 9 in this thesis were conducted with the beam-shaper.

Stokes vector measurement

The light quantities of interest are the Stokes operators. We mainly measure $\hat{S}_y$, as it is changed strongest by the interaction. For that we use a $\frac{\lambda}{2}$-plate and a polarization beamsplitter and measure the number of photons polarized in 45° and $-45°$ accordingly. Thus by subtracting the photocurrent of the two detectors we get a signal proportional $S_y = \frac{1}{2}(n_{+45°} - n_{-45°}) = \sqrt{S_x} \cdot y$. The signal strength is given by the strength of the classical input pulse. Similarly we can measure $\hat{q}$ ($\hat{S}_z$) with help of an extra $\frac{\lambda}{4}$-plate.
Our measurement is similar to normal homodyning measurements [BRLR98], where for us the local oscillator (LO) and the weak quantum field are not spa-

[6] The phase-frequency discriminator was originally designed in the MIT, Boston. It is based on an ultrahigh speed phase/frequency discriminator from Analog Devices (AD9901).

[7] beam shaper for collimated beams from ΠShaper.

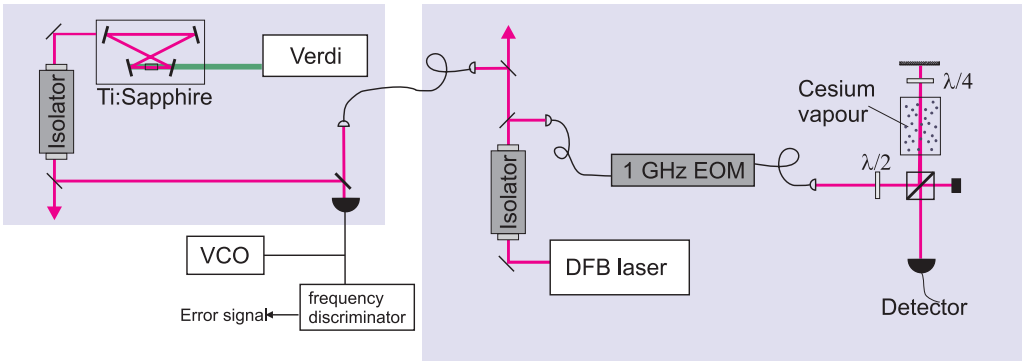

Figure 4.4: Probe laser setup, including the different locking systems. On the right the DFB-laser and the saturation absorption spectroscopy setup are depicted. On the left the Ti:Sa laser is shown which is frequency locked via a beat lock.

tially separated, but belong to orthogonal polarization modes. In most of our measurements the LO is y-polarized and the quantum field is x polarized. Thus the mean value of $\langle S_y \rangle = 0$. The amplitude noise of the driving laser is canceled, and only the "quantum" noise is detected. Of course one can not achieve perfect noise suppression, so called balancing. We routinely achieve a suppression of classical noise by a factor of 400-1000. For a balancing of 1000 a shot noise measurement, with an extremely noisy light source with 100 times shot noise additional intensity modulation, will still only reveal one per mill additional noise compared to the shot noise level.

As we are interested in the light variable components at a certain frequency, we use a lock-in amplifier[8] that supplies us with the strength of the difference detector signal at a chosen frequency. The two components which the lock-in gives out are the components of the input signal in phase and 90° out of phase with the reference RF-signal. After normalization, this corresponds to the cosine and the sine component of the Stokes operator $\hat{S}_{y,c(s)}$.

The detectors we use are peaked around the frequency we are interested in (see [She06]), but broader than the filtering of the lock-in amplifier. The photo diodes[9] have a high quantum efficiency of around 98% at the used wavelength. Around 4% of the incident light are reflected, so this reduces the efficiency. This reduction can be avoided by back-reflecting the reflections onto the detector. This approach is advisable, whenever feedback of the measurement results is applied. If the measurement is used only to characterize the quantum state of

[8] A Stanford research systems SR844 200 MHz RF lock-in amplifier is used with an external reference. The simple working principal is as follows: the input signal is multiplied with a signal oscillating with reference frequency and phase. The resulting signal has a component which is oscillating with the sum frequency of input an reference and at the difference frequency. After a low-pass filter only the signal close to DC are left.

[9] Hamamatsu photodiode S33994

light (or atoms via the light) the slightly worse quantum efficiency can easily be compensated for, as we are only dealing with Gaussian states.

The noise coming from the whole detection system lies at around 1% of the shot noise of light for a light power of 5mW.
For some experiments, like the test of orientation, the signal from the lock-in amplifier can be recorded with help of a digital oscilloscope.
For the noise measurements that require many repetitions the data acquisition is conducted such that for every measurement pulse the lock-in amplifier output is sampled at a rate of 10 kHz[10]. Those points are multiplied with a given mode function and added up. Then for a set of measurements the mean value and the variances are calculated and stored.

4.2 Characterization of the atomic state

After the atomic system is initialized with the pump beams we want to assume that the atoms are in the CSS. In this section some of the measures characterizing the atomic state are discussed. Starting with the measurement of the macroscopic spin in section 4.2.1 we describe an investigation of the orientation in section 4.2.2 followed by a discussion of the effect of the probe light onto the atoms, not including decay which will be discussed in detail in section 4.3.

4.2.1 Faraday angle

To determine the length of the macroscopic spin in the x-direction, we send a weak, detuned probe of linearly polarized light in the direction of the orientation of the spin. This weak measurement is a probe of $\langle \hat{J}_x \rangle$, with a negligible effect on the atoms. The polarization of the probe beam is rotated proportionally to the mean spin in x-direction. This is discussed in detail in [Jul03] and summarized in appendix D. The rotation angle, in the following called Faraday angle θ_F, is given by (see equation D.3)

$$\theta_F = \frac{\gamma_0 a_1 \lambda^2 \langle J_x \rangle}{16 A \Delta 2\pi} \approx \frac{\gamma a_1 \lambda^2 4 N_a}{16 A \Delta 2\pi}, \tag{4.1}$$

where the right side is true for a fully oriented sample, meaning almost all the atoms are sitting in $F = 4, m = 4$. If all atoms are in $F = 4$ but the ensemble is not fully oriented, one has to add the orientation $o_{F=4} = \frac{1}{4} \sum_m m \cdot p_m$ to the formula, where p_m are the populations of the different m levels in $F = 4$. After the interaction, we measure the angle by sending the Faraday probe through a polarizing beam splitter (PBS)[11] with a DC detector in each output port. From

[10] Labview FPGA is used.

[11] A Glan Thompson polarizing beamsplitter is used that provides high purity in polarization.

the detector signals the polarization rotation can be calculated. According to equation 4.1 it is thus possible to obtain the number of atoms. Of course this is only true for the CSS and we must be very careful as to check if our pumping procedure is efficient. Therefore a measurement of the orientation of atoms in $F = 4$, called magneto optical resonance (MORS) will be discussed in section 4.2.2. The MORS measurement does not give any information about atoms in $F = 3$, but by using a rather large power of the repump power for which the Faraday angle is saturated, one can be sure not to leave many atoms in $F = 3$.

Sometimes it might be interesting to work at settings where a controlled part of the atoms are in $F = 3$. One can for example reduce the power of the repump laser in the pumping pulse. This is an easy way to reduce the number of atoms participating in the interaction. The atoms in $F = 3$ are strongly detuned, so they interact much weaker with the light. Also, they have a different g factor and precess therefore at a different Larmor frequency. Their contribution to the detection of the transversal spin via the light is small. The atoms in $F = 3$ do have a small effect on θ_F and equation D.5 can be used to calculate a compensated Faraday angle which gives the polarization rotation that purely comes from the rotation of the atoms in $F = 4$. Some issues arise here, as one needs to have information about the orientation of the atoms in $F = 3$. Most of the time, we will work with settings where this will be close to one. Otherwise, we might be able to use the techniques described in the next section to learn something about the orientation. Anyhow, in most cases the polarization rotation originating from atoms in $F = 3$ is very small and can be ignored.

The Faraday angle measurement is conducted regularly in every measurement series. It is an important control measure as the coupling constant is depending on the macroscopic spin arising from the atoms in $F = 4$.

4.2.2 Characterization of the atomic orientation

It is very important to verify that the atomic ensemble is in the CSS as part of the model describing the light-atom interface relies on this knowledge. A first step is to measure the orientation of the atomic ensemble. To check the orientation of the atomic $F = 4$ ground state, we use an RF magnetic field to excite coherences and then read out the transversal spins that are given by the coherences. This can be done in the frequency or time domain. The former is a known method introduced in [AGC+87, JSSP04] and discussed in detail in [Jul03, She06] and called magneto optical resonance signal (MORS). The setup for a MORS experiment is shown in figure 4.5 and explained in the caption. I will give a brief discussion here and some details are included in appendix E, since it is an important tool for the state characterization. Then the method of measuring and analyzing a MORS in time domain is discussed.

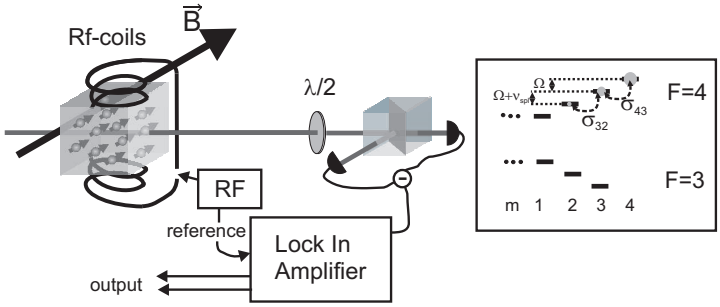

Figure 4.5: Setup for MORS measurement.An RF field is applied to the atoms and a detuned light beam is sent through the atoms. After the interaction the light hits the polarization homodyning setup. The difference signal from the detectors is analyzed with a lock-in amplifier that uses a reference, coming from the same signal generator that supplies the signal for the RF field. On the right side the magnetic sublevels of the ground state are shown. The detected signal on the light will have components proportional to the coherence strengths. The two coherences depicted here (σ_{43} and σ_{32}) oscillate at different frequencies and can thus be resolved.

Frequency spectrum of atomic coherences

For the MORS experiment, a DC magnetic RF field is applied perpendicular to the macroscopic spin, as sketched in graph 4.5. The RF field creates an excitation of $\Delta m = 1$ coherences, whenever the frequency is on resonance. The resonances have a certain width and, due to the quadratic Zeeman shift, they precess with different frequencies. The quadratic Zeeman effect which becomes relevant for atoms in magnetic fields of intermediate strength is discussed for the presented experiment in [Jul03]. The effect is rather small and leads to a splitting of the coherence frequencies of around 22Hz ($\Omega_L = 2\pi 322$), but due to the long spin coherence times and thus narrow lines in the MORS it gives us the possibility to resolve the different lines allowing us an analysis of the spin state.

The transversal spins that we probe in our measurement are sums of all the spins of the atoms which are given by the coherences as
$\hat{j}_y = \sum_m \sqrt{F(F+1) - m(m+1)}(\hat{\sigma}_{m+1,m} + \hat{\sigma}_{m,m+1})$ and
$\hat{j}_z = \sum_m i\sqrt{F(F+1) - m(m+1)}(\hat{\sigma}_{m+1,m} - \hat{\sigma}_{m,m+1})$ with $\hat{\sigma}_{i,j} = |i\rangle\langle j|$. When we look at mean values coming from equation 2.35, our measurement quantities $\langle \hat{y}^{\text{out}}_{c,s} \rangle \propto \langle \hat{j}_{y,z} \rangle$ will be proportional to the two transversal spins in the rotating frame. The MORS is given by $R = \sqrt{\langle \hat{y}^{\text{out}}_c \rangle^2 + \langle \hat{y}^{\text{out}}_s \rangle^2}$ and follows equation E.3. For the case of a slowly varying RF frequency, the spins are given by the sum of Lorenzians at the resonance frequency of each coherence $\hat{\sigma}_{m,m+1}$. The strength of every peak is given by the population difference in the two levels m and $m+1$ and the factor $F(F+1) - m(m+1)$. To create an imbalance between the magnetic sublevels in order to see any signal in the mean values, the repump laser can be turned on. On the left of figure 4.6 the trace for such a scenario is

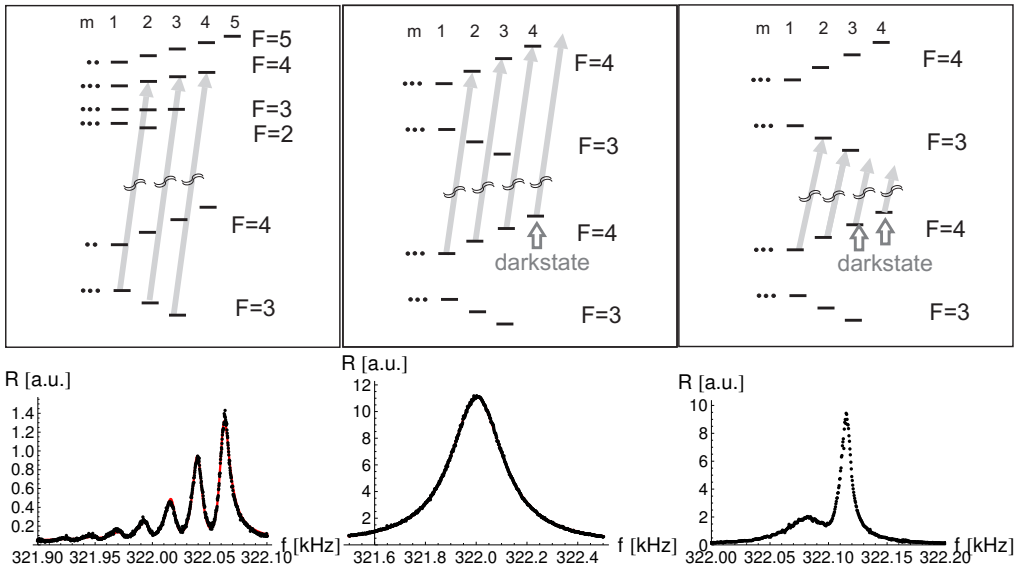

Figure 4.6: Different MORS for $F = 4$ are shown together with the relevant levels of Cesium. On the left only the repump laser is creating an imbalance in the ground state populations. The repump laser is far off resonance to all transitions from the F=4 ground level states. Therefore it has a negligible effect on the width and the splitting frequency of the resonances. In the middle also the pump laser is turned on, which is resonant with the D_1 line $F = 4 \rightarrow F' = 4$. This causes a broadening of the lines an makes the extraction of the orientation difficult. On the right the pump laser was locked to the D_1 $F = 4 \rightarrow F' = 3$ transition. For σ_+ light, $m = 4$ and $m = 3$ are dark states. Therefore the σ_{43} coherence is not broadened. The polarization of the pump can be optimized by maximizing the peak of the $4 - 3$ coherence.

shown. The main peak represents the $\sigma_{4,3}$ coherence and can be maximized by adjusting the polarization of the repump laser.

In figure 4.7 frequency domain MORS traces are shown for different probe laser power and probe laser polarization. Not only the signal strength, but obviously also the width of the single peaks depends on the probe power. This is due to decay introduced by the probe and will be discussed in more detail in section 4.3. Also the splitting between the peaks differs from the 20Hz at low powers caused by the quadratic Zeeman shift. This originates in the quadratic Stark shift coming from the a_2 terms in the Hamiltonian 2.18. In [Jul03, She06] this is described for our experiment. The Stark shift also causes a displacement of all coherences with the same value. This was compensated for in the measurements of 4.7, by adjusting the magnetic field, but needs to be considered in protocols where light is switched on and off.

When all the atoms are in $m = 4$, we do not care about the splitting of the frequencies of the coherences, since we are only interested in the transition from $m = 4$ to $m = 3$. But whenever we investigate other atomic states (meaning other than the CSS), such as the thermal state (section 5.2.1) or a more com-

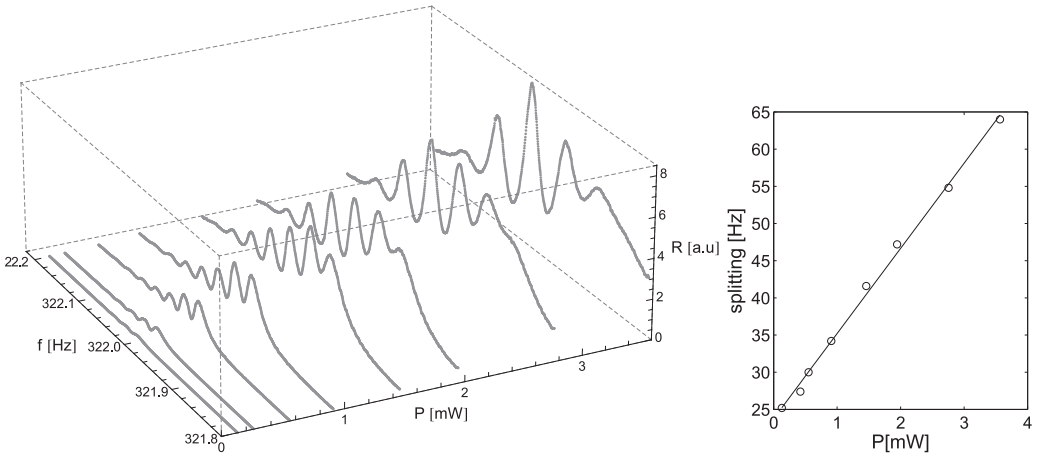

(a)

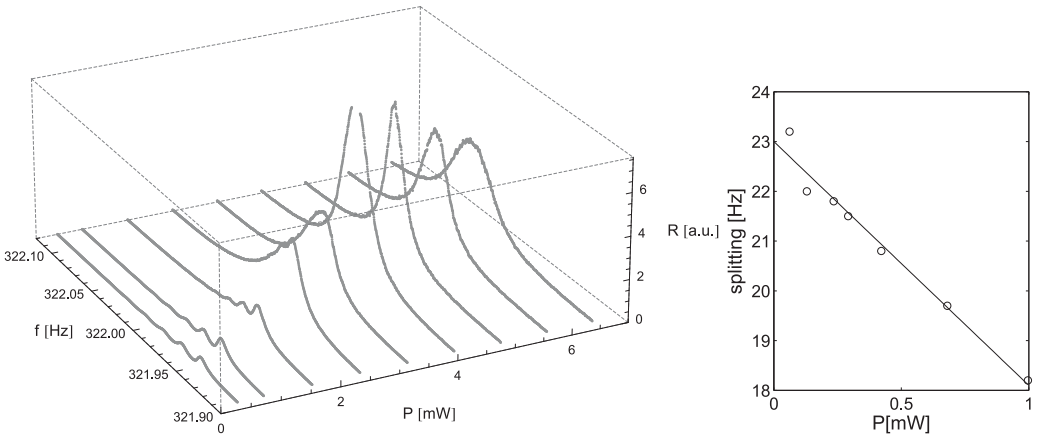

(b)

Figure 4.7: MORS signal for horizontal (a) and vertical (b) polarization of the probe beam at $\Delta = 825$MHz for different probe power. The signal is proportional to the squared sum of the rotating transversal spins. The frequency on the x axis is the frequency of the RF field applied. The frequency was varied very slowly (one scan took about 10s) and the response of the spins was recorded in a setup such as depicted in figure 4.5. The magnetic coherences are split due to the quadratic Zeeman shift and due to the quadratic Stark shift. For vertical polarization there is one setting where the two shifts cancel each other and all the coherences precess at the same frequency. In most cases, we work at this point or close to it.

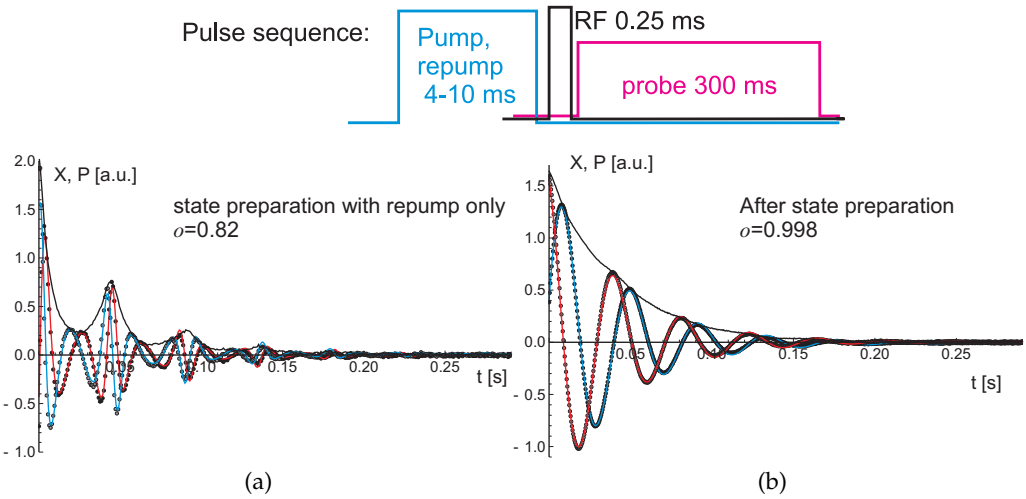

Figure 4.8: Pulsed MORS signal for a pumping cycle with only repump light (a) and for the full pumping (b). The black dots are the measurement results for the two atomic quadratures and the red and blue lines is a fit. The orientation that can be extracted from the fits are 0.82 and 0.998. In (a) the beating of the 43-coherence and the 32-coherence can clearly be seen as the second peak and even a third peak is visible. But also in (b) the structure of the envelope is clearly more complicated than a single exponential decay.

plicated squeezed atomic state (chapter 7), we need to consider this frequency mismatch. For those cases we often chose to work at the setting where quadratic Zeeman and Stark shift cancel (see figure 4.7b), which means working with vertical polarization around 4.5-5mW.

From fits to the MORS we can extract the orientation $o_{F=4} = \frac{1}{4}\sum_m m p_m = \frac{1}{4}\sum_m m\langle\sigma_{m,m}\rangle$. For pumped samples we assume exponentially decaying populations, as ϵ^{4-m}, thus reducing the amount of fitting parameters drastically. We will see that this assumption gives good results. Alternatively, we can assume the populations of the outer sublevels to be zero, which will lead to similar results in the populations coming from the fit. From the graph on the left of figure 4.6 we get orientations of $p \approx 0.8$. Obviously we want to know the orientation of the atoms, when the full pumping mechanism is applied - meaning that the optical pump is turned on. Since the optical pump is resonant with the D_2 line for the $F = 4$ ground state the lines get broadened, such that the single coherences can not be seen anymore and it is hard to extract any information about the orientation. Such a MORS is shown in the middle of figure 4.6.

MORS in the time domain

To probe the orientation of the fully pumped state, we need to establish a different method where we first optically pump the atoms into what we believe

to be the CSS and afterwards ramp down the pump and repump light and do a measurement with a weak probe. Then the signal coming from the atoms observed in time can be found by Fourier transformation of the equations in appendix E:

$$R \propto |\sum_m (F(F+1) - m(m+1) e^{i\Omega_{m+1,m}t} e^{-\Gamma t} (\sigma_{m+1,m+1} - \sigma_{m,m})|. \tag{4.2}$$

with Γ being the width of the coherences. Instead of a sum of Lorentzians there is a sum of oscillating terms with different frequencies which decay exponentially. The orientation can be extracted due to the beating of the signals with different frequencies coming from the different coherences. The timing of such an experiment is shown on the top of graph 4.8. The two graphs below show the decaying signal coming from the spin rotating at 322kHz. R is shown, together with X and P, the two out of phase signals coming from J_y and J_z in the rotating frame. One can see that the measurement frequency and the Larmor frequency actually differ slightly, as can be observed by the oscillations of the two signals. For the measurement run, shown in figure 4.8a, only a repump pulse was applied, for graph 4.8b both repump and pump laser were turned on. The beating between the coherences is clearly reduced. The extracted orientations are 0.820(2) and 0.998(2).

Difficulties with the orientation fit

In the previously presented data, we assumed a high orientation of the sample, we would like to fit. For this it is assumed that the populations of the different sublevels behave as ϵ^{4-m}. This model suits our data very well and also seems like a very intuitive model, characterizing the quality of our pumping procedure, with a dark state in $m = 4$. I just want to stress that in situations where we do not know as much about the state our atoms are in, we can not always extract the exact orientation from the MORS signal. The reason can be understood as explained in the following. The signal is comprised out of 2F peaks, while there are 2F+1 populations. Additionally the MORS is observed with a usually unknown overall strength A_{MORS} and every coherence is weighted with the corresponding transition matrix elements. Of course the populations have to add up to one $\sum p_m = 1$. Now this is similar to having 2F+2 unknowns and 2F+1 equations[12]. In the figure 4.9a, a DC-MORS signal is depicted for the atoms in $F = 3$, when applying a weak pump laser (150μW), resonant with $F = 4 \rightarrow 4$ on the D_1 line and a probe field at 8mW, close to the $F = 4 \rightarrow 5$ transition of the D_2 line. All seven peaks are visible. Without assuming any-

[12] A precise calibration of all experimental quantities should grant us some knowledge of A_{MORS}. However, in the presented data further below we can not even measure the ratio of atoms in $F = 3$ and $F = 4$, thus making such an attempt difficult.

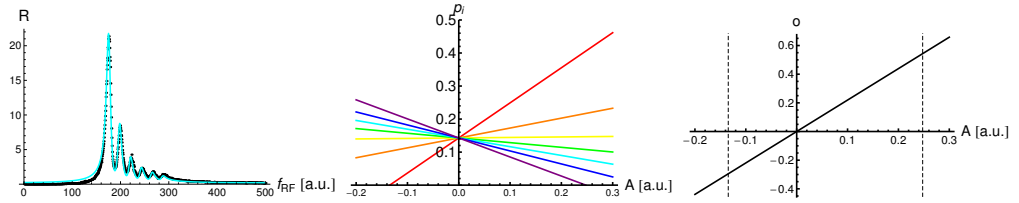

(a) (b) (c)

Figure 4.9: MORS for atoms in F=3, when a strong probe with $\Delta = 850$MHz from $F = 4 \rightarrow 5$ transition of the D_2 line and a pump resonant to $F = 4 \rightarrow 4$ on the D_1 line. The $F = 3$ sublevels remain unbroadened. With the hight of the peaks an approximate range of the population distribution (in (b) where $p_3, p_2, p_1, p_0, p_{-1}, p_{-2}, p_{-3}$ are shown in red, orange, yellow, green, cyan, blue, purple) and orientation (in (c)) can be estimated.

thing of the orientation of the atoms in $F = 3$, one can use the heights of the peaks to determine an estimate of the difference of the populations in the different m levels depending on the unknown factor A_{MORS}. From this, depending on A_{MORS}, one can plot the possible population distributions (see figure 4.9b). Obviously, only the range where all populations are positive is relevant. Also, clearly there can not be a negative orientation in a scenario where a σ_+ oriented pump field is applied. Still, we need more information to determine the orientation which is plotted in 4.9c, over the unknown parameter A. Here we only succeed in limiting the possible orientation. This question becomes relevant in chapter 8 where we would like to correct for the Faraday-rotation, coming from atoms in $F = 3$, after a long probing pulse.

4.3 Atomic decay

There are two different decay constants describing the decay of the collective spin T_1 and T_2. The decay of the mean spin $\langle \hat{J}_x \rangle = \langle \hat{J}_x^0 \rangle e^{-t/T_1}$ is characterized by T_1. The decay of $\langle \hat{J}_x \rangle$ can directly be measured by the decrease of the Faraday rotation over time. T_1 in the dark lies around 100-200ms. When the probe light is turned on, the rate becomes faster, because of spontaneous emission. The decay of the mean spin can result from population transfer into $F = 3$ where atoms contribute only very little to the Faraday rotation (see appendix D) thus leading to a considerable reduction in the Faraday angle. The spontaneous emission can also lead to transfer into different magnetic sublevels in $F = 4$ - to first order $m = 3, 2$. Those atoms still contribute to the Faraday rotation, reduced with a factor $\frac{3}{4}$ and $\frac{1}{2}$. By evaluating the different transition strengths [Ste03] or by measurement of population distribution in $F = 4$ it can be determined that most atoms ($\sim 80\%$) are lost to $F = 3$. In figure 4.10a the dependency of $1/T_1$ on the transmitted probe power P is shown for the two

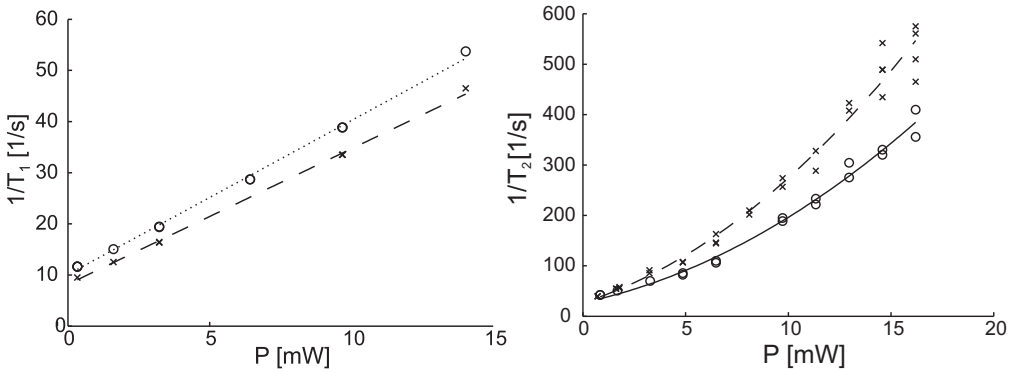

(a) (b)

Figure 4.10: (a) shows the dependence of the longitudinal decay on probe power at $\Delta = 855$ MHz. The two sets of data are for two different cells. (b) shows the decay constant $1/T_2$, depending on power. One set of data points (circles) were taken with a bigger beam ($d_\gamma = 5.6$mm), the other for a smaller beam (($d_\gamma = 1.6$mm)). A big Gaussian beam was used and clipped with an iris. In the newer experiments we work with a flat top beam profile with a diameter of 2cm improving the decay times further.

cells. Since we are far away from saturation, P is proportional to the intensity in the cells.

The decay constant T_2 describes the decoherence of the transversal spin. We often measure the decay of a mean value in the rotating transversal spins as $\langle \hat{J}_{y,z} \rangle = \langle \hat{J}^0_{y,z} \rangle e^{-t/T_2}$. This decay is the main cause of imperfections and limitations of our experiments in quantum communication protocols and quantum state engineering. The decay $\gamma = \frac{1}{T_2}$ depends on light power P and atom number in the cell. Experimentally, it can be parameterized as:

$$\gamma = a_\gamma + b_\gamma \cdot \theta_F + c_\gamma \cdot P + d_\gamma \cdot \theta_F P + e \cdot P^2, \tag{4.3}$$

The constant contribution a_γ comes amongst others from wall collisions, atom losses to the stem and magnetic field instabilities. The part proportional to the Faraday angle probably comes mainly from atom-atom collisions and the part proportional to the light power from spontaneous emission induced by the probe. The quadratic part in light power arises from the inhomogeneous intensity distribution over the sample. A reason for this could be dephasing of the atoms, because they experience different Stark shifts in different places of the cell. In graph 4.10b the dependance of the decay on the light power is shown for two different beam sizes.

The last contribution, $d_\gamma \cdot \theta_F P$ is a collective effect, of the sort predicted in chapter 3. This part does not add decoherence in the sense that noise is added, but it contributes to the dynamics, coming from the a_2 term of the Hamiltonian. Decay measurements were taken for different detunings for different powers

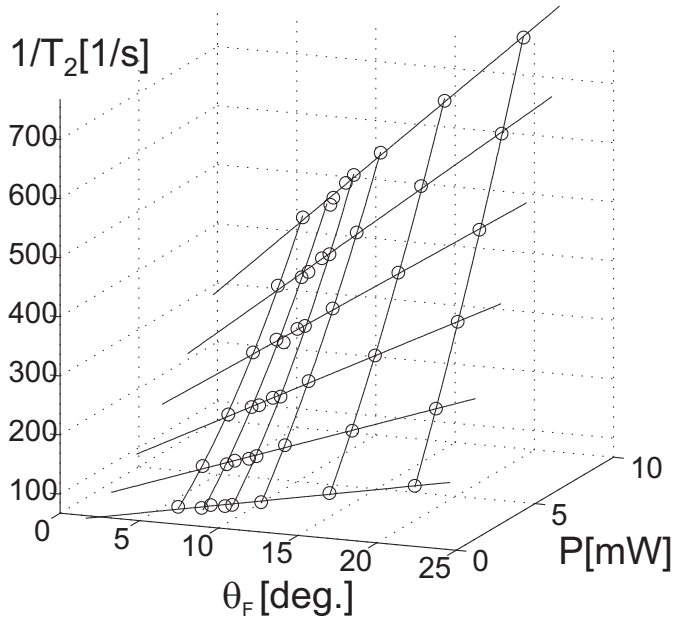

Figure 4.11: A measurement set of $1/T_2$ for different power and number of atoms is shown for a detuning of $\Delta = 700$MHz. The number of atoms was monitored with the Faraday angle θ_F

.

and atomic densities. In graph 4.11 one set of measurements for $\Delta = 700MHz$ is shown. From the measurement set for every detuning, one can extract all the prefactors from equation 4.3. First, a linear fit to the data for the same power to θ ($\gamma = o + s\theta_F$) was performed and then the outcomes of the offset $o = a_\gamma + c_\gamma P(+e_\gamma P^2)$ and slope $s = b_\gamma + d_\gamma P$ were evaluated for different power. The parameters a_γ and b_γ should exhibit no dependency on Δ. The measurement points are quite scattered and for the lowest blue detunings (700,900 and 1125 MHz) it was necessary to fix a_γ to the mean value of the measurements from the other detunings. The reason lies in the quadratic behavior of the low detuning data sets, where the additional free parameter e_γ otherwise makes the outcomes of a_γ and c_γ too uncertain. This course of actionas has no effect on the b_γ and d_γ-measurements. The averaged outcomes for the overall offset are $a_\gamma = (15 \pm 3)\ \mathrm{s}^{-1}$ and for the pure density term $b_\gamma = (1.8 \pm 0.5)\mathrm{s}^{-1}\mathrm{deg.}^{-1}$.
In figure 4.12 c_γ and d_γ are shown over the detuning. The parameter d_γ is especially interesting for us, as it is part of the dynamics which we established in chapter 3. They fit very well with the predictions made with help of equation 3.8:

$$d_\gamma = \frac{\gamma_s}{\theta[^\circ] \cdot P[\mathrm{mW}]} = \frac{\lambda^3 \gamma_0 \cdot 7a_2(\Delta) \cdot 180^\circ}{16\Delta Ahc \cdot 10^{-3}}. \tag{4.4}$$

The scaling with the light power given by c_γ is explained by spontaneous emission.

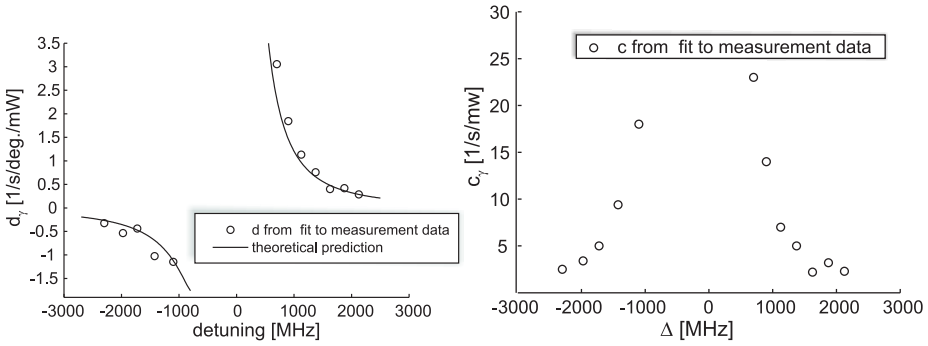

(a) (b)

Figure 4.12: In (a), from measurement extrapolated values for d_γ (circles) are shown together with the γ_s from theory. Theory and measurement fit very well. The agreement is poorest for the points with lowest detuning ($\Delta = 700$MHz and -900 MHz). This is probably due to the fact that there the Doppler broadening can not be neglected. In (b) the pure light effect c_γ is shown. This corresponds to the absorption profile of a fully oriented state.

For our experiments we have to specifically evaluate, which setting gives us the desired coupling and the lowest decay. It is interesting to follow how the decay γ behaves compared to the collective decay γ_s. In 4.13 this ratio $1 - \epsilon^2 = \frac{\gamma_s}{\gamma}$ is shown for constant atom number (4.13a - equivalent to the number of atoms at room temperature) and for constant light power (4.13b: $P \sim 5mW$). In this setting ϵ^2 decreases for higher powers for the lower detunings, due to the quadratic behavior. Heating the atomic sample from room temperature ($N_a \sim 2.5 \cdot 10^{11}$) to a temperature in which the cell contains around twice as many atoms should supply us with a better ratio, however we experience a different problem at the higher atomic densities. The atomic measurements display an additional noise component at higher temperatures, for which we have not found a source yet. The optimal detuning which we can extract from the graphs lies between $700 - 1000$ MHz. The measurements were taken with a Gaussian beam which caused additional decay. If one discards the term which is quadratic in the light power, one achieves a situation at RT which fits with later experiments, where a smaller $\epsilon^2 \approx 0.2 - 0.4$ was recorded when a very smooth beam profile was used.

4.4 Coupling strength

An important experimental parameter is the coupling constant κ. We can measure it by measuring noise of known atomic states like the projection noise of the CSS or the thermal atomic state (see section 5.2.1). Another approach is to transfer a coherent light state with a known displacement to the atoms and

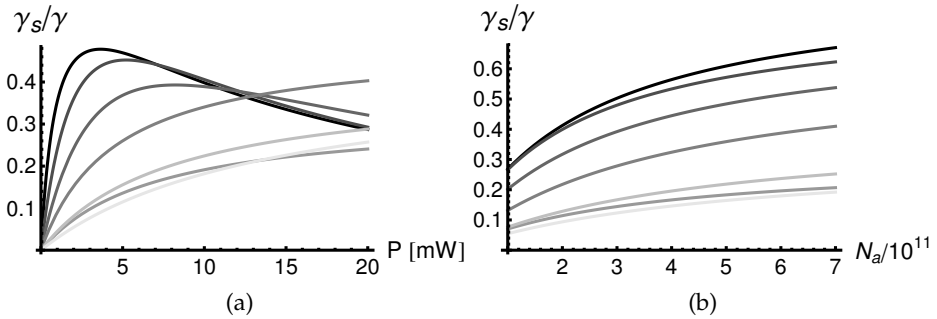

Figure 4.13: The lines show the extrapolated behavior (from the measurements of $a_\gamma, b_\gamma, c_\gamma, d_\gamma, e_\gamma$) of the ratio of the collective rate γ_s to the whole decay rate γ: $\gamma_s/\gamma = 1 - \epsilon^2$. The curves represent $\Delta = 700, 900, 1125, 1375, 1625, 1875, 2125$ MHz where the darkest curve belongs to $\Delta = 700MHz$ and the lightest to $\Delta = 2125MHz$. In (a) the power was varied and the number of atoms held constant (room temperature). In (b) the power was held constant at 5mW and the number of atoms was varied.

then read out the atomic state [8]. This procedure is sketched in the following, followed by an explanation of some of the experimental details below.

First, a pulse is sent through two oppositely oriented atomic samples with a displacement in $\hat{q}^{1st}_{c,s}$, so in S_z. This leaves the atomic sample with a mean value in the X-quadrature.

$$\langle \hat{X}_{c,s} \rangle = \kappa \langle \hat{q}^{1st}_{c,s} \rangle. \tag{4.5}$$

To be able to read out those atomic mean values, we apply a π-pulse to the atomic spin rotating $\hat{X}$ into $\hat{P}$. This can be done by adding a magnetic field in the x-direction, so that the spins rotate a little faster in between the pulses. Then we send a second light pulse for the read out. The outcome of the light measurement of the second pulse reveals

$$\langle \hat{y}^{2nd}_{c,s} \rangle = \kappa \langle \hat{P}_{c,s} \rangle = \kappa^2 \langle \hat{q}^{1st}_{c,s} \rangle. \tag{4.6}$$

The coupling strength can be calculated: $\kappa^2 = \frac{\langle \hat{y}^{2nd}_{c,s} \rangle}{\langle \hat{q}^{1st}_{c,s} \rangle}$. The pulse sequence is shown in figure 4.14.

There are different approaches as to how to produce the displaced coherent light states. In [She06] it is discussed, how a strongly polarized beam can be sent through an electro optical modulator (EOM) whose optical axis is slightly tilted compared to the input polarization. Then a DC voltage and a small modulation at 322 kHz can be used to rotate a small portion of the big classical S_x into $\hat{S}_y$ and $\hat{S}_z$. The value of the DC voltage sets the working point of the modulator in a $\hat{S}_y$-$\hat{S}_z$ plane on the Poincare sphere - it determines the phase of the generated displacement in phase space. The strength and phase of the RF modulation determine the size of the displacement of the cosine and sine modes.

This is a rather easy way to create a displacement in the light quadratures, but the input light experiences a considerable loss due to reflection losses on the crystal surfaces of the EOM. Those losses are not important when we work with coherent states, but the approach is disadvantageous for light states which are more sensitive to losses such as squeezed states. Therefore, when squeezed light is used, the displacement is created in a polarizing interferometer where the strong local oscillator is in one arm and in the other arm the quantum mechanical state is generated. This includes, if desired, the squeezed state with help of second harmonic generation and parametric down conversion. Additionally a weak seed beam is fed in that is phase and amplitude modulated at the desired sideband frequency with help of two consecutive EOMs. The first EOM is followed by a PBS for amplitude modulation and the second EOM is used purely for phase modulation. By a suitable linear combination of modulation strengths on the EOMs $\hat{y}_{c,s}$ and $\hat{q}_{c,s}$ can be accessed.

To evaluate the signal coming from the atoms, $\langle q_{c,s} \rangle$ needs to be calibrated. This is usually done before the measurement of the mean value transfer. A $\frac{\lambda}{4}$-plate is inserted in the detection path to switch to a $\hat{S}_z$ measurement. To test if the measurement is set up correctly, one can compare a fixed signal coming from the atoms that is created for example by a magnetic RF pulse. Following equations 3.12, the atomic signal should be suppressed by ξ^2 in a $\langle \hat{S}_z \rangle$- compared to a $\langle \hat{S}_y \rangle$-measurement.

κ^2 can be measured by mean value transfer in dependency of light power, atomic number or pulse duration. In figure 4.14 measurements of κ^2 is shown for a variation of power and number of atoms.

Below, the γ is decomposed in γ_s and γ_{extra} where $\gamma_s \propto P \cdot \theta_F$ and $\gamma_{\text{extra}} = a_\gamma + b_\gamma \cdot \theta_F + c_\gamma \cdot P + e \cdot P^2$.
The measured slope for γ_s lies for graph (d) 13% and 6% for graph (e) above predictions calculated from the theory. Considering the high uncertainties in the measurement of d_γ as well as some of the numbers used for the prediction, and the fact that the theory is highly simplified (not even the Doppler profile is considered here), this is a reasonable agreement. In the reconstruction of the atomic state, the most important measure is κ^2 which is directly measured.

In chapter 5, it is discussed how κ^2 can be measured by noise measurements.

4.4.1 Effect of light losses on κ^2 measure

Light losses after the cells are easily included into the model. In the calibration we would measure a suppressed $\sqrt{\eta}\langle \hat{q}_{c,s}^{1st} \rangle$ which is just due to the fact that the light power is reduced and a suppressed and a similarly reduced $\sqrt{\eta}\langle \hat{y}_{c,s}^{2nd} \rangle$, so that the measured κ stays the same. But the light power on the detectors is of course also reduced by η. Thus one needs to take care that the losses are held

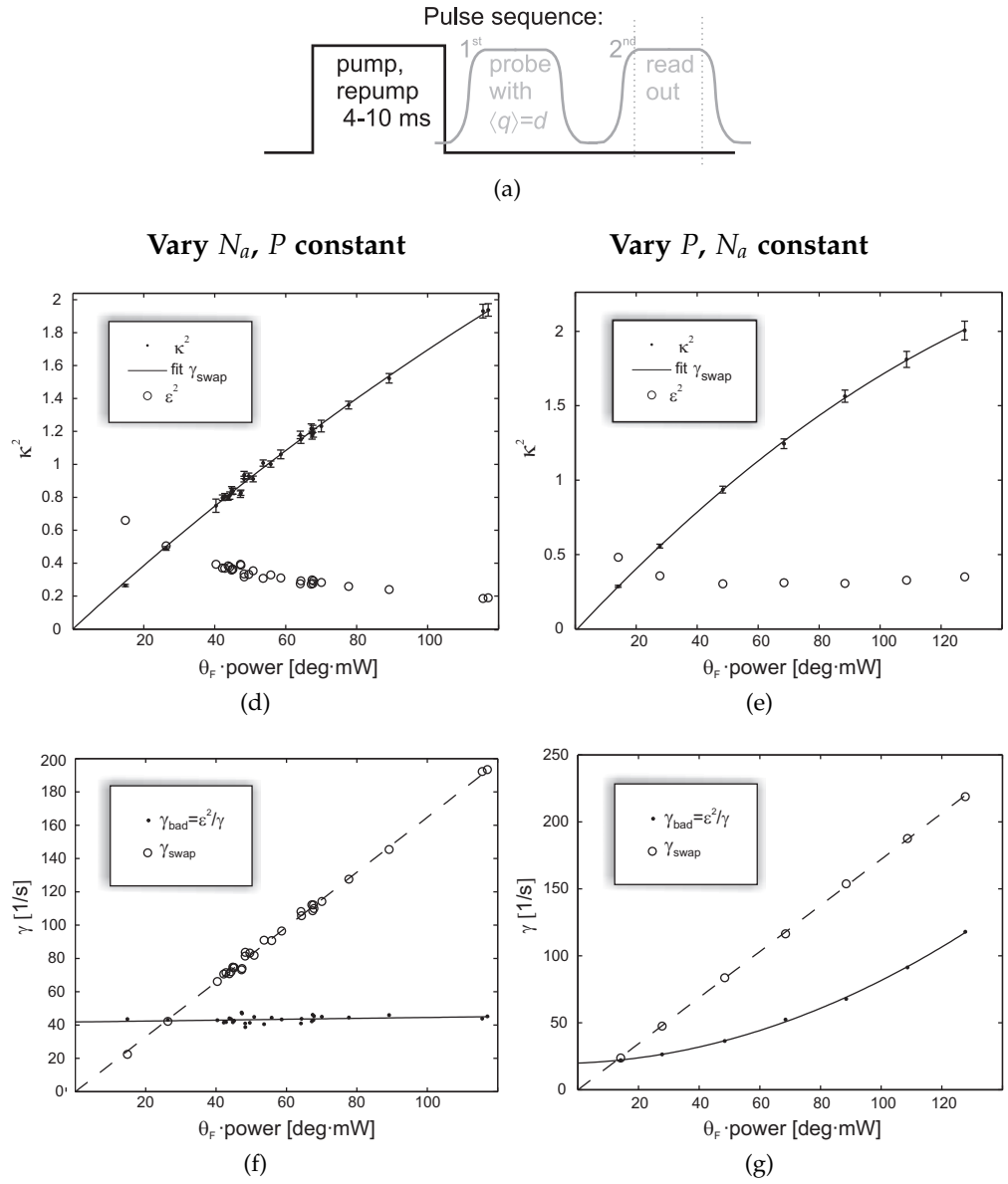

Figure 4.14: in (a) the pulse sequence is shown. The probe light is turned on and off smoothly to avoid noise contributions at 322kHz. (a) shows κ^2 for a varied number of atoms and a light power $P = 5mW$, in (c) measurements of κ^2 at room temperature are presented for different light power. The x axis is given by the product of the light power P and the Faraday angle θ_F, to compensate for drifts and fluctuations in the quantity that was not varied.
(e) and (f) show the corresponding decay constants γ_{extra} and γ_s.

constant or monitored carefully between calibration and actual measurement, so they can be compared.

Losses η_b between the cells give a different effect. If we assume that we keep the power in cell 2 constant that means that higher losses between the cells lead to a higher light power in cell 1 and thus a higher κ. If we stick to rather small losses, in which case we can assume κ^2 to be linear in power as it is the case in the QND approximation, this leads to a measured $\frac{1+\eta_b}{2\eta_b} \cdot \kappa^2_{cell2}$, where κ^2_{cell2} - and thus the light power on the detectors - is constant.

Chapter 5

Quantum noise

This chapter is devoted to measurements of quantum fluctuations. The measurement of the variances of the quantum variables of concern, is in general the most important aspect of all our measurements. Due to the fact that all states I will be concerned with throughout the thesis are Gaussian, the measurement of the mean value and the variance generally suffice for a full characterization of the state.
When we evaluate the atomic states, we need to exercise caution that we interpret the interaction setting right, i.e. if we are close to the fully oriented ensemble, which justifies part of our approximations.

Part of the noise measurements discussed here are calibrations, such as the measurement of light noise and of classical atomic states like the CSS and the thermal state. The chapter will conclude with a discussion of the measurement of collective variables, e.g. of two atomic samples or a light beam and a single atomic ensemble. Evaluating the variance of such collective variables gives us the possibility to measure entanglement between two systems.

5.1 Light noise

The measurement of the Stokes operators was discussed in the previous chapter. The light noise is used as the basic calibration of our whole measurement setup. From equations 2.11 to 2.14 we see that for coherent light

$$\mathrm{Var}(\hat{S}_y^{(c,s)}) = \frac{S_x}{2} = \frac{n_{ph}}{4}, \tag{5.1}$$

with the number of photons n_{ph}. If the measurement is limited by quantum fluctuations, the noise should thus scale linear with the number of photons.

Since we are considering the variances, any additional classical noise contribution can be seen as a quadratic component in the scaling[1]. When linear scaling is observed, we can use the measurement to find the gain of our detection system. This leaves us with a calibration with which we can evaluate the measured noise at a known light power also for other light states. We generally measure two orthogonal light modes, the cosine and sine component at 322kHz with help of the lock-in amplifier. The output can be multiplied with a temporal mode function that evolves much slower than the oscillation at RF as stated in equation 2.16. For the coherent input states in our light noise calibration, the choice of mode-function has in principle no influence on the measurement outcome, if the mode function is normalized properly. However, small variations can be observed, if there lies too much weight on the beginning or end of the pulse. This happens for one because the pulses are not turned on and off instantaneously, but smoothly, to suppress 322kHz components on the edges and because of the finite detection bandwidth. One measurement pulse usually takes 1-10ms. This is repeated 2.000-10.000 times and from the measurement outcomes the variance and the mean value can be extracted.

For the light noise measurements, the same beam path as for the atomic measurements is used, meaning that the light transverses through the atomic sample. To achieve a pure light noise measurement, the strength of the magnetic field is changed significantly, so the Larmor frequency is detuned. That way no signal coming from the atomic spins is recorded in the 322kHz sideband.

For the calibrations, the mean values of $\hat{S}_y$ and $\hat{S}_z$ are zero, or at least very small considering the number of photons participating. We can call the measurement a balanced measurement, referring to the fact that the classical signal is evenly distributed on the two detectors and then canceled out, including all classical amplitude noise contributions. It can be understood similar to standard homodyne detection - a kind of polarization homodyning - where the local oscillator and the weak quantum field belong to two orthogonal polarization modes, as opposed to different spatial modes.

The signal of one of the detectors alone displays the noise coming from half of the photons, without any noise cancelation, and we can observe the classical noise present for half the light power. A measurement for the balanced setting along with a single detector measurement for the DFB laser and the Ti:Sa laser is shown in graph 5.1. The DFB laser has very low amplitude noise, while the noise of the Ti:Sa laser is considerable. To suppress this a noise eater [BRLR98] was build, based on a feedback loop, using the signal generated by a small portion of the beam on a detector. The signal was mixed with a 125MHz RF field and fed back onto an AOM. The first order diffraction of the beam was

[1]The variation of the light power is done by attenuating the beam without changing any laser settings.

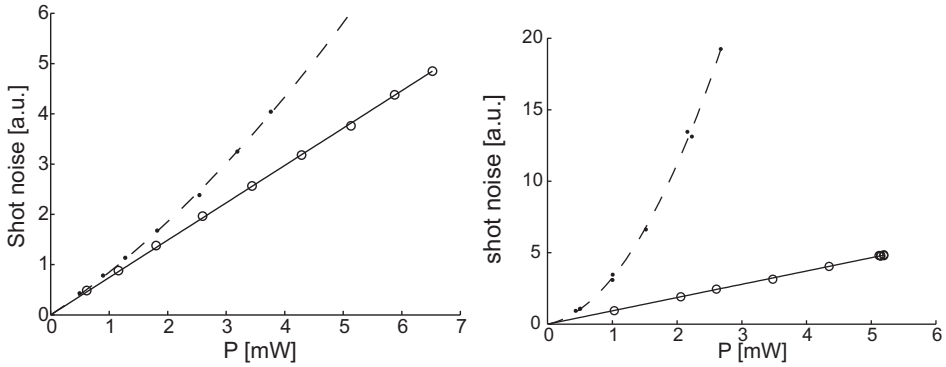

(a) (b)

Figure 5.1: Light noise for the balanced setting (circles) and a single detector measurement (dots) for the DFB laser (a) and the Ti:Sa laser (b). The balanced measurement is shot noise limited, while the single detector measurements exhibit quadratic behavior. The DFB laser is at the measurement frequency and the used powers close to shot noise limited. The measurements of the Ti:Sa laser show a much stronger quadratic component. The additional noise comes partly directly from the laser and partly from the fact that the spatial mode is cleaned with help of a cavity which is stabilized to the laser frequency.

dumped, and the strength of this diffraction determined by the signal from the detector. That way a reduction of the single detector noise close to the shot noise level could be achieved. For lasers which had better initial noise properties such as the DFB laser 10-20dB sub-shot noise could be observed [Jen07] inside the feedback loop - that is on the detector used for the feedback. This effect is called squashing [Wis99, BGS+99].

As will be seen later, it is possible to utilize squeezed light states for some of our experiments. The squeezed light is produced in another QUANTOP experiment with well known down conversion techniques [SSP02, NNNH+06]. The generated squeezing is usually of the order of around 6dB (11dB anti squeezing). On the setup for the atomic interface, the light is subject to considerable losses, due to optical elements, and the uncoated glass surfaces of the cells holding the atoms. The total losses amount to around 35%, leaving around 3dB of squeezing on the detectors after the atomic cells. In figure 5.2 the noise of one of the quadratures is shown in black for a scan over the squeezing phase. The dark gray line shows the shot noise of light which clearly lies above part of the black line.

5.2 Reconstruction of the atomic spin noise

The atomic state tomography reveals some difficulties, as the atomic observables can not be measured directly with a simple scheme as the one used for

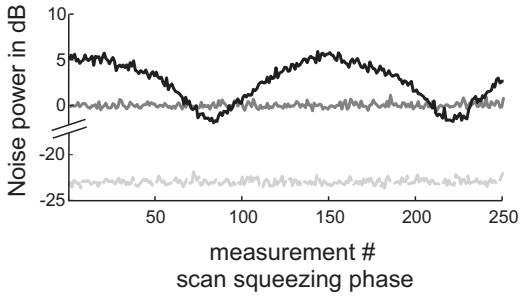

Figure 5.2: Power spectrum of the light noise, recorded with a spectrum analyzer at 322 kHz. The dark gray line shows the shot noise level. The black line shows the noise of light coming from the squeezing source, where the phase of the local oscillator was scanned. Clearly the noise goes below the coherent state noise level, proving squeezing. The light gray line shows the electronic noise.

the light measurement. We need to utilize the light atom interaction to evaluate the atomic state. One of the light quadratures is measured after the interaction, and from the measurement outcomes we reconstruct the mean value and variance of the atomic state, by employing the different input-output relations developed in chapters 2 and 3. The measured atomic state is thus obstructed by the input light noise. This corresponds to a measurement of light with a bad detection efficiency - this concept will be discussed in greater detail in section 7.5.2. We are only considering Gaussian states, so the variances of the atomic state can be extracted from our raw experimental data with the measured variance $\sigma^2_{\text{measured}}$. We can calculate the atomic variance (AN)

$$AN = \frac{1}{\mathrm{C}}\left(\frac{\sigma^2_{\text{measured}} - \sigma^2_{\text{el}}}{\mathrm{SN}} - \mathrm{EN}\right), \tag{5.2}$$

where the shot noise (SN) can be determined by a measurement of the light power, and with the calibration from graph 5.1 and σ^2_{el} is the noise floor coming from the measurement apparatus. The coupling C and the extra noise EN differ for different realizations, as will be explained in the following.

In the case of the simple QND two cell equations 2.42 we can extract the noise of $\hat{P}_{c,s}$

$$\mathrm{Var}(P_{c,s}) = \frac{1}{\kappa^2_{\text{QND}}}\left(\mathrm{Var}(\hat{y}_{c,s})^{\text{out}} - \mathrm{Var}(\hat{y}_{c,s})^{\text{in}}\right).$$

In most cases we work with coherent light states as input, so that $\mathrm{Var}(\hat{y}_{c,s})^{\text{in}}$ can be set to be $\frac{1}{2}$. In the presented measurement graphs the variances are often expressed in units of shot noise, then $EN = \mathrm{Var}(\hat{y}_{c,s})^{\text{in}} = 1$ and $C = \kappa^2$.

For a single cell on the other hand we can extract $\mathrm{Var}(p)$ and $\mathrm{Var}(x)$ with

$$EN = \mathrm{Var}(\hat{y}^{\text{in}}_{c,s}) + \frac{\kappa^2_{\text{QND}}}{16}\mathrm{Var}(\hat{q}^{\text{in}}_{s,c}) + \frac{\kappa^2_{\text{QND}}}{48}\mathrm{Var}(\hat{q}^{\text{in}}_{s,c,1}) = 1 + \frac{\kappa^2_{\text{QND}}}{12},$$

setting	coupling (C)	EN	κ^2
QND two cells - thermal noise	κ^2_{QND}	1	$a \cdot S_x J_x T$
simple single cell	$\frac{\kappa^2_{\mathrm{QND}}}{2}$	$1+\frac{\kappa^2}{12}$	
Swap two cells	κ^2	$1\text{-}\kappa^2\xi^2$	$\frac{1-e^{-2\gamma_s T}}{\xi^2}$
swap single cell	$\frac{\kappa^2}{2}$	B.13	
Swap two cell, including decay	κ^2	B.10	$(1-\epsilon^2)\frac{1-e^{-2\gamma T}}{\xi^2}$
Swap single cell, including decay	$\frac{\kappa^2}{2}$	B.12	

Table 5.1: Relevant quantities for noise reconstruction. Some of the lengthy expressions are stated in appendix B. The additional noise EN is given in units of shot noise of light.

while the coupling C is given by $\kappa^2_{\mathrm{QND}}/2$.

For the highly oriented atomic state, the higher order Hamiltonian from equation 3.3 can be employed. Including also additional decay (see appendix B) the additional noise becomes more complicated, but can be extracted from equation 3.21 for the two cell setting. For the single cell in the case of low coupling, equation B.5 can be used. In table 5.1 all the relevant components for the atomic noise reconstruction are summarized. It is important to note that κ^2 is generally measured and not calculated from the formulas.

5.2.1 Thermal state of the atoms

We start by looking at an atomic sample which is not oriented, meaning that the sublevels are evenly populated. This setting is fully symmetric and for every atom this means

$$\hat{f}_y^2 = \hat{f}_z^2 = \hat{f}_x^2 = \frac{F(F+1)}{3} = \frac{20}{3}.$$

Since in the thermal state all atomic sublevels have the same population, we have to consider that part of the atoms are in $F = 3$. These atoms are not observed in our measurement, since the probe laser is much further detuned for those atoms. Also they have a different Larmor frequency, which lies beside our detection frequency ($\approx 1kHz$). The observed noise will thus be $\frac{20}{3} \cdot \frac{9}{16} = \frac{15}{4}$, since there are in total 16 sublevels, 9 of which belong to $F = 4$. Compared the minimum uncertainty noise $F/2$, this is a factor $\frac{15}{8}$ - almost twice - the noise of a CSS. Clearly, if noise measurements are used to calibrate e.g. the coupling constant κ, we need to have an additional knowledge about the orientation of the atoms, which can be gained by measurements described in section 4.2.2.

The thermal noise can be measured in a two cell setting, or in a single cell

setting in both cases the additional noise EN is equal to $\mathrm{Var}(\hat{y}_{c,s})^{\mathrm{in}}$. For the single cell measurement the back action of light on itself is not present, since the coupling of the light variable to the atomic spin variable (see equation 2.32) is enhanced by J_x and for the thermal state $\langle j_x \rangle = 0$. This is discussed in detail in appendix F. Also the higher order corrections are negligible for a not oriented sample. This leads to simpler input-output relations (equation F.3) for the light:

$$\hat{y}^{\mathrm{out}}_{c(s)} = \hat{y}^{\mathrm{in}}_{c(s)} + \frac{\kappa_{\mathrm{thermal}}}{\sqrt{2}}\hat{x}(\hat{p}),$$

which (a) does not feature the suppression of the input light state and (b) has a coupling constant $\kappa_{\mathrm{thermal}}$ that slightly differs from the κ which includes the swap operation. It is given by $\kappa_{\mathrm{thermal}} = \kappa_{\mathrm{QND}} = \frac{a_1}{7a_2} \cdot \gamma_s \cdot T$. Thus, when one measures the coupling constant with help of the thermal state noise to interpret measurements in or close to the CSS, the difference between $\kappa_{\mathrm{thermal}}$ and the oriented-sample κ has to be taken into account. In figure 5.3 the ratio $\kappa^2_{\mathrm{thermal}}/\kappa^2$ is shown for two different detunings.

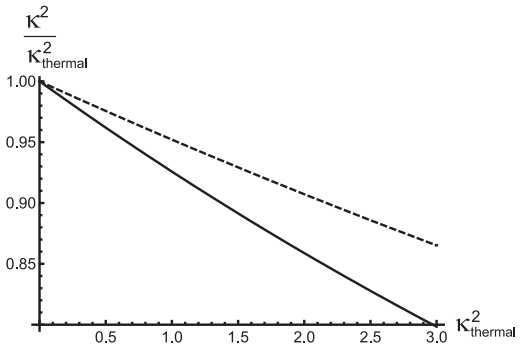

Figure 5.3: Theoretical comparison of $\kappa_{\mathrm{thermal}}$ and the κ for the CSS. The solid line shows the ratio $\kappa^2/\kappa^2_{\mathrm{thermal}}$ for $\Delta = 855$MHz and the dashed one for$\Delta = 1.5$GHz.

The thermal noise should scale linearly with the number of atoms. Figure 5.4 shows a measurement series where the thermal noise was measured for different atomic numbers, monitored by a Faraday angle measurement of the optically pumped ensembles. Clearly we observed the expected linear behavior. In the figures $\kappa_{\mathrm{thermal}}$ was extracted from the noise measurements.

When the light power is varied we see - especially for the horizontal polarization - a saturation of the noise (see figure 5.5). The main reason is that in the thermal state all coherences in $F = 4$ contribute to the measurement. As discussed in section 4.2.2 those coherences oscillate at different frequencies depending on the light power due to the Stark shift. The saturation effect originates in the fact that some of those frequencies will lie outside the detection bandwidth for high powers at horizontal polarization. We measure therefore usually thermal noise only for settings where the splitting of the coherences is close to zero, meaning for vertical polarization around 5mW. Also the sponta-

neous emission gives a depletion of the $F = 4$ level and thus a small deviation from a linear scaling. It is important to note that the observed behavior is due to a different effect than the saturation of κ^2 for vertical polarization for the CSS. The swap and squeeze behavior, coming from the higher order corrections leads to a faster saturation of κ^2 in the vertical polarization, while for the horizontal polarization the coupling strength actually grows faster than linear - it does not saturate.

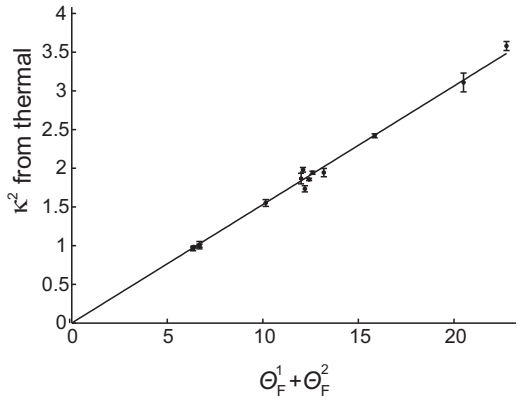

Figure 5.4: κ_{thermal}, extracted from the thermal noise for different numbers of atoms monitored by the Faraday angles θ_F^i measured for the two ensembles. $\kappa^2_{\text{thermal}}$ is proportional to the extracted normalized noise AN, which rises linearly as expected.

5.2.2 CSS noise

The fully oriented atomic state - or the coherent spin state (CSS) - is regularly utilized in our experiments. In section 4.1.2 it was described, how the CSS is achieved with optical pumping. In section 4.2.2 a method to confirm a high

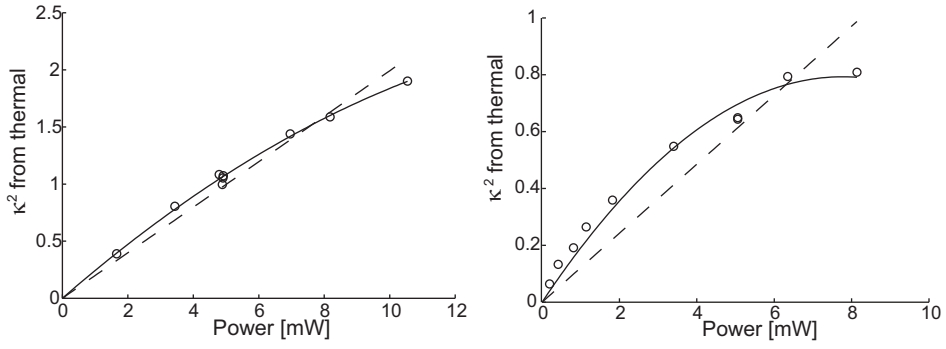

Figure 5.5: Thermal noise for different light powers for vertical polarization of the probe beam (a) and horizontal polarization (b). The dashed/solid lines show linear/quadratic fits.

orientation of the atomic ensemble is presented. Now we want to measure the variance of the normalized rotating transversal spins of the CSS. Equation 5.2 is used for the reconstruction of AN from light measurement and EN and C is set in according to table 5.1, depending on if we measure in the two cell or the one cell setting. Usually we measure in the balanced setting, and in the QND approximation the additional noise EN is just one unit of shot noise. If we include the higher order corrections the additional noise is given by the suppressed light noise and the coupling is given by κ^2. Until recently the projection noise measurements for two cells were used to calibrate κ, with the equations in the QND approximation. This lead to a miscalibration of κ; κ^2 was underestimated when a vertical polarized driving probe beam was used which is our usual setting, since the light noise suppression was not considered. The measurement of κ via the CSS was mainly used for the reconstruction of atomic noise in unknown quantum states close to the CSS, like in the evaluation of the teleportation experiment reported on in chapter 6. The underestimation of κ will in those cases only lead to a small atomic reconstruction error, which will be presented in more detail in section 6.4.

In figure 5.6 a measurement of CSS noise (black dots) is shown for different Faraday-angles $\theta_F \propto N_a$. The number of atoms in the glass cell was varied by heating the cell. The noise was fit with a linear function, displayed as the blue line. From this fit κ^2 can be extracted according to the QND theory by subtracting one unit of shot noise which is shown by the blue dashed line. The red dashed line show a κ^2 extrapolation originating from a κ^2 measurements by mean value transfer (section 4.4) - this clearly lies higher. With help of the more complicated theory presented in chapter 3 the expected observed noise of a CSS on light is plotted as the red line. This line lies close to the measured noise for lower couplings. The QND approximation therefore seems adequate for lower couplings. Here, for higher atom numbers the AN appears to lie slightly above the CSS noise.

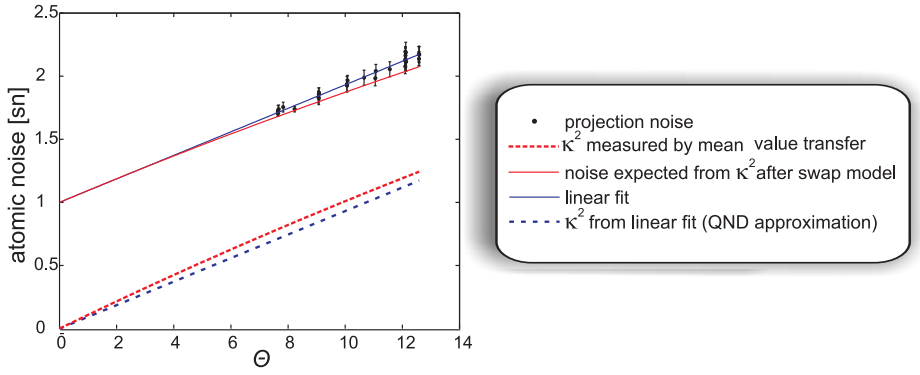

Figure 5.6: Atomic noise for different numbers of atoms characterized by the Faraday angle, evaluated with the QND model and the corrected model.

5.2.3 Detection efficiency

The reduction of the detection efficiency η is due to several mechanisms which spoil the detection. The main degradation of the measurement quality comes from losses on the cell surfaces. Also the optical elements used for the detection, even though they are antireflection coated, contribute to the losses. The optical elements after the cell are two lenses used to decrease the beam size appropriately for detection, a wave plate and a polarizing beam splitter. The reflections from the detectors (around 4%) can be reflected back onto the detectors. This is often done for experiments where feedback of the measurement results is applied onto the atoms. The remaining loss mechanism is the detection inefficiency of the detectors. The effect on the light variable can be modeled by a beamsplitter with vacuum in one input port:

$$\hat{y}_{c,s}^{\text{out}'} = \sqrt{\eta}\hat{y}_{c,s}^{\text{out}} + \sqrt{1-\eta}\hat{Vac} \tag{5.3}$$

To measure η, one can measure the dominating light losses directly and estimate the detection efficiency. There are some uncertainties, as to how to include the losses in between the cells. For small attenuations between the cells, including those losses with a factor $1/2$ into η gives reasonable results (see section 4.4.1).

We can also establish the detection efficiency by analyzing the AN, for different numbers of atoms as follows. Consider a small technical noise contribution on the spin variance. The technical noise scales quadratically with the number of atoms. The normalized AN should then be linearly depending on the number of atoms and a line fitted to the measured AN for different atom numbers should go through one unit of vacuum noise for zero atoms. Such a measurement is shown in figure 5.7. The extrapolated detection efficiency and the directly measured η in both those cases lay at $\eta = 0.84(4)$.

Yet another way to find η is to measure κ with two different methods which are effected differently by the detection efficiency. E.g. when κ^2 is measured via the mean value transfer discussed in section 4.4, the effects of the light losses are as discussed in section 4.4.1. Losses after the cells have no effect on the measured κ^2. On the other hand, if we measure the noise of a known atomic state, such as the CSS or the thermal state, the noise contribution of the atomic state on the light measurement will be damped by η according to equation 5.3. Comparing two of these measurements can give a more exact measurement of the detection efficiency. However, there are some problems to this. If we wish to use the CSS-noise for κ^2 calibration, we need to be sure that there are no additional noise components. We can also measure the thermal state which is much less sensitive to additional noise sources, because it is not oriented and we do not

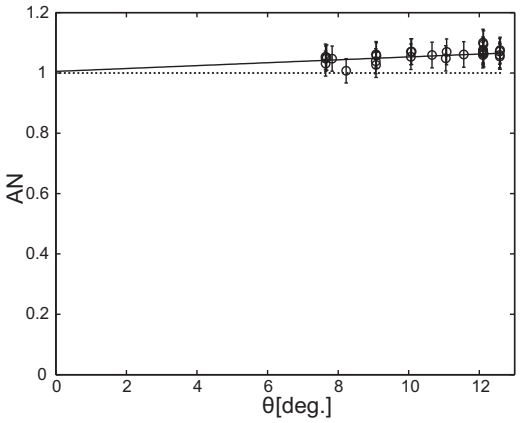

Figure 5.7: Reconstructed atomic noise (AN) for different numbers of atoms characterized by the Faraday angle. The detection efficiency η was set to $\eta = 0.84$

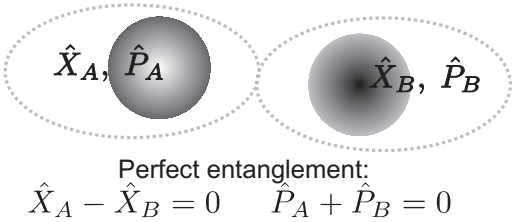

Figure 5.8: Entanglement shown by correlation of collective variables

need to use the optical pump lasers. But, as discussed earlier, then we have to make assumptions about the connection of κ^2 for the oriented ensembles and $\kappa^2_{\text{thermal}}$.
Considering those uncertainties the η that has been measured on several occasions by the latter method fits reasonably well to the result obtained with the other two methods (well inside the uncertainty).

5.3 Combined Variables of two systems and entanglement criterion

In this section we will discuss combined variables of two systems. In our system, this can either be the spins of two atomic samples as given in equations 2.40, the upper and lower sideband quadratures of light, or combinations of light and atomic variables. Those collective variables are introduced because their variances can be used to characterize entanglement.

5.3.1 Entanglement criterion

In chapter 1 the interest in entanglement is motivated. But how do we know that we have entanglement? Two systems A and B are entangled, when their combined density matrix ρ^{AB} can not be decomposed into products of ρ^A and ρ^B:

$$\rho^{AB} \neq \sum_i a_i \rho_i^A \otimes \rho_i^B. \tag{5.4}$$

This will be hard to verify in a high dimensional system. Therefore, here we would like to have an entanglement criterion connected to the canonical operators which we use to characterize our system. If we consider an EPR kind of entanglement as sketched in figure 5.8, we can define collective operators[2] like $\hat{U} = \hat{X}_A - \hat{X}_B$ and $\hat{V} = \hat{P}_A + \hat{P}_B$ with a commutator $[\hat{U}, \hat{V}] = 0$. We consider the two systems to be perfectly entangled, when $\hat{X}_A$ ($\hat{P}_A$) is perfectly anticorrelated (correlated) with $\hat{X}_B$ ($\hat{P}_B$), meaning that the variances of the collective variables are $\mathrm{Var}(\hat{U}) = \mathrm{Var}(\hat{V}) = 0$. In comparison, two uncorrelated states in the symmetric minimum uncertainty state would yield

$$\begin{aligned} &\mathrm{Var}(\hat{X}_A - \hat{X}_B) + \mathrm{Var}(\hat{P}_A + \hat{P}_B) \\ &= \mathrm{Var}(\hat{X}_A) + \mathrm{Var}(\hat{X}_B) + \mathrm{Var}(\hat{P}_A) + \mathrm{Var}(\hat{P}_B) = 4 \cdot \frac{1}{2} = 2. \end{aligned} \tag{5.5}$$

So the variances of the collective operators seem to include information about the entanglement.

In [DGCZ00] an inseparability criterion based on the collective variances of canonical operators was introduced. It reads:

$$\mathrm{Var}(\hat{X}_A - \hat{X}_B) + \mathrm{Var}(\hat{P}_A + \hat{P}_B) < 2. \tag{5.6}$$

Looking at the input-output relations in 2.35 and 2.39, one can see that light and atom variables are connected after the interaction. To check for entanglement, we can now employ equation 5.6.

5.3.2 Light atom entanglement

Let us consider the interaction of light with a single cell, as depicted in figure 2.5, not considering the higher order terms in the interaction.
In figure 5.9 the sum of the variances of the collective variables $\hat{U} = \hat{Y}' + \hat{x}^{\mathrm{out}}$ and $\hat{V} = \hat{Q}' - \hat{p}^{\mathrm{out}}$ are shown as a function of the coupling constant κ as the black line. $\hat{Y}'$ and $\hat{Q}'$ are the canonical light operators of the upper sideband to

[2] $[\hat{X}_i, \hat{P}_i] = i$

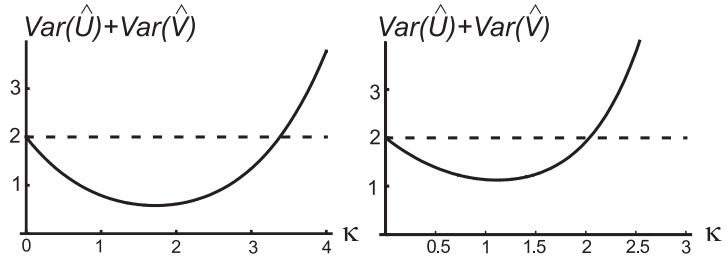

Figure 5.9: The graph shows the sum of the collective variances of the output variables of atoms and light. The dashed line is the limit below which atoms and light are entangled (see equation 5.6). The minimum is 0.58 for $\kappa = 1.7$. In the graph to the right decay and light loss are included. The change is quite big for high κ. At our working point of $\kappa \approx 1$ the collective variance increases from 0.8 to 1.1 which leaves still a fair amount of entanglement to work with.

within a sign correction:

$$\hat{Y}' = \frac{1}{\sqrt{2}} \cdot (\hat{y}_s^{\text{out}} + \hat{q}_c^{\text{out}}), \quad \hat{Q}' = -\frac{1}{\sqrt{2}} \cdot (\hat{y}_c^{\text{out}} - \hat{q}_s^{\text{out}}). \tag{5.7}$$

The predicted collective variances have a minimum which lies underneath the entanglement limit given by equation 5.6 shown as the dashed line. The one cell interaction can therefore be utilized to create light atom entanglement which can be used as resource for light atom teleportation. The first step of the teleportation protocol, discussed in 6, is therefore the interaction of light and atoms. In our experiment the coupling constant κ is of the order of 1 leading to a predicted sum of variances of 0.8 or 1.1, when relevant light losses and decay of the atomic spin are included.

We have seen that our two systems are entangled after the interaction, but is there a simple way to understand how this came about? An intuitive picture explaining the entanglement generation can be gained by considering figure 2.5. As a reminder, the corresponding interaction Hamiltonian 2.30 can for an oriented atomic state be written in terms of the atomic ladder operators in the rotating frame $\hat{b}'$, $\hat{b}'^{\dagger}$ and the creation and annihilation operators of the light for the upper (lower) sideband $\hat{a}_{+(-)}$, $\hat{a}^{\dagger}_{+(-)}$. Then the Hamiltonian has the simple form $\hat{H}_{int} \sim \frac{\kappa}{2\sqrt{T}}(\hat{a}^{\dagger}_{+}\hat{b}'^{\dagger} - \hat{a}^{\dagger}_{-}\hat{b}' + h.c)$. Since, the atoms are in the extreme $m = 4$ state, and since the quantum field is polarized in x-direction (π-polarized in the picture), we are in a situation where mainly one of the classical polarizations is relevant. In figure 2.5a a photon in the upper sideband is created together with an excitation of the atomic system - clearly an entangling interaction. The second process, including the lower sideband is suppressed, since the atoms are all pumped into $m = 4$, so $m = 3$ is empty.

Again for higher coupling we need to move to the theory presented in chapter 3. For this we can consider different light modes. First, I evaluate the light

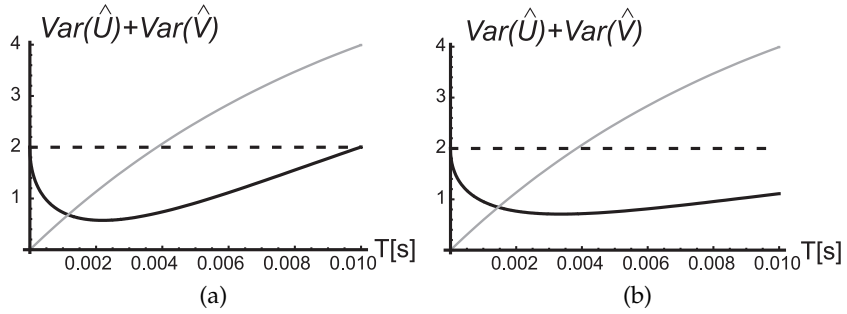

Figure 5.10: Entanglement variables, including the corrections from chapter 3. The solid lines show the variance of the combined atomic and light variable. The gray line is the corresponding κ^2 and the dashed line at 2 indicated the entanglement limit. In (a) the modes defined in equations 3.16 are evaluated and in (b) the upper sideband with an exponentially falling envelope function is used.

modes defined in equation 3.16 which are entangled with the atoms.

$$\hat{\tilde{Y}}^{\text{out(in)}} = \frac{1}{\sqrt{2}\xi}(\hat{q}_{c-(+)} \mp \xi^2 \hat{y}_{s-(+)}), \quad \hat{\tilde{Q}}^{\text{out(in)}} = \frac{1}{\sqrt{2}\xi}(\mp\hat{q}_{s-(+)} - \xi^2 \hat{y}_{c-(+)})$$

The variances of the entangled combined variable are shown in figure 5.10a. The minimal noise is then the same as in the unperturbed case. If we instead take the upper sideband weighted with suitable exponential functions, the achievable collective variances are shown in figure 5.10b. Here the variances are at optimum only reduced to 0.7 - but this lies very close to our measurement setting. Those values are calculated without the additional decay.

We can not verify this reduction in the collective variances directly. The problem is that our method to read out the atomic state is based on the assumption of these correlation between light and atoms. But in chapter 6 a successful experiment of teleportation between light and atoms based on this entanglement is presented. This can be seen as an indirect proof of the entanglement.

5.3.3 Atomic entanglement via QND measurement

In the end of chapter 2, I briefly touched upon the subject of quantum non demolition (QND) measurement. This concept describes a measurement of a quantum mechanical variable without disturbing it. A measurement on a light beam that has interacted with two atomic ensembles in a magnetic field with oppositely oriented spins, gives us the opportunity to perform this kind of measurement. Equation 2.41 shows that the collective atomic variables $\hat{P}_{c,s}$ remain unchanged through the interaction. Equation 2.42 shows the possibility to make a measurement on those variables by monitoring $\hat{y}_{c,s}$. After such a measurement, the outcomes $\tilde{y}_{c,s} = \hat{y}^{\text{out}}_{c,s} + \kappa \hat{P}^{\text{in}}_{c,s}$ can be fed back with a certain

gain g on the atomic variable. This can be done with a magnetic RF field with tunable field strength. The resulting atomic variable reads:

$$\hat{P}_{c,s}^{out'} = \hat{P}_{c,s}^{out'} + g\tilde{y}_{c,s} = \hat{P}_{c,s}^{\text{in}}(1+\kappa g) + g\hat{y}_{c,s}^{\text{in}}. \tag{5.8}$$

The gain can be adjusted to minimize the atomic variance $\text{Var}(\hat{P}_{c,s}^{out'})$. With a gain $g = -\frac{\kappa}{s+\kappa^2}$ where $s = 2\text{Var}(\hat{y}_{c,s}^{\text{in}})$ the variance is

$$\text{Var}(\hat{P}_{c,s}^{out'}) = \frac{1}{2}\frac{s}{s+\kappa^2} \leq \frac{1}{2} \tag{5.9}$$

which is smaller $\frac{1}{2}$ for every $\kappa > 0$. This means that the collective atomic variable becomes squeezed - and the two atomic ensembles become entangled. Since both $\hat{P}_c$ and $\hat{P}_s$ can be measured, the sums of the $\hat{J}_y$s and the $\hat{J}_z$s become squeezed.

The experiment including the feedback is described in [SJP07, She06]. It is also possible to leave out the actual physical feedback. Then we are left with a conditional entanglement. This means the collective atomic operators $\hat{P}_{c,s}$ follow Gaussian probability distributions with a reduced variance, but displaced with a certain value which is given by the measurement outcome. This conditional entanglement was first reported in [JKP01]. It can be verified by measuring with two consecutive light pulses and calculating the conditional variance: $L_{\mathcal{C}} = \text{Var}(\hat{y}_{c,s}^{\text{out},2} + \alpha\hat{y}_{c,s}^{\text{out},1})$, which can again be optimized with $\alpha = \kappa g$. Leading to the conditional variance $L_{\mathcal{C}} = \frac{1}{2}(s + \kappa^2\frac{s}{s+\kappa^2})$.

To improve the noise suppression one can increase κ or reduce the light noise. A set of experiments with squeezed light as an input was conducted. The light squeezing on the detectors was $s = 0.55 \pm 0.02$ in shot noise units (with considerably higher squeezing in the cells). The noise reduction was improved by 10% compared to the noise reduction achieved with a coherent light source. The atomic initial noise lay around 20% above the CSS noise, due to additional classical noise, so the achieved atomic entanglement did not surpass the best experiments we conducted with coherent light. Anyhow this experiment proves the possible benefit of using a squeezed light source.

Later in this thesis, in chapter 8, a QND type measurement is utilized to achieve a steady state entanglement.

Also another possibility to create atomic entanglement is discussed in chapter 7, namely nuclear electronic spin entanglement of the single atoms in the ensemble.

Part III

Quantum state engineering and transfer protocols

Chapter 6

Teleportation between light and matter

In this chapter I summarize an experiment on teleportation from light to atoms [1, 4], which was conducted in the previously introduced setup. The chapter starts with an introduction into the concept of teleportation, followed by a detailed description of the implementation in the available light atom interface. All discussions are based on the theory developed in chapter 2, but the influence of the effects described in chapter 3 are discussed.

6.1 Introduction to teleportation

6.1.1 Teleportation Principle

The non cloning theorem [WZ82] - the fact that an unknown quantum mechanical state can not be copied perfectly - leads to interesting possibilities. It is a corner stone of quantum communication - which opens up for the possibility of absolute secure communication [BB84]. But also new challenges arise from this quantum mechanical phenomenon. For example, one faces a problem, if one wishes to transfer a quantum mechanical state to a remote location in another way than physically moving the system bearing the state - a task that can prove to be very hard for fragile quantum systems. Now a different approach is needed, than what one might attempt in a classical setting, in which case measuring on the physical system and making a replica at another location would suffice. In 1993 Bennet et al. introduced the concept of teleportation for a spin- $\frac{1}{2}$-type two level system [BBC$^+$93], which was solving this task. Here, two parties, widely known as Alice and Bob, wish to transfer the quantum state of a system that Alice possesses to Bob. Since the quantum state is unknown to

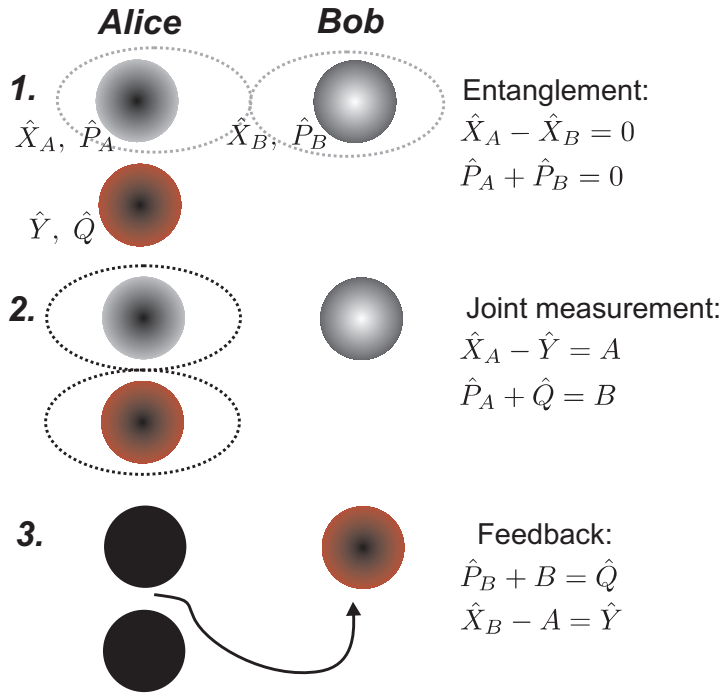

Figure 6.1: **Teleportation Scheme**
Quantum teleportation is the remote state transfer of a quantum system held by Alice to a quantum system held by Bob. The different steps of the teleportation protocol are shown on the left and will be described in the following.

1. Distributed Entanglement. Alice and Bob need to share an Einstein Podosky Rosen (EPR) entangled pair. This establishes the quantum link between them needed for the teleportation.

2. Bell measurement. Alice conducts a joint measurement on the two quantum systems held by her. That way the information on her input state is now distributed between her measurement results and Bob's quantum system. She can perform this measurement as $[\hat{X}_A - \hat{Y}, \hat{P}_A + \hat{Q}] = i - i = 0$.

3. Classical Communication/ Feedback. Alice tells Bob, what she measured, after which he can perform a local transformation on his system, recreating Alice's input state.

Alice, she can not perform a measurement, through which she gains the full information of the quantum state. The outcome of a measurement will crucially depend on the basis she chooses to measure in, so that she would need some information on the initial state to make a useful observation.
To overcome this problem, Bennet et al. employ an Einstein Podolsky Rosen (EPR) entangled pair [EPR35], of which Alice and Bob each hold one of the two parts. Then Alice can conduct a joint, so called Bell measurement, on the quantum state that she wishes to teleport and the one member of the EPR pair. After this the full information of the quantum state is distributed between Alice's measurement outcome and Bob's part of the entanglement pair. In a final step Alice only has to send her classical data over a classical channel to Bob who can then recreate the input state by performing a unitary transformation on his system.

While Bennet et al. deal with a discrete system, the teleportation protocol was later adapted for continuous variables [Vai94] by Vaidman. Here, the entanglement shows itself in the correlations of a set of non commuting variables of two separated systems as discussed in section 5.3. This concept is depicted in figure 6.1 and will be referred to throughout this chapter.

Quantum teleportation can be useful to more than just the transfer of a quantum mechanical state. It can be regraded as an essential building block for quantum information processing. In [FT07] continuous variable quantum teleportation and its applications in quantum information processing is discussed in detail, highlighting the impact of teleportation in this field.

6.1.2 Teleportation experiments

In the first successful teleportation experiment the polarization state of one photon was transferred to another photon by Bouwmeester et al. [BPM+97]. This setup follows the original proposal of Bennet et al. for a two level system. The input photon can be in an arbitrary superposition of two orthogonal polarizations (i.e. ± 45 deg). Suitable entanglement is created in a type II down conversion process where two polarization entangled photons are produced [KMW+95]. One of those photons is sent to Alice where a Bell measurement of one of the four Bell states is performed. Whenever this measurement is successful - so whenever the measurement projects the two photons in the specific Bell state (25% of all cases) - the third photon emerges in the original state of the input photon. The teleportation was verified for different input polarizations.
Soon after followed the realization of the first unconditional teleportation scheme [FSB+98]. Coherent light states, described by the continuous variables $\hat{X}, \hat{P}$, corresponding to the amplitude - phase quadratures of light, were teleported. Following the teleportation scheme depicted in figure 6.1, in the first step dis-

tributed entanglement is created. For this, two squeezed beams are generated by parametric down conversion and mixed on a beamsplitter [OPKP92, WKHW86]. At Alice's site her part of the entangled beams is mixed with another beam with an unknown input state on a 50/50 beamsplitter (BS). Then the joint measurement is performed by homodyne detection in the two output ports of the BS. Those measurement outcomes are sent to Bob who applies feedback to his light beam accordingly, thus recreating the input state. To describe the quality of a quantum mechanical state transfer, a commonly used quantity is the fidelity, which will be discussed later in more detail. In this experiment a fidelity of $F = 0.58 \pm 0.02$ was achieved exceeding the best classical fidelity of 0.5.
The first quantum teleportation between atoms was realized in 2004 between two closely positioned Ca+ ions in an ion trap [RHR+04]. A qubit is encoded in a superposition of internal states of one atom and then transferred via teleportation onto another atom.

Finally, in this chapter I will describe an experiment on light to atom teleportation [1]. This was the first time interspecies teleportation was experimentally realized.
Later the conditional teleportation of a photonic qubit onto an atomic qubit was shown [CCY+08]. There the atomic qubit, consisting of a single spin excitations of two atomic ensembles, was entangled with the polarization state of a photon. No direct feedback was included, but feedback after retrieving a photon from the atomic storage is possible.

In another experiment a state transfer from a photon to a single atom called remote state preparation was performed via a teleportation protocol [RBV+07]. Also teleportation between two ions in independent vacuum chambers separated by one meter was implemented [OMM+09]. This was achieved by conducting a joint measurement on two photons which were entangled with one atom respectively.

6.2 Teleportation experiment

In this section we will discuss the different steps of the teleportation scheme, described in figure 6.1, in detail for our experiment [HPC05]. The experimental system is sketched in figure 6.2. Also we will discuss how the teleportation experiment can be evaluated. We therefore introduce a quantity called fidelity, to characterize the performance of our protocol.

6.2.1 Teleportation principle

Input state

Before the first step of the teleportation protocol, Bob starts with an atomic ensemble in the vacuum state (CSS). Alice has an input state characterized by the quantum variables $\hat{Q}_{s,c}$ and $\hat{Y}_{s,c}$. The canonical operators she wants to teleport are combinations of those. They belong to the lower sideband at $\omega - \Omega$ where ω is the light frequency:

$$\hat{Y} = \frac{1}{\sqrt{2}}(\hat{Y}_c + \hat{Q}_s), \quad \hat{Q} = -\frac{1}{\sqrt{2}}(\hat{Y}_s - \hat{Q}_c) \rightarrow [\hat{Y}, \hat{Q}] = i. \tag{6.1}$$

To start with input states which are interesting which implies states other than vacuum, we need to create a displaced coherent state. The displacement can be achieved by using an electro-optic modulator (EOM), as already described in section 4.4 and in more detail in [She06]. Usually a strong DC voltage is used to access both operators of relevance, $\hat{S}_y$ and $\hat{S}_z$. In the experimental setup for the teleportation the DC voltage is not necessary. The reason is, that the displacements are introduced in one arm of an interferometer (see figure 6.2). The input state will be defined after the exit BS of this interferometer. Then the phase of the modulation can be changed by changing the length of the interferometer arm where the input state is created. That way the strength

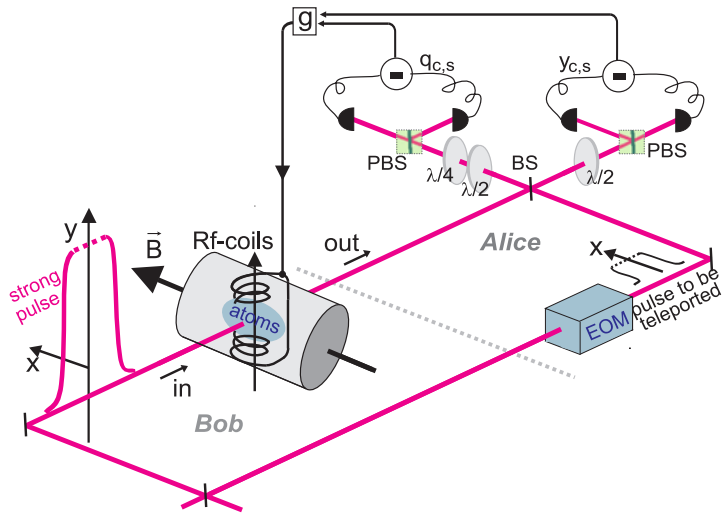

Figure 6.2: Schematic drawing of the teleportation setup. The input state is created in one arm of the interferometer by an electro optic modulator (EOM). In the other arm entanglement between atoms and light is created via interaction. The entangled beam and the input beam are mixed on a beam splitter (BS) and measurements of $\hat{S}_y$ and $\hat{S}_z$ are conducted in one arm each. The results are fed back to the atomic spins with help of RF coils.

of the RF-modulation on the EOM will give the size of the displacement and the phase can be chosen by adjusting the path difference. Since the EOM only creates a mean value, it will be easy to do the calibration of the input states. Behind the BS there will of course be additional noise, coming from the other arm. But, as we know the input is a vacuum state we know its noise properties and we are only interested in the mean values - so the size and phase of the displacement. In section 6.3 such measurements are shown.

Now we wish to teleport Alice's input state onto Bob's atoms. The description follows the steps outlined in figure 6.1.

Entanglement

Entanglement is the starting point of the teleportation protocol. In our case we want to link Bob's atomic ensemble to a system, with which a Bell measurement with the input state will be possible. The most well known form of such joint measurements are conducted between two light beams. Fortunately, as discussed in section 5.3.2, we are in possession of a light atom entanglement resource. Just by sending a light beam through our atomic ensemble with a suitable coupling, the entanglement criterion, discussed in section 5.3.1 can be fulfilled. The light quadratures of the upper sideband become entangled with the collective rotating spin of the atoms. The resulting entanglement looks slightly different than the pure EPR-type quadrature entanglement, depicted in figure 6.1. In [HWPC05] the entanglement generated by the used interaction scheme and EPR entanglement generated with the same coupling strength are compared. There it turns out that EPR entanglement is in the regime we are working in not much superior to our approach.

Bell measurement

The next step in the teleportation scheme is the Bell measurement. We would like to measure the collective variables of two light beams; one which is entangled with the atoms and the one bearing the input state. For this we combine the two beams on a 50-50 beam splitter (BS). After the BS we have the difference of the quadratures in one arm and the sum in the other arm (see figure 6.3).
We measure $\hat{S}_y$ by polarization homodyning in one arm (as discussed in 5.1) and $\hat{S}_z$ in the other arm. Measurements in the two output ports will now pro-

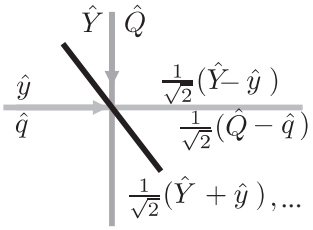

Figure 6.3: Two beams are mixed on a 50/50 beam splitter. At the output ports the sums and differences of the input quadratures can be measured.

vide us with four quantities:

$$\tilde{y}_{c,s} = \frac{1}{\sqrt{2}}(\hat{y}_{c,s} + \hat{Y}_{c,s}), \quad \tilde{q}_{c,s} = \frac{1}{\sqrt{2}}(\hat{q}_{c,s} - \hat{Q}_{c,s}). \tag{6.2}$$

Alice sends those measurement outcomes to Bob.
Combined with the right signs those yield a Bell measurement of the lower sideband of the light which is to be teleported and the upper sideband of the beam which is entangled with the atomic spin. Combining the measurement results yields:

$$\tilde{y}_s + \tilde{q}_c \propto \hat{q}_+ - \hat{Q},$$
$$\tilde{y}_c - \tilde{q}_s \propto \hat{y}_+ + \hat{Y}.$$

Thus the lower sideband of the input can be transferred to the atoms. This is a feature of our experimental setting. The Bell measurement selects the mode which is to be teleported. A different experimental setting would allow for the teleportation of the other sideband. If we had started with an atomic ensemble oriented oppositely to the magnetic field, the entanglement would lie in the lower sideband of the light quadratures. Then it would only be possible to teleport the upper sideband of the input beam. Also it is possible to imagine a completely different measurement scheme where we make a Bell measurement of the same sideband of the input and entangled beam, so that the entanglement and input would lie in the same sideband.

Feedback

To accomplish the feedback we send a pulsed RF signal to coils, which are depicted in figure 6.2, to generate a RF magnetic pulse to displace the atomic quadratures according to the outcomes of the measurements given by equation 6.2. As discussed before, the atomic quadratures are given by the spins in the rotating frame. In the laboratory frame they precess around x with the Larmor frequency Ω. Sending an RF signal to the coils creates a magnetic field orthogonal to the macroscopic spin, to perform the feedback. Using two RF-fields synchronized with the Larmor precession which are $\frac{\pi}{2}$ out of phase we can access both quadratures.

Now we wish to perform feedback of a combination of the four measurement outcomes in such a way that as much as possible of the noise which came from the entangling light pulse will be canceled out. After Bob does the feedback to the atoms according to Alice's measurement outcome, the atoms are left in the input state of the light which Alice wanted to teleport plus some additional

noise components:

$$\hat{X}^{\text{tele}} = \hat{x}^{\text{out}} - g_x \cdot (\tilde{y}_s + \tilde{q}_c), \tag{6.3}$$
$$\hat{P}^{\text{tele}} = \hat{p}^{\text{out}} - g_p \cdot (\tilde{y}_c - \tilde{q}_s). \tag{6.4}$$

When the gains $g_{x,p}$ are set to be one, we arrive at:

$$\hat{X}^{\text{tele}} = \hat{Y} + r_X, \hat{P}^{\text{tele}} = \hat{Q} + r_P. \tag{6.5}$$

The input quadratures $\hat{Y}$ and $\hat{Q}$ are written on the atomic quadratures and $r_{X,P}$ are the residual uncanceled components, coming from the input states of the atoms and the entangling light,

$$r_X = (1 - \tfrac{\kappa}{2})\hat{X}_{in} - \tfrac{1}{\sqrt{2}}(1 - \tfrac{\kappa}{2})^2\hat{q}_c^{\text{in}} + \tfrac{1}{\sqrt{2}}\hat{y}_c^{\text{in}} - \tfrac{1}{\sqrt{6}}(\tfrac{\kappa}{2})^2\hat{q}_{c,1}^{\text{in}}. \tag{6.6}$$

The noise added by those contributions degrades the teleportation. We need to determine how big the additional noise is and evaluate, if this teleportation is any better than a classical attempt of a state transfer.

As a meaningful quality measure, we use a quantity called fidelity F (see section 6.2.2). If the incoming and the outgoing state are identical the fidelity equals one, if there is no overlap between the states it is zero.

This feedback step finishes the teleportation protocol.

Verification

To check the performance of our teleportation protocol, we need to read out the atomic state after the whole protocol. We can not measure the atomic state directly. As described in section 5.2, we send another light pulse through the atoms, so that light and atoms become entangled via the interaction, and then measure on $\hat{y}_{c,s}^{\text{ver}}$ of the light. We run 10.000 teleportation experiments. From that we can, with help of equation 2.39 and including the beam splitter after the cells, derive the applied gain and the variances of the final states. The gain can be extracted from the mean values:

$$\langle \hat{y}_c^{\text{ver}} \rangle = g_P \cdot \frac{\kappa}{2} \langle \hat{P}^{\text{tele}} \rangle$$
$$\langle \hat{y}_s^{\text{ver}} \rangle = g_X \cdot \frac{\kappa}{2} \langle \hat{X}^{\text{tele}} \rangle. \tag{6.7}$$

Also the atomic variances $\sigma_{X,P}$ can be found with help of equation 2.39. They are calculated in the following way:

$$\sigma_{X,P}^2 = \frac{4}{\kappa^2}(\text{Var}(\hat{y}_{c,s}^{\text{ver}}) - \frac{\kappa^4}{48} - \frac{1}{2}). \tag{6.8}$$

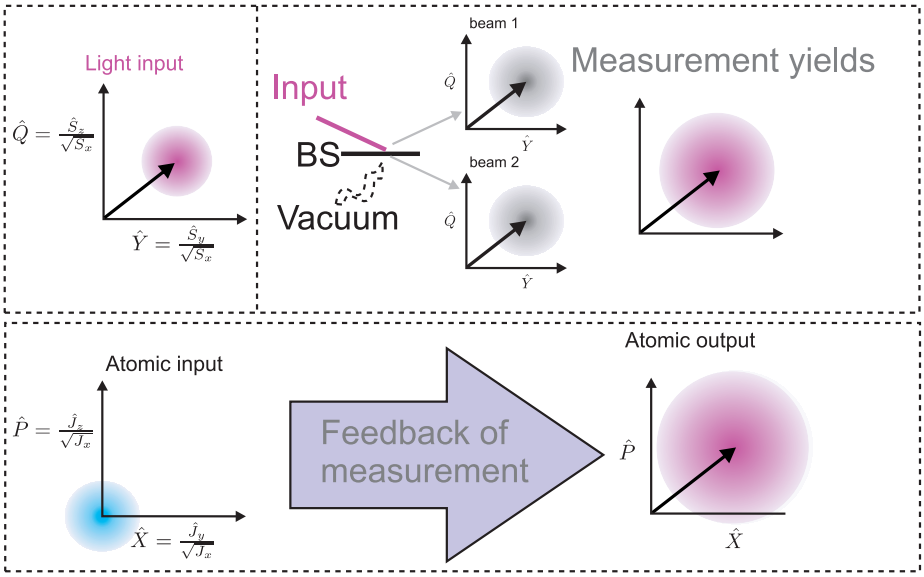

Figure 6.4: Classical transfer of a coherent state
1. Measurement The input state with a certain displacement is sent to a BS. On the two output ports two coherent states (i.e. with the same variance) with displacements which are reduced by a $\sqrt{2}$ are measured. When one likes to reconstruct the input from those measurements one unit of noise is therefore added
2. Feedback The atomic input state is in the best case also an minimum uncertainty state. Therefore, when a displacement according to the measurement result is conducted, the resulting output state has additional two units of vacuum noise.

Note that here one unit of shot noise is kept as $1/2$ to keep in analogy with the corresponding publications. Another factor of two, compared to the reconstruction quantities presented in table 5.1, arises from the BS. Now we will have to verify, if we have entered less noise in our experiment than possible classically.

6.2.2 Fidelity for coherent states

Since we are dealing with Gaussian states, the performance of our teleportation is fully characterized by the noise that we add to the quadratures in the process and the gain that the mean values experience. We now want to compare our experiment with possible classical protocols, and for this want to use a measure that will allow us to do this comparison. To characterize the quality of a protocol which transfers the quantum mechanical state from one system to another, the fidelity is a good measure. It gives the overlap of the input state with the output state for a certain input distribution. A classical benchmark of the fidelity can not be defined in all cases, but for coherent states it is known [HWPC05].
We start by looking at any "classical" transfer scheme. This will give us a bench-

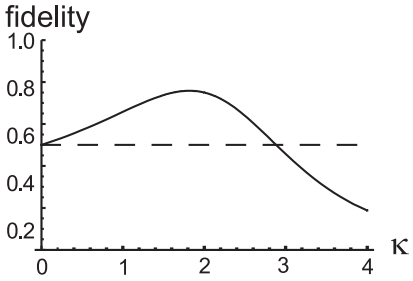

Figure 6.5: Optimal fidelity. The theoretically achievable fidelity for $g = 1$ is shown for the teleportation protocol that was applied. The dashed line indicates the best possible classical teleportation.

mark that we want to exceed utilizing our quantum tools like entanglement. Classically the best possibility would be to measure at one system and then transfer this knowledge onto another system. This scheme is depicted in figure 6.4. Unfortunately we will add noise in both of those steps. Firstly noise will be added, if we try to measure both quadratures of the input at the same time. Here the best approach will be homodyning after a beamsplitter. This will add a unit of vacuum noise in every quadrature. Also, the target system will have an input state with noise and thus induce at least one additional unit of vacuum noise for each quadrature. So the variances are increasing to three times their initial value, leading to a fidelity of $F = 0.5$. It has been proven that this is the best possible classical achievable fidelity for all possible approaches [HWPC05].
For coherent input states which follow a Gaussian probability distribution with the width n_0 the fidelity can be calculated from the gains and the variances of the output state:

$$F = \frac{2}{\sqrt{(n_0(1-g_x)^2+1+2\sigma_x^2)\cdot(n_0(1-g_p)^2+1+2\sigma_p^2))}} \tag{6.9}$$

with $\sigma_x^2 = \mathrm{Var}(\hat{X}^{\mathrm{tele}})$ and $\sigma_p^2 = \mathrm{Var}(\hat{P}^{\mathrm{tele}})$. When looking at all possible input states, the gain has to be set to one.

In figure 6.5 the best achievable fidelity for our setting is shown for $g = 1$ in dependency of κ. For $\kappa = 0$, meaning for no interaction and ergo no entanglement, the fidelity becomes $F = 0.5$. This is just the best discussed classical approach where Alice measures on her state and Bob does the feedback accordingly.

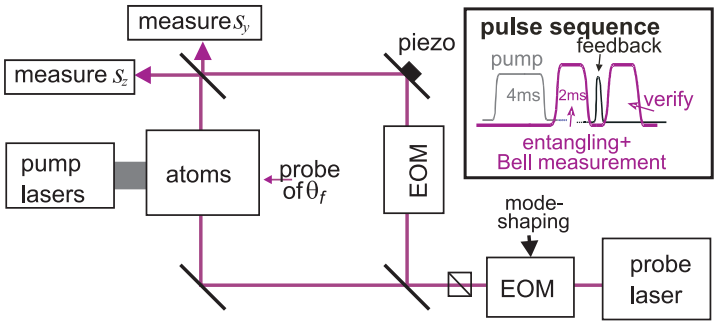

Figure 6.6: Schematic drawing of the experimental setup. On the right the probe laser and the EOM create the light pulses with a duration of 2 ms. The experimental pulse sequence is shown in the inset. On the left the interferometer is shown with the atomic ensemble in one arm and an EOM for the creation of the state to be teleported in the other. The phase can be varied by a mirror placed on a piezo electric element. On the two output ports of the interferometer measurements of S_y and S_z are conducted. The pump lasers are used to create the CSS and a weak probe beam measures the macroscopic spin.

6.3 Experimental realization

The experimental setting is sketched in figure 6.6. For the teleportation experiment an interferometer is set up. Using the same laser for the input arm and the entangling arm is the easiest way to ensure the necessary phase stability for the Bell measurement. In one arm the atomic cell is situated. A strong polarized beam is directed through the atoms and entanglement between the atoms and the light beam emerges from the interaction. In the other interferometer arm a weak beam is sent through an electro optical modulator (EOM) to create a displaced coherent state. The two beams are recombined on a beamsplitter. On the two output ports the Bell measurements take place as described in section 6.2.1. The interferometer is very stable over the measurement cycles of around a minute.

As described in section 6.2.1, we want to establish the gain of our teleportation. To determine the gain we compare the mean values of the measurements of the first pulse with the mean values of the second pulse. The pulse sequence of the experiment is shown in the inset in figure 6.6. The first value derives from the input state of light, since the entangled light beam carries no mean value. The second mean value is due to the atomic displacement after the teleportation, while no contribution is coming from the input arm.

To vary the mean value of the two quadratures of the input, we apply a constant modulation at 320kHz onto the EOM. Then we vary the path difference of the two arms, thus scanning the phase between the input beam and the strong local oscillator which was sent through the atoms. That way the mean value of the input state moves on a circle in quadrature phase space. Figure 6.7 shows

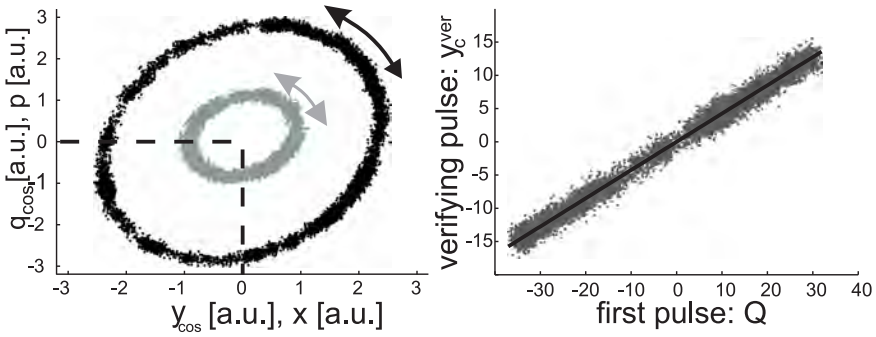

Figure 6.7: The graph to the left shows measurements of the two quadratures of the input and read out state. Here the phase between the two interferometer arms was scanned, while the displacement at 320 kHz (modulation with EOM) was held constant. Thus the mean value moved on a circle in the phase space around zero. The big black circle shows the mean values of the first pulse - so the displacement of the input state of light. The smaller gray circle shows the read out of the atomic displacement with the second pulse. The gain calibration is shown on the right. The mean value of the input state is compared with the final atomic state.

this for the input light (black) and for the read out of the atoms (gray). The radius is much smaller for the measurements, for which the mean values come from the atomic spin, because the read out is done with $\kappa/\sqrt{2} \approx 0.7$ and the beamsplitter gives another factor of $\sqrt{2}$. When looking at the quadrature mean value transfer we can calibrate the gains by doing a linear fit (see figure 6.7). Of course the intrinsic quantum noise is visible in the graph. With a fit for 10.000 points the slope $a = \kappa/2 \cdot g$ can be measured very precisely.

To look at the variances of the teleportation output, we use a constant input state and take 10.000 measurements. We can then reconstruct the variances of the resulting atomic state with equation 6.8, by using the variance of the second light pulse. Since the atomic state is Gaussian, it is fully characterized by the mean value and the variances. In graph 6.8 the Wigner function of such a reconstructed state is shown together with the best theoretical classical teleportation.

In figure 6.8 the reconstruction of an outgoing experimental state with a displacement of five units is shown. The achieved fidelity with a gain of one for this state is 0.57 ± 0.02. The uncolored curve in the graph shows the state which could have been achieved with the best classical teleportation. It is clear that the measured state is localized better.

For most protocols of relevance, a reduced input range of states will probably suffice. After the feedback the variances depend quadratically on the gain. For reduced input ranges the fidelity can be optimized and a lower gain might lead

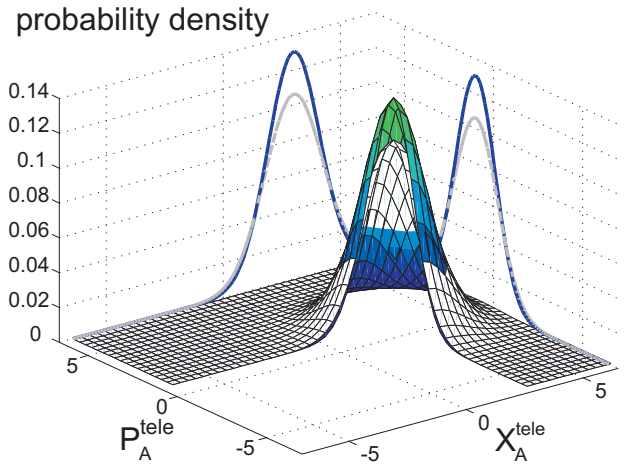

Figure 6.8: Here the probability distribution of the reconstructed state (colored) is shown together with the best possible classical teleported state (black and white). The final state achieved experimentally clearly rises above the classical teleported state. The displacement for this state corresponded to around 5 photons.

to a better performance of our protocol. One has to keep in mind that this extra information also leads to an increase in the classical fidelity limit [HWPC05].
Experiments were done with different gains for states with various displacements. In graph 6.9a the variances depend, as expected, quadratically on the gain. The displacement of the input state should not depend on the gain. This is also, what we observe for lower photon numbers, but for states with $d \geq 20$ technical instabilities led to higher noise.
From the measurements the fidelity (equation 6.9) can be optimized in the gain for different input ranges. This was done and is shown in graph 6.9b together with the best classical fidelities.
Measurements with higher displacements lead to lower fidelities, but in measurements with displacements corresponding to up to 200 photons the classical fidelity limit was still exceeded.

6.4 Correction with higher order Hamiltonian

This experiment was evaluated with the QND model. The question is, if the extrapolated atomic noise changes considerably, when we employ our more sophisticated model. The first thing is of course the deficient calibration of κ^2 by evaluating the CSS as discussed in section 5.2.2. The CSS was measured for different Faraday angles, and a slope of $0.139(2)/\text{deg}$. was measured. In section 5.2.2 we saw that close to the CSS the reconstructed noise with a κ^2 from a mean value transfer measurement was very close to the one where the calibration from the noise was used. For the teleportation results, we do the atomic noise

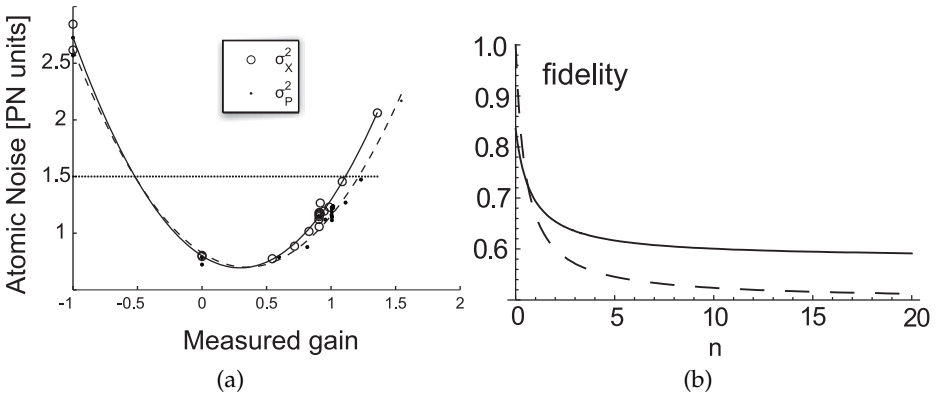

Figure 6.9: In figure (a), the gain was varied and the variances were measured. The displacements used in this graph lay between $d = 0$ and $d = 20$. The line at 1.5 - three times vacuum noise - correspond to the classical benchmark for $g = 1$. The uncertainty of the reconstructed variances due to calibration lies at 5%. In (b), the experimental data was used to extrapolate the optimal fidelity for input distributions with different widths n. The dashed curve shows the classically achievable fidelity.

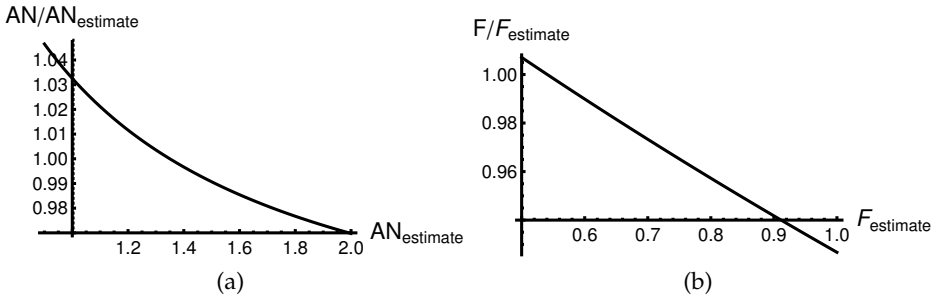

Figure 6.10: In (a) the atomic noise (AN_{estimate}) which is extracted with the QND based theory is compared to the AN reconstructed with the corrected theory. In (b) the corresponding effect on the fidelity is illustrated.

(AN) reconstruction with a κ^2, coming from the measured slope. We compare this with a noise reconstruction with a theoretical predictions of γ_s and an additional decay, leading to $\epsilon^2 = 0.3$. As can be seen in figure 6.10a, especially in the case for higher atomic noise, the AN was actually overestimated. In 6.10b, the fidelity for the new and old calibrations are compared for $g = 1$. This suggests a correction of the fidelity of a couple of percent was in order. Anyhow, since no suitable measurements of κ^2 and γ_s were taken at the time means we can not make a precise correction. Let it merely be stated that for future experiments the correction should be included and seems to increase the fidelities slightly.

6.5 Possible improvements

Equation 2.39 shows that the interaction leads to an admixture of other light modes. These are higher order temporal modes. As mentioned in section 2.2.3 this is due to a back action effect of light onto itself mediated by the rotating atomic spin. In figure 2.7 the temporal shapes of the first three modes are shown. Those additional modes limit the noise cancelation which can be achieved by the described feedback. Therefore the first step to improve the performance of the protocol is to include higher order modes into the feedback protocol.
All the $\hat{q}_{c(s),n}$ are conserved by the interaction. But obviously the higher order modes of the other quadrature $\hat{y}_{c(s),n}$ are changed. We include them into the protocol by defining a new input mode given by $\hat{Y} = \sum \frac{g_n}{\sqrt{2}}(\hat{y}_{s,n} + \hat{q}_{c,n})$ and $\hat{Q} = -\sum \frac{g_n}{\sqrt{2}}(\hat{y}_{c,n} - \hat{q}_{s,n})$ where $\sum g_n^2 = 1$ and feed back the combination of the measured quantities. The measurement of the higher orders can be accomplished by additional data processing, during the measurement. By including the first three modes and optimizing the gain this process will increase the theoretical fidelity limit from 0.72 to 0.80 for $\kappa = 1$ (light losses and decay not included) [1].

The part of the residual noise $\mathrm{Var}(r_{X,P})$ originating from the feed back of $\hat{y}^{\mathrm{in}}_{c(s)}$ of the entangling beam onto the atoms can be reduced using an entangling beam squeezed in this quadrature. Attention needs to be paid, since most available squeezed light sources will also be squeezed in the higher order modes $\hat{y}^{\mathrm{in}}_{c(s),n}$. That means the $\hat{q}^{\mathrm{in}}_{c(s),n}$ will be anti-squeezed, spoiling the teleportation results. But when the higher mode feedback is included this can be suppressed and for a squeezing source delivering 6 dB of squeezing and 10 dB anti-squeezed the fidelity can be pushed to 0.93 [1]. In our laboratory a squeezing source is available and first results coupling squeezed light to the atoms have been obtained in a mapping protocol described in section 9.2.

6.6 Conclusion and outlook

In the experiment teleportation of a light state onto a remote atomic ensemble was shown, exceeding the limitations of classical state transfer. This was done for distributions of coherent states with widths corresponding to up to 200 photons. Possible improvements were mentioned in the previous section leading to considerably higher fidelities.

The main application of the teleportation in quantum information processing is the transfer of entanglement. In this respect the reviewed experiment is a step in the right direction. The fact that the teleportation is performed with the

fidelity greater than the classical benchmark fidelity means that the protocol is capable of transferring entanglement. However, a more direct demonstration of such a transfer is desirable. In this respect, teleportation of an entangled state of light onto matter would be the next milestone. A memory experiment with two-mode entangled states was already conducted [9], which proves the possibility to couple our setup to a nonclassical light source (see section 9.2). Although the teleportation protocol described here has been performed using continuous variable formalism, it is capable of teleportation of discrete states, such as a qubit. The challenge here is to create a qubit state which is compatible with the atomic ensemble used for the teleportation. In the current setup the bandwidth of the input state of light has to be narrower than 1 kHz. If a single photon state with such bandwidth is available, the teleportation protocol described here can achieve the fidelity of teleportation of 0.72 as shown in [1], including light losses and atomic decay, which is above the classical benchmark of 2/3. An alternative approach would be to use an ensemble of cold atoms with the crossection of a fraction of a mm where a light qubit with the bandwidth of MHz can be used as a teleportation input state. Also, we currently investigate the possibility of fabricating much smaller Cesium cells, with a cross section of maybe 100x100μm^2 - which would lead to the possibility to use a faster pulse sequence. This is discussed briefly bin chapter 10.

Chapter 7

Spin squeezing by internal entanglement of single atoms

In chapter 5 the noise properties of different atomic states were discussed. The thermal state displays noise properties for which the product of the variances clearly lies above the right hand side of the Heisenberg uncertainty inequality 2.4. The CSS on the other hand is a minimum uncertainty state with symmetric variances. In the following we would like to construct spin states for which one of the two spin components perpendicular to the macroscopic orientation goes below the noise of the symmetric minimum uncertainty state.

I start with a general introduction into spin squeezing in 7.1 followed by a discussion of potential spin-squeezing mechanisms in section 7.2. In section 7.3 a feasible implementation for our setup is discussed, where the creation of superposition-states of the magnetic sublevels of the single atoms give the possibility for reduced spin noise. This differs from other experiments performed in the setup, where superposition states of the collective spins of the whole ensemble are generated to acquire squeezing. Finally the experimental realization is presented. The results were first reported in [2, 10].

7.1 Introduction to spin squeezing

7.1.1 Spin squeezing criteria

Starting from the coherent spin state with the minimum variance $\mathrm{Var}(\hat{J}_z) = \mathrm{Var}(\hat{J}_y) = \frac{J}{2}$ with J being the maximum $\langle \hat{J}_x \rangle$, one could think, that a good squeezing criterion would be that one of those variances has to be smaller than $\frac{J}{2}$. However, a better definition of spin squeezing [KY86, KU93] is defined by

the criterion

$$\zeta^2 = 2\frac{\mathrm{Var}(\hat{J}_\perp)}{\langle J_x\rangle} < 1. \tag{7.1}$$

Here $\hat{J}_\perp$ is one of the spin components orthogonal to the macroscopic orientation. The noise is compared to a CSS with the same length of J_x that can be considerably smaller than the maximal $J = 4N_a$. The criterion 7.1 defines potentially "useful" squeezing, as it leads to a reduced noise compared to classical systems like the CSS. The fidelity of state transfer schemes [JSC+04],[9] conducted in our setup can be improved with states fulfilling this criterion.

Another, even more restrictive squeezing measure is concerned with the reduction in spin angle uncertainty [WBI+92]:

$$\zeta_\alpha^2 = 2J\frac{\mathrm{Var}(\hat{J}_\perp)}{\langle J_x\rangle^2} < 1. \tag{7.2}$$

The criterion 7.2 implies entanglement of elementary spin 1/2 constitutents [SDCZ01]. Also it defines the necessary spin entanglement for the improvement of several clocks and other experiments whose accuracy relies on the angular uncertainty of the spin [WBI+92]. A magnetometry experiment conducted in our experiment [8] can also be improved with squeezed states meeting this criterion.

7.1.2 Squeezing experiments

The first reported experimental spin squeezing [HSSP99] was based on the state transfer of squeezed light to atoms. There squeezed light was absorbed on the D_2 line and the exited atoms where probed on the P-D transition. 1.4% of noise reduction was achieved.

In section 5.3.3 I discussed the possibility to achieve atomic two mode squeezing via a QND measurement [JKP01]. This is a known approach and was used in most spin squeezing attempts that followed. In [KMB00] continuous QND probing of one transversal spin by a Faraday interaction lead to a significant noise reduction for 10^7 atoms. In [GSM04], real time feedback was used to create spin squeezing of a cold Cesium ensemble. However, this article was retracted, as the authors failed to reach a quantitative understanding of their results, and later determined that there was no spin squeezing observed in the reported experiment. In [AWO+09, WOH+09] spin squeezing via a QND measurement in a cold Cesium cloud inside an interferometer was shown on the clock transition. Many other experiments utilizing the QND approach were conducted, amongst others [TVLK08, TFNT09, SSLV10].
The different spin squeezing approaches have been used to improve metrology

experiments, such as magnetometery in theory [PMM05] and experiment [8]. Also atomic interferometry with ensembles has been considered in [KBM98]. Entanglement of three and two ions has been used to improve spectroscopy experiments like Ramsey spectroscopy [LBS+04] and [RCK+06].

In the experiment discussed here an interaction of the atoms with light is used to engineer a Hamiltonian which is nonlinear in the spin components of the single atom and thus leads to spin squeezing of the single atom, instead of the collective atomic state. This possibility arises, due to the multilevel structure of the Cesium ground state. For spins with a certain length, the achievable minimum increases, the more spin $\frac{1}{2}$ entities participate. Our case with $F = 4$ is equivalent to eight spin-$\frac{1}{2}$ constituents. When the state generation is designed carefully, also the spin of an atomic ensemble can be squeezed in this way. The optimal achievable spin squeezing for spins of certain length is discussed in [SM01].

The squeezing mechanism is described in detail in the following chapter and let it just be mentioned here that similar states are generated in [CMH+07]. There the generation of a vast amount of states in the $F = 3$ manifold via controlling light and magnetic fields is reported. The states are observed in the weak coupling regime and the average single atom density was determined. This does not give the possibility to make statements about the collective state of the atomic ensemble. The preparation of the states has to be done in a very precise fashion to avoid collective effects, which can lead to correlations between the atoms. When the atoms are not in a product state, the average single atom density matrix is not sufficient to evaluate the collective spin operators. The strong read out we apply here, on the other hand, will give us the possibility for an analysis of this collective state.

7.2 Squeezing mechanism

The most well known form of squeezing is quadrature light squeezing. The generation of such squeezed light states is usually achieved by employing a nonlinear Hamiltonian which leads to the generation of two identical photons. This requires a nonlinear optical medium. Correspondingly, generating spin squeezing can be accomplished by a Hamiltonian which is nonlinear in one, or several spin components. Similarly as in the light case double excitations are created, which means in the case of single atoms excitations with $\Delta m = 2$ between the states. Such Hamiltonians, can for example be accomplished by engineering the interaction of an atom with suitable, off resonant light fields, leading to a Raman process.

In the following, I first introduce two general possible spin-squeezing Hamil-

tonians, followed by the description of the implementation in our experiment.

7.2.1 One and two axes twisting

Two similar approaches to achieve spin squeezing, starting from an oriented state, with different Hamiltonians are described here. This section is in accordance with [KU93].

One axis twisting

Let us consider a Hamiltonian for a single atom of the form[1]:

$$\hat{H} = \alpha \hat{j}_z^2. \tag{7.3}$$

This Hamiltonian leads to an effect described as one axis twisting in [KU93] (see sketch in figure 7.1). It is straight forward to solve the Schrödinger equation, for a single atom for our case. Here we consider a quantization in x-direction, because the starting point in the experiment is usually a fully oriented state in x-direction.

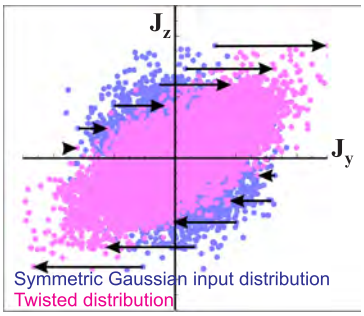

Figure 7.1: Schematic illustration of one axis twisting for a Gaussian input distribution.

$$\frac{d}{dt}|\psi\rangle = \frac{\hat{H}}{i}|\psi\rangle, \qquad |\psi\rangle = \sum_{m=-4}^{4} c_m(t)|m\rangle, \tag{7.4}$$

and for the single components, this reads:

$$\begin{pmatrix} \dot{c}_4(t) \\ \dot{c}_3(t) \\ \dot{c}_2(t) \\ \dot{c}_1(t) \\ \dot{c}_0(t) \\ . \\ . \\ . \end{pmatrix} = \begin{pmatrix} -i\left(-\sqrt{7}\alpha\cdot c_2(t) + 2\alpha\cdot c_4(t)\right) \\ -i\left(-\frac{3}{2}\sqrt{7}\alpha\cdot c_1(t) + \frac{11}{2}\alpha\cdot c_3(t)\right) \\ -i\left(-3\sqrt{\frac{5}{2}}\alpha\cdot c_0(t) + 8\alpha\cdot c_2(t) - \sqrt{7}\alpha\cdot c_4(t)\right) \\ -i\left(\frac{19}{2}\alpha\cdot c_1(t) - \frac{3}{2}\sqrt{7}\alpha\cdot c_3(t) - 5\alpha\cdot c_{-1}(t)\right) \\ -i\left(10\alpha\cdot c_0(t) - 3\sqrt{\frac{5}{2}}\alpha\cdot c_2(t) - 3\sqrt{\frac{5}{2}}\alpha\cdot c_{-2}(t)\right) \\ . \\ . \\ . \end{pmatrix}$$

Clearly, the states with $\Delta m = 2$ couple via this interaction. The equation is symmetric in $\pm m$, so the equations for c_m with $m < 0$ do not give any additional information. As the input state we choose the atoms oriented in the x-direction,

[1] Here $\hat{j}_z^2$ refers to the single atom spin, as opposed to the position-depending ensemble spins previously used.

so that $|\psi(0)\rangle = |4\rangle$. Then the differential equations for $c_m(t)$ are solved. I will not state the solutions explicitly, but instead show plots of the time evolution of relevant observables. In figure 7.2a the populations of the m sublevels in x-direction are shown. Only the even sublevels become populated. After $\alpha \cdot t = \pi$, the whole population is transferred to $m = -4$ and thus the macroscopic spin flips sign.

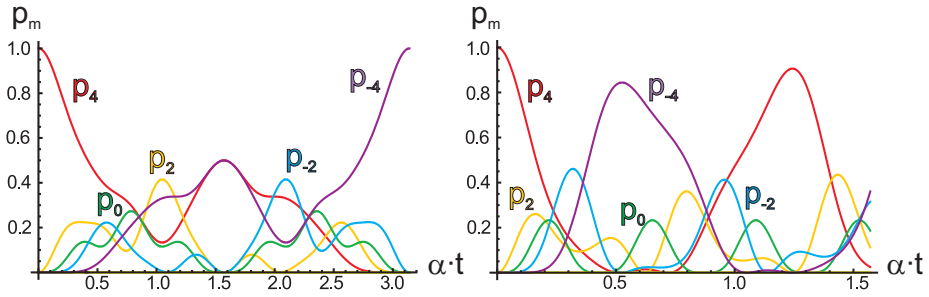

(a) 1-axis twisting (b) 2-axes twisting

Figure 7.2: The development of the populations p_m of the different m-sublevels in x-direction are shown for (a) a Hamiltonian of the kind of 7.3 and (b) a Hamiltonian of the kind of 7.5. The populations of the odd m levels remain zero.

Now let us look at the development in the transversal plane. In figure 7.3, the statistics of the populations of the magnetic sublevels in the y-z-plane are depicted for different states which can be reached. In 7.3a the probability distribution for the different m is depicted for the fully oriented CSS for a single atom. In a measurement of several atoms in the CSS, most atoms will be found in $m = 0$. The CSS is symmetric in the transversal plane, and therefore has the same distribution in y- and z-direction.

The statistics of the population after a certain, optimal interaction time of the two transversal directions are shown in 7.3b and 7.3c. The distribution in y-direction is distinctly wider than the one of the oriented state, shown in figure 7.3a. Figure 7.3c shows the unchanged z-direction. This was to be expected as the Hamiltonian commutes with $\hat{j}_z$, while $\hat{j}_y$ is displaced corresponding to $\hat{j}_z$. The generated squeezing lies at another angle in the x-y plane. At this angle ϕ_{opt}, we can observe the minimum variance of the spin. The statistics of the population distribution in the corresponding direction is shown in figure 7.3d and shows a narrower profile. The anti squeezed spin component that lies rotated by 90° in the transversal plane has an extremely broad profile with high probabilities for the two extreme states.

In figure 7.4b, the variances of the transverse spins $\hat{j}_y, \hat{j}_z$ are depicted depending on time together with the mean of $\hat{j}_x$. Those are the values of interest, if one wishes to evaluate the squeezing parameters discussed in section 7.1.1.

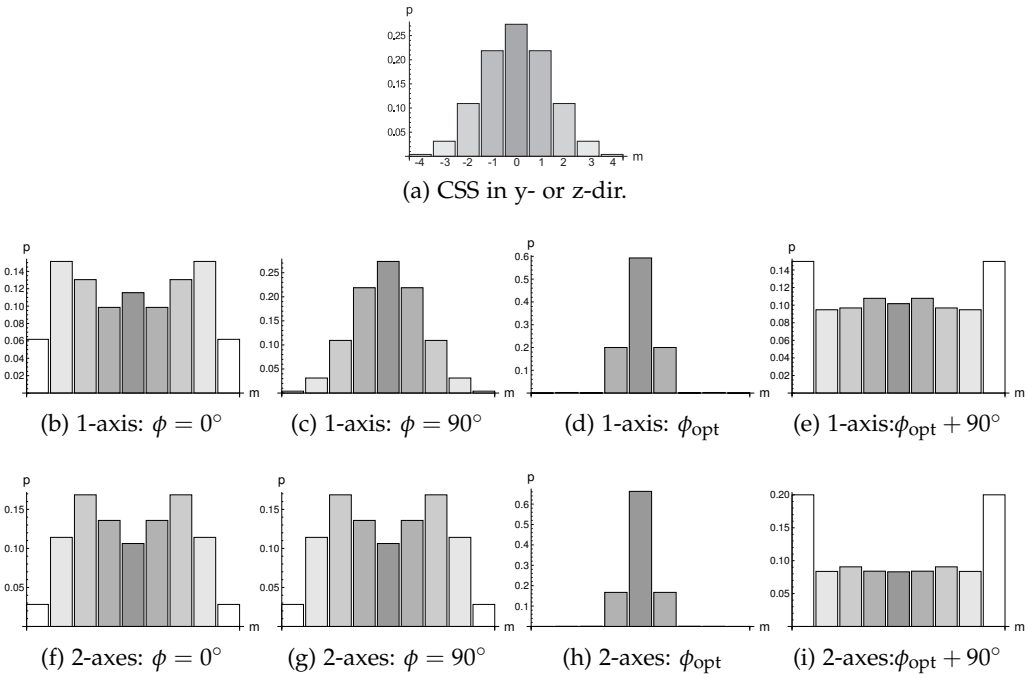

(a) CSS in y- or z-dir.

(b) 1-axis: $\phi = 0°$ (c) 1-axis: $\phi = 90°$ (d) 1-axis: ϕ_{opt} (e) 1-axis:$\phi_{\text{opt}} + 90°$

(f) 2-axes: $\phi = 0°$ (g) 2-axes: $\phi = 90°$ (h) 2-axes: ϕ_{opt} (i) 2-axes:$\phi_{\text{opt}} + 90°$

Figure 7.3: Populations of Zeeman levels along quantization-axes orthogonal to the mean spin. In (a) the statistical distribution of the CSS is shown. (b)-(e) display the maximally squeezed state reachable via one axis squeezing in various directions and in (f)-(i) the same is shown for the optimal two axes squeezing. The state vector was calculated in x-basis and then rotated by an angle ϕ around x and 90° around the y axis. This was done with help of the Wigner D matrix. $D^j_{mm'}(\phi, \Pi/2, 0) = e^{-i\phi m} d_{m,m'}(\pi/2)$.

$\text{Var}(\hat{j}_z)$ remains unchanged by the Hamiltonian, while $\text{Var}(\hat{j}_y)$ grows, as additional noise contributions from $\hat{j}_z$ are piling up. However, $\hat{j}_y$ and $\hat{j}_z$ are no longer independent - the distribution which the transversal spins follow was twisted around the z axis as illustrated in figure 7.1. Thus the squeezed spin components in the transversal plane lies at an angle ϕ_{opt} to the y axis. The development of the variance of the turned quadrature is shown in figure 7.4c. The optimal acquired squeezing after criterion 7.1 is achieved after $\alpha t \approx 0.257$, at an angle $\phi \approx 1.083$ with $\zeta^2 \approx 0.288$. The optimum after criterion 7.2 is achieved slightly earlier, after $\alpha t \approx 0.228$, at an angle $\phi \approx 1.061$ with $\zeta^2_\alpha \approx 0.354$. The obvious reason for the earlier optimum is that the reduction of $\langle j_x \rangle$ has a stronger effect here, since the normalization factor is $\langle j_x \rangle^2$.

Two axes twisting

Another approach, also discussed in [KU93] is the so called two axes twisting achieved by a Hamiltonian

$$\hat{H} = a(\hat{j}_z^2 - \hat{j}_y^2). \tag{7.5}$$

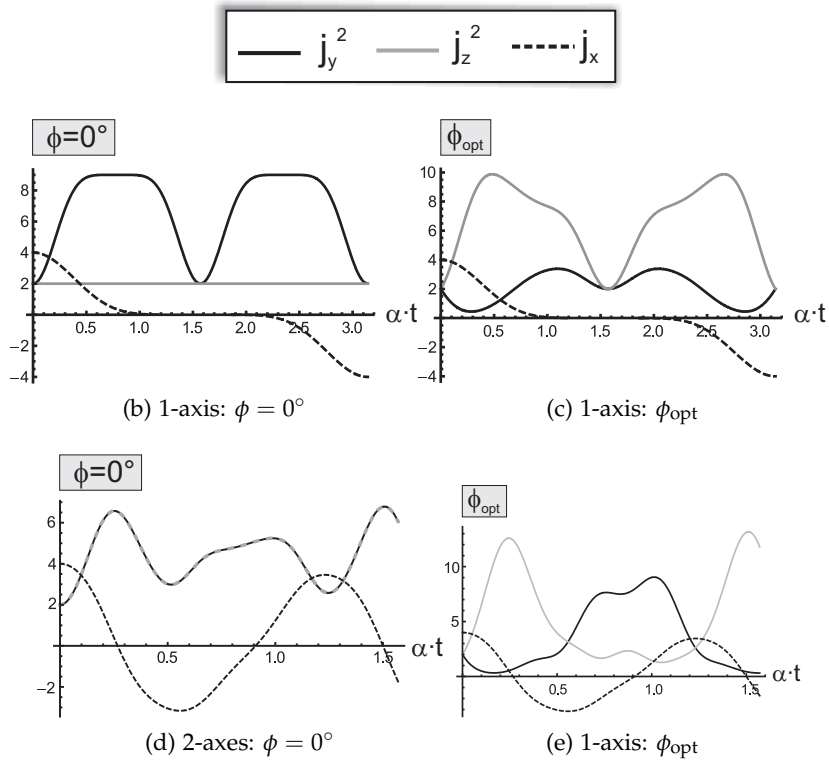

(b) 1-axis: $\phi = 0°$ (c) 1-axis: ϕ_{opt}

(d) 2-axes: $\phi = 0°$ (e) 1-axis: ϕ_{opt}

Figure 7.4: The variances of the transverse spins $\hat{j}_y, \hat{j}_z$ are depicted depending on time as the black and gray lines. The mean of $\hat{j}_x$ is shown as the black dashed line. The upper two figures are the one axis twisting case at angle $0°$ and ϕ_{opt}. The lower line show the scenario for the two axes twisting case.

This squeezing process achieves slightly better results, than the simpler one axis twisting case. The final squeezed spin state lies at $45°$ to the initial axes. In the third row of figure 7.3 the distributions of the optimal squeezing point which can be achieved with this process are shown. A slight improvement is visible. The reason for this better outcome is essentially that the Hamiltonian 7.5, as compared to 7.3, does not induce any differential energy shift between the magnetic sublevels.[2] The improved achievable squeezing lies at $\phi = \pi/4$ and has the values $\zeta^2 \approx 0.248$ after $\alpha t \approx 0.137$ and $\zeta^2_\alpha \approx 0.327$, achieved slightly earlier at $\alpha t \approx 0.119$.

[2]This becomes clear, if one considers that the diagonal elements of single atom spin operators are canceled:

$$\begin{aligned} \hat{j}^2_{y,z} &= \frac{1}{4}\sum_m [\pm C(F,m)(\sigma_{m+1,m-1} + \sigma_{m-1,m+1}) + (F(F+1) - m(m+1))(\sigma_{m,m} + \sigma_{m+1,m+1})] \\ \hat{j}^2_y - \hat{j}^2_z &= \frac{1}{2}\sum_m C(F,m)(\sigma_{m+1,m-1} + \sigma_{m-1,m+1}). \end{aligned} \tag{7.6}$$

with $C(F,m) = \sqrt{\{F(F+1) - m(m+1)\}\{F(F+1) - m(m-1)\}}$ and $\sigma_{i,j} = |i><j|$.

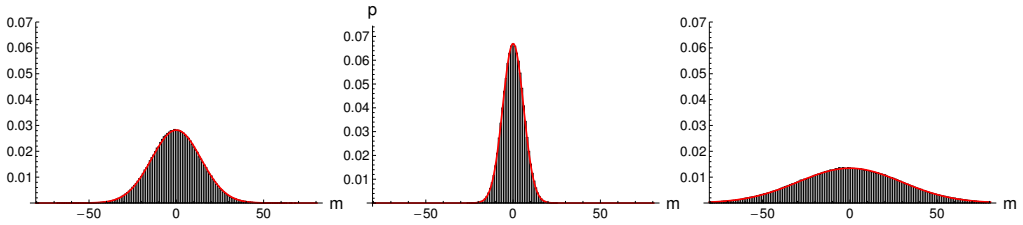

(a) CSS (b) 2-axes: α_{opt} (c) 2-axes:$\alpha_{opt} + 90°$

Figure 7.5: Statistical distribution for the collective transversal spin for 100 atoms for (a) a CSS, (b) the squeezed quadrature for the optimally 2 axis twisted squeezed state and (c) the corresponding anti-squeezed spin component. The red lines show Gaussian distributions with the expected variance for a single atom times the number of atoms. The Gaussian clearly fits the distribution extremely well.

Collective spin

When we read out the spins with our standard techniques, discussed in earlier chapters, we will not measure the spin of an individual atom, but the quasi continuous collective spins. Due to the central limit theorem for independent atoms we observe a Gaussian distributions for the transversal spins with the variance given by N times the variances of the distributions shown in figure 7.3. To illustrate this, in figure 7.5 a simulation of the statistics of 100 atoms are shown, together with the Gaussian distributions with the width corresponding to 100 times the variance of the distribution of a single atom, which can be very far from Gaussian.

7.3 Implementation

Squeezing Hamiltonian

In the experimental realization, we implement the desired Hamiltonian by shining a light beam detuned from the D_1 line onto the atoms. We are interested in the effects which are nonlinear in the spin components and sending the beam in direction of the macroscopic spin makes it possible to neglect the effect of the linear term of the Hamiltonian from equation 2.18, if $\langle S_z \rangle$ is small. If the beam is directed in y- or z-direction instead, the enhanced coupling of the $\Delta m = 1$ coherences of the atoms to the vacuum field in π-polarization introduces correlations between the atoms in the sample, after which the atoms are not in a product state any longer. Theses correlations can lead to additional noise in the observed spin noise. When the beam is traveling in the quantization direction, the light has no co-propagating π polarized component.

Now, for a beam propagating along x, linearily polarized in z- or y-direction with the photon flux ϕ, the Hamiltonian for the single atom reads[3]:

$$\hat{H} = \frac{1}{2}\alpha\phi(\hat{j}_x^2 \pm \hat{j}_y^2 \mp \hat{j}_z^2) \rightarrow \alpha\phi\hat{j}_{z(y)}^2, \tag{7.7}$$

with $\alpha = \frac{\hbar\gamma_1\lambda^2 \cdot a_2}{4a\Delta_R 2\pi}$ and where Δ_R is depicted in figure 7.6a. I left out the parts of the Hamiltonian that only give rise to a collective shift to all levels. In the case of z-polarized input light, the Hamiltonian will be proportional to $\hat{j}_z^2$, while for y-polarized light it is given by $\hat{j}_y^2$. The occuring observable of the light field ϕ can be treated classically.

Note that the a_2 featured in the pre-factor is referring to the D_1 line. This factor can be calculated, as discussed in [Jul03] with help of the transition moments and reduced matrix elements presented in [Ste03]. The coefficients are stated in appendix G.1. The ratio of $\frac{a_2}{a_1}$ can become higher than what we observe on the D_2-line, which is the essential reason why we chose to work on the D_1 line for this experiment. Especially when the light is tuned in between the two exited levels, we will see that we observe a very strong effect. The optimal position will be determined experimentally, by comparing the induced decay to the strength of the Raman transition. In figure 7.6b the ratio $\frac{a_2}{a_1}$ is shown for the D_1 and the D_2 line where the second order effects are clearly less pronounced.

Effect of the magnetic field

In our experiment we also add a magnetic field and consider the spins in the rotating frame. To remain with the simple Hamiltonian, we send in two light beams which are σ_+ and σ_- polarized and have frequencies that differ by $2\pi f_R \approx 2\Omega$.[4] This way the light fields are kept on resonance for the two photon process which is responsible for the squeezing generation. In figure 7.6a this is shown schematically. The atoms start out in the extreme $m = 4$ sublevel. The Raman beams are tuned to two photon resonance and thus always two quanta are transferred to the atom. As mentioned, this is similar to the generation of light squeezing in a nonlinear medium where even photon number states are produced and this leads to quadrature squeezing.

Another effect of the magnetic field, besides the Larmor-precession, is the second order Zeeman shift, due to which the $\Delta m = 1$ coherences precess at different frequencies. The corresponding effective Hamiltonian that describes this impact of the magnetic field is $\hat{H}_Z = \beta\hat{j}_x^2$, as discussed in [Jul03]. Thus the

[3] Note: $j_x^2 + j_y^2 + j_z^2 = \frac{F(F+1)}{2}$

[4] To be exact $2\pi f_R = \Omega_{43} + \Omega_{32}$. In the description of the experiment I keep stating one Larmor frequency for all coherences for simplicity. This is of course not always the case due to the second order effects and will be considered later in this chapter.

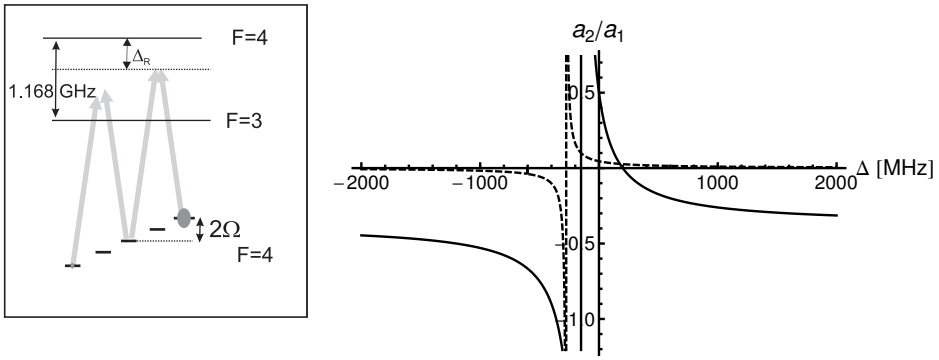

(a) (b)

Figure 7.6: (a) Schematic light atom coupling on the D_1 line leading to squeezing. Two beams with σ_+ and σ_- polarization detuned by twice the Larmor frequency Ω. Thus population transfer from the $m = 4$ to $m = 2$ and 0 is induced.
(b) Comparison of the ratio of a_2 and a_1 for the D_1 line with the D_2 line (dashed). The divergencies are situated where a_1 is zero - this is usually close to resonance and thus suppressed by the Doppler width and we work further away from the resonances (as a reminder the resonances lie at 0Hz and -1.2GHz)

Hamiltonian during the interaction (again where the terms giving a collective energy shift are left out) reads:

$$\hat{H} = (\alpha - \beta)\hat{j}_z^2 - \beta\hat{j}_y^2. \tag{7.8}$$

By adjusting $\alpha = 2\beta$ with detuning and light power, we arrive at the slightly superior two axes squeezing Hamiltonian. So we can utilize the fact that the second order Stark shift of the energy levels can be compensated by the second order Zeeman shift.

Faraday rotation of Raman beams

Finally, I would like to consider the effect of the linear terms of the Hamiltonian on light. I have laid out the necessity to lead the light through the cells in the direction of the mean spin to suppress the effect of mapping of light noise onto the atoms. But what about the effect on the light? We know that linearly polarized light traveling in the direction of the mean spin experience a polarization rotation due to the Faraday effect. This corresponds to different phases acquired by the σ_+ and σ_- light. For the produced squeezing this translates into different squeezing angles in the $y - z$-plane, generated at different positions in the sample. The Faraday angles we measure are quite small in the detuning areas of interest. Another important point to note is that the atoms move a lot on our interaction time scale. In [Jen07] the effect of the Faraday

rotation was simulated and it was observed that there is only a negligible effect on the squeezing outcome for the duration regime of interest.

7.4 Experimental realization

7.4.1 Setup

In figure 7.7a the setup for the generation of the two light beams which are used for the Raman transition is depicted. The laser beam with detuning Δ_R from the $F = 4 \rightarrow F' = 4$ transition of the D_1 line is divided with a PBS into two even parts. In each of the two arms an AOM is situated. The two AOMs are modulated with RF pulses with frequencies differing by f_R. The first order diffracted light beams thus have frequencies differing exactly by this amount. Those first order beams are recombined on a PBS and a quarter wave plate transfers the polarization of the two beams into σ_+ and σ_- respectively. The overlap was optimized, by checking the visibility achieved with the interferometer and a visibility of 95% was accomplished.

The beam is combined with the pump laser beam on a BS. The beam in the second output port of the BS is sent on a PBS, and onto a detector. The output signal is demodulated at $f_R \approx 644kHz$ with a lock-in-amplifier and thus the difference in phase of the RF component of the two beams can be monitored. This way fluctuations in the two beam paths can be observed and compensated, e.g. by changing the phase of the RF modulation imposed on one of the beams.

The laser which is used to drive the Raman transition is a Ti:Sa laser that is frequency-locked via a beat lock similar to the locking setup described in the experimental introduction in chapter 4. Here the optical pump laser is used as the reference frequency. An additional, variable RF frequency is admixed to the beating signal to have the possibility to change Δ_R.

7.4.2 Effect on the orientation monitored by the Faraday angle

As discussed in the beginning of this chapter, the squeezing is accompanied with a reduction of $\langle \hat{j}_x \rangle$ of the single atom. This can be easily understood, as there is a population transfer from $m = 4$ to $m = 2, 0, -2, -4$ which can be seen in figure 7.2. For the Raman process to happen effectively, the frequency difference of the two Raman beams $2f_R$ should be equal to the two photon resonance frequency $\omega_R/2\pi \approx 2\Omega/2\pi$. Of course also spontaneous emission in the presence of the Raman beam creates a reduction of $\langle \hat{j}_x \rangle$, but this should not depend on the difference frequency f_R of the two Raman beams.

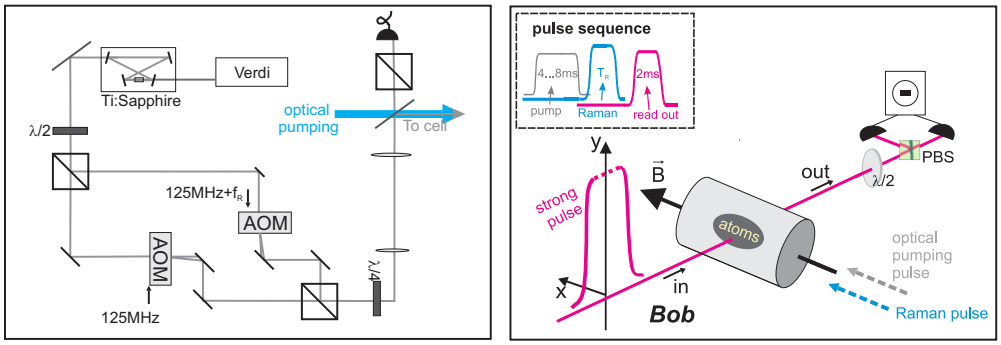

(a) (b)

Figure 7.7: In (a) the generation of the two Raman beams is shown. The Ti:Sa laser is used as the light source. The Raman beams with frequencies differing by f_R are created in an interferometer with help of two AOMs. After their recombination they are combined with the the pump beams on a BS and sent to the cell. In (b) the experiment where squeezing is produced and observed is depicted. The inset shows the pulse sequence.

To observe the two photon resonance, the orientation in $F = 4$ which is proportional to $\langle \hat{J}_x \rangle$ was observed for a scan over f_R. The Faraday angle - so the polarization rotation of a weak linearly polarized beam, propagating in x-direction - was used to monitor the length of J_x (see section 4.2.1) after a Raman pulse with a fixed duration. In figure 7.8 θ_F is shown over f_R as the black curve. The plot features a bimodal structure; beside the sharp dip, originated in the desired two photon process, one can observe a broad background dip. In this measurement the Raman beams filled only a small portion of the cell due to spatial limitations in the beam preparation. The broad background dip arises due to atoms that stay inside the beam only for a short time. The asymmetry originates from the different Stark shifts which the atoms experience at different positions.

The gray curve in figure 7.8 shows the same experiment with an expanded beam where the broad structure is suppressed. This is the setting, in which all data presented in the following was taken.

7.4.3 Optimal experimental parameters

To choose the optimal detuning and power of the Raman beams, the questions to consider are twofold. To achieve the superior two axes twisting, the second order Zeeman-shift and Stark shift should cancel, so that the $\Delta m = 1$ coherences are synchronized during the interaction. For this purpose, we used the MORS techniques, described in section 4.2.2. Secondly, we wish to find a situation where the induced spontaneous emission is small compared to the desired effect.

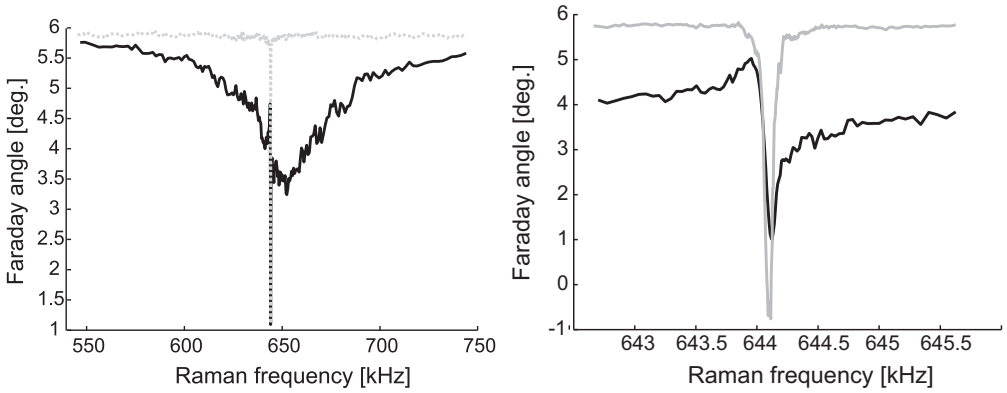

Figure 7.8: The detuning of the two Raman beams f_r was scanned, and the Faraday angle $\theta_f \propto N_{at}\langle j_x \rangle$ was monitored. The black curves are for a setting where the Raman beam covers only a small portion of the cell. For the gray curves, the beam has been blown up to have a width of almost 2cm. All curves feature a narrow reduction at the two photon resonance $f_R = \omega_R/2\pi$

Strength of Raman process and induced decay

We measured the decay-constant of the macroscopic spin in presence of the Raman beams, but detuned from the two photon resonance. The result is shown in figure 7.9a. Only the part of the decay coming from the Raman beam is shown, so the dark decay rate was subtracted. When the laser is tuned in between the two exited lines, there lies a local maximum of the decay time, in the middle between the Doppler broadened transitions. For larger detunings the decay time gets longer and longer.

Also the strength of the Raman process was tested for the same detunings. As a simple measure for this, we chose the light power which is needed to achieve a certain reduction in $\langle j_x \rangle$ for a fixed duration of the Raman pulse on two photon resonance. Without the magnetic field this method would essentially determine the scaling of the prefactor α of the squeezing Hamiltonian in equation 7.7. Here the required light power will also depend on how close the situation is to two axes twisting. We choose a sensible duration of the Raman pulse and a reduction of $\langle j_x \rangle$ close to optimal squeezing for one axis and two axes twisting so that this characterization method will give us an idea of the scaling of the magnitude of the process anyhow. A measurement of the dip in the Faraday angle, as described in the section before was performed for different light powers for every detuning and the size of the dip was observed. In figure 7.9b the light power which was needed for a 10% reduction of the Faraday angle for f_R on resonance is plotted. In between the lines, much less power is needed, than for bigger detunings. If we assume that the induced $\Gamma = \frac{1}{T_1}$ scales linearly

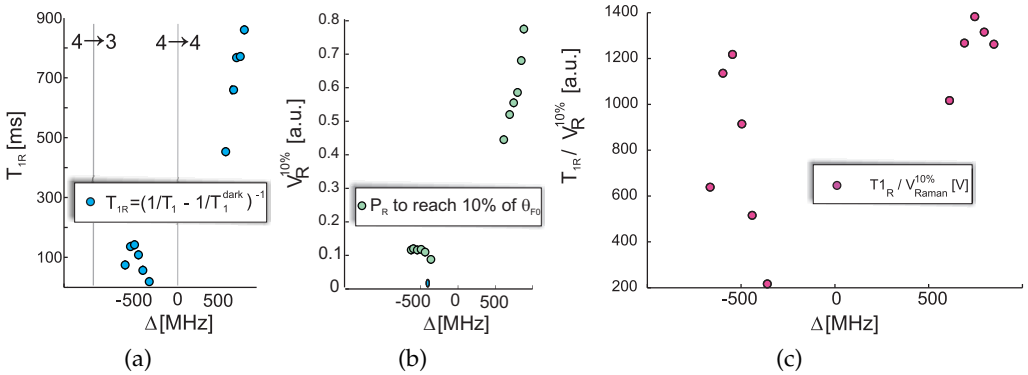

Figure 7.9: In (a) measurements of the decay time of the macroscopic spin induced by the Raman beam are shown for a fixed light power and different detuning Δ_R, while the beams are not on the two photon resonance. The gray lines depict the resonance frequencies for the transition of $F = 4$ to the two exited lines. In (b) the light power needed to create a 10% reduction of θ is shown while f_R is tuned to the two photon resonance. (c) depicts a combination of the two measurements. The decay time is divided by the power which is used as a figure of merit to define the optimal working position - where the longest decay time compared to a certain population transfer is achieved

with the light power, as it should, we can calculate the extrapolated induced decay for the 10% reduction by dividing T_1 by the power and it becomes clear that to achieve the same reduction in the Faraday angle there are two similar positions: one between the two exited lines and one at around $\Delta = 750MHz$. We choose to work in between the lines, which will give us the possibility to cancel out the second order Zeeman-shift. If a blue detuning is chosen, the nonlinear Hamiltonian of the light gets the same sign as the second order Zeeman shift and two axes twisting becomes impossible.

Splitting of the coherences

In figure 7.10, a measurement of the splitting for different light powers is shown for the chosen red detuning $\Delta = -550MHz$. MORS traces were recorded for different powers of the Raman beam and $\omega_R = \Omega_{43} + \Omega_{32}$ and the splitting of the coherences $2\pi\nu_s = \Omega_{43} - \Omega_{32}$ was measured. As the x-axis we use the frequency (energy) difference ω_R of the substates $m = 4$ and 2 which is shifted due to the Stark shift by the Raman light. The splitting can only be measured for small powers and the zero point $\nu_s = 0$ extrapolated. Most of our experiments however, are conducted for

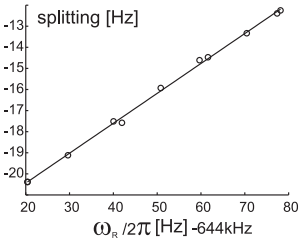

Figure 7.10: Splitting of the coherences for different Raman powers over ω_R.

higher light powers. The reason is that dephasing and
decay make a faster preparation superior even though this lies between the one axis and the two axes case.

7.5 Results

On the path to optimize the single atom squeezing experiments, many different measurement series were taken. As mentioned in the previous chapters, to achieve optimal results the beam shape and the procedure of how to produce the Raman beams needed to be optimized and detuning and light power were picked carefully. Until now I have only considered measurements of $\langle j_x \rangle$, but of course the important measurement size is the spin noise in the two spin components, which will be discussed in the following.

7.5.1 Atomic variances and mean spin

The measurement outcomes of the read out pulse depicted in the inset of figure 7.7b, can be used for the atomic state reconstruction of the collective state. The knowledge of the shot noise and κ^2 are crucial to gain information about the noise properties of the created state. The coupling constant was calibrated by thermal noise measurements (section 5.2.1). The atomic noise was reconstructed with the assumption of a one cell interaction with a QND-type Hamiltonian, following the procedure which was described in section 5.2, applying the second line of table 5.1. We should pick the phase of the demodulation with the lock-in amplifier at Ω such, that the squeezed/antisqueezed variances lie in the atomic quadratures $\hat{x}$ and $\hat{p}$ which are read out with $\hat{y}_c$ and $\hat{y}_s$[5]. All RF phases - of the AOM modulations and the atomic reference signal - are reset in the beginning of every duty cycle.

The QND approximation, which only features linear terms in the Hamiltonian, is valid for all orientations. The model developed in chapter 3 depends on an approximation valid only for high orientation and can therefore not be used here. If we want to evaluate the effect of the higher order terms in the Hamiltonian on our reconstruction procedure, we need to find another method. In section 7.5.3 such a procedure is described and the mistake made in the reconstruction due to higher order terms in the Hamiltonian is estimated.

[5] Alternatively one can extract the squeezed and antisqueezed variances with a different phase afterwards. For this one takes a measurement series and finds the minimum uncertainty angle of the set of measurements in the phase space and then evaluates the variance.

Measurements of the time evolution

In the measurement presented in figure 7.11 the duration of the Raman-pulse was varied, while keeping the Raman power and f_R[6]. For every duration 10.000 points were taken and the atomic variance reconstructed. The squeezed variances are shown by the magenta dots. The blue dots indicate the behavior of the mean spin, but normalized such that it shows the variance of a CSS with corresponding spin length. Measured variances beneath the blue points therefore indicate spin squeezing after criterion 7.1, we observe thus spin squeezing in the first 1-1.5 ms.
The development of the measured sizes resembles the theoretical predicted behavior of the variance and mean spin depicted in figure 7.4e. But there are some apparent differences.

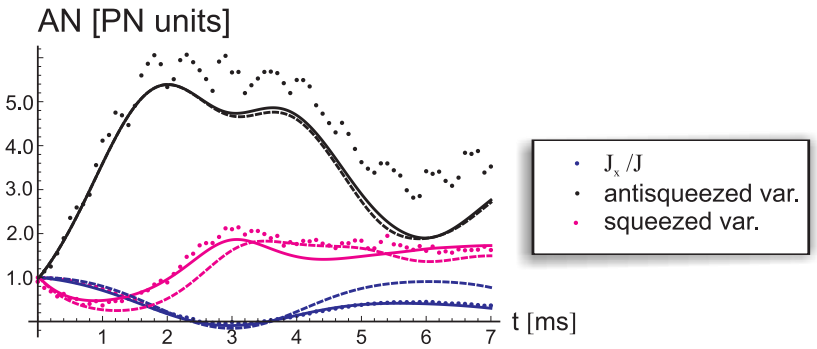

Figure 7.11: In (a) the time evolution of the squeezing is shown. The duration t of the Raman pulse was varied and a consecutive probe pulse was used to analyze the atomic state. The blue dots show the noise of a CSS with the equivalent macroscopic spin (which was measured via a Faraday rotation measure). The magenta dots show the variance of the optimally squeezed spin component in units of CSS-noise and the black dots show the variance of the corresponding anti-squeezed component. The lines come from a theoretical model which is using the light power of 0.88mW. The dashed lines are based on a model not including decay, while the solid lines show the predictions from the model including decay due to spontaneous emission and collisions with the wall. The uncertainty of the points is not depicted and lies at around 10% (coming from calibration uncertainties and statistical uncertainty) for the variances and 1% for the macroscopic spin.

The mean spin behaves different to the prognosis. $\langle j_x \rangle$ barely flips sign and comes back to a reduced value. This conduct is originating amongst others in the fact that the setting lies between one-axis and two axes twisting. Thus the Raman beams can not be on resonance for all possible two photon processes at the same time. The dashed lines in figure 7.11 show the theoretical evolution of the mean spin and the variances for the full Hamiltonian for this setting. There is a strong similarity in the experimental and theoretical curves established by

[6]Set to the two photon resonance for a short pulse duration.

leaving the light power in the cell as a free parameter. This needed to be done, as part of the losses of the light towards the cell were not characterized. The discrepancies between the dashed curve and the measurement points are the decaying mean spin and higher measured noise in the squeezed variance. This is apparently originating from the different decay mechanisms.

Spin decay during squeezing generation

To achieve a better agreement I want to include decay in our predictions. Previously, we had some success in making a very simple addition to the model in order to include the decay, by use of the Langevin operators. The decay was assumed to be directed towards the CSS (or the thermal state). The earlier described interaction were not based on population transfer, but kept somewhat close to the CSS, thus the assumptions gave good results. It would be possible to make a similar ansatz for a decay towards a different state, but when the population of the different levels changes so drastically during the interaction, so will the state that the atoms decay to.

As we are only interested in the evolution of the atomic ensemble, we can consider the time evolution of the atomic density matrix, and include Lindblad terms $\mathbf{L}_n$ (step operators with rates) for the decay. The corresponding formulas are shown in appendix G.2. There are different decay types to consider. Most importantly, there is spontaneous emission. Due to this, a big fraction of atoms will leave the observed subsystem ($F = 4$), reducing the mean spin and the noise of the observed spin components. This can easily be modeled, by adding an ancillary state into our model which will not contribute to our observables. This will be seen as a loss of atoms and reduces $\langle \hat{j}_x \rangle$ and the variances of the transversal spins accordingly. Spontaneous emission back to the $F = 4$ level will add different amounts of noise, depending on the final m_f state. Additionally a decay mechanism towards the thermal state, modeling processes like collisions was included. The time constant used for this was close to the measured T_1 in the dark. The time evolution was evaluated iteratively with the formulas stated in appendix G.2 and the result is shown as the solid curves in figure 7.11 - a good agreement was reached.[7]

Lifetime and stability of the generated squeezing

In figure 7.12a, the lifetime of the squeezing was tested. The delay between the Raman light pulse, generating the squeezed state, and the read out was varied.

[7] The contribution of the atoms in $F = 3$ to the Faraday rotation was not included here. This could in principle be done by adding all substates of $F = 3$ into the model individually. The effect of this seems small compared to the precession of the fit, so I did not do it here.

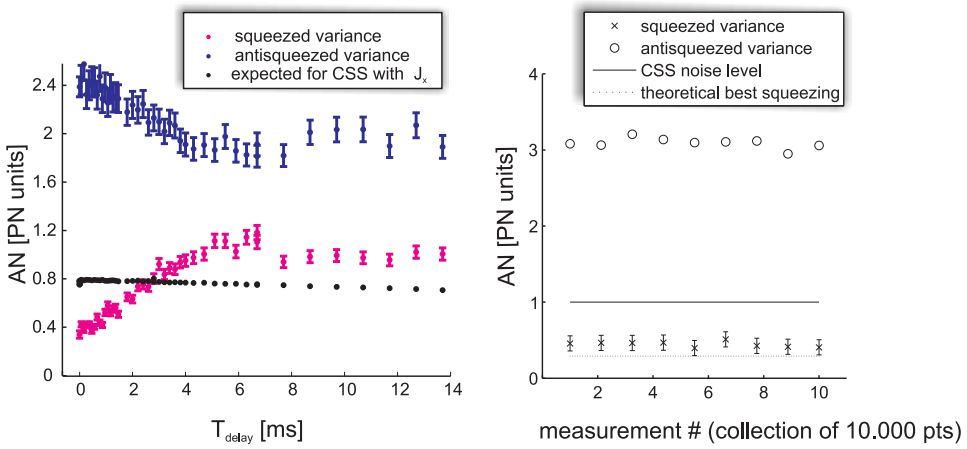

(a) (b)

Figure 7.12: In (a) the lifetime of the squeezing was tested. The first point is calculated from 100.000 measurements, while the others are measured with 10.000 repetitions. The variances of the two quadratures (blue and magenta) are shown together with the expected variance of a CSS (black) with the same length of the macroscopic spin J_x. the black points therefore indicates the boundary of the squeezing. In (b) the stability of the measurement is shown. Those measurements represent the first point with zero delay. Here the measurements are binned into 10 times 10.000 measurements and the fluctuations can be seen. The resulting standard deviation of those ten measured variances is bigger then expected, if the uncertainty would just come from the Gaussian nature of the measured variable. The additional uncertainty arises from instabilities in preparation. Other uncertainties, as in the kappa calibration, Faraday measurement and light noise are included in the error-bars.

Squeezing vanishes after 2.5ms. This arises from the usual decay mechanisms and dephasing of the magnetic coherences, due to the second order Zeeman shift which lets the coherences rotate at 20Hz different frequencies for neighboring coherences.
For the Raman duration which produced the best squeezing, the state was measured with 100.000 repetitions and in figure 7.12b the variances are shown for 10 points of 10.000 repetitions. The shown error bars come from uncertainties in the calibration of κ_{QND} and the shot noise. The squeezing parameters for those points are $\zeta^2 = 0.45 \pm 0.05$ and $\zeta_a^2 = 0.50 \pm 0.06$. The latter confirms the presence of nuclear-electronic entanglement in the individual atoms.

7.5.2 Atomic state reconstruction - Wigner function and density matrix

In figure 7.13a all the measurements, for which the binned variances are shown in 7.12b, are shown as a histogram. The pink curve displays a Gaussian distribution with the measured widths. The atomic state reconstruction is similar to

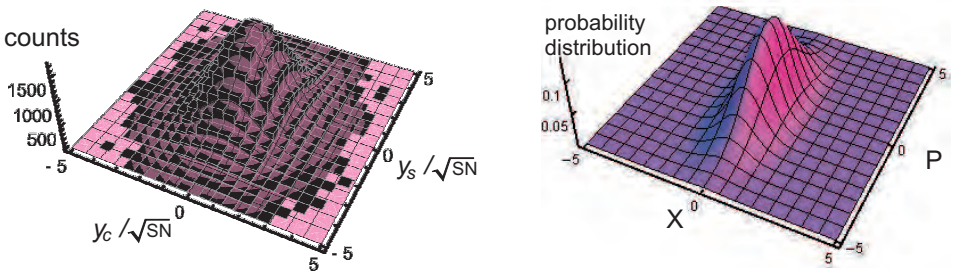

(a) (b)

Figure 7.13: In (a) the histogram of 100000 measurements are shown together with a Gaussian distribution with the measured widths. In (b) the reconstructed collective atomic state with $X = \frac{\hat{J}_y}{\langle \hat{J}_x \rangle}$ and $P = \frac{\hat{J}_z}{\langle \hat{J}_x \rangle}$

a measurement of a light state with a bad detection efficiency. In principle one can write the light variable on the detectors, similar as in [UTK06]:

$$\hat{y}_c^{\text{out}} = \mathcal{A}(\sqrt{\eta}\hat{p} + \sqrt{1-\eta}v\hat{a}c), \;\; \hat{y}_s^{\text{out}} = \mathcal{A}(\sqrt{\eta}\hat{x} + \sqrt{1-\eta}v\hat{a}c) \tag{7.9}$$

which just looks like the detection of two phases of a light state with a certain detection efficiency. The "detection efficiency" is given by $\eta = \frac{\kappa_{\text{QND}}^2}{2+\kappa_{\text{QND}}^2+\kappa_{\text{QND}}^4/6}$ and the gain $\mathcal{A}^2 = 1 + \frac{\kappa_{\text{QND}}^2}{2} + \frac{\kappa_{QND}^4}{12}$. Now, similar tools as for the analysis in optical homodyning [LP95] can be used. From the multiple of the polluted Wigner function in figure 7.13a, we can reconstruct the atomic Wigner function in phase space of the collective atomic state, assuming that the atomic state is Gaussian. The extracted atomic Wigner function is shown in figure 7.13b. While the measured distribution only shows a small asymmetry, for the reconstructed one with almost 3dB of squeezing the asymmetry can be seen easily. The Wigner function includes all information about the atomic state, so we can calculate the corresponding density matrix[LP95, NN08] for all atoms[8]. The relevant section of the obtained density matrix is shown in 7.14a.

If one does not want to make assumptions about the atomic state before the atomic reconstruction, the collective density matrix can be reconstructed with maximum likelihood methods[HMŘ06]. The method optimizes the likelihood of the density matrix, based on a certain measurement set of $\hat{q}(\theta) = \hat{x}\cos(\theta) + \hat{p}\sin(\theta)$. The measurements are binned and starting from a certain guessed density matrix, one defines the likelihood, e.g. as $\ln L(\rho) = \sum_{\theta,j} N_{\theta,j} p_{\theta,j}$ where $N_{\theta,j}$ is the number of measurements in bin j and $p_{\theta,j}$ is the probability of this

[8] $\rho_{mn} = 2\pi \int \int_{-\infty}^{\infty} W(x,p) W_{mn}(x,p) dx dp$ with $W_{mn} = \frac{1}{2\pi} \int_{-\infty}^{\infty} e^{iyp} < x - \frac{y}{2} | m-n | x + \frac{y}{2} > dy$

measurement outcome, based on the guessed ρ_0. Now ρ can be varied, but the trace needs to be held constant and ρ should be Hermitian and positive definite. All this can be granted by defining a suitable iterator $\hat{R}$ and calculating the likelihood for iteration k $\rho^k = R\rho^{k-1}R$ until the Likelihood stabilizes. As shown above, the fact that we measure the atomic state via light can be translated into an imperfect detection efficiency which can routinely be included in the procedure as shown amongst others in [HMŘ06, NN08]. The difference to usual settings is that instead of measuring a probability distribution for different angles θ after each other, we measure always $\hat{x}$ and $\hat{p}$ at the same time, with a bad detection efficiency (which is allowed by quantum mechanics).

In figure 7.14b the result of such a procedure for the presented points is shown[9]. It looks very similar to the density matrix shown in figure 7.14a which comes from the much simpler reconstruction based on the assumption of Gaussian states. To compare, in figure 7.14c the diagonal elements of the density matrices for the two methods are shown together. The values of the different elements vary by a few per mil. The assumption that we are working with Gaussian states seems justified.

In 7.14d the single atom density matrix from the theoretical predictions which lead to the theoretical curves in 7.11 is shown for the point after 1ms. The element in the upper right corner shows the predicted population of all $F = 3$ substates. Also here, mainly the even states become populated, but there is some pollution of the pure squeezed state, coming from the decay. It can not be compared to the other two density matrices quantitatively as it arises from a completely different measurement set.

7.5.3 Corrections of the reconstruction

It is harder to evaluate the accuracy of the atomic state reconstruction here than it was in the case of the teleportation experiment. The reason is that, as we ventured away from the CSS and away from the possibility of limiting ourself to a two-level system, we needed to establish another estimate of the higher order corrections. In the appendix C a perturbational approach is taken. Again the full Hamiltonian is considered and, like previously the relevant terms extracted. This time the linearizing step is not taken, instead the first order perturbation is calculated for the variable of interest for the read out. The corrected read out

[9]The result of the ML reconstruction are shown by the courtesy of Thomas Fernholz, who programmed the maximum likelihood evaluation program.

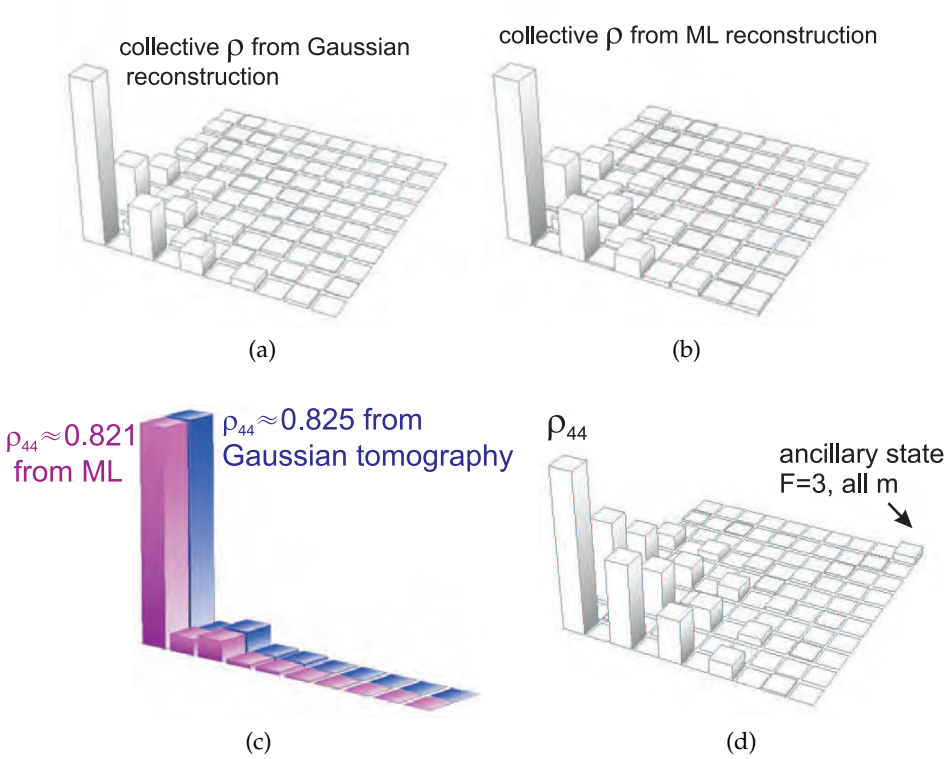

Figure 7.14: In (a) the density matrix from the simple reconstruction or Gaussian states is shown, for the measurements from the histogram 7.13a. In (b) the upper corner of the collective density matrix which is reconstructed by maximum likelihood is depicted[10]. The two matrixes look similar. To compare, in (c) the diagonal elements of the two matrixes are plotted together.
In (d) the single atom density matrix, corresponding to the optimal squeezing point of the theoretical curve featured in figure 7.11 is shown. The upper right corner is showing the population of all sublevels of $F = 3$.

formula C.10 reads:

$$\begin{aligned}\hat{y}_c^{\text{out}} = \quad & \hat{y}_c^{\text{in}}(1 - \frac{\kappa_{\text{QND},0}^2\zeta^2}{16}(\hat{j}_x^2 - \hat{j}_y^2)) + \frac{\kappa_{\text{QND}}}{\sqrt{2}}\hat{p}^{\text{in}}(1 - \frac{\kappa_{\text{QND},0}^2\zeta^2}{16}(\hat{j}_x^2 - \hat{j}_y^2)) \\ - \quad & \frac{\kappa_{\text{QND}}^2}{4}(\hat{q}_s^{\text{in}} + \frac{1}{\sqrt{3}}\hat{q}_{s,1}^{\text{in}}) - \frac{\kappa_{\text{QND},0}^2\zeta^2}{16\sqrt{3}}\hat{(j}_x^2 - \hat{j}_y^2)y_{c,1}^{\text{in}}\end{aligned}$$

with $\zeta^2 = 4\frac{a_2}{a_1}$. Clearly, there are similar corrections, as the ones coming from the scenario discussed in chapter 3. There is a suppressed coupling constant, and a suppressed light noise contribution. The κ_{QND}^2 was measured via the thermal noise. More precisely the coupling constant, suppressed by the detection efficiency η was measured. Now, to analyze the quality of our state reconstruction the remaining question is, what we would like to set as $\langle \hat{j}_x^2 - \hat{j}_y^2 \rangle$. This entity

has its maximal value for the CSS, for which the value is 14. Obviously, for the squeezed states it gets smaller and smaller. Plotted in figure 7.15a are the variances for the QND analysis as dots together with the the maximal correction (for the CSS) as circles, which lie around 15% above the noise evaluated with the QND theory. The crosses show variances evaluated with an estimate for $\langle \hat{j}_x^2 - \hat{j}_y^2 \rangle$ from the theoretical predictions which is shown in figure 7.15b. This presumably better correction corrects the measured atomic variances upwards for small times and minimally downwards for later times. The corrections do not change the quality of the experiment, but e.g. the optimal squeezing is increased by 7% of PN. There are some remaining uncertainties to the precession of this correction, amongst others, what the detection efficiency was in this specific setting. For future experiments the quantities relevant for the correction should be measured with specific care to achieve a more accurate correction.

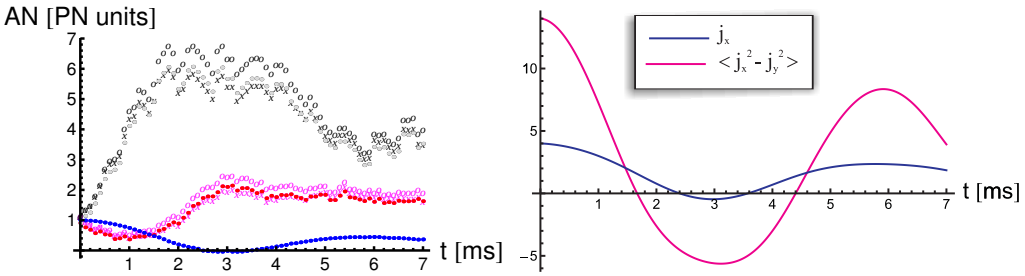

(a) (b)

Figure 7.15: In (a) the corrected squeezing points are shown, the crosses utilized a value of $\langle \hat{j}_x^2 - \hat{j}_y^2 \rangle$ directly from the model (shown in (b)) while the circles where reconstructed by setting $\langle \hat{j}_x^2 - \hat{j}_y^2 \rangle = 14$ which is the maximal value. The variances reconstructed with the QND model ares shown in red and gray.

7.6 Conclusion and outlook

In this section I showed a method of generating spin squeezing in the spin of the single atom. It was verified that this procedure leaves also the collective atomic state in a noise reduced state, so that the squeezing is useful for ensemble applications, such as clocks or atomic magnetometers. It also became clear that a very careful choice of the experimental conditions starting from the direction of the beam to frequency and spatial properties and duration is necessary to achieve a good result. The squeezing of 3dB is similar or actually slightly higher than the achieved QND squeezing for room temperature atoms. The corrections from the higher order terms of the Hamiltonian were estimated, and though they are not negligible, they do not change the quality of the experiment.

One might attempt to combine such a squeezing procedure with a QND mea-

surement to achieve a higher degree of squeezing. The reasoning is simple, as a QND measurement should always enhance the knowledge about one quadrature of the system, no matter what the input state. In [KM10] the possibility of employing both concepts of spin squeezing is investigated for either first generating the single atom entanglements followed by a QND measurement, or the other way around. Also the possibility of using both procedures simultaneously was discussed. The outcome is that, even though the two squeezing procedures can produce a better result together than the internal spin squeezing alone, no matter which procedure starts the squeezing it reduces the effect of the following. The reasons are very simple: if the Raman squeezing is applied first, the length of the macroscopic spin is decreased, also decreasing the coupling strength. Thus the QND measurement becomes less effective. When the QND measurement is applied first, one does not start in the pure CSS state and applying the Raman process then leads to a mixing of unwanted levels as well.

Another difficulty using both squeezing procedures together is the necessity of employing two atomic ensembles with oppositely oriented spins. This needs to be carefully evaluated, and the choice of probing and pumping parameters must probably be done in such a way, that the quadratic Zeeman- and Stark-shifts cancel, otherwise the spins in the two ensembles will precess differently in the magnetic field.

Also the effect on a memory was discussed in [KM10]. Starting from an introduction of a Holstein Primakoff approximation for product states other than the CSS, it becomes clear that the described collective oscillator modes are not squeezed in this discription. The squeezing still helps the protocol, as the new normalization of those oscillator modes leads to an increase in the coupling strength for one of the quadratures.

Chapter 8

Steady state atomic entanglement via dissipation and measurement

This chapter is dedicated to an experiment where our current setup is used to generate atomic entanglement via the light atom interaction. By carefully designing the interaction settings, we can reach a scenario in which the entanglement prevails as long as the interaction is kept on - the collective spins of the ensembles of atoms reach an entangled steady state.

Two concepts for entanglement generation are employed to achieve this steady state. Starting with the interaction described by the theory presented in chapter 3, two mode squeezing is achieved without any measurement on light. To understand the nature of this entanglement generation better, one can also describe the process such that the atomic system is driven by dissipation into the desired state. The corresponding theory is touched on in section 8.2.1.

The achieved two mode squeezing can be improved in quality and duration by employing a particular measurement scheme. This is similar to the known QND approach where the atomic system is squeezed conditioned on a measurement which is conducted on light after the interaction with the atoms.

8.1 Atomic entanglement

The value of entanglement has already been mentioned in several contexts, simply as a striking feature of quantum mechanics, as a resource for quantum communication and quantum information or as needed to improve metrology experiments. Atomic entanglement is of special interest as it can in principle

be distributed and then stored until one wishes to use it. However, exactly in the storage lies a major problem in most previously conducted atomic entanglement experiments. Atomic entangled states proved to be extremely fragile, wether they were generated by measurement [JKP01, CDRF+05, EAM+05, MCJ+06, YCZ+08, AWO+09] or atomic interactions [GZN+10, RBL+10], and also the entanglement described earlier in this thesis (chapter 7) displayed lifetimes of only a couple of ms.

The coupling to the environment leads to decoherence which until now irresistibly was followed by the disappearance of entanglement after a certain time. Several proposals have been made, of how to use carefully engineered environments to create a situation where entanglement is reached by dissipation to overcome this shortcoming. More specifically, dissipatively generated entanglement was proposed for our system in [MPC10]. Due to certain restraints in the experimental realization like the decay and a limited reachable optical depth, the proposed entanglement generation process lead to a long entanglement duration, but not the wanted steady state entanglement. Combining with a measurement on the light output gives the possibility of steady state entanglement, as will be shown in the course of this chapter.

8.2 Theoretical model

The theory described in chapter 3 was until now used solely to estimate corrections of the previously employed QND theory. However, I briefly mentioned that the Hamiltonian does two things; it swaps the state of light and atoms and at the same time performs a squeeze operation on both systems, leaving both light and atoms in a two mode squeezed state. The resulting squeezed light was measured and the results reported in [5].

Here, I would like to turn towards the possibility to achieve squeezed atomic states by applying the interaction for longer interaction times, than previously employed. As we are using a two cell setup, the achieved two mode squeezing of the collective operators translates into entanglement between the spin operators of the two atomic cells. One of the advantages of this is, compared to the QND approach to entanglement, that this is an unconditional entanglement without the feedback of a light measurement. This means that the atomic entanglement is not achieved, mediated by the light atom entanglement after the interaction. The light is used simply as a common reservoir, leading to entanglement by dissipation. For convenience I will use the same kind of equations as in the rest of the thesis to describe the phenomenon. But the experiment can also be described fully in the language generally used for describing a dissipation-driven process - with the master equation in the Lindblad form. This concept will be briefly introduced in the next section, before moving

on to the discussion of entanglement generation with help of the input-output equations in section 8.2.2.

8.2.1 Entanglement by dissipation

In the introduction the fragility of entanglement was pointed out. As a matter of fact, for any quantum mechanical system that couples to an environment only states to which the decay is directed towards remain, while all other quantum states are subject to decoherence. The degradation of entanglement, and other interesting quantum states by coupling to the environment has been studied in several contexts (amongst others [MKT+00, BLW+08, BSG+10, BPP10]). However, recently several proposals have been made of how to engineer the environment in a suitable fashion to utilize dissipation, caused by the coupling to this environment, to engineer interesting quantum states which thus prevail as long as the coupling to the environment is kept the same. Also proposals to realize quantum computation by dissipation [VWC09] have been made.

In [PCZ96] it was proposed how to couple two laser fields to an ion to create Schrödinger cat states. In [KC04] a possibility to create two distant entangled atomic ensembles by shining two squeezed light beams onto them is discussed. A very small squeezing is sufficient to create substantial entanglement. Also in [DMK+08] and [KBD+08] the preparation of quantum systems into desired quantum states via specific design of the environment are presented.

All these approaches are dealing with the coupling of the systems of interest to an environment and the final quantum state of the environment is not of concern. The way to describe the scenario is the Lindblad form of the master equations. The crucial point is to find suitable surroundings so that the dissipation leads towards a steady state that is the state of interest.

Imagine a desired final state $|\Psi_d\rangle$ with $\hat{A}|\Psi_d\rangle = \hat{B}|\Psi_d\rangle = 0$ for $\hat{A} = \mu\hat{b}_1 + \nu\hat{b}_2^\dagger$ and $\hat{B} = \mu\hat{b}_2 + \nu\hat{b}_1^\dagger$ where the indices 1 and 2 refer to two different modes. In our case this could point to the first and second ensemble. For $\mu = \cosh(s)$ and $\nu = \sinh(s)$ this corresponds to a two mode squeezed state with squeezing parameter s. Such a state can be created in a process, described by the master equation

$$\frac{d}{dt}\rho P = c_a(A\rho A^\dagger - AA^\dagger\rho/2 - \rho AA^\dagger/2) + c_b(B\rho B^\dagger - BB^\dagger\rho/2 - \rho BB^\dagger/2) \quad (8.1)$$

More specifically, in [MPC10] a Hamiltonian describing the interaction of two oppositely oriented atomic ensemble in a magnetic field interacting with a light field is introduced:

$$\hat{H} \propto \int_{\omega_+} (\hat{A}a_{\mathbf{k}}^\dagger + \hat{A}^\dagger a_{\mathbf{k}})dk + \int_{\omega_-} (\hat{B}a_{\mathbf{k}}^\dagger + \hat{B}^\dagger a_{\mathbf{k}})dk, \quad (8.2)$$

where $a^\dagger_{\mathbf{k}}$ is the creation operator for a photon with wave vector $\mathbf{k}$. The integrals run over the upper (+) and lower (-) sideband. The master equation for the atomic state after the light has been traced out looks more complicated than equation 8.1. In [MPC10] the full state evolution it is stated, including several additional decay processes.

The model is similar to the theory we have used until now with one major exception. In the analysis in the Heisenberg picture, we have treated the light field as a single mode - in fact the one common emission mode for the two ensembles. Here all modes are considered and thus the part of the spontaneous emission which is not enhanced is included. The outcome of both approaches is therefore only the same in the limit of very high optical depth where spontaneous emission can be neglected. This is a far more rigorous approach than the previously used description, but with the main drawback that the light measurement is not included in the theory.

The understanding we reach this way is that the entanglement is generated by the interference of different processes in the two ensembles for which an indistinguishable photon is emitted in the common mode. The processes in the forward direction are collectively enhanced and a photon emitted at, for example the upper sideband stands for an atomic excitation in ensemble one, or an annihilation in ensemble two.

Since we wish to include the light measurement into the discussion, I limit myself in the following to the input-output descriptions. However, the model which is presented in [MPC10] fits nicely with the experimentally obtained data, as has been shown in [7]. Currently efforts are made to include the measurement into the master equation approach.

8.2.2 Discussion of entanglement generation with input-output equations

Equations 3.10 directly display the squeezing characteristics for the atomic operators which we are interested in. The limit of long interaction times is given in equations 3.13. The final steady state is squeezed by a factor $\frac{1}{\xi^2}$ of the input variance of light. The time scale in which this state is reached is around 20-100ms for relevant experimental settings. In figure 8.1 the black lines show the predicted behavior of the atomic variances. Here, the steady state is reached after around 50ms.
Unfortunately, on this timescale the decay of the atomic spin can not be neglected and needs to be included in the theory. Earlier in this thesis, decay towards the CSS was modeled and the equations for atomic operators after the interaction are given by equation 3.21. There, the final steady state is characterized by the squeezed variance $\epsilon^2 + \xi^2(1-\epsilon^2)$. However, this decay model

is only valid for timescales considerably shorter than the decay of the macroscopic spin J_x which decays with $T_1 \sim 0.4 - .1$s. Due to this decay atoms will start populating $m = 3$ and the $F = 3$ ground-state. Every atom in $m = 3$ contributes 2.7 times as much noise as atoms in $m = 4$ which comprise the CSS. Meanwhile J_x is shrinking due to the atoms leaving the fully oriented state. I include this slow decay in equations 3.21 by letting $\gamma_s \rightarrow \gamma_s(t)$ decrease, as the macroscopic spin and let the transversal spin decay towards a state, characterized by the noise operator $\hat{F}_x$ with $\mathrm{Var}(\hat{F}_x) = \mathrm{Var}(CSS)(r \cdot 1 + (1 - r) \cdot 2.7)$ where r gives the ratio of atoms in $m = 3$ of the $F = 4$ subset. This seems like a crude model, but it will give us an idea of what we can expect. Technically the state evolution is then evaluated by letting the state evolve by the equation 3.21 for small steps, where the coupling strength is decreased for every increment. This is easier than solving the full equations with the time dependent decay constant. The approach can be justified by arguing that the process, governed by γ_s is faster then the decay of J_x.

In figure 8.1 all three predictions are shown for room temperature atoms and 5.6mW probe laser power at $\Delta = 850$MHz. The solid lines represent the variances originating from the equations without decay. The dashed lines where a decay towards the CSS was included display similar behavior with a steady state with reduced degree of squeezing. The dotted lines where the decay of the macroscopic spin was added do not level out, but display a minimum after a certain interaction time. This means that we can not expect steady state entanglement in our experiment with the usual course of action.

Different approaches can be taken to improve the situation. To avoid the high noise originating in atoms populating $m = 3$, we can apply a weak pump laser for which $m = 4$ is a dark state. This will lead to a higher orientation in the $F = 4$ subset. It will also deplete the macroscopic spin even faster, as atoms decay towards $F = 3$. To avoid this an additional repump laser can be employed. Both laser fields will shuffle atoms incoherently back to the two level system of interest, therefore increasing the achievable steady state atomic noise. However, for carefully selected settings a steady state with a quadrature with reduced noise compared to the CSS could in principle be obtainable.

8.2.3 Including light measurement

In section 5.3.3, it is discussed, how a QND measurement can be used to generate a squeezed state. The basic idea was to use the knowledge about the atomic state gained by a measurement on light which has interacted with the atoms to reduce the uncertainty of the atomic state. This can be done by applying feedback whose strength is given by the measurement outcome to the atoms. Instead one can produce conditional entanglement [JKP01] where the atomic

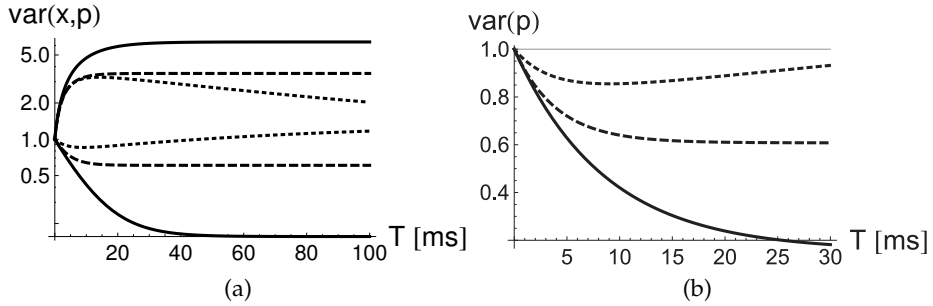

Figure 8.1: Atomic variances with and without decay. The full lines show the prediction for the variances for a relevant setting (room temperature, P=5.6mW) over the interaction time. For the dashed lines, a decay toward the CSS is included with a time constant $T_2 = 8$ms, as we measure for these settings in our experiment. The dotted curves also include the decay of the macroscopic spin with $T_1 \approx 60$ms, as explained in the text. In (a) the squeezed and anti-squeezed variances are shown and in (b) only the more interesting squeezed variances are plotted.

spin state is a displaced squeezed state whose displacement is given by the measurement outcome times a known number α.

The underlying interaction does not allow a pure QND measurement. But we can still attempt to utilize the light measurement to squeeze the atoms, as long as the light contains any information about the final atomic state. Let us first consider the equations without the added decay.
From equations 3.10 and 3.12 we can calculate a conditional variance of the atoms after the interaction, by subtracting the light measurement outcome from the atomic operators $\hat{P}_{c,s}$ [JKP01, SJP07]:

$$\mathrm{Var}(\hat{P}^{\mathrm{out}}_{c,s} - \alpha \hat{y}^{\mathrm{out}}_{c,s-}) = AN \cdot (\sqrt{1-\kappa^2\xi^2} - \alpha\kappa)^2 + LN \cdot (\kappa\xi^2 + \alpha\sqrt{1-\kappa^2\xi^2}) \tag{8.3}$$

The optimal $\alpha_o = \kappa(AN - \xi^2)\sqrt{1-\kappa^2\xi^2}/(1 + (AN - \xi^2)\kappa^2)$ only depends on the coupling constants and the input noise of atoms (here the light noise was set to $LN = 1$). No matter what the input noise was, the final variance of the atoms and the final conditional variance coincide at the level $1/\xi^2$. In figure 8.2 this is illustrated for two different atomic input states.

Even though the measurement can reduce the atomic noise on short timescales, this method does not seem beneficial for the steady state. This makes sense as in the steady state the atoms are in a pure state and therefore the atomic state can not be correlated with the light state. The scenario changes drastically, when decay with the decay constant γ_{extra} of the transversal spin is included in the theory. The steady state is then not a minimum uncertainty state, so that a measurement of the outgoing light in principle could contain informa-

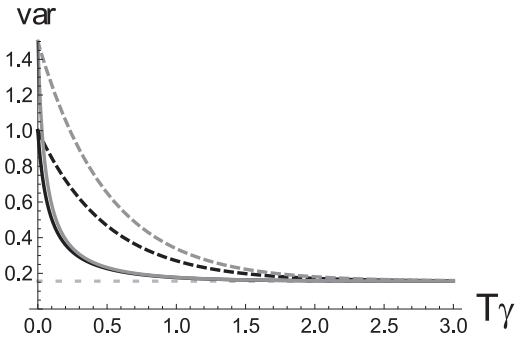

(a) No decay

Figure 8.2: Conditional noise. The full lines show the optimal conditional variance after equation 8.3 of the atomic $\hat{P}$ operators, the dashed lines show the original variance of these operators after the interaction. The light noise $LN = 1$, like for coherent light and the atomic input noise $AN = 1$ for the black line and $AN = 1.5$ for the gray lines. The dotted light-gray line indicates the $\frac{1}{\xi^2}$. The conditional variances for both atomic input states are similar after short time

tion about the atoms. However, it seems that the light mode of the output light which has an exponential falling mode function might be unsuitable, as it contains minimal information about the noise component which is piling up in the atomic operators. So what is the optimal light mode to squeeze the atomic state? Let us consider the out-coming light mode characterized by the function $f(t) = e^{-\gamma_m t}/N_m$ with an arbitrary rate γ_m and where $N_m = \sqrt{1/2 \int_0^T e^{-2\gamma_m t}}$ is the normalization factor with a factor $\sqrt{1/2}$, due to the fact that we consider cosine or sine modes. The input-output relation for this mode reads (here for the cosine case)[1]:

$$\hat{y}^{\text{out}}_{c,m} = B \cdot \hat{P}^{\text{in}}_{c} + \hat{y}^{\text{in}}_{c,*} + \hat{\tilde{F}}^{\text{in}}_{P,\star}, \tag{8.4}$$

with $B = \frac{a}{\sqrt{2}N_m} \int_0^T e^{-(\gamma+\gamma_m)t} dt$. The light and noise operators marked by the tilde are not normalized and have the un-normalized mode functions[2]:

$$\begin{aligned} \tilde{f}_*(t) &= \frac{1}{N_m}(e^{-(\gamma_m+\gamma)t} - 2\gamma_s A(t) e^{\gamma t}), \\ \tilde{f}_\star(t) &= \frac{a\sqrt{\gamma_{\text{extra}}}}{N_m} A(t) e^{\gamma t} \end{aligned} \tag{8.5}$$

with $A(t) = \int_t^T e^{-(\gamma+\gamma_m)t'} dt'$. The atomic output (equation 3.21) only depends on the rising input modes of the light and noise operators. For the relevant

[1] Constants correspond to the ones introduced in chapters 2 and 3

[2] Because of earlier conventions I do not pull the cosine and sine into the mode function. Like before the light modes marked with the indices c or s are cosine and sine modes with the envelope given by f. This is important for normalization.

operator this looks as:

$$\hat{P}_c^{\text{out}} = \sqrt{1-\kappa^2\xi^2}\hat{P}_c^{\text{in}} - \sqrt{1-\epsilon^2}\kappa\xi^2\hat{y}_{c+}^{\text{in}} + \epsilon\kappa\xi\hat{F}_{P+}.$$

To calculate the correlation between the atomic and the light output, the light and noise modes, defined in 8.5 need to be expressed as a linear combination of the rising modes and a mode orthogonal to the rising mode. For this we find $\tilde{f}_{c+}^{\perp}(t) = c \cdot \tilde{f}_*(t) + f_{c+}(t)$ and $\tilde{f}_{+}^{\perp}(t) = d \cdot \tilde{f}_\star(t) + f_{+}(t)$,[3] such that:

$$\int_0^T \tilde{f}_{c+}^{\perp}(t) f_{c+}(t) dt = 0, \int_0^T \tilde{f}_{+}^{\perp}(t) f_{+}(t) dt = 0.$$

Then we end with

$$\hat{y}_{c,m}^{\text{out}} = B \cdot \hat{P}_c^{\text{in}} + \frac{1}{c}(-\hat{y}_{c+}^{\text{in}} + N_{c\perp}\hat{y}_{c\perp}^{\text{in}}) + \frac{1}{d}(-\hat{F}_{P+} + N_{\perp}\hat{F}_{P\perp}), \tag{8.6}$$

where $N_{c\perp} = \sqrt{\frac{1}{2}\int_0^T (\tilde{f}_{c+}^{\perp}(t))^2 dt}$ and $N_{\perp} = \sqrt{\int_0^T (\tilde{f}_{+}^{\perp}(t))^2 dt}$. Now we can evaluate the conditional variance and the noise for different ϵ^2. In figure 8.3 the noise was evaluated for $\epsilon^2 = 0, 0.22, 0.5$ and 0.75 over different interaction durations T for characteristic experimental settings. For simplicity the decay is again modeled to be directed towards the CSS[4]. In the two graphs below, the optimal gain α and mode constants are shown. Without additional decay, the scenario described earlier, with $\gamma_m = \gamma$ is optimal. As soon as there is additional decay, γ_m becomes negative and in the steady state settles at a negative value, smaller than $-\gamma$ leading to a fast growing mode-function. It does seem quite intuitive, that those light measurements nearest in time to the point in time for which we wish to squeeze the atomic state need to be weighted most. This new knowledge about the use of optimal modes makes the conditional squeezing superior to the ones performed before [JKP01] where the achieved entanglement was limited in duration by decay. Besides creating a slightly better squeezing result the refined method also gives the possibility to employ the idea discussed in the end of the previous section, of introducing additional pump beams which will open up for the possibility of achieving a squeezed atomic steady state. In the steady state where noise and J_x are stable, even if the collective atomic noise lies above the entanglement limit, the correlations between outgoing light and atomic state can be used to attempt to squeeze the atomic collective operators. The pump beams will also introduce additional decay towards the CSS and therefore the minimum conditional noise will be higher the more pump light is used.

[3] Again f_+ and f_{c+} are the exponential rising (envelope) mode function, differing by a factor of $\sqrt{2}$ in the normalization, with the time constant γ.

[4] This assumption anticipates either short time scales compared to T_1 or a scenario which will be discussed later where a weak pump and repump laser introduce a decay towards the CSS.

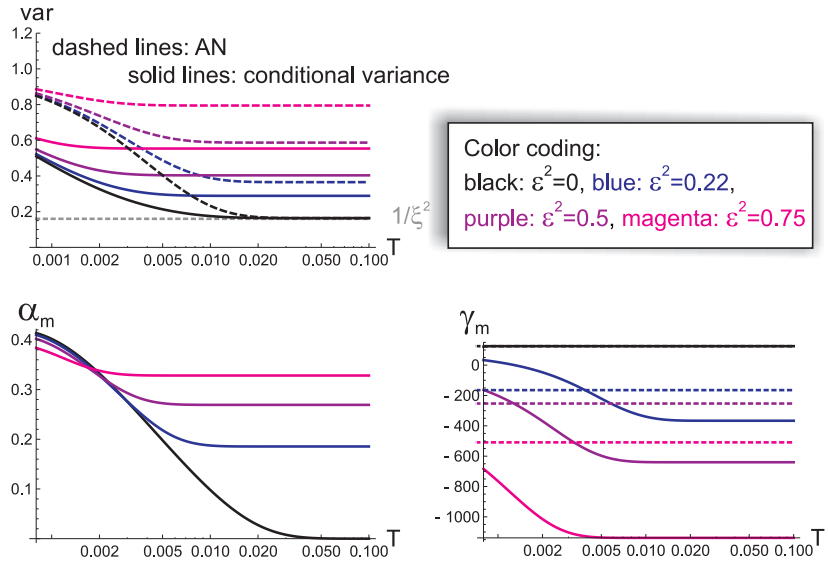

Figure 8.3: In the upper graph the modeled behavior over time for the atomic noise (AN) is shown as the full lines, and the conditional variance as the dashed lines. Below the optimal gain α_m is shown on the left and the optimal mode constant γ_m is depicted together with the respective decay rates $-\gamma$ as the dashed lines. Three different ϵs are assumed, while γ_s was kept constant. All curves have $AN = 1$ for $t = 0$, which can not be seen in the graphs, due to the logarithmic scaling of the x-axis.

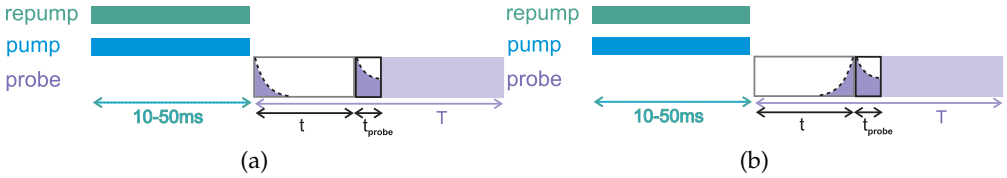

Figure 8.4: Time sequence to optimize squeezing. In (a), the whole preceding light pulse is used to conditionally reduced the atomic variance with a decaying mode function, as optimal in the case of no additional decay. In (b) the same is shown for the optimal case with included decay.

In the experimental realization we measure the conditional variance $\mathcal{C} = \mathrm{Var}(\hat{P}_c^{\mathrm{out}} - \alpha\hat{y}_{c,m}^{\mathrm{out}})$ by sending a second readout pulse through the atoms. Then we evaluate $L_{\mathcal{C}} = \mathrm{Var}(\hat{y}_c^{\mathrm{out},2} - \alpha\hat{y}_{c,m}^{\mathrm{out}})$ where for the second pulse we need to use an exponential falling mode function with $\gamma_m = \gamma$. Then, by using the usual noise reconstruction we extract $\mathcal{C}$ from $L_{\mathcal{C}}$, corresponding how we usually reconstruct the atomic noise AN from $\mathrm{Var}(\hat{y}_c^{\mathrm{out},2})$. A measurement time sequence is depicted in figure 8.4b

8.3 Experimental realization

The experimental setup corresponds to the sketch in figure 2.8. The outgoing light is measured via a $\hat{S}_y$ measurement. Measurements of different temporal modes of $\hat{S}_y$ are used on the one hand to conditionally squeeze the atomic state and on the other hand to evaluate the atomic noise as will be discussed in the following.

8.3.1 Data acquisition and analysis

In all the previously described measurements, we recorded two values for every measurement pulse with duration T - the outcome of the measurement of $\int_0^T f(t)\cos(\Omega t)\hat{S}_y(t)dt$ and the orthogonal $\int_0^T f(t)\sin(\Omega t)\hat{S}_y(t)dt$. For the experiment discussed here, it is crucial to use very long probe pulses and then evaluate different parts of the pulse with suitable mode functions $f(t)$. At the same time it should be possible to chose the mode function after the measurement is done. It would be possible to register more points, let us say one every 100μs over a period of 20-200ms. To evaluate variances one usually needs to repeat a measurement 10.000 times. When many different experimental situations are realized with long pulses this will sum up to a lot of measurement points. Therefore, instead the covariance matrix over the measurement pulse for N_{rep} many repetitions is stored. In practise $\langle x(t_i)x(t_j)\rangle$ is recorded where x is the measurement variable, so for example $\hat{S}_{y,c}$ and $t_i = i\cdot\Delta t$ with Δt being the step size, often chosen to be $80-200\mu$s. This gives a matrix with the dimensions $n\times n$ where $n = T/\Delta t$. Also the mean values $\langle x(t_i)\rangle$ are put on file and collected in the vector $\bar{x}$. The covariance matrix $\bar{x}\bar{x}$ can then be calculated from those two measurement sets. The elements are given by $\bar{x}\bar{x}_{i,j} = \langle x(t_i)x(t_j)\rangle - \langle x(t_i)\rangle\langle x(t_j)\rangle$.

In figure 8.4 a long measurement pulse is shown and a certain section, starting with $t = k\Delta T$, with a duration of $t_{\text{probe}} = m\Delta T$ is indicated. For this section the mean value and the variance can now easily be calculated.
We construct a mode function vector u which has elements $u_i = 0$ for $i < k, i > k+m$ and $u_i = 1/N_u\cdot f((i-k)\Delta t)$ for all other. Now the variance and mean value of the measured $\hat{x}$ in this section is:

$$\sigma^2(x)_{t,T_0} = u^*\cdot\bar{x}\bar{x}\cdot u, \qquad \langle x\rangle_{t,T_0} = u^*\bar{x}. \tag{8.7}$$

When we evaluate the conditional variance, we split the pulse in different sections as shown in figure 8.4*b* and choose two mode functions for the first and second section. The first pulse is then used to try to squeeze the atomic state and should have an exponentially growing mode-function $f_1(t)$ with an optimal rate γ_1, while the second pulse which is used to do atomic state re-

construction needs to be evaluated with an exponentially falling mode with rate $\gamma = \frac{1}{T_2}$. The size of interest is $\mathrm{Var}(\hat{y}^{\mathrm{out}}_{c-}|_t^{t+t_{\mathrm{probe}}} - \alpha\hat{y}^{\mathrm{out}}_{c,m}|_0^t)$, to reconstruct $\mathrm{Var}(\hat{P}^{\mathrm{out}}_{c(s)}(t) - \alpha\hat{y}^{\mathrm{out}}_{c(s),m}|_0^t)$. For this we need to assume that the light contribution in the two pulses are uncorrelated, so we leave out a small slice in between the pulses to avoid correlations due to the finite bandwidth of measurement. The two mode vectors are given by $\mathbf{u}_1$ with $u_{1i} = f_1(i\Delta t)$ for $i\Delta t < t$ and otherwise $u_{1i} = 0$, and $\mathbf{u}_2$ defined as above. Then

$$\begin{aligned}
\sigma^2(x|_t^{T_e} - \alpha x|_0^t) &= u_2{}^* \cdot \bar{xx} \cdot u_2 + \alpha^2 u_1{}^* \cdot \bar{xx} \cdot u_1 - \alpha(u_2{}^* \cdot \bar{xx} \cdot u_1 + u_1{}^* \cdot \bar{xx} \cdot u_2), \\
\sigma^2(x|_t^{T_e} - \alpha x|_0^t)_{opt} &= u_2{}^* \cdot \bar{xx} \cdot u_2 - \frac{1}{4}\frac{(u_2{}^* \cdot \bar{xx} \cdot u_1 + u_1{}^* \cdot \bar{xx} \cdot u_2)}{u_1{}^* \cdot \bar{xx} \cdot u_1},
\end{aligned}$$

where the conditional variance was optimized for α in the last line. To avoid using the same data to find α, one can make a reference measurement beforehand to extract the optimal feedback gain.

In figure 8.5 two density plots for recorded $\bar{xx}$ matrices are shown. The graph 8.5a represents a light measurement, i.e. the atomic Larmor frequency is shifted outside the detection bandwidth by an additional magnetic field. In this case there should be only contributions on the diagonal of the matrix, as there ought not to be correlations between an earlier and later time. This is almost true and the small contributions in the first off diagonal matrix elements can be explained by the finite bandwidth of our measurement. The power spectrum of the measurement is shown in figure 8.5c.
In figure 8.5b $\bar{xx}$ for an atomic measurement is shown. There are clearly more correlations visible, as was to be expected, since the atomic signal on the read out prevails for some time. The fact, that there is a decay in the correlations tells us, that the atomic state decays. Also the variance decays over time. This is mainly due to the decay of the macroscopic spin, but also to a reduced variance compared to the macroscopic spin. The shown graph actually starts about 40% above the projection noise, since this way the reduction becomes clearer visible. The spectrum for the atomic measurement shows a well defined narrow peak, coming from the rotating atomic spins, as well as the broad light background. The recorded signal is demodulated at 322kHz. The signal at frequency 0 in the graphs corresponds therefore to the component of the measurement that rotates at the Larmor precession frequency. The small contribution at this frequency in the light spectrum can be attributed to a DC offset in the electronics of the system, after the demodulation of the signal.

8.3.2 Calibration measurements

The effect on the initial noise due to dissipation effects which we wish to observe here is small, compared to observations in previous experiments. Specific

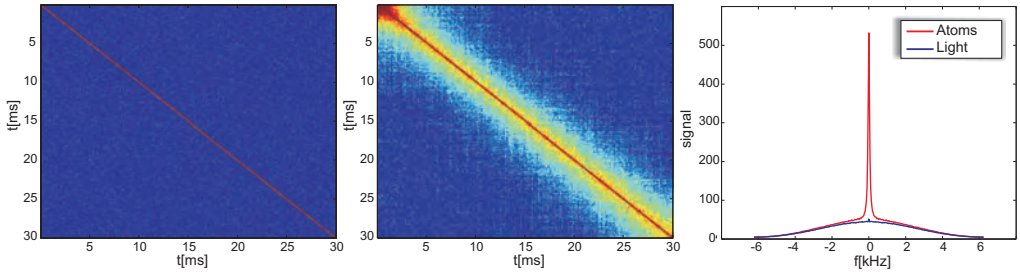

(a) (b) (c)

Figure 8.5: In (a) the correlation matrix from a pure light measurement is depicted. No correlations between earlier and later measurements are seen, except for small correlations due to the finite measurement bandwidth. In (b) the atomic state is measured via the light and thus correlations can be seen. In (c)the power spectra for both those measurements are shown. The light measurement displays a broad peak, showing the bandwidth of our measurement setup. The atomic signal is confined in a much narrower bandwidth.

care was therefore taken in the course of those measurements to verify that the atomic state was projection noise limited. The coupling constant κ^2 was measured by mean value transfer in the days, or weeks surrounding the single measurement set. So was the atomic noise. The atomic noise (AN) was measured in reference measurements with 1ms pulses, so the pulsed κ^2 measurements could be used. Thus the input noise was established. For long measurement pulses, we used this input atomic noise, to determine κ^2 (or the swap rate γ_s) of the first points from the initial noise. This means that our usual process of determining AN with a noise measurement, when we know κ^2 is reversed. Now we know AN, and then determine κ^2 and thus γ_s. From this we can extrapolate κ^2 throughout the whole measurement, as we know that γ_s scales with the macroscopic spin, while the other decay constants remain constant. Therefore we can evaluate the noise, compared to the CSS, for all t until $T - t_{\text{probe}}$. Of course the assumptions for our reconstruction have to be met, like a sufficiently high orientation. The orientation was therefore tested for different scenarios.

In figure 8.6a the orientation was tested after different pulse durations of the probe. The orientation keeps high which justifies the use of our model. In figure 8.6b the measured orientation was transferred into the excess atomic noise that arises from atoms in $m = 3$. Clearly the decrease of the orientation is counteracting the squeezing procedure.

Another problem to consider is the growing number of atoms in the $F = 3$ ground state. The Faraday rotation, which is used for the characterization of the size of J_x therefore needs to be compensated. This is easily done as discussed in appendix D, but one needs to assume a certain orientation of the atoms in $F = 3$. If one considers $o_{F=3} = 1$ we get the lowest possible J_x, which will

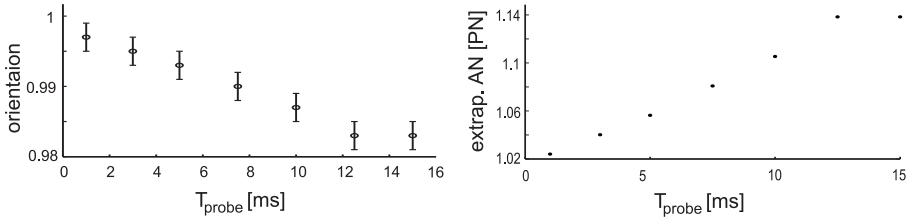

(a) (b)

Figure 8.6: In (a) the orientation of atoms in $F = 4$ was tested with help of the pulsed MORS technique after different probe durations. In (b) the measured orientation was transferred into the normalized atomic noise, taking only $m = 4$ and $m = 3$ into account.

give us a worst case scenario for the normalized spin-noise. In very specific situations, when there is no laser resonant with any transition starting in $F = 3$, the steady state orientation of the $F = 3$ atoms can be estimated with help of a MORS signal. A signal like this for the case of probe and a small pump beam on is shown in figure 4.8. It is much more difficult to think about ways to extract the noise which the atoms in the $F = 3$ ground state are contributing to the measurement. Presumably it is small in all situations which will be considered compared to the noise component arising from atoms in $F = 4$. The coupling to the light falls of with $1/\Delta^2$ and it will be additionally suppressed by the frequency difference in the Larmor precession and our final bandwidth. We ignore this noise contribution for now.

8.3.3 Noise measurements

We wish to evaluate the behavior of atomic noise over time. In figure 8.7 the measured evolution of the mean of the variances of P_c and P_s is shown for different atom numbers in units of projection noise (PN). The probe power was set to 5mW. The entanglement limit then reads:

$$\frac{1}{2}(\mathrm{Var}(\hat{P}_c) + \mathrm{Var}(\hat{P}_s)) = \frac{1}{4}(\mathrm{Var}(\hat{p}_1 + \hat{p}_2) + \mathrm{Var}(\hat{x}_1 - \hat{x}_2)) = \frac{1}{8\langle J_x\rangle}(\mathrm{Var}(\hat{J}_{z1} + \hat{J}_{z2}) + \mathrm{Var}(\hat{J}_{y1} + \hat{J}_{y2})) < \frac{1}{2}. \quad (8.8)$$

The black line in figure 8.7, indicates the limit of entanglement between the two samples[5]. The uncertainty of the measured noise level is 4%, mainly arising from uncertainty of κ^2, the shot noise of light and η.

The number of atoms was increased by heating the cell with a warm airflow. The number of atoms was varied from $2 \cdot 3.4 \cdot 10^{11}$ to $2 \cdot 5.9 \cdot 10^{11}$ and $2 \cdot 1.1 \cdot$

[5] $\frac{1}{2}$ is one unit of PN in equation 8.8

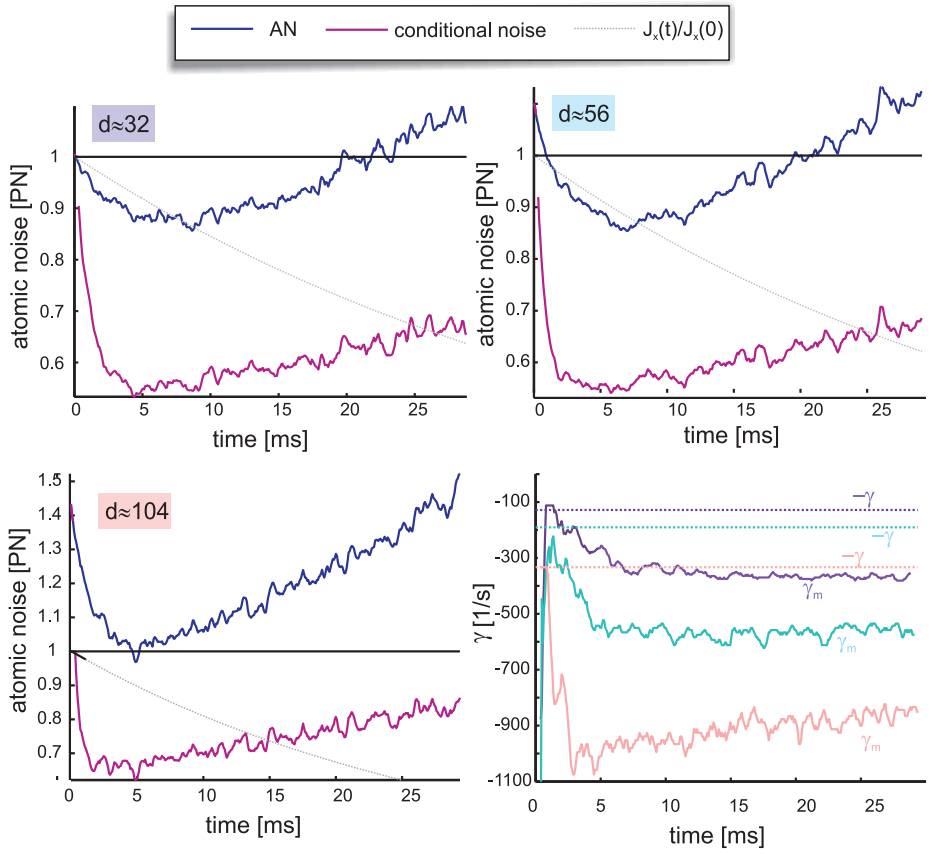

Figure 8.7: Time evolution of atomic noise. The two upper graphs and the one in the bottom left corner show the behavior of the atomic noise over time for different numbers of atoms. The dark blue lines show the reconstructed atomic noise and the gray lines show the decay of the mean spin which was calculated from the measured Faraday rotation in x-direction including a compensation for atoms in $F = 3$, this compensation lies maximally at around 5%. The coupling constant κ and the ϵ^2 are calculated from the mean of the initial points, for which the atomic noise is known, because it has been measured in an independent set of measurements. The behavior of κ^2 can then be extrapolated, since we know that γ_s depends linearly on J_x. The magenta lines show the conditional noise calculate with optimal mode constant γ_m and feedback α. The uncertainty on the input noise is 4%, mainly arising from uncertainty of κ, the shot noise of light and η.
In the lower right the determined optimal mode constants γ_m are shown together with $-\gamma$ for all three settings (color coded as shown in the legends). The behavior looks similar to the modeled graphs in 8.1 and 8.5.

10^{12}, corresponding to optical depths on resonance of approximately 32, 56 and 104. In all three graphs, the atomic noise reaches a minimum and then starts growing again. The reason is the decay of the macroscopic spin displayed in gray which leads to an orientation lower than one in $F = 4$. Unoriented states yield higher normalized noise. At the same time γ_s decreases with J_x, making the process driving the collective state into entanglement slower and slower.

Though the relative noise reduction is bigger for the higher optical depths, as was expected, the absolute reached minimum noise is similar for the first two graphs and higher for the highest optical depth. This is due to the fact that the initial noise grows the more we heat. To a certain extent this can be explained by the classical noise on the atoms growing quadratically with the number of atoms. However, additionally we experience an onset of an extremely high additional noise contribution, starting from a certain number of atoms. In most experiment, we keep therefore to room temperature or a slightly warmer setting with around twice the number of atoms.

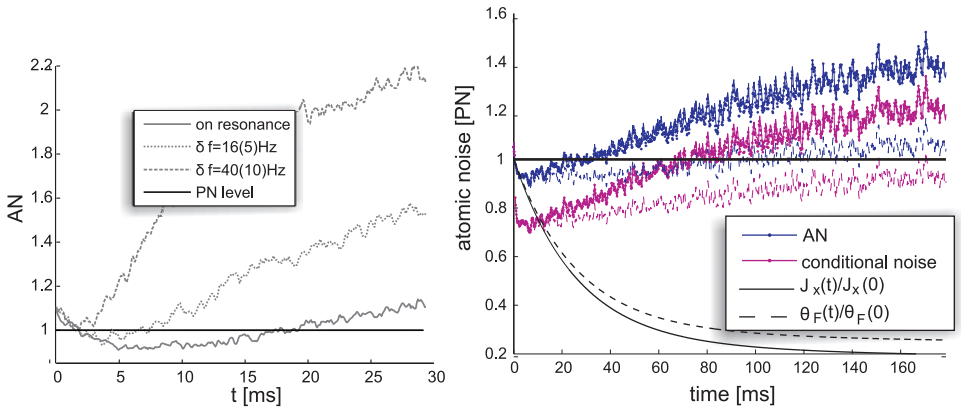

(a) (b)

Figure 8.8: In (a) the magnetic field in the two cells was changed such that the atomic spins precessed with Larmor frequencies differing by δf_L. In (b) an additional pump laser on the D_1 line is applied during the probing. The circular polarized beam was directed along the x-axis like our usual pump beam, the pump power lay at around 100μW and the induced decay is around $1/10ms$. The solid lines are the behavior of the noise, when the behavior of J_x was calculated, assuming the orientation in $F = 3$ was 1. The dashed lines show the behavior, if there was no correction from the atoms in $F = 3$ - so for an assumed orientation of 0

.

Detuned Larmor precession

The sensitivity of the process to optimal calibration is illustrated by the measurement shown in figure 8.8a. In this measurement series, the magnetic fields of the two cells were slightly changed, such that the Larmor precession of the spins had frequencies differing by δf_L. The photons emitted in the two cells become thus distinguishable and the entanglement without feedback vanishes after shorter timescales.

Additional pump field

In the shown experiments, one of the major problems, was the growing noise, due to decaying atomic orientation. To avoid this, a weak pump beam was used simultaneously with the probe beam. The power of this pump beam can be optimized and one will get a trade off between achieved orientation and added decoherence which leads to a shallower dip in noise. The drawback of this approach is an even faster decay of the macroscopic spin due to spontaneous emission in the presence of the pump beam into $F = 3$. In figure 8.8b such a measurement is shown for 180ms. The decay of the macroscopic spin is substantial so that J_x in $F = 4$ can no longer be assumed to be proportional to the Faraday rotation angle θ. Thus the compensation due to atoms in $F = 3$ is taken into account with an orientation of the $F = 3$ ground state $o_3 = 1$. This leads to the maximal possible correction, compared to the case if we would ignore the atoms in $F = 3$. To illustrate the effect, I show the noise curve for $o_3 = 0$ (no correction) and $o_3 = 1$ (maximal correction). The latter is definitely closer to the actual situation, but the lifetime of entanglement is probably a little longer than the thus estimated 40ms. Since collisions and scattering into other m levels will bring about an $o_3 < 1$. In as similar measurement scenario the orientation of $F = 3$ was measured via MORS to be $o_3 \approx 0.9$. The fact that the AN rises above the projection noise level indicates that the decay is not only directed towards the CSS. Additionally the big number of atoms in $F = 3$ might contribute noise for longer times.

Steady state with probe, pump- and repump-field

The decay of the mean spin can be counteracted by adding a weak repump laser. In [7] and [MPC10] theoretical predictions for this scenario are shown for different optical depths, showing that one can reach an entangled steady state, without additional measurement. However, in the experiment we have not observed this. One reason is the limited optical depth we can achieve and another the fact that we can not apply bigger amounts of repump compared to the pump power without adding noise. The reason for the latter might be a small polarization pollution in the pump and repump beam which shuffles too many atoms in states other than $m = 4$.

However, adding the measurement and looking at the conditional variance, we can produce a steady state, in which the conditional noise is still below the entanglement limit. In figure 8.9b a measurement with a probe of 8mW, and a pump and repump beam with around 150μW and 300μW respectively is shown. The normalized noise stabilizes quickly. The final J_x^{steady} is 0.95 of the maximal $J_x = 4N_a$. The points, which can be seen on the upper end of the time scale arise from a pure steady state measurement. For this, we simply

leave all lasers on DC and, after the steady state is reached, average the noise over around one hour. We looked at 10 ms time slices and for the conditional variance we used at least 3ms of measurement. The observed conditional noise lies at 0.80(4) PN units.
The noise level reached should not depend on the value of the input noise, if this level is higher due to different preparation. In figure 8.9 there are therefore two measurement curves for different starting conditions. A state with higher input noise was created by turning off all pump fields for 150ms, this way a poor orientation is reached, leading to a lower mean spin and to a higher normalized noise. The input noise can be calibrated in an independent calibration sequence where the same pulse sequence as shown in the figure was used, but a 1ms calibration pulse preceded the long pulse, so that our usual calibrations for the atomic noise reconstruction could be used. The calibration of the state with low orientation is not as accurate as our usual reconstruction, due to the fact that the model relies on high orientation. That being said, I want to stress, that the precise initial noise value is not of much interest - the important conclusion from this measurement is, that the final state is independent of the input state.

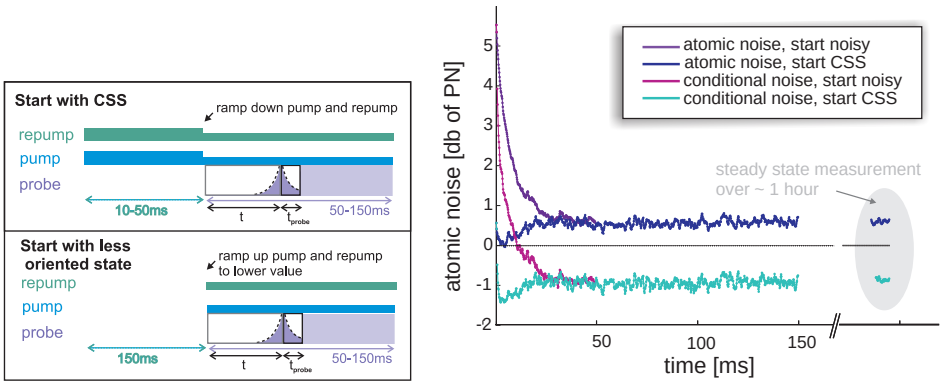

(a) (b)

Figure 8.9: In (a) the pulse sequence for the measurement starting at the CSS and for the measurement starting at a state with lower orientation are shown. To achieve a lower orientation, we wait around 150ms, which is of the order of T_1 in the dark. In (b) the noise evolution for both starting conditions is show. The reached noise level is very similar. The points to the far right are extracted from a measurement where all beams were DC and the noise was averaged over around 1 hour. The power of the laser beams were 8mW for the probe laser, around 150μW for the pump and 300μW for the repump laser.

8.4 Conclusion and outlook

In this chapter I reported on the generation of steady state entanglement of two atomic systems. While without the additional light measurement, the atoms

reach only a quasi steady state with long entanglement durations, adding the measurement leaves the two systems in a conditionally entangled state. In most relevant uses of entanglement, the additional information needed, can be distributed by classical means. If a protocol requires unconditional entanglement, feedback can be added to the protocol in two fashions. One possibility is to feed back the measurement outcomes continually or one can wait until the entanglement is needed and one can apply a short RF pulse. The latter has the advantage that the outgoing noise will be the same as the conditional noise presented in the section above [SJP07]. The optimal gain and mode function can be applied in the same fashion. However, it creates a time delay of at least the feedback duration of around $100\mu s$. The continuous feedback option has not been treated here, and it needs to be analyzed carefully, what the outcome would be. However, the conditional noise is not very sensitive to the choice of the mode constant, as long as one uses a function weighting later times more. Since the atomic state is decaying and with this also the contribution of earlier feed back, the outcome will probably be similar to the conditional noise.

Chapter 9

More experiments with the light atom interface

This chapter is intended to give an overview over other experiments conducted in the setup, during the duration of my PhD which I was less involved in. I will only briefly review these observations and give references for further information. The experiments were first reported in [5, 8, 9] and additional references are [11, 12, 13].

9.1 Narrow band two mode light squeezing

In several places I mentioned the possibility of using the squeeze and swap Hamiltonian to produce squeezed light. To be more precise, the interaction gives the possibility to produce two mode squeezed light in a very narrow bandwidth around the Larmor frequency of the atoms. In [5] the realization of this experiment with an achieved squeezing of light of -3.5(1)dB of a single temporal mode is reported. The experimental setup is almost equivalent to the experiment reported in chapter 8. The most important difference in the setup is that since the $\hat{q}$ quadrature of light is squeezed, the detection system has to be changed slightly. For this a $\hat{S}_z$ measurement is realized by adding a quarter wave plate.

9.2 Memory for squeezed states

The basic principle of a quantum memory protocol is the transfer of the canonical quantum variables of light to the corresponding atomic ones. We know from

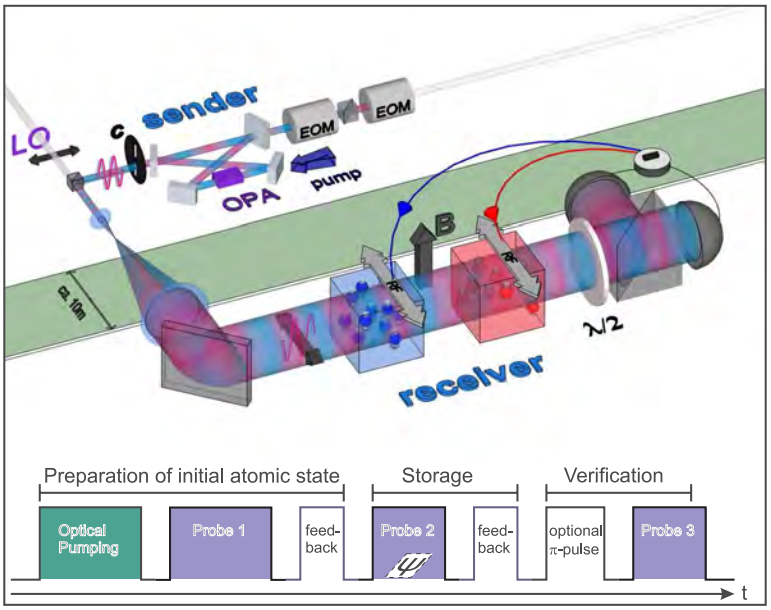

Figure 9.1: Two-mode entangled (squeezed) light is generated by an optical parametric amplifier (OPA). A variable displacement of the state is achieved by injecting a coherent input into the OPA which is displaced with help of electro-optical modulators (EOM). The output of the OPA is shaped by a chopper, and combined on a polarizing beam-splitter with the local oscillator (LO) beam, such that the squeezed light is only on during the second probe pulse. A beam shaper and a telescope create an expanded flat-top intensity profile. The light is then send to the memory consisting of two oppositely oriented ensembles and the homodyne detection system. The detector signal is processed electronically and used as feedback onto the spins via RF magnetic field pulses. Below, the pulse sequence is shown. After preparing the squeezed spins state, the actual storage takes place, followed by a verification pulse.

the input-output equations 3.10 and 3.12, that if we could achieve the long interaction time regime, the underlying interaction would swap the states of the two systems. However, as this is not possible for our experimental realization due to decoherence, a trick is applied to achieve the desired state transfer; the $\hat{y}_{c,s}$ of the outgoing light are measured and the measured results are fed back to the atoms. Let us assume a coupling constant $\kappa = 1$ and a feedback gain, which is also 1. The collective atomic operators are then left as:

$$\hat{P}_{c,s}^{fin} = -\hat{y}_{c,s}^{\text{in}}, \quad \hat{X}_{c,s}^{fin} = \sqrt{1-\xi^2}\hat{X}_{c,s}^{\text{in}} + \hat{q}_{c,s}^{\text{in}} \tag{9.1}$$

Clearly the input light state is mapped onto the atoms with some additional noise, coming from the atomic $\hat{X}$ operators. A memory based on a similar protocol was conducted for coherent states [JSC+04] in the setup exceeding the achievable fidelity for any classical memory. The next obvious step was to map non classical states, like squeezed light states. A squeezed light source [SSP02] was used to produce displaced squeezed states, which were mapped onto the

atoms. The setup is shown in figure 9.1 and described briefly in the caption and in more detail in [9].

The experiment was refined by employing an additional probe pulse after the preparation of the atomic CSS to reduce the input noise of $\hat{X}_{c,s}$. The achieved squeezing was approximately -14%. The initial light state was squeezed by 6dB.

To evaluate the performance the fidelity of certain sets of input states was calculated and compared to a classical benchmark that is also presented in [9]. The classical benchmark was beaten for a certain input set with a square displacement range with a maximum displacement of 3.8 and two possible squeezing phases.

9.3 Magnetometry

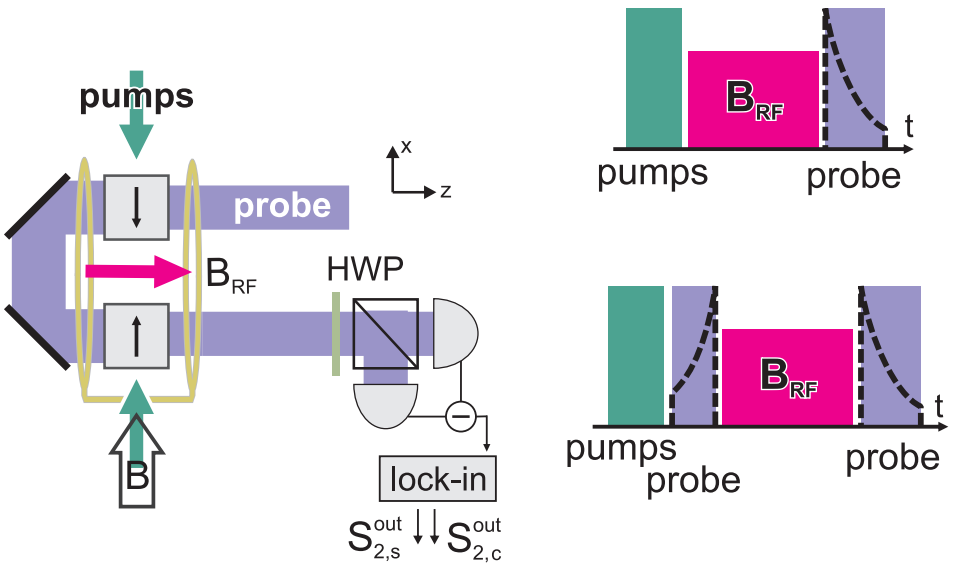

(a) (b)

Figure 9.2: (a) The experimental setup is similar to the usual settings. A pulse of B_{RF} at the frequency Ω is applied orthogonally to the B field, such that the created displacement in the spin lies in the same direction for both cells. (b) The pulse sequence for projection noise limited magnetometry is also similar to previous experiments. The temporal mode function for the probe is indicated as the dashed black curve. The lower pulse sequence shows the scenario including the temporal modes for entanglement-assisted magnetometry.

A completely different application of the oriented atomic ensembles is the measurement of small magnetic RF fields. The projection noise limited performance of the light measurement of the atomic spin is an excellent tool for measure-

ments of small displacements of the rotating spin operators. The displacement of the rotating spins by a magnetic field on resonance with the Larmor frequency grows linearly with the number of atoms. When varying the exposure duration of the atoms to the RF field, the maximal created displacement is limited by the decoherence time of the spins. Therefore the light fields are turned off during the RF pulse, so that the T_2 time is maximal. This is one of the reasons that the magnetometry experiment reported in [8] achieves a similar sensitivity as the state of the art magnetometries, even though two orders of magnitude less atoms are used. The optimal achieved sensitivity was $B_{RF}\sqrt{T} \cdot SNR = 4.2(8) \cdot 10^{-16} Tesla/\sqrt{Hz}$ for the exposure time of $T = 22ms$. The signal to noise ratio (SNR) was optimized by varying probe power and atom number, as well as optimizing the mode function of the measurement. The optimal SNR can be reached with $\gamma_m \approx 2\gamma$, which maximizes the atomic signal compared to other noise sources as input light noise and noise arising from the decay. The light noise was suppressed considerably due to a high coupling constant, such that the measured sensitivity is close to be PN limited. Ignoring the preparation time the value lies 30% above the PN limit. The additional noise arises due to the decay of the spin and the residual light noise.

In principle it should be possible to improve the sensitivity by venturing away from the CSS and towards squeezed atomic spins. The drawback is that due to the short lifetimes of the squeezing compared to the optimal exposure time, the optimal setting can not be improved in such a way. However, it is possible to improve the measurement performance for shorter RF-pulses or larger bandwidths. An additional probe pulse was used to conditionally squeeze the atomic input operators prior to the exposure to the RF field. In figure 9.3 a measurement series of the atomic noise and the SNR is shown, both for the original scenario and where initial squeezing was used. An improvement of around 15% in the SNR can be seen for short pulses.

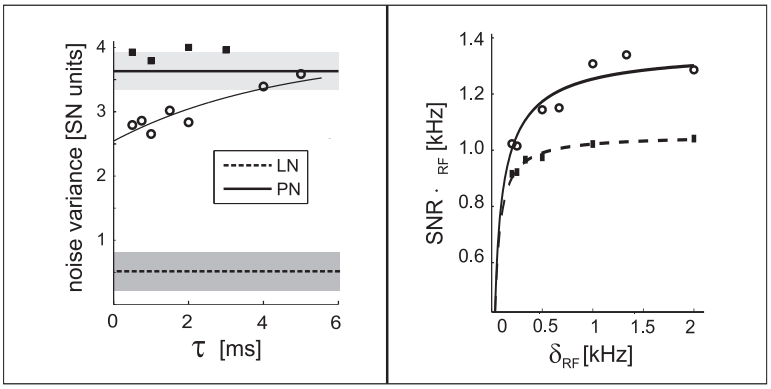

Figure 9.3: On the left the atomic noise in units of shot noise of light is shown for different durations of the RF pulse. The dashed line at 0.5 is the contribution of the probe light noise(LN). The average noise level of the initial spin state (squares) is 1.10(8) in projection noise (PN) units. The PN level is shown as the solid horizontal line. Grey bands have the width equal to twice the standard deviation. The noise for the entangled state vs. the delay between the two probe pulses is shown as circles. The fit yields an entanglement lifetime of 4ms. The $B_{RF} = 36$ fT pulse is applied to $N_a = 3.6(3) \cdot 10^{11}$ atoms. The duration of the first/second probe pulse is 2/3ms, the duration of the pumping pulse 6ms. On the right the SNRs times the RF bandwidth (inverse pulse duration) of the magnetometer for the entanglement assisted magnetometer (circles) and in the absence (squares) of the entanglement are shown.

Chapter 10

Conclusion and outlook

The room temperature Cesium cell experiment which is the focus of this thesis has been an extremely versatile tool for the implementation of interesting quantum mechanics experiments and protocols which show the possibility of the realization of certain quantum communication building blocks. Entanglement between separate atomic systems [JKP01], [7] in the single atoms of the ensemble [2], between light and atoms [1] and between two light modes [5] have been generated with similar setups, albeit partly with very different approaches. Quantum communication protocols like memory [JSC+04], [9] and teleportation [1] have been conducted successfully. Besides giving a detailed description on three of the mentioned experiments, in this thesis I tried to detail the theoretical background of the experiment, with an emphasis on a recently developed refined understanding of the interaction. One focus were the temporal modes and their importance for the correct analysis of the atomic states, when venturing into a stronger coupling regime. Even though more involved than the formerly used QND presentation, the new description holds the possibility, not only to describe the system more correctly, but also to improve some of our old methods. The entanglement generation by measurement was extended such that the inclusion of mode shapes into the measurement scheme gave us the possibility to achieve a steady state entanglement.

There are many proposals for experiments, which could be realized in the current setup. The quantum cloning of a light state onto the atoms [FCP04] is one of those proposals. Also several protocols, where the light should transverse the ensembles several times from different directions, enabling a memory that includes a possibility for state retrieval were suggested for two cells [SSF+06] and one cell [MHPC06]. Also multipartite entanglement (cluster states) can be generated with this kind of setup including two - or several atomic ensembles either by letting the light pass sequentially through several ensembles [SRP+09]

or by letting one memory unit (two ensembles) consecutively interact with several squeezed light states (theoretical work in progress).

One of the most intriguing protocols which remains to be realized in the current setting is the teleportation of a state from one atomic ensemble to another. Different approaches can be taken to realize atomic teleportation, including either three or two atomic ensembles, but I would like to highlight a specific one here in the following. The layout of the possible teleportation experiment is sketched in figure 10.1. The main difference, compared to all other two cell experiments is that the macroscopic spins of both cells are oriented in the same direction. The teleportation protocol can be realized as follows. The first atomic ensemble at Bob's site gets entangled with the light that is passing through. Then one makes a combined measurement of the light and the second ensemble bearing the input state at Alice's site by directing the light through the second cell and conducting a measurement on the light afterwards. The measurement outcomes are communicated to Bob, who makes a feedback to the atoms accordingly. The protocol has been analyzed theoretically for the input-output equations stated in chapter 2 from which the possibility to perform this protocol with a fidelity better than classically possible is deduced [She06]. However, the scenario, where the protocol could be realized successfully is for rather high coupling constants $\kappa > 1$. Therefore it is essential, that the protocol is analyzed with the knowledge gained in chapter 3 which is a current work in progress.

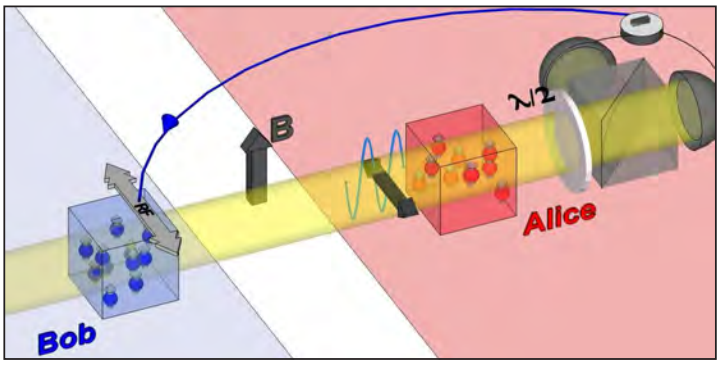

Figure 10.1: Schematic drawing of possible atomic teleportation setup. The two atomic ensembles are oriented in the same direction.

Let me now turn to a completely different course for future experiments. Miniaturizing the room-temperature Cesium cell experiment could provide the opportunity of a complete new set of experiments [LKM+04, BUB+10]. Currently, all experiments that we are able to incorporate are limited to Gaussian quantum states. This seems a strange limitation, as experiments like mapping and teleportation of a light state onto the atomic ensembles should give us the

possibility to transfer other light states as single photons [NNNT+07] or even Schrödinger kitten states [NNNH+06] to atoms. However, those experiments produce light states with bandwidths of around 10MHz which is unsuitable for the interaction times of milliseconds that we need to achieve suitable coupling. The density of atoms can not be increased much by heating due to the properties of the paraffin coating, and a higher optical power leaves us with technical difficulties in the detection as well as problems with growing classical noise. Shorter interaction times present us with another problem, as it is very important for us that the atoms cross the beam several times in the interaction time, because the transfer protocols rely on an averaged spatial atomic mode. The latter problem can easily be resolved by scaling down the cell parameters. As the coupling constant scales in the same fashion with time as with the inverse cross section, the pulse duration can be reduced retaining the coupling constant and the number of wall collisions per atom per pulse.

Instead of mapping a non Gaussian state with a low fidelity protocol onto the atoms, one can also attempt to produce a single excitation state directly in the atoms. This can be done by integrating single photon detection in the polarization mode orthogonal to the drive field (see figure 10.2). Conditioned on a measurement event, a single excitation distributed over the whole atomic ensemble would be reached. With the number of photons, currently used such an approach is unfeasible due to limitations in filtering. But as argued before, a reduced area will allow us to use a reduced duration and light power and thus filtering is getting closer to realizability. To enable additional filtering possibilities, the magnetic field can be increased such that the emitted photon becomes distinguishable in frequency from the drive field. In figure 10.2 a possible setup is sketched, allowing for single photon detection and homodyning. This way an atomic state reconstruction, similar to the ones utilized in chapter 7 can be implied.
To decrease the needed number of photons even more, we would like to integrate the cells inside a low finesse cavity. The light atom coupling can thus be enhanced by the finesse of the cavity.

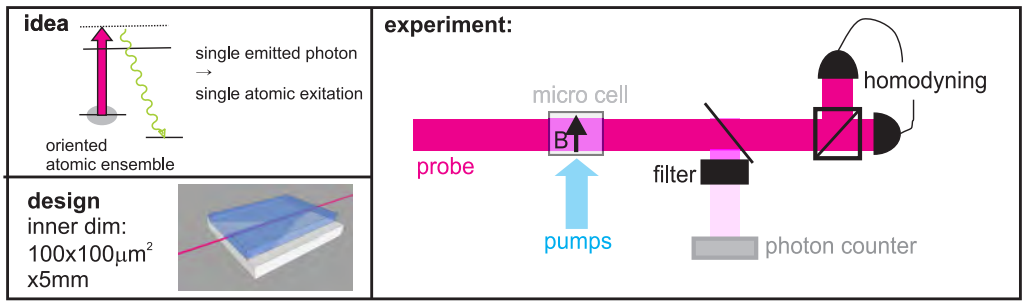

Figure 10.2: Simple idea for an experiment with a micro cell, generating one atomic excitation and being able to make a full state tomography.

In conclusion, there is a whole range of interesting possibilities to explore. Especially an improved, miniaturized setup with future possibilities of integrating the whole setup into a fiber system seems like a route worth investigating, with the perspective of several coupled micro cells on the path to a quantum network.

Part IV

Appendix

Appendix A

Linearization

One can calculate the Heisenberg equations of motion for the spins and the Stokes operators for the full Hamiltonian given in equation 2.18. In [Jul03], those equations are states, and I repeat them here with some minor corrections:

$$\begin{aligned}
\frac{\partial}{\partial t}\hat{J}_x(z,t) &= \frac{\gamma}{8A\Delta}\frac{\lambda^2}{2\pi}\{a_1\hat{S}_z J_y\} && \text{(A.1)}\\
&+ a_2\{2\hat{S}_y[J_x J_z + J_z J_x] - (2\hat{S}_x - \hat{\phi})[J_z J_y + J_y J_z]\},\\
\frac{\partial}{\partial t}\hat{J}_y(z,t) &= \frac{\gamma}{8A\Delta}\frac{\lambda^2}{2\pi}\{-a_1\hat{S}_z\hat{J}_x\}\\
&+ a_2\{7 - (2\hat{S}_x + \hat{\phi})[\hat{J}_x\hat{J}_z + \hat{J}_z\hat{J}_x] - 2\hat{S}_y[\hat{J}_z\hat{J}_y + \hat{J}_y\hat{J}_z]\}, && \text{(A.2)}\\
\frac{\partial}{\partial t}\hat{J}_z(z,t) &= \frac{\gamma}{8A\Delta}\frac{\lambda^2}{2\pi}a_2\{4\hat{S}_x[\hat{J}_x\hat{J}_y + \hat{J}_y\hat{J}_x] - 4\hat{S}_y[\hat{J}_x^2 - \hat{J}_y^2]\}, && \text{(A.3)}
\end{aligned}$$

$$\begin{aligned}
\frac{\partial}{\partial z}\hat{S}_x(z,t) &= \frac{\gamma}{8A\Delta}\frac{\lambda^2}{2\pi}\{a_1\hat{S}_y\hat{J}_z + a_2\cdot 2\hat{S}_z[\hat{J}_x\hat{J}_y + \hat{J}_y\hat{J}_x]\}, && \text{(A.4)}\\
\frac{\partial}{\partial z}\hat{S}_y(z,t) &= \frac{\gamma}{8A\Delta}\frac{\lambda^2}{2\pi}\{-a_1\hat{S}_x\hat{J}_z - a_2\cdot 2\hat{S}_z[\hat{J}_x^2 - \hat{J}_y^2]\}, && \text{(A.5)}\\
\frac{\partial}{\partial z}\hat{S}_z(z,t) &= \frac{\gamma}{8A\Delta}\frac{\lambda^2}{2\pi}a_2\{2\hat{S}_y[\hat{J}_x^2 - \hat{J}_y^2] - 2\hat{S}x[\hat{J}_x\hat{J}_y + \hat{J}_y\hat{J}_x]\}. && \text{(A.6)}
\end{aligned}$$

All stated spin operators have a dependency on position and time. Now we can reexpress the quadratic spin components as discussed in section 3.1, if we

consider a fully oriented spin. We end with the following approximations:

$$\hat{j}_y\hat{j}_x + \hat{j}_x\hat{j}_y \approx \pm 7\hat{j}_y, \tag{A.7}$$
$$\hat{j}_z\hat{j}_x + \hat{j}_x\hat{j}_z \approx \pm 7\hat{j}_z, \tag{A.8}$$
$$\hat{j}_y\hat{j}_z + \hat{j}_z\hat{j}_y \approx 0, \tag{A.9}$$
$$\hat{j}_x^2 - \hat{j}_y^2 \approx 14, \tag{A.10}$$
$$\hat{j}_z^2 \approx \mp\frac{7}{2}\hat{j}_x + 16 \cdot \mathbb{1}. \tag{A.11}$$

After the linearization, we can, by the same arguments as in chapter 3 limit ourselves to the important components and thus we end with the same Heisenberg equations of motion that were also achieved by calculating the equations of motion directly with the approximated Hamiltonian 3.3.

Appendix B

Calculations to inclusion of decay in higher order equations

Following equation 3.20, the time dependance of the atomic $\hat{p}$-operator in the rotating frame is as follows:

$$\dot{\hat{\tilde{p}}}(t) = e^{\gamma t}(-a\hat{q}(0,t)\sin(\Omega t) + a\xi^2\hat{y}(0,t)\cos(\Omega t) + \sqrt{2\gamma_{ex}}\hat{F}_p). \tag{B.1}$$

Here $\hat{\tilde{p}} = pe^{\gamma t}$ and $\hat{F}_p$ is the noise operator belonging to the rotating wave spin. Thus the time dependent rotating spin operator reads:

$$\begin{aligned}\hat{p}(t) = e^{-\gamma t}\hat{p}^{in} &\mp a\int_0^t e^{-\gamma(t-t')}\hat{q}(0,t)\sin(\Omega t)dt'... \\ &+ a\xi^2\int_0^t e^{-\gamma(t-t')}\hat{y}(0,t)\cos(\Omega t)dt' + \sqrt{2\gamma_{ex}}\int_0^t e^{-\gamma(t-t')}\hat{F}_p dt'\end{aligned} \tag{B.2}$$

From this one can directly infer the input-output equations 3.21. Attention needs to be paid, when normalizing the modes, as the integrated noise operator[1] has a normalization factor differing by a factor $\sqrt{2}$ from the cosine and sine modes of light.

Now, the equations for the light operators can be calculated. I do that here for

[1] $\hat{F}_{p,+} = 1/N_F \int_0^T e^{-\gamma(T-t)}\hat{F}_p dt$

$\hat{y}_c$. We use:

$$\begin{aligned}\int_0^T \cos^2(\Omega t)e^{-2\gamma t}(\int_0^t f(t')dt')dt &= \int_0^T f(t')(\int_t^T \cos^2(\Omega t)e^{-2\gamma t})dt' \\ &= \int_0^T \frac{e^{-2\gamma t}-e^{-2\gamma T}}{4\gamma}f(t)dt. \qquad \text{(B.3)}\\ \int_0^T \cos^2(\Omega t)e^{-2\gamma t}dt &\approx \frac{1-e^{-2\gamma T}}{4\gamma}. \qquad \text{(B.4)}\end{aligned}$$

Combining equations 3.5 and B.3 leads to:

$$\begin{aligned}\hat{y}^{\text{out}}_{c,-} = \hat{y}^{\text{in}}_{c,-} + \sqrt{1-\epsilon^2}\frac{\kappa}{\sqrt{2}}\hat{p}^{in} &\mp \frac{1-\epsilon^2}{2\xi^2}(\hat{q}^{\text{in}}_{s,-} - \sqrt{1-\kappa^2\xi^2}\cdot\hat{q}^{\text{in}}_{s,+})... \\ &- \frac{1-\epsilon^2}{2}(\hat{y}^{\text{in}}_{c,-} - \sqrt{1-\kappa^2\xi^2}\cdot\hat{y}^{\text{in}}_{c,+})... \\ &+ \frac{\epsilon\sqrt{1-\epsilon^2}}{\sqrt{2}\xi}(\hat{F}^{\text{in}}_{p,-} - \sqrt{1-\kappa^2\xi^2}\cdot\hat{F}^{\text{in}}_{p,+}).\end{aligned} \qquad \text{(B.5)}$$

For two cells we arrive at equation 3.23 where the second term, including the $\hat{q}_i$s, drops out. The exponentially decaying and rising modes are not orthogonal. To analyze the noise of the light, to do a reconstruction of the atomic noise, we need to express the input-output relations of the light operators with a set of orthogonal modes. We calculate, the mode function that is orthogonal to the exponentially rising mode $u_+(t) = \frac{1}{N}e^{-\gamma(T-t)}$with $N = \sqrt{\frac{1-e^{-\gamma T}}{2\gamma}}$over the interaction time: $\int_0^T u_+(t)\cdot u_+^{\perp}(t)dt = 0$. Then we get:

$$\begin{aligned}u_+^{\perp}(t) &= \tfrac{1}{N_\perp}(u_+(t) - \frac{\sinh(\gamma T)}{\gamma T}u_-(t)), \qquad \text{(B.6)}\\ \text{with } N_\perp &= \frac{\sqrt{\cosh(2\gamma T)-1-2\gamma^2T^2}}{\sqrt{2}\gamma T}\end{aligned}$$

We can express the falling mode as a linear combination of $u_+(t)$ and $u_+^{\perp}(t)$, to end with equations that only feature independent operators:

$$u_-(t) = \frac{\gamma T}{\sinh(\gamma T)}u_+(t) - \sqrt{1-\frac{\gamma^2T^2}{\sinh(\gamma T)}}u_+^{\perp}(t). \qquad \text{(B.7)}$$

The equations after this are rather lengthy. In most settings, we are interested in the measured noise, and divide it up in an atomic contribution and the rest:

$$LN = \kappa^2\cdot AN + EN, \qquad \text{(B.8)}$$

where LN is the output light noise, AN the atomic noise and EN all additional

noise contributions. The coupling constant, we measure is given by:

$$\kappa^2_{\text{measure}} = (1-\epsilon^2)\frac{1-e^{-2\gamma T}}{\xi^2}. \tag{B.9}$$

With B.5 and 3.23 we calculate the additional noise term for the two cell case:

$$\begin{aligned} EN &= (\frac{1}{e^{2\gamma\cdot T}-1}(\text{Sinh}(2\gamma\cdot T)+(1-2\epsilon^2)(1-\text{Cosh}(2\gamma\cdot T))-... \\ &- 2\epsilon^2(1-\epsilon^2)(\frac{1}{\xi^2}-1)(2\gamma\cdot T-\text{Sinh}(2\gamma\cdot T)))). \end{aligned} \tag{B.10}$$

As a reminder, not considering decay, the extra noise is given by the suppressed light noise:

$$EN = 1-\kappa^2\xi^2. \tag{B.11}$$

For the single cell case, we can also calculate the light and decay contribution of the noise:

$$\begin{aligned} EN &= \frac{(1-\epsilon^2)^2(-\sqrt{e^{-2T\gamma}}+T\gamma\text{Csch}(T\gamma))^2}{4\xi^4}+\frac{\epsilon^2(1-\epsilon^2)(-\sqrt{e^{-2T\gamma}}+T\gamma\text{Csch}(T\gamma))^2}{2\xi^2}... \\ &+ \frac{1}{4}(\sqrt{e^{-2T\gamma}}(1-\epsilon^2)+T\gamma(1+\epsilon^2)\text{Csch}(T\gamma))^2+\frac{1}{4}(1+\epsilon^2)^2(1-T^2\gamma^2\text{Csch}(T\gamma)^2)... \\ &+ \frac{(1-\epsilon^2)^2(1-T^2\gamma^2\text{Csch}(T\gamma)^2)}{4\xi^4}+\frac{\epsilon^2(1-\epsilon^2)(1-T^2\gamma^2\text{Csch}(T\gamma)^2)}{2\xi^2}. \end{aligned} \tag{B.12}$$

This can be compared to the single cell light noise output without decay, coming from equations 3.15:

$$\begin{aligned} EN &= \frac{1}{4\xi^2}(2-(2+\kappa^2)\xi^2+2\xi^4-\kappa^2\xi^6+2T\gamma\sqrt{1-\kappa^2\xi^2}(-1+\xi^4)\text{csch}(T\gamma)... \\ &+ 2T^2\gamma^2\xi^2\text{csch}(T\gamma)^2). \end{aligned} \tag{B.13}$$

These lengthy equations do hardly yield any information that can be grasped at first glance. To see the effect of the decay on the noise compared to the case with no additional decay, one can consult figure B.1. Here, the light noise contribution is shown for the case of a balanced cell setting in B.1a and B.1b, and the single cell setting in B.1c and B.1d. While the solid lines show the additional noise calculated from the equations including the decay, the dashed lines show the original light noise $1-\kappa^2\xi^2$, but using the measured suppressed κ given by equation B.9.

In the two cell case, the decay leads to an increase of the EN contribution. This

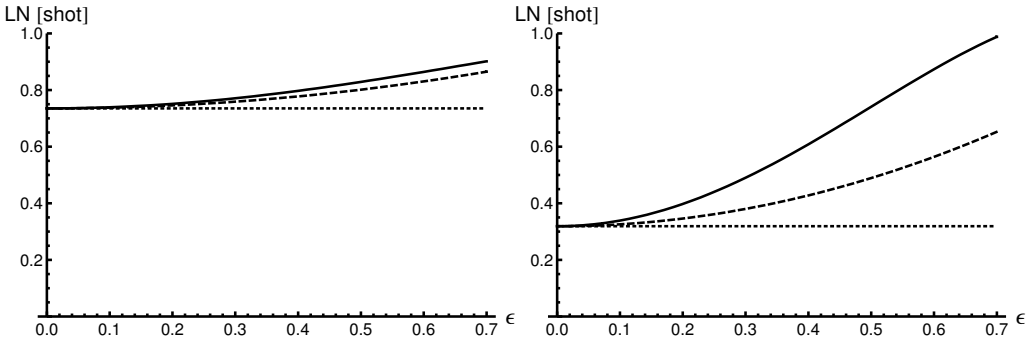

(a) Two cells, low coupling

(b) Two cells, high coupling

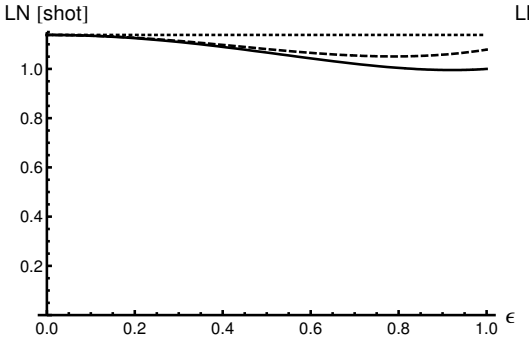

(c) Single cells, low coupling

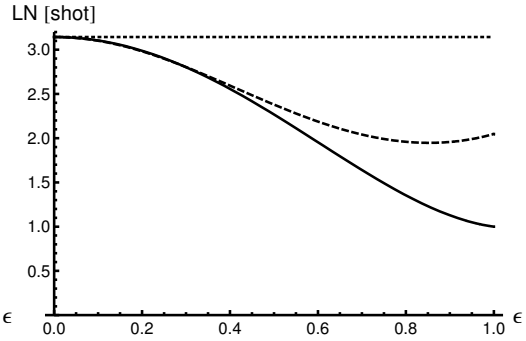

(d) Single cells, high coupling

Figure B.1: The light noise contribution is shown over $\epsilon = \sqrt{\frac{\gamma_{\text{extra}}}{\gamma}}$ for the case of a balanced cell setting in B.1a and the single cell setting in B.1c , for a relevant experimental low power setting with $T = 1ms$, $\gamma = 6.5ms$ (room temperature, $P \approx 8mW$). We usually experience ϵ^2 between 0.2 and 0.4. The solid lines show the additional noise, when the decay is included. The dashed lines show the light noise, calculated from the simple model, using the measured κ^2, which is suppressed by $(1 - \epsilon^2)$.
The figures on the right show the same curves for around triple light power - so much higher coupling. The scaling of the two graphs for the single cell case are different.

extra noise calculated with the simple model with the measured κ only gives a couple of percent different result for the most relevant settings. The effect increases for stronger coupling, so that it becomes very important to take it into account for the atomic state reconstruction. The reason is that small light noise - meaning light noise suppressed strongly by the swap interaction - is effected very strongly, when vacuum is mixed in. For the single cell case the effect for the low coupling is also comparatively small.

Appendix C

Perturbation of the input-output equations in the magnetic field

In this section I want to evaluate equations A.2, A.3 and A.5, A.6 perturbational in the presence of a magnetic field. I will only consider the terms that are also considered in the rest of the thesis, but without the linearizing step. The equations for the atomic spins read:

$$\dot{\hat{j}}_y(z,t) = d\hat{j}_x(z,t)\hat{S}_z(z,t) - \Omega\hat{j}_j(z,t) \tag{C.1}$$

$$\dot{\hat{j}}_z(z,t) = -d\zeta^2(\hat{j}_x^2 - \hat{j}_y^2)(z,t)\hat{S}_y(z,t) + \Omega\hat{j}_y(z,t). \tag{C.2}$$

The additional term, compared to the QND theory is proportional to $\zeta^2 = 4\frac{a2}{a1}$ which is small for reasonable detunings. Also the term $\hat{j}_x^2 - \hat{j}_y^2$ is part of the perturbation term. In all calculations for input output equations we need to assume that $\hat{j}_x$ is constant throughout the interaction and now also $\langle \hat{j}_x^2 - \hat{j}_y^2 \rangle_L$ is assumed constant during the measurement. In the measurements we usually take $\langle j_x \rangle_L = J_x/L$ as the normalization factor.

It follows for the spins in the rotating frame[1]:

$$\dot{\hat{j}}_y^*(z,t) = d\langle \hat{j}_x \rangle_L \hat{S}_z \cdot \cos(\Omega t) - d\zeta^2 \langle \hat{j}_x^2 - \hat{j}_y^2 \rangle_L \hat{S}_y \sin(\Omega t) \tag{C.3}$$

$$\dot{\hat{j}}_z^*(z,t) = -d\langle \hat{j}_x \rangle_L \hat{S}_z \cdot \sin(\Omega t) - d\zeta^2 \langle \hat{j}_x^2 - \hat{j}_y^2 \rangle_L \hat{S}_y \cos(\Omega t) \tag{C.4}$$

[1] $\hat{j}_y^* = \cos[\Omega t]\hat{j}_y + \sin[\Omega t]\hat{j}_z, \hat{j}_z^* = \cos[\Omega t]\hat{j}_z - \sin[\Omega t]\hat{j}_y$

And for $\hat{S}_y$ and $\hat{S}_z$ we have

$$\hat{S}'_y(z,t) = b\hat{j}_z = b(\hat{j}^*_y \sin(\Omega t) + \hat{j}^*_z \cos(\Omega t)) \quad \text{(C.5)}$$

$$\hat{S}'_z(z,t) = -b\frac{\zeta^2}{2}(\hat{j}_y\hat{j}_x + \hat{j}_x\hat{j}_y)\hat{j}_z \quad \text{(C.6)}$$

with $d = \frac{\gamma\lambda^2}{8A\Delta 2\pi}a_1$ and $b = dS_x$.[2] Thus the equation for $\hat{S}_y$ is the same as without the perturbation. This is the light variable of interest, as we wish to understand the effect of the ζ^2 term on our atomic reconstruction which is done via a S_y measurement.

C.1 Zeroth order, $\zeta^2 = 0$

Like in the QND equations presented in chapter 2, $\hat{j}_z$ and $\hat{S}_z$ remain constant:

$$\begin{aligned}
\hat{S}_y(z,t) &= \hat{S}_y(0,t) + bz(\hat{j}^*_y \sin(\Omega t) + \hat{j}^*_z \cos(\Omega t)) \\
\hat{S}_z(z,t) &= \hat{S}_z(0,t) \\
\hat{j}^*_y(z,t) &= \hat{j}^*_y(z,0) + d\cdot\langle\hat{j}_x\rangle_L \int_0^t dt'(\hat{S}_z(0,t)\cos(\Omega t')) \\
\hat{j}^*_z(z,t) &= \hat{j}^*_z(z,0) + d\cdot\langle\hat{j}_x\rangle_L \int_0^t dt'(\hat{S}_z(0,t)\sin(\Omega t'))
\end{aligned}$$

C.2 First order perturbation in ζ^2

First we integrate the atomic equations

$$\begin{aligned}
\hat{j}^*_y(z,t) &= \hat{j}^*_y(z,0) + d\cdot\langle\hat{j}_x\rangle_L \int_0^t \cos(\Omega t')\hat{S}_z(t',z)dt' - d\zeta^2\langle\hat{j}^2_x - \hat{j}^2_y\rangle_L \int_0^t \sin(\Omega t')\hat{S}_y(t',z)dt' \\
\hat{j}^*_z(z,t) &= \hat{j}^*_z(z,0) - d\cdot\langle\hat{j}_x\rangle_L \int_0^t \sin(\Omega t')\hat{S}_z(t',z)dt' - d\zeta^2\langle\hat{j}^2_x - \hat{j}^2_y\rangle_L \int_0^t \cos\Omega t')\hat{S}_y(t',z)dt' \\
\hat{j}^*_y(z,t) &= \hat{j}^*_y(z,0) + d\cdot\langle\hat{j}_x\rangle_L \int_0^t \cos(\Omega t')\hat{S}_z(t',0)dt' - ... \\
&- d\zeta^2\langle\hat{j}^2_x - \hat{j}^2_y\rangle_L \int_0^t \sin(\Omega t')\{\hat{S}_y(t',0) + bz[\hat{j}^*_y \sin(\Omega t) + \hat{j}^*_z \cos(\Omega t)]\}dt' \quad \text{(C.7)} \\
\hat{j}^*_z(z,t) &= \hat{j}^*_z(0)(1 + \frac{dbz\zeta^2 T}{2}) - d\langle\hat{j}_x\rangle_L \int_0^t \sin(\Omega t')S_z(t',0)dt' - ... \\
&- db\zeta^2\langle\hat{j}^2_x - \hat{j}^2_y\rangle_L \int_0^t \cos(\Omega t')S_y(t',0)dt' \quad \text{(C.8)}
\end{aligned}$$

For the last two lines we approximated the integral over a squared cosine with $\frac{T}{2}$, as we have done previously. For the light equations we consider the cosine

[2] $bdTL\langle j_x\rangle = \kappa^2$ and $b\sqrt{T}\sqrt{J_x/Sx} = \kappa$.

or sine modes[3]:

$$\begin{aligned}\hat{S}^{\text{out}}_{y,c} &= \sqrt{\frac{2}{T}}\int_0^T \hat{S}_y(z,t)\cos(\Omega t)dt \\ &= \hat{S}^{\text{in}}_{y,c} + bz\sqrt{\frac{T}{2}}\hat{j}_z(0)\{1-\frac{dbL\zeta^2T}{4}\langle\hat{j}_x^2-\hat{j}_y^2\rangle_L\} - \frac{db\langle\hat{j}_x\rangle_L TL}{4}(\hat{S}^{\text{in}}_{z,s}+\frac{1}{\sqrt{3}}\hat{S}^{\text{in}}_{z,s,1})+... \\ &\quad -\frac{db\zeta^2TL}{4}\langle\hat{j}_x^2-\hat{j}_y^2\rangle_L(\hat{S}^{\text{in}}_{y,c}+\frac{1}{\sqrt{3}}\hat{S}^{\text{in}}_{y,c,1}) \qquad \text{(C.9)}\end{aligned}$$

For the normalized case and with $\hat{j}_z \rightarrow <\hat{j}_z>_L = \hat{J}_z/L$;

$$\begin{aligned}\hat{y}^{\text{out}}_c = \quad & \hat{y}^{\text{in}}_c(1-\frac{\kappa^2_{\text{QND},0}\zeta^2}{16}(\hat{j}_x^2-\hat{j}_y^2)) + \frac{\kappa_{\text{QND}}}{\sqrt{2}}\hat{p}^{\text{in}}(1-\frac{\kappa^2_{\text{QND},0}\zeta^2}{16}(\hat{j}_x^2-\hat{j}_y^2)) \\ - \quad & \frac{\kappa^2_{\text{QND}}}{4}(\hat{q}^{\text{in}}_s+\frac{1}{\sqrt{3}}\hat{q}^{\text{in}}_{s,1}) - \frac{\kappa^2_{\text{QND},0}\zeta^2}{16\sqrt{3}}(\hat{j}_x^2-\hat{j}_y^2)y^{\text{in}}_{c,1} \qquad \text{(C.10)}\end{aligned}$$

where $\kappa_{\text{QND},0}$ is the coupling constant for the fully oriented CSS, while κ_{QND} scales with $\sqrt{J_x}$ as usual. The factors $\hat{j}_x^2-\hat{j}_y^2$ stated in the last equation are referring to single atom spins, not the spatial depending ensemble spins. The differences compared to the equations derived without any considerations of ζ^2 terms, are threefold

1. A reduced readout coupling (smaller than κ measured from thermal noise.)
2. A reduced input light noise.
3. Additional light noise because of incoupling of $y_{c,1}$.

All three effects appear small and can be easily estimated. The influence of this on the atomic noise reconstruction depends crucially on the input state. It will be largest for atomic variances below the minimum uncertainty noise. The reason is that then the suppression of the light noise will begin to play a more important role. Also, all the correction terms are proportional $(\hat{j}_x^2-\hat{j}_y^2)$. For the CSS it is equal 14 and the corrections get similar to equation 3.19 which is only valid for highly oriented ensembles. Equation C.10 can now be used to evaluate the correction on the atomic state reconstruction by the QND mode.

[3]Note: $\int_0^T\cos^2(\Omega t)dt \approx \frac{T}{2}$, $\int_0^T\cos^2(\Omega t)\int_0^t\cos(\Omega t')^2dt'dt \approx \frac{T^2}{4}$ and $\int_0^T\cos^2(\Omega t)\int_0^t f(t')dt'dt \approx \int_0^T(\frac{T-t}{2})f(t)dt$

Appendix D

Faraday angle measurement

For the Hamiltonian in equation 2.18 the propagation direction of light is the z-direction. Here I will discuss the effect on a weak probe beam traveling through the cell in x direction. I will therefore circularly exchange the spin operators so that the spin in propagation direction is $\hat{j}_x$. In this scenario, apart from the main component proportional to $a_1\hat{S}_z\hat{j}_x$ there will only be one component proportional a_2, which is potentially of relevance. To specify the negligible terms, the term $\hat{j}_y\hat{j}_z + \hat{j}_z\hat{j}_y \approx 0$ for relevant states. Again we leave out the terms proportional $\hat{\phi}$, with which all Stokes operators commute. The additional term, we are left with is $7a_2\hat{j}_x\hat{S}_x$. While the strong first term $\propto a_1$ causes a rotation from $\hat{S}_x$ to $\hat{S}_y$ and vice versa, the second term $\propto a_2$ leads to a rotation in the $\hat{S}_y$-$\hat{S}_z$ plane. In the experiment, where $\hat{S}_z(0) = 0$ the effect on $\hat{S}_y$ is undetectable (on the order of 0.00001%). $\hat{S}_z$ does change, but this is not of interest here. It is therefore enough to consider the simple Hamiltonian from equation 2.20. Then $\hat{S}_x$ and $\hat{S}_y$ after the sample have changed in the following fashion:

$$\hat{S}_x(L) = \hat{S}_x(0) \cdot \cos(2\theta_F) + \hat{S}_y(0) \cdot \sin(2\theta_F) \tag{D.1}$$

$$\hat{S}_y(L) = \hat{S}_y(0) \cdot \cos(2\theta_F) - \hat{S}_x(0) \cdot \sin(2\theta_F). \tag{D.2}$$

The Stokes operators are proportional to the difference of the power of light in orthogonal polarization directions. The macroscopic spin rotates the linear polarization of the probe beam by the Faraday angle:

$$\theta_F = \frac{\gamma\lambda^2\langle J_x\rangle a_1}{16A\Delta 2\pi} \approx \frac{\gamma a_1\lambda^2 4N_a}{16A\Delta 2\pi}. \tag{D.3}$$

The left part of the equation holds also for atoms in $F = 3$. Of course a_1 and the detuning need to be adjusted accordingly. For large detunings a_1 is close to 1 for $F = 4$ and -1 for $F = 3$. Since the splitting of the hyperfine levels is rather big the rotation coming from atoms in $F = 3$ will always be

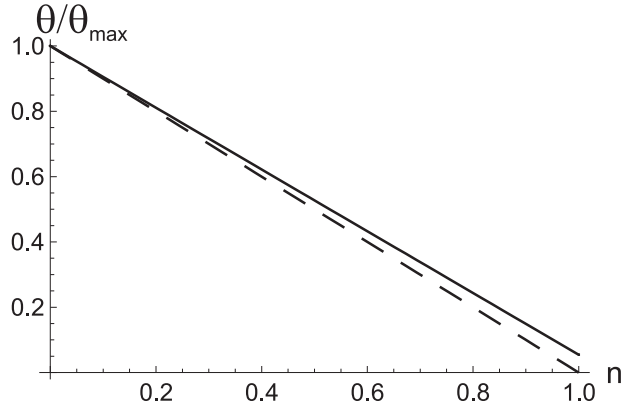

Figure D.1: The solid line shows the measured Faraday angle $\theta_{\text{measure}}/\theta_{\text{max}}$, while the dashed line shows the Faraday angle, we would measure, if only atoms in $F = 4$ would contribute. $n = N_{a,F=3}/N_a$ is the ratio of atoms in $F = 3$ to all the atoms.

very small as the probe light is detuned by $\Delta_{34} - \Delta$, with $\Delta_{34} = 9.2GHz$ form the transitions starting in $F = 3$. If one knows the maximal Faraday angle θ_{max}, which stands for the polarization rotation, when all atoms are in $F = 4$, then one can easily calculate the compensated Fardaday angle $\theta_{F=4}$, which is the polarization rotation, coming from the atoms in $F = 4$. Starting with the measured Farday angle, for the situation that $N_{a,F=4}$ atoms are in $F = 4$ and $N_{a,F=3}$ atoms are in $F = 3$:

$$\begin{aligned} \theta_{\text{measure}} &= \theta_{F=4} + \theta_{F=3} \\ &= \frac{\gamma\lambda^2}{16A2\pi}(4N_{a,F=4} \cdot o_{F=4} \cdot \frac{a_1^{F=4}}{\Delta} + 3N_{a,F=3} \cdot o_{F=3} \cdot \frac{a_1^{F=3}}{\Delta - \Delta_{34}}). \end{aligned} \tag{D.4}$$

Where the $o_F = \frac{1}{F}\sum_{m_F} m_F \cdot p_{m_F}$ are the orientations, given by the distribution of the populations of the magnetic sublevels m_F of the hyperfine state F.
Setting both orientations to one, this lead to

$$\begin{aligned} \theta_{F=4} &= \theta_{\text{measure}} - \theta_{F=3} \\ &= \frac{1}{1-C}(\theta_{\text{max}} - C\theta_{\text{measure}}) \end{aligned} \tag{D.5}$$

with $C = \frac{\Delta}{\Delta 34 - \Delta}\frac{3a_1^3}{4a_1^4}$ and the maximal Faraday angle for all atoms in $F = 4$, $\theta_{\text{max}} = \frac{a_1\gamma\lambda^2}{8A\Delta 2\pi}4N_{\text{a}}$. In certain situations, the orientations can differ substantially from one (especially of $F = 3$), so that we have to take them into account.

Appendix E

Magneto optical resonance signal (MORS)

RF excitation of the transversal spins

I will summarize some important equations that are used for the state analysis with the MORS method. This will follow strictly [JSSP04] and the PhD theses [Jul03, She06].

The atoms in a magnetic field $\mathbf{B}$ follow the Hamiltonian $\hat{H} = \mu_b g_F \mathbf{J}\mathbf{B} + o(\mathbf{B}^2)$ with g_F being the gyromagnetic factor for $F = 4$. In our setting we have a strong DC field in x-direction. For the MORS experiment an RF field with the frequency Ω_{RF} in y-direction is added. The time derivatives of the collective rotating transversal spins thus read:

$$\dot{\hat{J}}_y = \omega_s \sin(\Omega t)\sin(\Omega_{RF} t) J_x, \quad \dot{\hat{J}}_z = \omega_c \cos(\Omega t)\cos(\Omega_{RF} t) J_x \tag{E.1}$$

with $\omega_{c,s} = B_{c,s} g_F \mu_B g_F / h$ where $B_{c,s}$ is the amplitude of the RF cosine and sine component. When the field is on resonance so $\Omega = \Omega_{RF}$ and we look at time scales long compared to the oscillation, the quadratic oscillating terms can be replaced with a factor $\frac{1}{2}$. Now the RF field on resonance clearly creates a displacement in the rotating spin. We can measure the rotating spins with help of the light atom interface. When we scan the RF frequency we expect to see a resonance at the Larmor frequency around 322 kHz, which represents an excitation of all $\Delta m = 1$ coherences that make out the transverse spins $\hat{j}_y = \sum_m \sqrt{F(F+1) - m(m+1)}(\hat{\sigma}_{m+1,m} + \hat{\sigma}_{m,m+1})$ and
$\hat{j}_z = i \sum_m \sqrt{F(F+1) - m(m+1)}(\hat{\sigma}_{m+1,m} - \hat{\sigma}_{m,m+1})$. But the quadratic Zeeman effect, which is discussed in [Jul03] in detail for our experiment, leads to a splitting of the coherence frequencies by $20Hz$. This is of course a very small effect

compared to the Larmor frequency but it gives us the possibility to resolve the different coherences of the atoms at frequencies $\Omega_{m,m+1}$. When the frequency of the RF field is scanned slowly, the response will be a sum of Lorenzians at different frequencies with the widths $\Gamma_{m,m+1}$

$$\begin{aligned} \hat{J}_y &= \mathrm{Re}(A\sum_m \frac{F(F+1)-m(m+1)}{i(\Omega_{m,m+1}-\Omega_{RF})-\Gamma_{m,m+1}/2} e^{i\Omega_{RF}}[\sigma_{m+1,m+1}-\sigma_{m,m}]) \\ \hat{J}_z &= \mathrm{Im}(... \end{aligned} \tag{E.2}$$

where $\sigma_{m,m}$ is the population of level m. When we measure the cosine and the sine component of $\hat{S}_y$ after the interaction, it is equivalent to those two measurements. The MORS signal R is actually the square root of the squared sum $R^2 = \sqrt{S_{y,c}^2 + S_{y,s}^2}$ which is proportional to.

$$R^2 \propto |\sum_m \frac{F(F+1)-m(m+1)}{i(\Omega_{m,m+1}-\Omega_{RF}-\Gamma_{m,m+1}/2)} e^{i\Omega_{RF}}[\sigma_{m+1,m+1}-\sigma_{m,m}]|^2. \tag{E.3}$$

Often we work with very low probe powers, so that the probe light does not give rise to line broadening.

Appendix F

Thermal state noise measurement

For the calibration of $\kappa_{\text{thermal}} = \kappa_{\text{QND}}$, one can measure the noise of the atoms in a thermal state. As we know, for the CSS the variance of the transverse spin components for the single atoms $\text{Var}(j_y) = \text{Var}(j_z) = \frac{F}{2} = 2$ (with $< j_x^2 >= F^2$). The variance of the thermal state is symmetric, so $\text{Var}(j_x) = \text{Var}(j_y) = \text{Var}(j_z) = \frac{F(F+1)}{3} = \frac{20}{3}$. Since there are 9/16 of all atoms in the hyperfine state $F = 4$, the variance of the thermal state that we measure should be 15/4.

Now we would like to find out, what happens to our single cell input-output relations for light and atoms. First we look at the Heisenberg equations for the spins. Most additional terms which are considered in chapter 3 are left out. This can be justified, as the terms in the Hamiltonian average out for the thermal state.

$$\begin{aligned} \frac{\partial \hat{j}_z(z,t)}{\partial t} &= 0 \quad , \\ \frac{\partial \hat{j}_x(z,t)}{\partial t} &= a\hat{S}_z(z,t)\hat{j}_y(z,t), \\ \frac{\partial \hat{j}_y(z,t)}{\partial t} &= -a\hat{S}_z(z,t)\hat{j}_x(z,t), \end{aligned} \tag{F.1}$$

with $a = \frac{\gamma\lambda^2}{8A\Delta 2\pi}$. Since $\hat{S}_z$ is constant in time the equations lead to an oscillation between $\hat{j}_x$ and $\hat{j}_y$. This is a very small effect and for relevant settings leads to a frequency of around 10^{-4} Hz, fluctuating with $\text{Var}(\hat{P}) = \text{Var}(\hat{S}_z/\sqrt{S_x})$.
Since our timescales are in the ms-range, we can consider all the spins to be unaffected by the interaction. Of course going to the rotating frame will not change this.

Looking at the light variables, we see that only $\hat{S}_y$ is changed by the spins and

we get (now with collective rotating frame spins)

$$\begin{aligned} \hat{S}_y^{\text{out}} &= \hat{S}_y^{\text{in}} + aS_x(\hat{J}_y \sin\Omega t + \hat{J}_z \cos\Omega t) \\ \hat{S}_{y,c(s)}^{\text{out}} &= \hat{S}_{y,c(s)}^{\text{in}} + \frac{aS_xT}{2}\hat{J}_{y(z)} = \hat{S}_{y,c(s)}^{\text{in}} + \frac{\kappa_{\text{thermal}}\sqrt{S_xT}}{2\sqrt{J}}\hat{J}_{y(z)} \end{aligned} \tag{F.2}$$

where $J = 4N_{at}$. Then we get for the normalized operators ($\hat{x} = \frac{\hat{J}_z}{\sqrt{J}}, \hat{p} = \frac{\hat{J}_y}{\sqrt{J}}$):

$$\hat{y}_{c(s)}^{\text{out}} = \hat{y}_{c(s)}^{\text{in}} + \frac{\kappa_{\text{thermal}}}{\sqrt{2}}\hat{x}(\hat{p}) \tag{F.3}$$

Compared to the usual input-output relations for an oriented sample in a magnetic field, the back-action of light is indeed missing.

When we now measure the variance $\text{Var}(\hat{S}_y^{\text{out}})$, we can extract $\kappa_{\text{thermal}}^2$

$$\frac{\kappa_{\text{thermal}}^2}{2} \cdot \frac{15}{16} = \text{Var}(\hat{y}_{c(s)}^{\text{out}}) - \text{Var}(\hat{y}_{c(s)}^{\text{in}}). \tag{F.4}$$

Appendix G

D_1 numbers

G.1 a_i prefactors of D_1 line

a_0, a_1 and a_2 can be calculated following the introduction of the effective Hamiltonian in [Jul03] and with help of the transition moments and reduced matrix elements presented in [Ste03]

$$a_0 = \frac{1}{4}(5 + \frac{3}{1 - \Delta_{34}/\Delta}) \tag{G.1}$$

$$a_1 = \frac{1}{8}(1 + \frac{7}{1 - \Delta_{34}/\Delta}) \tag{G.2}$$

$$a_2 = \frac{1}{16}(1 - \frac{1}{1 - \Delta_{34}/\Delta}). \tag{G.3}$$

a_0, a_1 and a_2 are shown in figure G.1, not considering the Doppler broadening

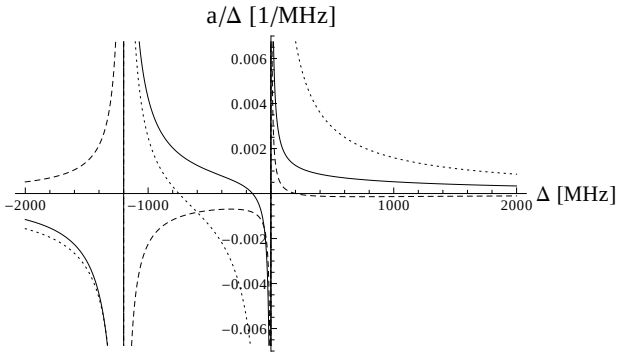

Figure G.1: The solid line shows a_1/Δ, the dashed line a_2/Δ and the dotted line a_0/Δ of the D_1 line. In between the two exited lines, there a_1 gets zero. If one includes the Doppler broadening the zero crossing is probably not visible.

G.2 Lindblad terms

I want to model the decay of the atomic states during the creation of the squeezed state via Raman transitions. The evolution of the density matrix looks as:

$$\dot{\rho} = -\frac{i}{\hbar}[\hat{V}, \rho] + \sum_n (2\mathbf{L}_n \rho \mathbf{L}_n^\dagger - \mathbf{L}_n^\dagger \mathbf{L}_n \rho - \rho \mathbf{L}_n^\dagger \mathbf{L}_n) \tag{G.4}$$

where $\hat{V}$ is the previously used single atom interaction Hamiltonian and where the Lindblad terms L_n stand for certain decay channels and consists of a step operator and a decay rate. They can be identified by considering different decay types. One decay mechanism is spontaneous emission. The step operators for the ground state and their strength can be calculated with help of the transition matrix elements by adiabatic elimination of the exited states. The principle idea is described in [Sto] and in appendix G.2.1 the terms are stated.

Additional decay mechanism towards the thermal state, modeling processes like collisions are also included and the Lindblad operators are given in G.2.2.

G.2.1 Spontaneous emission

We are interested in spontaneous emission driven by the two Raman beams. They are tuned close to the D_1 line, detuned by $\Delta_R = -550Mhz$, the linewidth of the transition is $\gamma = 4.2MHz$. The two beams are σ_- and σ_+ polarized, the emitted photon can have any polarization. Depending on the initial state, the atom can after one process therefore end up with $m_f = m_i$, $m_f = m_i \pm 1$, $m_f = m_i \pm 2$. The strength of those processes are given by the product of the transition elements[Ste03] $d_{D1}(F, m, F', m')$ of the involved processes:

$$d_{D1}(F_1, m_1, F_2, m_2) = < Fm|e\mathbf{r}|F'm' > =$$
$$< Fm|F'1m's > (-1)^{F'+J+1+I} \sqrt{(2F'+1)(2J+1)} \begin{Bmatrix} J & J' & 1 \\ F' & F & I \end{Bmatrix} < J||e\mathbf{r}||J' > \tag{G.5}$$

where $< J||e\mathbf{r}||J' >$ is the reduced matrix element that can be found in [Ste03]. The strength of the process is given by $\Omega_s = \sqrt{\frac{P/2 \cdot 3\lambda^3}{A \cdot 32\pi^2 c\hbar}} \frac{\gamma}{\Delta_r + i\gamma}$. We use half the power $P/2$ of the light beam, as half of the light is right hand circular polarized and half is left hand circular polarized.
The corresponding step operators that stand for the process of taking one atom from m_i in $F = 4$ to m_f in $F = 4$ over the exited F'.

$$L(m_i, m_f, F', s) = \frac{\Omega_S}{2} d_{D1}(F, m_i, F', m_i + s) d_{D1}(F', m_i + s, F, m_f) |m_f >< m_i| \tag{G.6}$$

where $s = \pm 1$, stands for the two possible polarizations of the exiting photon. A similar description is derived in [Sto].
Additionally, we add an ancillary state to collect all decays into $F = 3$, in the same fashion as above.

G.2.2 Collisions

A process, like collisions that takes any input state and transfers it into any other state

$$L(m_i, m_f) = \frac{1}{\sqrt{16}T_1^{dark}}(|m_f><m_i| + |m_i><m_f|) \tag{G.7}$$

As all $F = 3$ states are collected in one ancillary state the process towards it is enhanced by $\sqrt{7}$

$$L(m_i, m_{F=3}) = \frac{1}{\sqrt{16}T_1^{dark}}(\sqrt{7}|m_{F=3}><m_i| + |m_i><m_{F=3}|) \tag{G.8}$$

with the decay constant of the macroscopic spin in the dark T_1^{dark}.

List of publications

[1] J. Sherson, H. Krauter, R. Olsson, B. Julsgaard, K. Hammerer, and I. Cirac. Quantum teleportation between light and matter. *Nature*, 443:557–560, 2006.

[2] T. Fernholz, H. Krauter, K. Jensen, J.F. Sherson, A.S. Sørensen, and E.S. Polzik. Spin squeezing of atomic ensembles via nuclear-electronic spin entanglement. *Physical Review Letters*, 101(7):073601, 2008.

[3] J. Sherson, H. Krauter, R.K. Olsson, B. Julsgaard, and E.S. Polzik. Quantum memory and teleportation using macroscopic gas samples. *Journal of Physics B: Atomic, Molecular and Optical Physics*, 41:223001, 2008.

[4] H. Krauter, J. Sherson, and E.S. Polzik. Quantum state transfer between light and matter via teleportation. *Laser & Photonics Reviews*, 4:685–696, 2009.

[5] W. Wasilewski, T. Fernholz, K. Jensen, L.S. Madsen, H. Krauter, C. Muschik, and E.S. Polzik. Generation of two-mode squeezed and entangled light in a single temporal and spatial mode. *Optics Express*, 17(16):14444–14457, 2009.

[6] M.V. Balabas, K. Jensen, W. Wasilewski, H. Krauter, L.S. Madsen, J.H. Müller, T. Fernholz, and E.S. Polzik. High quality anti-relaxation coating material for alkali atom vapor cells. *Optics Express*, 18(6):5825–5830, 2010.

[7] H. Krauter, C.A. Muschik, K. Jensen, W. Wasilewski, J.M. Petersen, J.I. Cirac, and E.S. Polzik. Entanglement generated by dissipation. *Arxiv preprint arXiv:1006.4344*, 2010.

[8] W. Wasilewski, K. Jensen, H. Krauter, J.J. Renema, M.V. Balabas, and E.S. Polzik. Quantum noise limited and entanglement-assisted magnetometry. *Physical Review Letters*, 104(13):133601, 2010.

[9] K. Jensen, W. Wasilewski, H. Krauter, T. Fernholz, B.M. Nielsen, M. Owari, M.B. Plenio, A. Serafini, M.M. Wolf, and E.S. Polzik. Quantum memory for entangled continuous-variable states. *Nature Physics*, 7(1):13–16, 2010.

[10] H. Krauter, J. Sherson, K. Jensen, T. Fernholz, D. Oblak, P.J. Windpassinger, N. Kjaergaard, J. Neergaard-Nielsen, B. Melholt-Nielsen, A. Hilliard, C. Olausson, J.H. Muller, and E. S. Polzik. Quantum interface between light and atomic ensembles. In M. Kasevich Eds. L. Hollberg, J. Bergquist, editor, *Laser Spectroscopy: Proceedings of the XVIII International Conference on ICOLS 2007*. Eds. World Scientific, 2008.

[11] K. Jensen, W. Wasilewski, H. Krauter, T. Fernholz, B.M. Nielsen, J.M. Petersen, J.J. Renema, M. V. Balabas, M.B. Owari, M. Plenio, A. Serafini, M.M. Wolf, C.A. Muschik, J.I. Cirac, J.H. Müller, and E.S. Polzik. Quantum memory, entanglement and sensing with room temperature atoms. In *ICAP 2010 conference proceedings*, 2010.

[12] K. Jensen, W. Wasilewski, H. Krauter, B. Renema, J. J. Nielsen, T. Fernholz, and E.S. Polzik. Room-temperature atomic ensembles for quantum memory and magnetometry. In *Laser Spectroscopy: Proceedings of the XIX International Conference ICOLS 2009*, page 137. World Scientific Publishing Company, 2010.

[13] K. Jensen, W. Wasilewski, H. Krauter, J.J. Renema, M.V. Balabas, and E.S. Polzik. Quantum noise limited and entanglement-assisted magnetometry. In *Lasers and Electro-Optics (CLEO) and Quantum Electronics and Laser Science Conference (QELS), 2010 Conference on*, pages 1–2. IEEE, 2010.

Bibliography

[ABB+02] E.B. Alexandrov, M.V. Balabas, D. Budker, D. English, D.F. Kimball, C.H. Li, and V.V. Yashchuk. Light-induced desorption of alkali-metal atoms from paraffin coating. *Physical Review A*, 66(4):42903, 2002.

[ABP+96] E.B. Alexandrov, M.V. Balabas, A.S. Pasgalev, A.K. Vershovskii, and N.N. Yakobson. Double-resonance atomic magnetometers: from gas discharge to laser pumping. *Laser Physics*, 6:244–251, 1996.

[ADR82] A. Aspect, J. Dalibard, and G. Roger. Experimental test of Bell's inequalities using time- varying analyzers. *Physical Review Letters*, 49(25):1804–1807, Dec 1982.

[AGC+87] G. Avila, V. Giordano, V. Candelier, E. de Clercq, G. Theobald, and P. Cerez. State selection in a cesium beam by laser-diode optical pumping. *Physical Review A*, 36(8):3719–3728, Oct 1987.

[AWO+09] J. Appel, P.J. Windpassinger, D. Oblak, U.B. Hoff, N. Kjærgaard, and ES Polzik. Mesoscopic atomic entanglement for precision measurements beyond the standard quantum limit. *Proceedings of the National Academy of Sciences*, 106(27):10960–10965, 2009.

[B+64] J.S. Bell et al. On the Einstein-Podolsky-Rosen paradox. *Physics*, 1(3):195–200, 1964.

[BB66] M.A. Bouchiat and J. Brossel. Relaxation of optically pumped Rb atoms on paraffin-coated walls. *Physical Review*, 147(1):41–54, 1966.

[BB84] C.H. Bennett and G Brassard. Quantum cryptography: Public key distribution and coin tossing. *Proceedings of IEEE International Conference on Computers, Systems, and Signal Processing*, pages 175–179, 1984.

[BBC+93] C. H. Bennett, G. Brassard, C. Crépeau, R. Jozsa, A. Peres, and W. K. Wootters. Teleporting an unknown quantum state via dual classical and einstein-podolsky-rosen channels. *Physical Review Letters*, 70:1895–1899, Mar 1993.

[BDCZ98] H.-J. Briegel, W. Dür, J. I. Cirac, and P. Zoller. Quantum repeaters: The role of imperfect local operations in quantum communication. *Physical Review Letters*, 81(26):5932–5935, Dec 1998.

[BGS+99] B.C. Buchler, M.B. Gray, D.A. Shaddock, T.C. Ralph, and D.E. McClelland. Suppression of classic and quantum radiation pressure noise by electro-optic feedback. *Optics letters*, 24(4):259–261, 1999.

[BLLO83] G.C. Bjorklund, M.D. Levenson, W. Lenth, and C. Ortiz. Frequency modulation (FM) spectroscopy. *Applied Physics B: Lasers and Optics*, 32(3):145–152, 1983.

[BLW+08] M. Branderhorst, P. Londero, P. Wasylczyk, C. Brif, R.L. Kosut, H. Rabitz, and I.A. Walmsley. Coherent control of decoherence. *Science*, 320(5876):638–643, 2008.

[BPM+97] D. Bouwmeester, J.-W. Pan, K. Mattle, M. Eibl, H. Weinfurter, and A. Zeilinger. Experimental quantum teleportation. *Nature*, 390:575–579, 1997.

[BPP10] R. Bloomer, M. Pysher, and O. Pfister. Entanglement protection by the quantum engineering of decoherence. *Arxiv preprint arXiv:1007.2369*, 2010.

[BRLR98] H.A. Bachor, T.C. Ralph, S. Lucia, and T.C. Ralph. *A guide to experiments in quantum optics*. wiley-vch, 1998.

[BSG+10] J.T. Barreiro, P. Schindler, O. Gühne, T. Monz, M. Chwalla, C.F. Roos, M. Hennrich, and R. Blatt. Experimental multiparticle entanglement dynamics induced by decoherence. *Nature Physics*, 6:943–946, 2010.

[BUB+10] T. Baluktsian, C. Urban, T. Bublat, H. Giessen, R. Löw, and T. Pfau. Fabrication method for microscopic vapor cells for alkali atoms. *Optics letters*, 35(12):1950–1952, 2010.

[BvL05] S. L. Braunstein and P. van Loock. Quantum information with continuous variables. *Rev. Mod. Phys.*, 77(2):513–577, Jun 2005.

[CCLP07] N.J. Cerf, N.J. Cerf, G. Leuchs, and E.S. Polzik. *Quantum information with continuous variables of atoms and light*. Imperial College Press, 2007.

[CCY+08] Y.A. Chen, S. Chen, Z.S. Yuan, B. Zhao, C.S. Chuu, J. Schmiedmayer, and J.W. Pan. Memory-built-in quantum teleportation with photonic and atomic qubits. *Nature Physics*, 4:103, 2008.

[CDRF+05] C.W. Chou, H. De Riedmatten, D. Felinto, S.V. Polyakov, S.J. Van Enk, and H.J. Kimble. Measurement-induced entanglement for excitation stored in remote atomic ensembles. *Nature*, 438(7069):828–832, 2005.

[CMH+07] S. Chaudhury, S. Merkel, T. Herr, A. Silberfarb, I. H. Deutsch, and P. S. Jessen. Quantum control of the hyperfine spin of a Cs atom ensemble. *Physical Review Letters*, 99(16):163002, Oct 2007.

[CS78] J.F. Clauser and A. Shimony. Bell's theorem. Experimental tests and implications. *Reports on Progress in Physics*, 41:1881, 1978.

[DCZP00] L.-M. Duan, J. I. Cirac, P. Zoller, and E. S. Polzik. Quantum communication between atomic ensembles using coherent light. *Physical Review Letters*, 85(26):5643–5646, Dec 2000.

[DGCZ00] L.-M. Duan, G. Giedke, J. I. Cirac, and P. Zoller. Inseparability criterion for continuous variable systems. *Physical Review Letters*, 84:2722–2725, March 2000.

[DLCZ01] L.M. Duan, M.D. Lukin, J.I. Cirac, and P. Zoller. Long-distance quantum communication with atomic ensembles and linear optics. *Nature*, 414(6862):413–418, 2001.

[DMK+08] S. Diehl, A. Micheli, A. Kantian, B. Kraus, H.P. Büchler, and P. Zoller. Quantum states and phases in driven open quantum systems with cold atoms. *Nature Physics*, 4(11):878–883, 2008.

[EAM+05] M.D. Eisaman, A. André, F. Massou, M. Fleischhauer, A.S. Zibrov, and M.D. Lukin. Electromagnetically induced transparency with tunable single-photon pulses. *Nature*, 438(7069):837–841, 2005.

[Ein71] A. Einstein. *The Born-Einstein Letters: Correspondence Between Albert Einstein and Max and Hedwig Born from 1916 to 1955*. Macmillan, 1971.

[EPR35] A. Einstein, B. Podolsky, and N. Rosen. Can quantum-mechanical description of physical reality be considered complete? *Physical Review*, 47:777–780, 1935.

[ERIR+07] K. Eckert, O. Romero-Isart, M. Rodriguez, M. Lewenstein, E.S. Polzik, and A. Sanpera. Quantum non-demolition detection of strongly correlated systems. *Nature Physics*, 4(1):50–54, 2007.

[FCP04] J. Fiurášek, N.J. Cerf, and E.S. Polzik. Quantum cloning of a coherent light state into an atomic quantum memory. *Physical Review Letters*, 93(18):180501, 2004.

[FSB+98] A. Furusawa, J.L. Sørensen, S.L. Braunstein, C.A. Fuchs, H.J. Kimble, and E.S. Polzik. Unconditional quantum teleportation. *Science*, 282:706–709, 1998.

[FT07] A. Furusawa and N. Takei. Quantum teleportation for continuous variables and related quantum information processing. *Physics Reports*, 443(3):97–119, 2007.

[GSM04] J.M. Geremia, J.K. Stockton, and H. Mabuchi. Real-time quantum feedback control of atomic spin-squeezing. *Science*, 304(5668):270–273, 2004.

[GZN+10] C. Gross, T. Zibold, E. Nicklas, J. Estève, and MK Oberthaler. Nonlinear atom interferometer surpasses classical precision limit. *Nature*, 464(7292):1165–1169, 2010.

[Hap72] W. Happer. Optical pumping. *Reviews of Modern Physiscs*, 44(2):169–249, Apr 1972.

[Hil08] Andrew James Hilliard. *Collective scattering in a Bose-Einstein condensate*. PhD thesis, University of Copenhagen, 2008.

[HMN+97] E. Hagley, X. Maitre, G. Nogues, C. Wunderlich, M. Brune, J.M. Raimond, and S. Haroche. Generation of Einstein-Podolsky-Rosen pairs of atoms. *Physical Review Letters*, 79(1):1–5, 1997.

[HMŘ06] Z. Hradil, D. Mogilevtsev, and J. Řeháček. Biased tomography schemes: an objective approach. *Physical Review Letters*, 96(23):230401, 2006.

[HP40] T. Holstein and H. Primakoff. Field Dependence of the Intrinsic Domain Magnetization of a Ferromagnet. *Physical Review*, 58:1098–1113, 1940.

[HPC05] K. Hammerer, E.S. Polzik, and J.I. Cirac. Teleportation and spin squeezing utilizing multimode entanglement of light with atoms. *Physical Review A*, 72:052313, 2005.

[HPC06] K. Hammerer, E.S. Polzik, and J.I. Cirac. High-fidelity teleportation between light and atoms. *Physical Review A*, 74:064301, 2006.

[HSP10] K. Hammerer, A.S. Sørensen, and E.S. Polzik. Quantum interface between light and atomic ensembles. *Reviews of Modern Physics*, 82(2):1041–1093, 2010.

[HSSP99] J. Hald, J. L. Sørensen, C. Schori, and E.S. Polzik. Spin squeezed atoms: A macroscopic entangled ensemble created by light. *Physical Review Letters*, 83(7):1319–1322, Aug 1999.

[HWPC05] K. Hammerer, M.M. Wolf, E.S. Polzik, and J.I. Cirac. Quantum benchmark for storage and transmission of coherent states. *Physical Review Letters*, 94:150503, 2005.

[Jen07] Kasper Jensen. Classical and quantum noise of light and atoms. Master's thesis, Niels Bohr Institute, University of Copenhagen, 2007.

[JKP01] B. Julsgaard, A. Kozhekin, and E.S. Polzik. Experimental long-lived entanglement of two macroscopic objects. *Nature*, 413:400–403, September 2001.

[JSC+04] B. Julsgaard, J. Sherson, J.I. Cirac, J. Fiurasek, and E.S. Polzik. Experimental demonstration of quantum memory for light. *Nature*, 432:482–486, 2004.

[JSSP04] B. Julsgaard, J. Sherson, J.L. Soerensen, and E.S. Polzik. Characterizing the spin state of an atomic ensemble using the magneto-optical resonance method. *Journal of Optics B*, 6:5–14, 2004.

[Jul03] B. Julsgaard. *Entanglement and quantum interactions with macroscopic gas samples*. PhD thesis, University of Aarhus, 2003.

[KBD+08] B. Kraus, H.P. Büchler, S. Diehl, A. Kantian, A. Micheli, and P. Zoller. Preparation of entangled states by quantum Markov processes. *Physical Review A*, 78(4):42307, 2008.

[KBM98] A. Kuzmich, N.P. Bigelow, and L. Mandel. Atomic quantum non-demolition measurements and squeezing. *EPL (Europhysics Letters)*, 42:481, 1998.

[KC04] B. Kraus and J.I. Cirac. Discrete entanglement distribution with squeezed light. *Physical Review Letters*, 92(1):13602, 2004.

[Kim08] H.J. Kimble. The quantum internet. *Nature*, 453(7198):1023–1030, 2008.

[Kit63] C. Kittel. *Quantum Theory of Solids*. Wiley, New York, 1963.

[KM10] Z. Kurucz and K. Mølmer. Multilevel Holstein-Primakoff approximation and its application to atomic spin squeezing and ensemble quantum memories. *Physical Review A*, 81(3):32314, 2010.

[KMB00] A. Kuzmich, L. Mandel, and N.P. Bigelow. Generation of spin squeezing via continuous quantum nondemolition measurement. *Physical Review Letters*, 85(8):1594–1597, Aug 2000.

[KMS+05] D.V. Kupriyanov, O.S. Mishina, I.M. Sokolov, B. Julsgaard, and E.S. Polzik. Multimode entanglement of light and atomic ensembles via off-resonant coherent forward scattering. *Physical Review A*, 71(3):32348, 2005.

[KMW+95] P.G. Kwiat, K. Mattle, H. Weinfurter, A. Zeilinger, A.V. Sergienko, and Y. Shih. New High-Intensity Source of Polarization-Entangled Photon Pairs. *Physical Review Letters*, 75:4337–4341, 1995.

[KNDM10] M. Koschorreck, M. Napolitano, B. Dubost, and M. W. Mitchell. Quantum nondemolition measurement of large-spin ensembles by dynamical decoupling. *Physical Review Letters*, 105(9):093602, Aug 2010.

[KU93] M. Kitagawa and M. Ueda. Squeezed spin states. *Physical Review A*, 47(6):5138–5143, Jun 1993.

[KY86] M. Kitagawa and Y. Yamamoto. Number-phase minimum-uncertainty state with reduced number uncertainty in a kerr nonlinear interferometer. *Physical Review A*, 34(5):3974–3988, Nov 1986.

[LBS+04] D. Leibfried, M.D. Barrett, T. Schaetz, J. Britton, J. Chiaverini, W.M. Itano, J.D. Jost, C. Langer, and D.J. Wineland. Toward Heisenberg-limited spectroscopy with multiparticle entangled states. *Science*, 304(5676):1476–1478, 2004.

[LKM+04] L.A. Liew, S. Knappe, J. Moreland, H. Robinson, L. Hollberg, and J. Kitching. Microfabricated alkali atom vapor cells. *Applied Physics Letters*, 84:2694, 2004.

[LOJ+05] C. Langer, R. Ozeri, J.D. Jost, J. Chiaverini, B. DeMarco, A. Ben-Kish, R.B. Blakestad, J. Britton, D.B. Hume, W. M. Itano, D. Leibfried, R. Reichle, T. Rosenband, T. Schaetz, P.O. Schmidt, and D.J. Wineland. Long-lived qubit memory using atomic ions. *Physical Review Letters*, 95(6):060502, Aug 2005.

[LP95] U. Leonhardt and H. Paul. Measuring the quantum state of light. *Progress in Quantum Electronics*, 19(2):89–130, 1995.

[MCJ+06] D.N. Matsukevich, T. Chanelière, S.D. Jenkins, S.-Y. Lan, T.A.B. Kennedy, and A. Kuzmich. Entanglement of remote atomic qubits. *Physical Review Letters*, 96(3):030405, Jan 2006.

[MHPC06] C.A. Muschik, K. Hammerer, E.S. Polzik, and J.I. Cirac. Efficient quantum memory and entanglement between light and an atomic ensemble using magnetic fields. *Physical Review A*, 73(6):62329, 2006.

[MKP05] O. Mishina, D. Kupriyanov, and E.S. Polzik. Macroscopic quantum information channel via the polarization-sensitive interaction between the light and spin subsystems. *Proceedings of the NATO Advanced Research Workshop*, 199:346, 2005.

[MKT+00] C.J. Myatt, B.E. King, Q.A. Turchette, C.A. Sackett, D. Kielpinski, W.M. Itano, C. Monroe, and D.J. Wineland. Decoherence of quantum superpositions through coupling to engineered reservoirs. *Nature*, 403(6767):269–273, 2000.

[MPC10] C.A. Muschik, E.S. Polzik, and J.I. Cirac. Dissipatively driven entanglement of two macroscopic atomic ensembles. *Arxiv preprint arXiv:1007.2209*, 2010.

[NN08] Jonas Schou Neergaard-Nielsen. *Generation of single photons and Schrödinger kitten states of light*. PhD thesis, University of Copenhagen, 2008.

[NNNH+06] J.S. Neergaard-Nielsen, B. Melholt Nielsen, C. Hettich, K. Mølmer, and E.S. Polzik. Generation of a superposition of odd photon number states for quantum information networks. *Physical Review Letters*, 97(8):083604, 2006.

[NNNT+07] J.S. Neergaard-Nielsen, B.M. Nielsen, H. Takahashi, A. I. Vistnes, and E.S. Polzik. High purity bright single photon source. *Optics Express*, 15(13):7940–7949, Jun 2007.

[OMM+09] S. Olmschenk, D.N. Matsukevich, P. Maunz, D. Hayes, L.M. Duan, and C. Monroe. Quantum teleportation between distant matter qubits. *Science*, 323(5913):486, 2009.

[OPKP92] Z.Y. Ou, S.F. Pereira, H.J. Kimble, and K.C. Peng. Realization of the Einstein-Podolsky-Rosen paradox for continuous variables. *Physical Review Letters*, 68:3663–3666, 1992.

[PCZ96] J.F. Poyatos, J.I. Cirac, and P. Zoller. Quantum reservoir engineering with laser cooled trapped ions. *Physical Review Letters*, 77(23):4728–4731, 1996.

[PMM05] V. Petersen, L.B. Madsen, and K. Mølmer. Magnetometry with entangled atomic samples. *Physical Review A*, 71(1):012312, Jan 2005.

[RBL+10] M.F. Riedel, P. Böhi, Y. Li, T.W. Hänsch, A. Sinatra, and P. Treutlein. Atom-chip-based generation of entanglement for quantum metrology. *Nature*, 464(7292):1170–1173, 2010.

[RBV+07] W. Rosenfeld, S. Berner, J. Volz, M. Weber, and H. Weinfurter. Remote preparation of an atomic quantum memory. *Physical Review Letters*, 98:050504, 2007.

[RCK+06] C.F. Roos, M. Chwalla, K. Kim, M. Riebe, and R. Blatt. 'Designer atoms' for quantum metrology. *Nature*, 443(7109):316–319, September 2006.

[RHR+04] M. Riebe, H. Haeffner, CF Roos, W. Haensel, J. Benhelm, GPT Lancaster, TW Koerber, C. Becher, F. Schmidt-Kaler, and DFV James. Deterministic quantum teleportation with atoms. *Nature*, 429:734–737, 2004.

[RLR+04] C.F. Roos, G.P.T. Lancaster, M. Riebe, H. Häffner, W. Hänsel, S. Gulde, C. Becher, J. Eschner, F. Schmidt-Kaler, and R. Blatt. Bell states of atoms with ultralong lifetimes and their tomographic state analysis. *Physical Review Letters*, 92(22):220402, Jun 2004.

[SDCZ01] A. Sorensen, L.-M. Duan, J.I. Cirac, and P. Zoller. Many-particle entanglement with Bose-Einstein condensates. *Nature*, 409(6816):63–66, January 2001.

[She06] Jacob F. Sherson. *Quantum memory and teleportation using macroscopic gas samples*. PhD thesis, University of Aarhus, 2006.

[SJP07] J. Sherson, B. Julsgaard, and E.S. Polzik. Deterministic atom-light quantum interface. *Advances in Atomic Molecular and Optical Physics*, 54:82, 2007.

[SM01] A.S. Sørensen and K. Mølmer. Entanglement and extreme spin squeezing. *Physical Review Letters*, 86(20):4431–4434, May 2001.

[SRP+09] J. Stasinska, C. Rodó, S. Paganelli, G. Birkl, and A. Sanpera. Manipulating mesoscopic multipartite entanglement with atom-light interfaces. *Physical Review A*, 80:062304, 2009.

[SSF+06] J. Sherson, A.S. Sørensen, J. Fiurášek, K. Mølmer, and E.S. Polzik. Light qubit storage and retrieval using macroscopic atomic ensembles. *Physical Review A*, 74(1):11802, 2006.

[SSLV10] M.H. Schleier-Smith, I.D. Leroux, and V. Vuletić. States of an ensemble of two-level atoms with reduced quantum uncertainty. *Physical Review Letters*, 104(7):73604, 2010.

[SSP02] C. Schori, J.L. Sørensen, and E.S. Polzik. Narrow-band frequency tunable light source of continuous quadrature entanglement. *Physical Review A*, 66(3):033802, Sep 2002.

[Ste03] D.A. Steck. Cesium D line data. 2003.

[Sto] J. K. Stockton. Adiabatic elimination with a multi-level alkali atom driven off-resonance.

[SZ97] M. Scully and M. Zubairy. *Quantum Optics*. Cambridge, 1997.

[TFNT09] T. Takano, M. Fuyama, R. Namiki, and Y. Takahashi. Spin squeezing of a cold atomic ensemble with the nuclear spin of one-half. *Physical Review Letters*, 102(3):033601, Jan 2009.

[TVLK08] I. Teper, G. Vrijsen, J. Lee, and M.A. Kasevich. Backaction noise produced via cavity-aided nondemolition measurement of an atomic clock state. *Physical Review A*, 78(5):051803, Nov 2008.

[TWK+98] Q.A. Turchette, C.S. Wood, B.E. King, C.J. Myatt, D. Leibfried, W.M. Itano, C. Monroe, and D. J. Wineland. Deterministic entanglement of two trapped ions. *Physical Review Letters*, 81(17):3631–3634, Oct 1998.

[UTK06] K. Usami, J. Takahashi, and M. Kozuma. How to measure the quantum state of collective atomic spin excitation. *Physical Review A*, 74(4):43815, 2006.

[Vai94] L. Vaidman. Teleportation of quantum states. *Physical Review A*, 49:1473–1476, 1994.

[VMC10] K.G.H. Vollbrecht, C.A. Muschik, and J.I. Cirac. Entanglement distillation by dissipation and continuous quantum repeaters. *Arxiv preprint arXiv:1011.4115*, 2010.

[VWC09] F. Verstraete, M.M. Wolf, and J.I. Cirac. Quantum computation and quantum-state engineering driven by dissipation. *Nature Physics*, 5(9):633–636, 2009.

[WBI+92] D. J. Wineland, J. J. Bollinger, W. M. Itano, F. L. Moore, and D. J. Heinzen. Spin squeezing and reduced quantum noise in spectroscopy. *Physical Review A*, 46(11):R6797–R6800, Dec 1992.

[Win08] Patrick Joachim Windpassinger. *Non-destructive quantum state measurements and quantum noise squeezing*. PhD thesis, University of Copenhagen, 2008.

[Wis99] H.M. Wiseman. Squashed states of light: theory and applications to quantum spectroscopy. *Journal of Optics B: Quantum and Semiclassical Optics*, 1:459, 1999.

[WKHW86] Ling-An Wu, H.J. Kimble, J.L. Hall, and Huifa Wu. Generation of squeezed states by parametric down conversion. *Physical Review Letters*, 57(20):2520–2523, Nov 1986.

[WOH+09] P.J. Windpassinger, D. Oblak, U.B. Hoff, A. Louchet, J. Appel, N. Kjaergaard, and E.S. Polzik. Squeezing of atomic quantum projection noise. *Journal of Modern Optics*, 56(18):1993–1998, 2009.

[WZ82] W. K. Wootters and W. H. Zurek. A single quantum cannot be cloned. *Nature*, 299:802–803, October 1982.

[YCZ+08] Z.S. Yuan, Y.A. Chen, B. Zhao, S. Chen, J. Schmiedmayer, and J.W. Pan. Experimental demonstration of a BDCZ quantum repeater node. *Nature*, 454(7208):1098–1101, 2008.

[ZBB+05] P. Zoller, Th. Beth, D. Binosi, R. Blatt, H. Briegel, D. Bruss, T. Calarco, J. I. Cirac, D. Deutsch, J. Eisert, A. Ekert, C. Fabre, N. Gisin, P. Grangiere, M. Grassl, S. Haroche, A. Imamoglu, A. Karlson, J. Kempe, L. Kouwenhoven, S. Kröll, G. Leuchs, M. Lewenstein, D. Loss, N. Lütkenhaus, S. Massar, J. E. Mooij, M. B. Plenio, E. Polzik, S. Popescu, G. Rempe, A. Sergienko, D. Suter, J. Twamley, G. Wendin, R. Werner, A. Winter, J. Wrachtrup, and A. Zeilinger. Quantum information processing and communication. *The European Physical Journal D - Atomic, Molecular, Optical and Plasma Physics*, 36:203–228, 2005. 10.1140/epjd/e2005-00251-1.